

mi.

58 Copies

NATIONAL AERONAUTICS AND SPACE ADMINISTRATION

*Space Programs Summary 37-50, Vol. II*

*The Deep Space Network*

For the Period January 1 to February 29, 1968

GPO PRICE \$ \_\_\_\_\_

CFSTI PRICE(S) \$ \_\_\_\_\_

Hard copy (HC) 3.00

Microfiche (MF) .65

ff 653 July 65

FACILITY FORM 602

N 68-25631  
(ACCESSION NUMBER)

104  
(PAGES)

CR 94862  
(NASA CR OR TMX OR AD NUMBER)

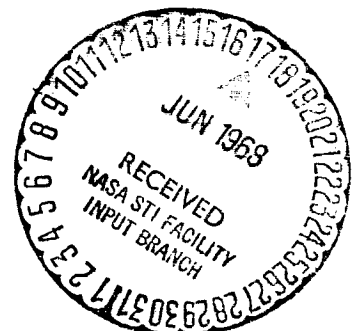
(THRU)

(CODE)

07  
(CATEGORY)

JET PROPULSION LABORATORY  
CALIFORNIA INSTITUTE OF TECHNOLOGY  
PASADENA, CALIFORNIA

March 31, 1968



NATIONAL AERONAUTICS AND SPACE ADMINISTRATION

*Space Programs Summary 37-50, Vol. II*

*The Deep Space Network*

For the Period January 1 to February 29, 1968

JET PROPULSION LABORATORY  
CALIFORNIA INSTITUTE OF TECHNOLOGY  
PASADENA, CALIFORNIA

March 31, 1968



**SPACE PROGRAMS SUMMARY 37-50, VOL. II**

Copyright © 1968

Jet Propulsion Laboratory  
California Institute of Technology

Prepared Under Contract No. NAS 7-100  
National Aeronautics & Space Administration

## Preface

The Space Programs Summary is a bimonthly publication that presents a review of engineering and scientific work performed, or managed, by the Jet Propulsion Laboratory for the National Aeronautics and Space Administration during a two-month period. Beginning with the 37-47 series, the Space Programs Summary is composed of four volumes:

- Vol. I. *Flight Projects* (Unclassified)
- Vol. II. *The Deep Space Network* (Unclassified)
- Vol. III. *Supporting Research and Advanced Development* (Unclassified)
- Vol. IV. *Flight Projects and Supporting Research and Advanced Development* (Confidential)

Approved by:

A handwritten signature in dark ink, appearing to read "W. H. Pickering", is written over a horizontal line.

W. H. Pickering, Director  
Jet Propulsion Laboratory

## Contents

<b>I. Introduction</b>	1
A. Description of the DSN	1
B. Description of DSN Systems	3
1. Telemetry System	
M. L. Yeater	3
<b>II. Mission Support</b>	15
A. Introduction	15
B. Interplanetary Flight Projects	17
1. Pioneer VI Mission Support	
A. J. Siegmeth	17
C. Planetary Flight Projects	26
1. Mariner Mars 1969 Mission Support	
K. W. Linnes	26
D. Manned Space Flight Project	27
1. Apollo Mission Support	
P. S. Goodwin	27
<b>III. Advanced Engineering</b>	34
A. Tracking and Data Acquisition Elements Research	34
1. Low Noise Receivers: Microwave Maser Development, Second Generation Maser Instrumentation	
R. C. Clauss	34
2. Solid State and Superconducting Electronics	
R. W. Berwin	36
3. Improved RF Calibration Techniques: Receiving System Noise-Temperature Calibration	
C. T. Stelzried and T. Y. Otoshi	41
4. Radio Star Tracking at Mars Deep Space Station	
R. E. Cormack	47
5. Receiving System Noise-Temperature Performance at X-Band	
D. A. Bathker	48
6. Efficient Antenna Systems: X-Band Gain Measurements	
D. A. Bathker	49
7. Low- and Medium-Rate Telemetry	
M. H. Brockman	52

## Contents (contd)

B. Communications System Research . . . . .	54
1. Mariner Venus 67 Ranging System Digital Processing Design <i>W. A. Lushbaugh and L. D. Rice</i> . . . . .	54
2. Mariner Venus 67 Ranging System Digital Rack <i>W. A. Lushbaugh</i> . . . . .	56
3. Mariner Venus 67 Ranging System Program <i>L. D. Rice</i> . . . . .	62
4. Programmable RF Attenuator <i>S. Fisher</i> . . . . .	69
5. System Design of a Sequential Decoding Machine <i>W. A. Lushbaugh and J. W. Layland</i> . . . . .	71
6. Subroutines to Permit SDS FORTRAN II to Handle Magnetic Tapes With Arbitrary Formats <i>W. B. Kendall</i> . . . . .	78
7. Digital Processing of the Mariner Venus 67 Occultation Data—Frequency Shifting and Filtering <i>W. B. Kendall</i> . . . . .	80
C. Tracking and Navigational Accuracy Analysis . . . . .	86
1. DSN Inherent Accuracy Project <i>T. W. Hamilton and D. W. Trask</i> . . . . .	86
2. An Approximate Solution to the Estimate of Navigational Accuracy for a Deep Space Probe During the Planetary Encounter Phase <i>L. Kingsland, Jr., and W. E. Bollman</i> . . . . .	90
3. Recent Changes to the Tropospheric Refraction Model Used in the Reduction of Radio Tracking Data From Deep Space Probes <i>A. Liu</i> . . . . .	93
4. Effect of New Tropospheric Corrections on Lunar Orbiter II Cruise Solution Vector <i>N. A. Mottinger</i> . . . . .	97
5. An Algorithm for Integrating Lifetime Orbits in Multirevolution Steps <i>D. Boggs</i> . . . . .	104
6. Preliminary Surveyor VI Postlanded Tracking Data Analysis <i>F. B. Winn</i> . . . . .	110
7. Mariner V Real-Time Cruise and Encounter Orbit Determination Results <i>G. E. Pease</i> . . . . .	125
8. Pioneer VIII—A Comparison of the Preflight Nominal and Actual Trajectories <i>J. F. Gallagher</i> . . . . .	141

## Contents (contd)

<b>IV. Development and Implementation</b>	143
A. SFOF Development	143
1. Advanced Data Systems Project: Higher Level Programming Language	
<i>W. N. Walker</i>	143
2. Advanced Data Systems Project: Operating System Recommendations	
<i>R. E. Loesh</i>	144
3. SFOF Mission Display System	
<i>C. A. Yamarone and C. J. DeForrest</i>	146
4. Communications Processor/7044 Computer Redesign System Test Series	
<i>R. G. Polansky</i>	150
B. GCF Development	151
1. Configuration Changes	
<i>F. E. Bond, Jr.</i>	151
C. DSIF Development	151
1. 210-ft Antenna Tower Positional Stability	
<i>H. D. McGinness</i>	151
2. 210-ft Antenna Quadripod Structural Analysis	
<i>M. S. Katow and S. R. Paine</i>	158
3. 450-kW Transmitter Mechanical Design	
<i>C. P. Wiggins and V. B. Lobb</i>	161
4. High-Power Tests of 2388-MHz Feed	
<i>R. L. Leu and M. A. Gregg</i>	163
5. Lunar Bounce Clock Synchronization Project	
<i>J. R. Smith</i>	165
6. Venus DSS Operations	
<i>E. B. Jackson, J. D. Campbell, M. A. Gregg, and A. L. Price</i>	165
7. DSIF Station Control and Data Equipment	
<i>E. Bann, R. N. Flanders, A. Burke, J. K. Woo, D. Hersey, P. C. Harrison, and E. A. Garcia</i>	166
8. DSIF/Ground Communications Interface Assembly	
<i>E. A. Garcia</i>	168
9. DSIF Control Room Reconfiguration	
<i>R. L. Weber</i>	172
10. Compatibility Test Area Antenna Mechanical Installation	
<i>C. Lundy</i>	174
11. Compatibility Test Area Implementation	
<i>R. C. Rydgig</i>	175

## Contents (contd)

12. Bolt Characteristics Test Program—Phase 2	
<i>V. B. Lobb and D. L. Lambdin</i>	177
13. Antenna Mechanical Field Instrumentation Modules	
<i>C. Lundy and D. L. Lambdin</i>	179
14. DSN S-Band Receiver—Exciter Upgrade	
<i>J. H. Wilcher and C. Chatburn</i>	181
15. DSIF Monitor System Phase I Program	
<i>R. M. Thomas</i>	181
<b>V. Operations and Facilities</b>	186
A. SFOF Operations	186
1. SFOF Training Program	
<i>L. H. White and G. S. Voden</i>	186
B. GCF Operations	187
1. Flight Project Support	
<i>F. E. Bond, Jr.</i>	187
C. Facility Engineering	187
1. Feeder Selectivity Switching Between Generated and Commercial Power Services at Deep Space Tracking Stations	
<i>L. H. Kushner</i>	187
2. SFOF Uninterruptible Power System	
<i>W. C. Tiedge and J. G. Grosch</i>	189
3. Robledo de Chavela Foundation Study	
<i>A. A. Riewe</i>	191
4. DSIF Communications Facilities	
<i>E. L. Yinger</i>	196
5. Goldstone DSCC Minor Construction Progress	
<i>W. W. Lord and B. M. Sweetser</i>	196

# I. Introduction

## A. Description of the DSN

The Deep Space Network (DSN), established by the NASA Office of Tracking and Data Acquisition under the system management and technical direction of JPL, is responsible for two-way communications with unmanned spacecraft traveling approximately 10,000 mi from earth to interplanetary distances. It supports, or has supported, the following NASA deep space exploration projects: *Ranger*, *Surveyor*, *Mariner Venus 1962*, *Mariner Mars 1964*, *Mariner Venus 67*, and *Mariner Mars 1969* (JPL); *Lunar Orbiter* (Langley Research Center); *Pioneer* (Ames Research Center); and *Apollo* (Manned Spacecraft Center), as backup to the Manned Space Flight Network (MSFN). The DSN is distinct from other NASA networks such as the MSFN, which has primary responsibility for tracking the manned spacecraft of the *Apollo* Project, and the Space Tracking and Data Acquisition Network (STADAN), which tracks earth-orbiting scientific and communications satellites.

The three basic functions performed by the DSN in support of each flight project are as follows:

- (1) *Tracking*. Accomplished by radio communication with the spacecraft, tracking provides such metric data as angles, radial velocity, and range (distance from the earth to the spacecraft).

- (2) *Data acquisition*. Using the same radio link, the data acquisition function consists of the recovery of information from the spacecraft in the form of telemetry, namely, the engineering measurements recorded by the spacecraft and the scientific data obtained by the onboard instruments.
- (3) *Command*. Using the same radio link, the command function involves sending information to the spacecraft to initiate equipment which, for example, operates propulsion systems for changing the trajectory of the spacecraft, changes data transmission rate to earth, or reprograms onboard computers which determine the sequence of spacecraft engineering events.

The DSN can be characterized as a set of the following systems: (1) telemetry, (2) tracking, (3) command, (4) monitoring, (5) simulation, and (6) operations control. Alternately, it can be considered as being comprised of three facilities: the Deep Space Instrumentation Facility (DSIF), the Ground Communications Facility (GCF), and the Space Flight Operations Facility (SFOF).

The DSIF is a worldwide set of deep space stations (DSSs) that provide basic radio communications with spacecraft. These stations and the deep space communications complexes (DSCCs) they comprise are as follows:

Pioneer, Echo, and Mars DSSs (and Venus DSS, described later), comprising the Goldstone DSCC in California; Woomera, Tidbinbilla, and Booroomba<sup>1</sup> DSSs, comprising the Canberra DSCC in Australia; Johannesburg DSS in South Africa; and Robledo, Cebreros, and Rio Cofio<sup>1</sup> DSSs, comprising the Madrid DSCC in Spain. The overseas stations are normally staffed and operated by government agencies of the respective countries, with some assistance from U.S. support personnel.

In addition, the DSIF operates a spacecraft monitoring station at Cape Kennedy, which is used for verifying flight-spacecraft/DSN compatibility prior to launch, and a flight-project/tracking and data system interface laboratory at JPL, which is used during the development of the spacecraft to assure a design compatible with the network. A spacecraft guidance and command station on Ascension Island serves to track the spacecraft in the latter part of the launch trajectory while the spacecraft is relatively low in altitude.

To enable continuous radio contact with spacecraft, the stations are located approximately 120 deg apart in longitude; thus, a spacecraft in flight is always within the field-of-view of at least one station, and for several hours each day may be seen by two stations. Furthermore, since most spacecraft on deep space missions travel within 30 deg of the equatorial plane, the stations are located within latitudes of 45 deg north or south of the equator.

Radio contact with a spacecraft usually begins when the spacecraft is on the launch vehicle at Cape Kennedy, and it is maintained throughout the mission. The early part of the trajectory is covered by selected network stations of the Air Force Eastern Test Range (AFETR) which are managed by the Goddard Space Flight Center. Normally, two-way communications are established between the spacecraft and the DSN within 30 min after the spacecraft has been injected into lunar, interplanetary, or planetary flight. The Cape Kennedy DSS, having supported the preflight compatibility tests, monitors the spacecraft continuously during the launch phase until it passes over the local horizon. The deep space phase begins with acquisition by either the Johannesburg, Woomera, or Tidbinbilla DSS. These stations, with large antennas, low-noise phase-lock receiving systems, and high-power transmitters, provide radio communications to the end of the flight. By international agreement, the

radio frequencies assigned for these functions are 2290–2300 MHz for spacecraft-to-earth downlink data transmission and 2110–2120 MHz for earth-to-spacecraft command and uplink data transmission.

To maintain a state-of-the-art capability, research and advanced development work on new components and systems has been conducted continuously at JPL since the establishment of the DSN. To support this work, the Goldstone DSCC has a research and development facility designated the Venus DSS, at which the feasibility of new equipment and techniques to be introduced into the operational network is demonstrated. When a new piece of equipment or new technique has been accepted for integration into the network, it is classed as Goldstone duplicate standard (GSDS), thus standardizing the design and operation of identical items throughout the network.

The GCF, using, in part, facilities of the worldwide NASA Communications Facility (NASCOM, managed and directed by the Goddard Space Flight Center), provides voice, high-speed data, and teletype communications between all stations of the network. Communications between the Goldstone DSCC and the SFOF are provided by a microwave system leased from common carriers. This microwave link has made possible the transmission, in real time, of video data received at the Goldstone DSCC to the SFOF and then to commercial TV systems, as was done during the *Ranger* and *Surveyor* missions.

The SFOF, located at JPL, receives data from all of the tracking stations and processes that information required by the flight project to conduct flight operations. Voice and data channels are distributed throughout the facility, and the following equipment and services are provided: (1) data-processing equipment for the real-time handling and display of tracking and telemetry data; (2) real-time and non-real-time telemetry processing; (3) simulation equipment for flight projects, as well as for network use in training of personnel; (4) monitoring equipment for evaluation of network performance in near-real time; (5) operations control consoles and status and operational display facilities required for the conduct of flight operations; and (6) technical areas for flight project personnel who analyze spacecraft performance, trajectories, and generation of commands, as well as support services required to carry out those functions, such as internal communications by telephone, intercom, public address, closed-circuit TV, documentation, and

<sup>1</sup>Not yet authorized.



reproduction of data packages. The SFOF is equipped to support many spacecraft in flight and those under test in preparation for flight; e.g., over a 24-h period during 1967, as many as eight spacecraft in flight or in operational-readiness tests for flight were supported by the SFOF.

Thus, the DSN simultaneously conducts research and development for support of future flight projects, implements demonstrated capabilities for support of the more immediate flight projects, and provides direct support for the currently active missions, while accommodating differences in the individual projects. In this and future issues of the SPS, Vol. II, the current technical activities of the DSN in these three general categories will be reported under the following subject areas:

#### Introduction

- Description of the DSN

- Description of DSN Systems

#### Mission Support

- Introduction

- Interplanetary Flight Projects

- Planetary Flight Projects

- Manned Space Flight Project

#### Advanced Engineering

- Tracking and Data Acquisition Elements Research

- Communications System Research

- Tracking and Navigational Accuracy Analysis

- Supporting Research and Technology

#### Development and Implementation

- SFOF Development

- GCF Development

- DSIF Development

- DSN Project and System Development

#### Operations and Facilities

- DSN Operations

- SFOF Operations

- GCF Operations

- DSIF Operations

- Facility Engineering

In the subsection entitled "Description of DSN Systems," the status of recent developments for each of the six DSN systems listed above will be described. The more fundamental research carried out in support of the DSN is reported in Vol. III of the SPS, and JPL flight project activities for those missions supported by the DSN are reported in Vol. I.

## B. Description of DSN Systems

### 1. Telemetry System, M. I. Yeater

**a. Functions.** The DSN telemetry system serves to provide: (1) telemetry data to the flight project in both real time and non-real time, and (2) real-time spacecraft engineering data required for mission support operations to DSN and flight project personnel. The general functions performed on the telemetry data streams are data acquisition, handling/processing at the DSS, transmission, handling/processing at the SFOF, validation, and master data record (MDR) generation. The general data flow and the functions performed are illustrated in Fig. 1. The complexity of the data handling/processing at the DSS and SFOF varies depending on mission requirements and data types.

**b. System elements.** The subsystems and equipment of the DSIF that comprise, or contribute to the operation of, the current DSN telemetry system are as follows (Fig. 2):

- (1) DSS receiver subsystem.
- (2) Analog recording subsystems.
- (3) Mission-dependent data-handling equipment (MDE).
- (4) Telemetry and command processor (TCP), consisting of hardware and mission-related software.
- (5) Data transmission equipment (DSS/GCF interface), consisting of high-speed data channels and teletype channels.

Those of the SFOF (shown in Fig. 3), are:

- (1) Data transmission equipment (GCF/SFOF interface), consisting of high-speed data channels and teletype channels.
- (2) Telemetry processing system (TPS), consisting of programmed data processor (PDP) 7s and high-speed data channels.
- (3) IBM 7044 processor, consisting of hardware, software, and both mission-independent and mission-dependent programs.
- (4) IBM 7094 processor, consisting of hardware, software, and both mission-independent and mission-dependent programs.
- (5) Input/output (I/O) and display devices.

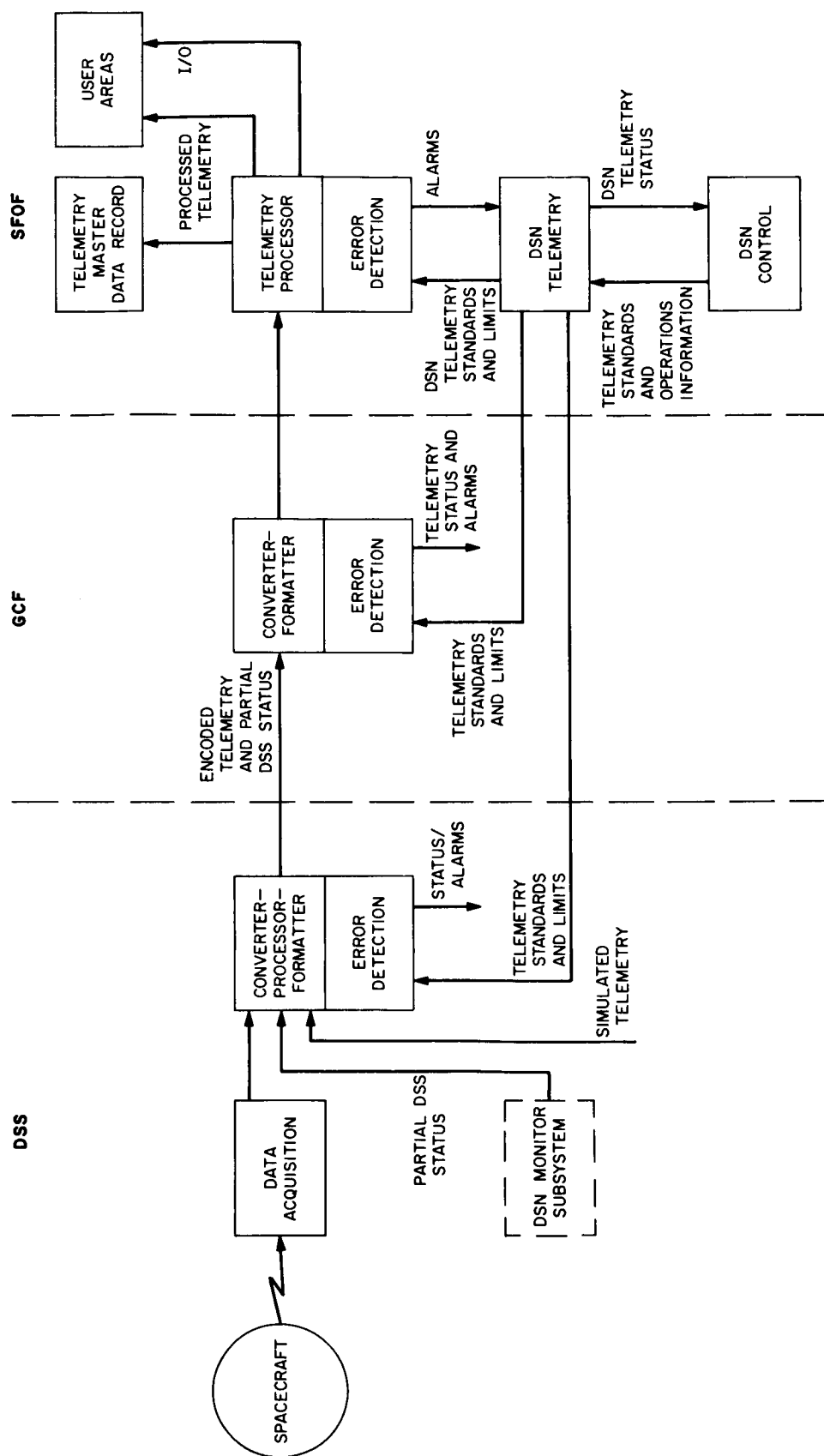


Fig. 1. DSN telemetry system

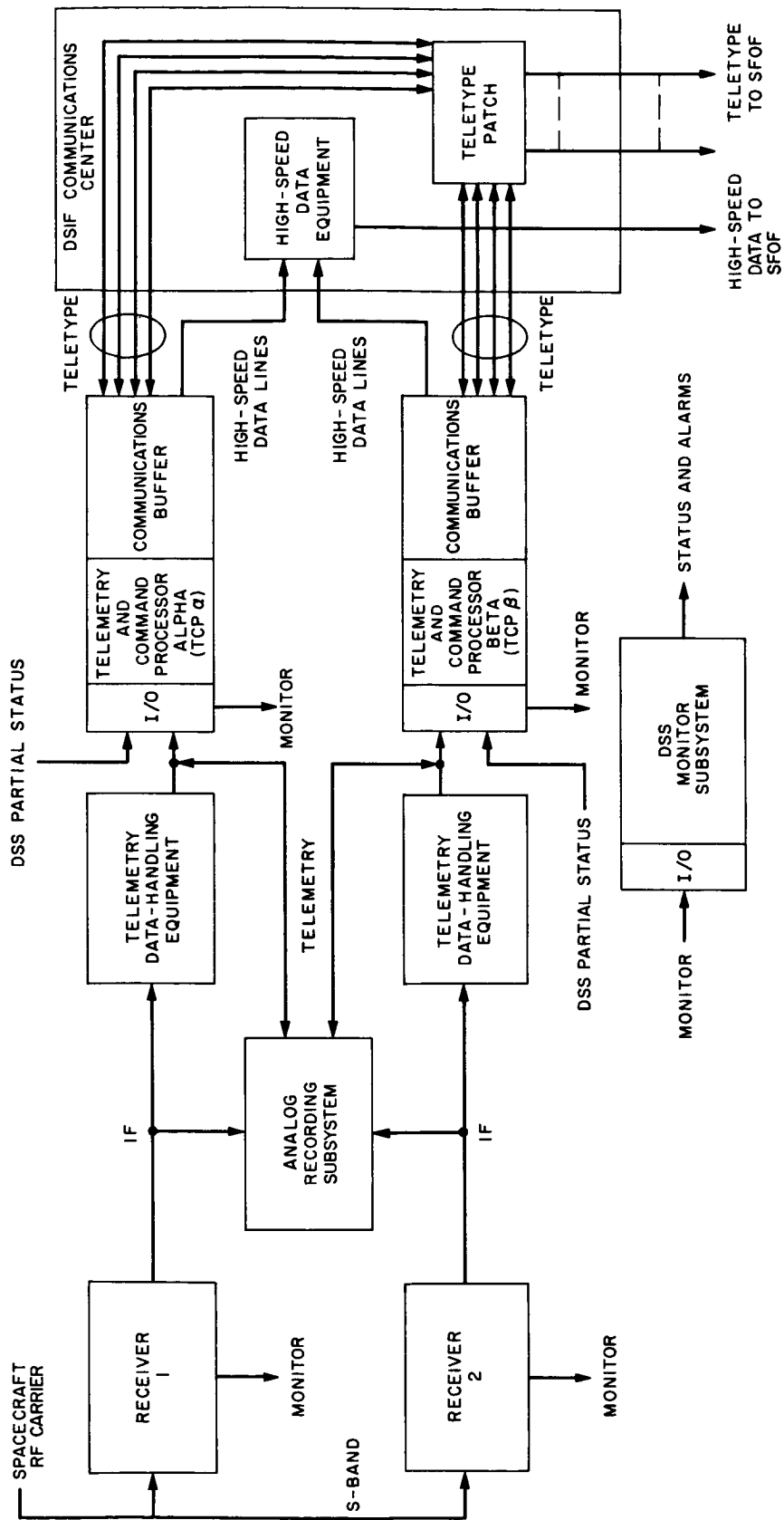


Fig. 2. DSS data-handling system

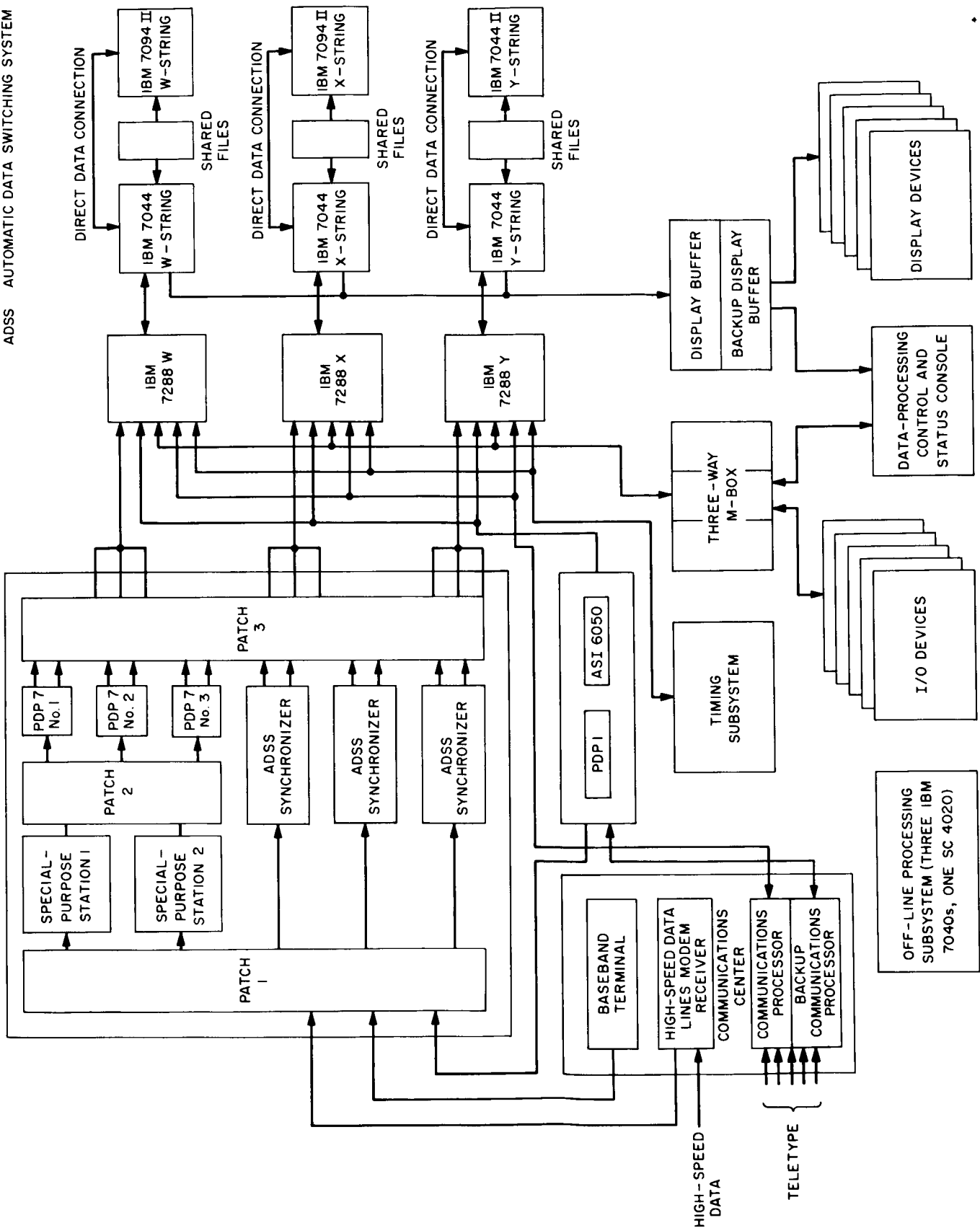


Fig. 3. SFOF data-handling system

### c. .System operation/subsystem description

**Data acquisition.** The data acquisition function, essentially the same for all data types, is provided by the receiver and analog recording subsystems. Following the lockup of the RF carrier in the DSS receiver, the composite telemetry signal with the necessary receiver status information is provided to the on-site data-handling equipment and to the analog recording subsystem for a backup data record (Fig. 2).

Each DSS receiver subsystem has two receivers, both of which provide the following telemetry channel outputs:

- (1) Channel A: 10-MHz fixed-bandwidth predetected IF spectrum.
- (2) Channel B: 10-MHz predetected IF spectrum with four selectable predetection bandwidths.
- (3) Channel C: 50-MHz IF bandwidth for reception of wide-band frequency-modulated spectrum.

Each analog recording subsystem consists of two Ampex-type FR-1400 tape machines with direct record/reproduce, wide-band FM record/reproduce, and digital record/reproduce capabilities.

**Handling/processing at the DSS.** Historically, the handling/processing function at the DSS has been accomplished by a set of MDE provided by each flight project. The TCP subsystem was added at each DSS as the first step toward making the DSS data-handling function less mission-dependent. The data-handling function in the current telemetry system is provided by the TCP with a mission-dependent software package and a set of MDE for each flight project. The telemetry data stream can be processed in real time and formatted for transmission to the SFOF. The processing can include the following operations:

- (1) Detection and bit synchronization.
- (2) Decommulating.
- (3) Editing.
- (4) Formatting.
- (5) Timing insertion.
- (6) Digital recording of formatted data.

The amount of processing in the MDE versus that in the TCP varies from project to project. For example, the

*Pioneer* Project MDE provides the capability for the functions of demodulation, synchronization, and bit detection and buffering for parallel transfer of the data to the TCP. In addition, it provides checkout equipment such as a test transponder, data-format generator, error-rate tester, module tester, and display equipment. The TCP/telemetry software functions are:

- (1) Frame/word synchronization.
- (2) Decommutation.
- (3) Determination of telemetry format and mode.
- (4) Computation of telemetry bit error rates.
- (5) Limit checking for certain engineering data words.
- (6) Typeout of calibrated data.
- (7) Editing and formatting of telemetry data for teletype output.

Certain changes are being made to this part of the DSN telemetry system for support of the *Mariner* Mars 1969 missions. (The anticipated DSIF and SFOF/GCF configurations for the *Mariner* Mars 1969 missions are shown in Figs. 4 and 5, respectively.) The DSN is developing a set of equipment to function as a telemetry demodulator and bit synchronizer between the DSS receiver and the TCP. This hardware is intended to provide a mission-independent capability for recovery of telemetry data streams at rates of up to 512 bits/s to eliminate the need for telemetry MDE at the DSS. This equipment, referred to as the Multiple-Mission Telemetry System (MMTS), is described in detail in SPS 37-46, Vol. III, pp. 175-243. Further progress is reported in this issue of the SPS, Vol. II.

In addition to the MMTS capability, the DSN is developing a prototype high-rate telemetry (HRT) demodulator subsystem to be demonstrated during the *Mariner* Mars 1969 missions for handling a high-rate (16.2-kbits/s Reed-Muller biorthogonal encoded) data stream. The equipment will be connected between the S-band receiver and a TCP computer and will perform demodulation and decoding of the telemetry stream. The TCP computer will write the decoded data stream on digital magnetic tape. The HRT Project was first reported in SPS 37-48, Vol. II, pp. 83-130. Further progress is reported in this issue. A functional diagram of the DSIF telemetry system with a prototype HRT subsystem is given in Fig. 6.

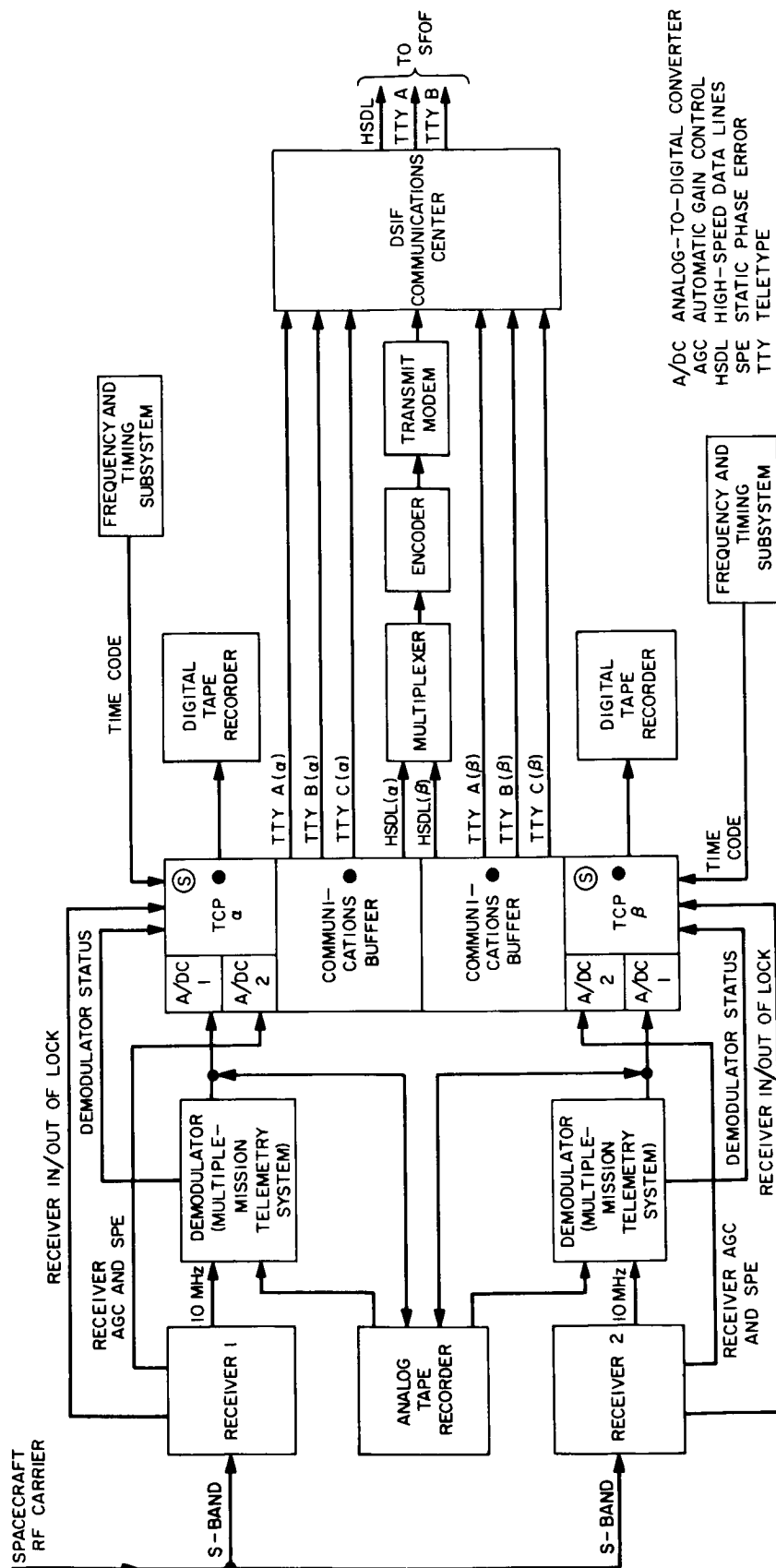


Fig. 4. DSIF telemetry system configuration for Mariner Mars 1969 missions

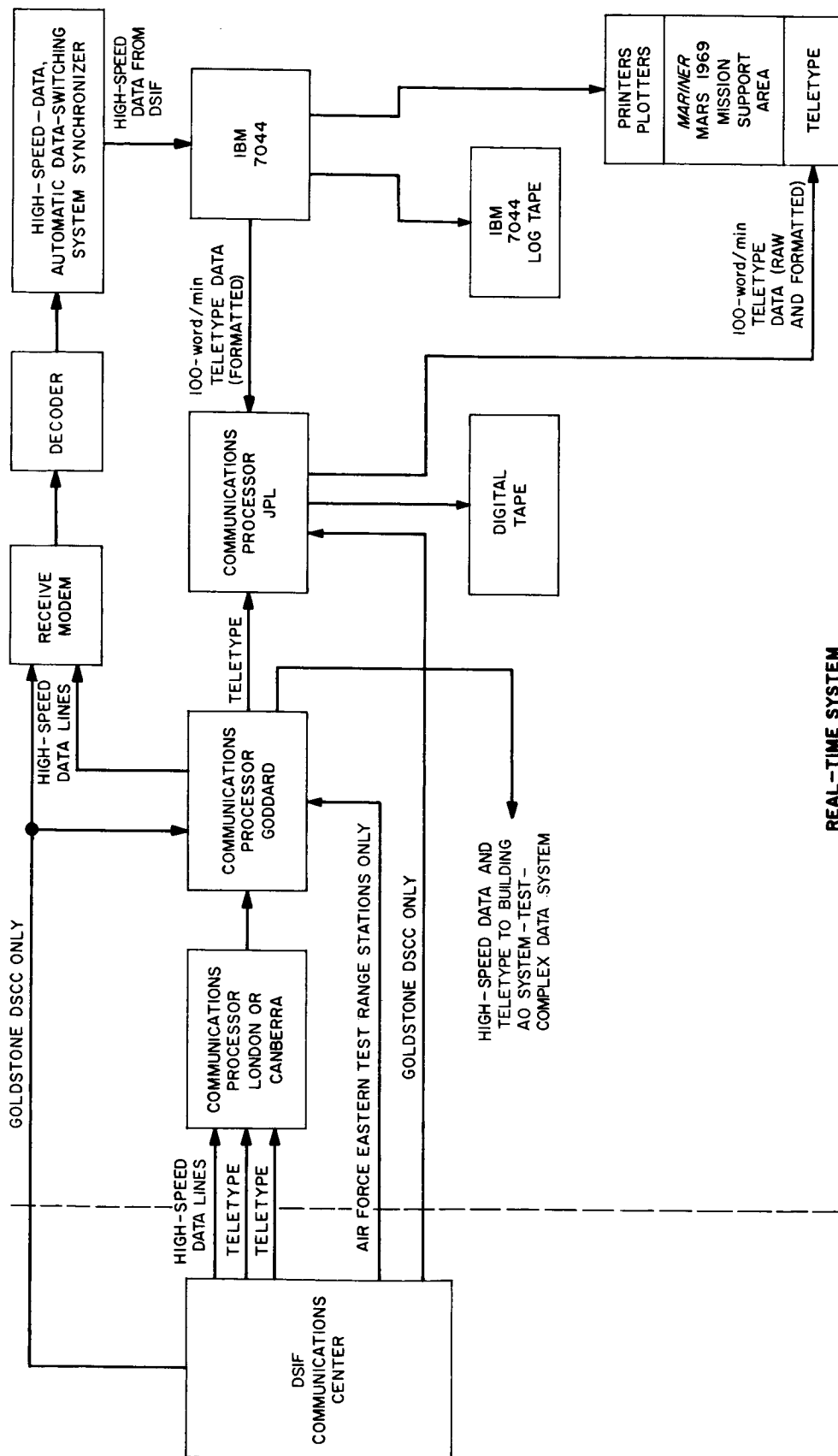


Fig. 5. SFOF/GCF telemetry system configuration for Mariner Mars 1969 missions

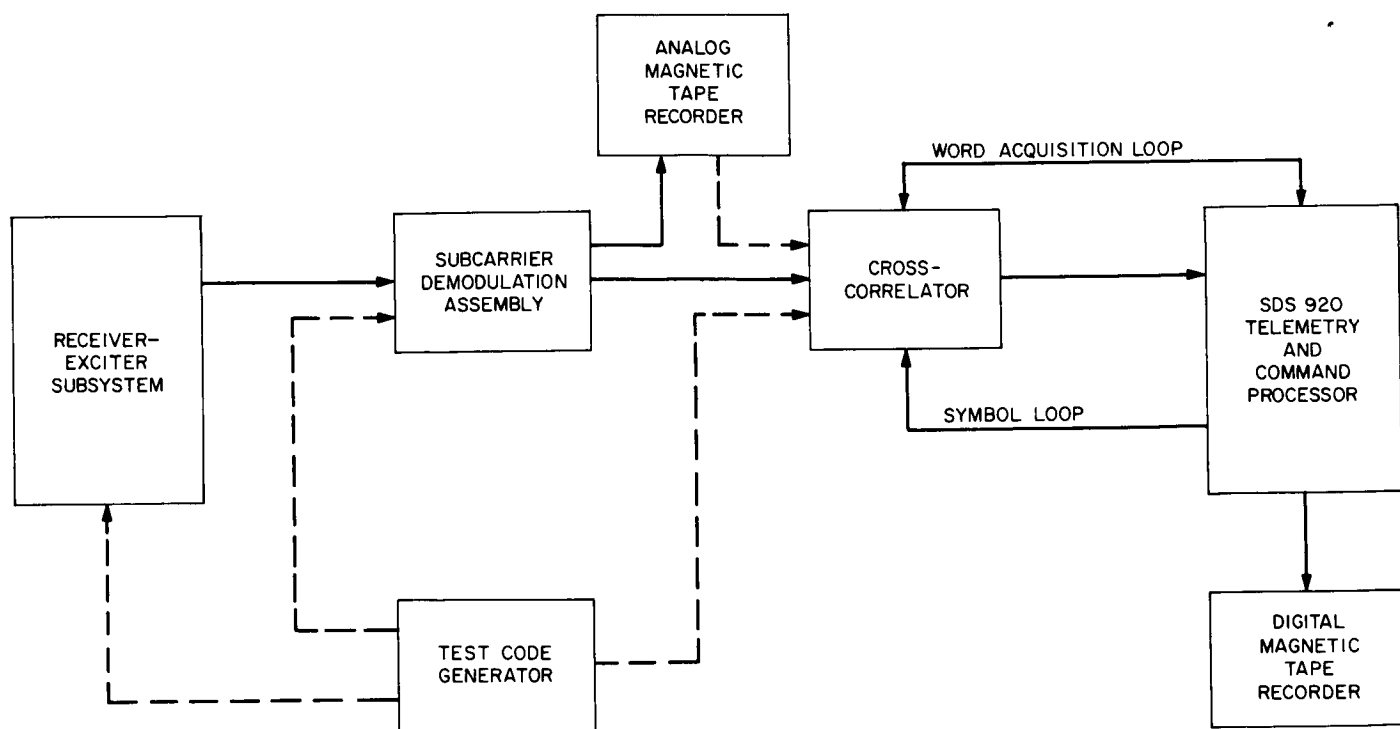


Fig. 6. DSIF telemetry system with prototype HRT subsystem

The TCP subsystem, comprised of two independent processing assemblies, provides a redundant telemetry data-processing capability. It also serves to provide a standardized interface to flight project MDE and the GCF interface, including high-speed data lines and teletype. A functional block diagram of the TCP subsystem is given in Fig. 7. Each data path consists of:

- (1) An SDS 920 digital computer with standard peripheral equipment.
- (2) Auxiliary I/O and interrupt devices.
- (3) A magnetic tape recording unit.
- (4) DSS subsystem data interface and conversion equipment.
- (5) A communications buffer assembly for high-speed and teletype data.

The general characteristics of the computers are: 16,384-word core memory, W- and Y- I/O buffers with 24-bit word register and 6-bit character register, power-fail-safe assembly, priority interrupt channels with interrupt arming, and memory interlace control with the Y-buffer. The computer peripheral equipment consists

of the following standard units (described in detail in Ref. 1):

- (1) Paper tape reader (300 characters/s).
- (2) Paper tape punch (60 characters/s).
- (3) I/O keyboard/printer (prints at 10 characters/s).
- (4) Keyboard/punch coupler.
- (5) Magnetic tape unit (200 characters/in.).
- (6) Communications buffer assembly.
- (7) Parallel input (PIN) and parallel output (POT) capabilities.

Each communications buffer provides for communication of telemetry data between the TCP and the SFOF via common carrier facilities, namely, four duplex teletype lines and one high-speed data line.

The interface with the flight project MDE is through the MDE patch panel unit, which can connect three sets of MDE. The patch panel provides for rapid switching of the MDE between the TCP  $\alpha$  and  $\beta$  computers. The DSS data interface to the TCP is now being upgraded to include a standard set of input channels for the MMTS and HRT equipment. These and other changes to the TCP have been described in the *Deep Space Network*



# OPERATIONAL COMMUNICATIONS SYSTEM INTERFACE

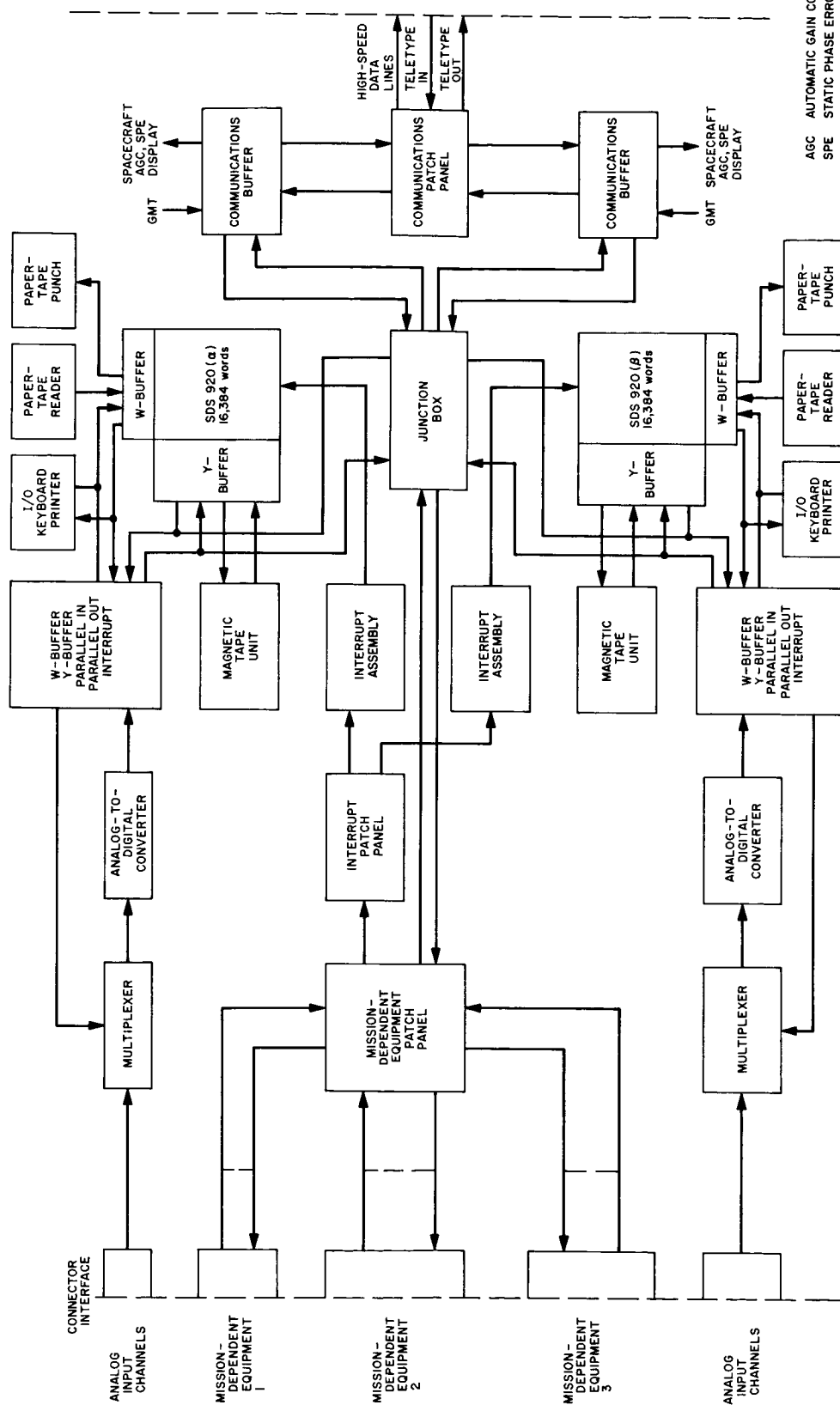


Fig. 7. Telemetry and command processor (TCP)

SPS volume under "DSIF Station Control and Data Equipment," beginning with SPS 37-41.

**Transmission.** The standard real-time transmission mediums for telemetry data from the DSS to the SFOF are the high-speed data line (2400 bits/s serial) and teletype. Non-real-time transfer of data is accomplished by shipment of analog and/or digital tapes for validation and sometimes processing in the TPS in the SFOF. Requirements for validation and processing of analog and digital tapes vary, depending on the flight project.

**Handling/processing at the SFOF.** The on-line computing equipment in the SFOF consists of multiple computer strings, each consisting of an IBM 7044 computer with a drum, an IBM 7094 II computer, and a shared IBM 1301 disk. The IBM 7044, which serves as the I/O processor, has an IBM 7288 data communications channel. The two major software elements within the 7044/7094 system are the 7044/7094 mission-independent program (MIP) and a mission-dependent program (MDP).

The SFOF data-processing system provides the capability to acquire spacecraft telemetry from one or more missions and to manipulate, analyze, and output formatted information regarding this data to the user areas for mission analysis and control. A detailed description of the data-processing system was presented in SPS 37-46, Vol. III, pp. 164-172.<sup>2</sup> The hardware elements of the system are shown in Fig. 3. All incoming data from the DSS are received into the IBM 7044 and the MIP from either the communications processor by teletype or by high-speed-data ADSS through the TPS. All telemetry data flow to and from the MDP is through the MIP. This flow of data is illustrated in Fig. 8.

(1) Flow of communications processor transmitted telemetry. The trap supervisor (TRSP) handles the trap generated by the communications processor, adds several control words, inserts the data as a logical record into the raw data buffer (RWDB) and the communications processor input buffer (CPIB), and causes turn-on of the mission-independent communications processor input program (CPIP). The RWDB is the buffer from which all input data are logged onto tape and to the disk where

the IBM 7094 programs can access the data. During its operation, the CPIP sorts all input data into the appropriate buffers and causes turn-on of the appropriate programs. For telemetry, the buffers are the mission-dependent input buffers TELB 1 and TELB 2, and the programs are the proper portions of the mission-dependent processors 1 and 2. Outputs generated by the respective portions of the mission-dependent processors may be directed to user area printers, plotters, and teletype circuits through the use of the IBM 7044 mission-independent output functions.

(2) Flow of TPS transmitted telemetry. The TRSP handles the trap generated by the TPS, adds control words, inserts the data as a logical record into the RWDB and the TPS input buffer (TPIB), and causes turn-on of the mission-independent TPS input program (TPIP). During its operation, the TPIP sorts all input data into the appropriate buffers and causes turn-on of the appropriate programs. For telemetry, the buffers are the mission-dependent input buffers TPSB 1 and TPSB 2, and the programs are the proper portions of the mission-dependent processors.

The MDPs are spacecraft-oriented and are generally unsuitable for any mission other than the one for which they are designed. The present system is designed so that two MDPs can operate in the IBM 7044 with the MIP. The interfaces with the MIP are the same for all MDPs.

The complexity of each MDP varies for different flight projects. For example, the *Pioneer* Project has no MIP for telemetry in the SFOF data-processing system, for all real-time processing is done at the DSS TCP. The *Mariner* Mars 1969 Project will process both engineering and science data in real time in the IBM 7044 system and engineering, science, and video data in non-real time in the IBM 7094 system.

**Telemetry data validation/MDR generation.** A principal function of the DSN in the acquisition of telemetry data for a flight project is the presentation of the data in a "suitable" form. The data validation function is necessary to verify that the DSN commitments to the flight project have been met. It consists of determining a measure of data quality and quantity based upon such items as:

(1) DSN monitor parameters, such as DSS receiver and demodulator lock status, telemetry data signal-to-noise ratio from the TCP, data-outage-period detections, and isolation of causes of data outages (e.g., TCP, GCF, IBM 7044, and MIP).

<sup>2</sup>The high-speed data input through the TPS has been updated to handle high-speed data blocks in the new NASCOM high-speed-data automatic data switching system (ADSS) format. This blocking of data and inserting of headers for routing allows multiple users to share a single high-speed data line. The multiplexer from the TCP to the high-speed data lines in Fig. 4 should be noted, as should the replacement of phone line formatters (PLF) by the ADSS synchronizer in the TPS area in Fig. 3.

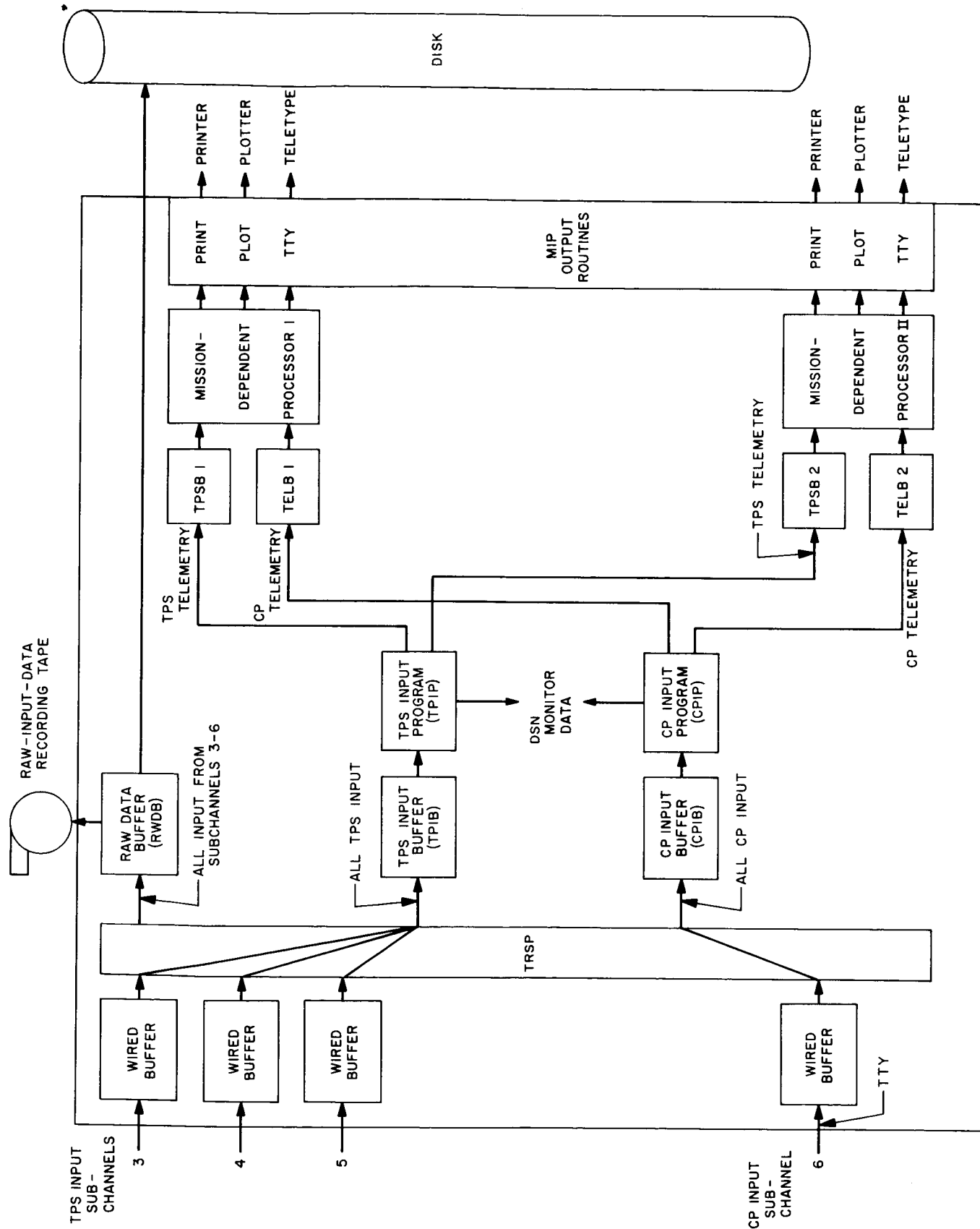


Fig. 8. Telemetry data flow in IBM 7044 system

(2) Certification of data on original data tapes.

In general, the DSN commitment to a flight project for an MDR has consisted of providing validated original data records (ODRs) to the flight project. The ODRs, depending on the flight project, could be the FR 1400 analog tapes from the DSS (*Pioneer* Project), the digital tapes generated by the TCP (*Mariner* Mars 1969 Project), or the IBM 7044 raw data log tapes.

The TPS (PDP 7 computer and validation program) in the SFOF provides for off-line processing, examination of the content of the analog and TCP digital tapes, and performance of the validation function. A detailed description of the TPS was presented in SPS 37-46, Vol. III, pp. 164-172.

**Reference**

1. *Publication 90009*. Scientific Data Systems, Inc., Santa Monica, Calif.

## II. Mission Support

### A. Introduction

The DSN, as part of the Tracking and Data System (TDS) for a flight project, is normally assigned to support the deep-space phase of each mission. Thus far, responsibility for providing TDS support from liftoff until the end of the mission has been assigned to the JPL Office of Tracking and Data Acquisition. A TDS Manager, appointed by the Office of Tracking and Data Acquisition for each flight project, works with the JPL technical staff at the AFETR to coordinate the support of the AFETR, MSFN, and NASCOM with certain elements of the DSN needed for the near-earth-phase support. A DSN Manager and DSN Project Engineer, together with appropriate personnel from the DSIF, GCF, and SFOF, form a design team for the planning and operational phases of flight support. A typical functional organization chart for *operations* is shown in Fig. 1.

Mission operations *design* is accomplished in a closely coordinated effort by the Mission Operations System (MOS) and TDS Managers. Mission operations, an activity distinct from the management element MOS, includes: (1) a data system, (2) a software system, and (3) an operations system. The data system includes all earth-based equipment provided by all systems of the flight project for the receipt, handling, transmission, pro-

cessing, and display of spacecraft data and related data during mission operations. Except for relatively small amounts of mission-dependent equipment supplied by the flight project, all equipment is provided and operated by the DSN. In the near-earth phase, facilities of the AFETR and the MSFN are included. The DSN also operates and maintains the mission-dependent equipment.

The software system includes all computer programs and associated documentation. The mission-independent software is provided as part of the DSN support. The mission-dependent software developed by the flight project is operated and maintained for the project by the DSN.

The operations system includes the personnel, plans, and procedures provided by both the MOS and TDS which are required for execution of the mission operations. The mission operations design organization is supported by the DSN in the manner shown in Fig. 2. The DSN Project Engineer heads a design team composed of project engineers from various elements of the DSIF, GCF, and SFOF. This team is primarily concerned with the data system defined above. The designs of the other systems are the responsibilities of the software system design team and the mission operations design team. The DSN supports these activities through its representative, the DSN Project Engineer.

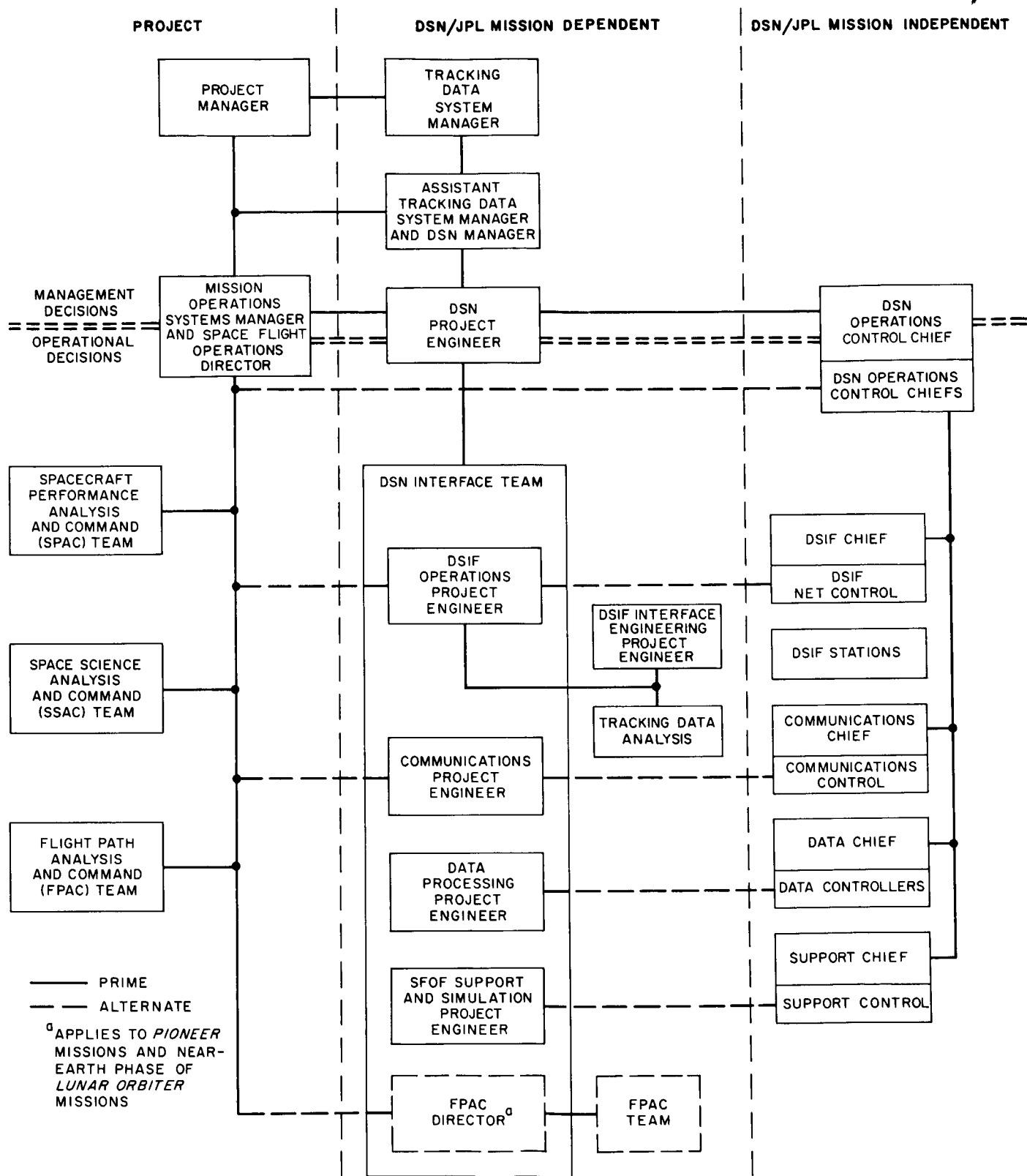
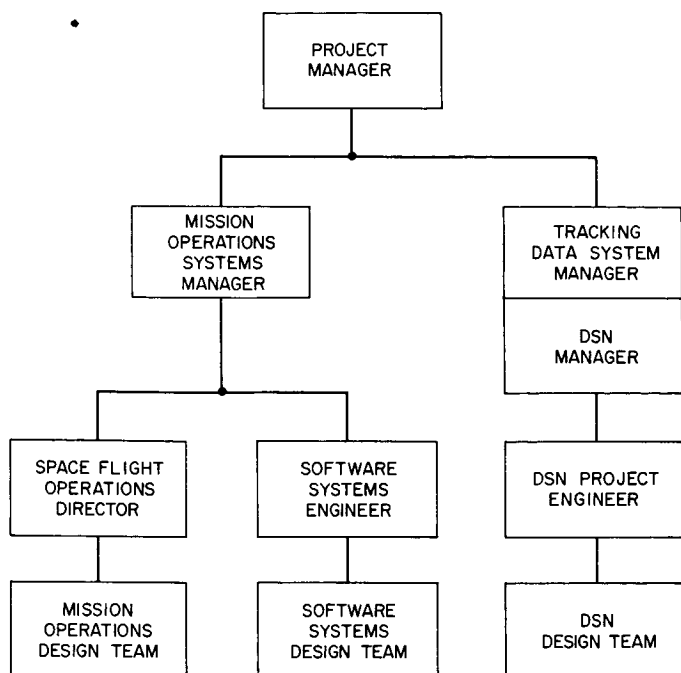


Fig. 1. Typical functional organization for DSN mission support operations



**Fig. 2. Mission operations design organization**

The mission operations design process which the DSN supports is shown in Fig. 3. From the Project Development Plan and the Mission Plan and Requirements are derived the guidelines for operational planning and the project requirements for TDS support. The mission operations design team formulates system-level functional requirements for the data, software, and operations systems. From these requirements, as well as from the TDS support requirements, the DSN design team formulates the DSN configuration to be used in support of the project. It also supports, through the DSN Project Engineer, the activities of the software and mission operations design teams in designing the software and operations systems. The interface definitions are accomplished by working groups from these design teams.

The TDS support required by the project is formulated in the Support Instrumentation Requirements Document (SIRD) and the Project Requirements Document (PRD). The PRD states project requirements for support by the U.S. Department of Defense through the AFETR. The NASA Support Plan (NSP) responds to the SIRD in describing the DSN, NASCOM, and MSFN support.

## **B. Interplanetary Flight Projects**

### **1. Pioneer VI Mission Support, A. J. Siegmeth**

*a. Introduction.* Previous issues of the *Deep Space Network* SPS volume contained reports on specialized

DSN support services rendered for the *Pioneer VI*, *VII*, and *VIII* missions. The overall DSN operational support for the *Pioneer VI* mission is summarized here. A detailed description of the mission is presented in Ref. 1. Future issues of the SPS, Vol. II, will contain similar summaries of the overall DSN operational support for the *Pioneer VII* and *VIII* missions.

### *b. DSN commitment for Pioneer VI mission support.*

The extent to which the facilities, equipment, and personnel of the DSN were committed to support of the *Pioneer VI* mission was officially defined on January 7, 1965. The hardware, software, and organizational interfaces between the *Pioneer VI* mission and the DSN were also established at that time. The functional organization was that shown in Fig. 1 (Section A). The DSN commitment included the furnishing of a medium-accuracy orbit for *Pioneer VI* and the development, jointly with the *Pioneer* Project, of all hardware, software, and interface documentation which was necessary to ensure efficient teamwork between the project and DSN management.

The Johannesburg, Tidbinbilla, Echo, and Cape Kennedy DSSs were assigned for basic support of the *Pioneer VI* mission. The Echo DSS was committed for one complete pass per day for the first 30 days; beginning on the thirty-first day until the end of the mission, three complete passes per week were planned. The Tidbinbilla DSS was committed for one complete pass per day for the first 30 days. The Johannesburg DSS was committed for one complete pass per day during the first four days of the mission. In addition, it was planned, within the limits of DSN loading and station availabilities, to use any or all of these stations to provide a minimum average coverage of the equivalent of one pass per day from the thirty-first day to the end of the mission. The Robledo, Pioneer, and Woomera DSSs, which were not equipped with *Pioneer* mission-dependent ground operating equipment, would also be available on an emergency backup basis to track and record the telemetry subcarrier on magnetic tape.

It was intended to meet all of the *Pioneer* Project's basic requirements for support of the *Pioneer VI* mission, with the understanding that, should circumstances permit, the maximum requirements would be met. Since the time of the original commitment, revisions were made, on a periodic basis, as required to meet the changing needs of the *Pioneer* Project and to make the commitment compatible with the advancing capabilities of the DSN. At the time of the commitment, the DSN had





capabilities to support the *Pioneer VI* mission only during the first 8 mo after launch. It was stipulated that, if the telemetry bit error rate reached an unacceptable level, the *Pioneer VI* support by the DSN would be terminated, based upon mutual agreement with the *Pioneer* Project Office. When, approximately 8 mo after launch, the telemetry detection threshold of the *Pioneer VI* S-band downlink signal was reached within the 85-ft antenna network, the Mars DSS with its 210-ft antenna was made available on an uncommitted best-effort basis.

In 1967, the SIRD and NSP for *Pioneers VI, VII, and C* were completed. The NSP superseded the previous commitment for *Pioneer* Project support by the DSN, and it was planned that the Mars DSS would furnish a minimum of 180 timebank h/mo of tracking and data acquisition support for the extended missions of *Pioneers VI, VII, and C*. This minimum tracking time was to be increased whenever possible. Also, it was planned to have daily tracks available for each *Pioneer* mission. Due to the limitations of a single-station capability, the support ratio among the *Pioneer* missions at the Mars DSS was to be coordinated for the best utilization of all spacecraft instruments.

*c. DSN support during prelaunch operations and initial phases of Pioneer VI mission.* Prelaunch checkout and preparation of the spacecraft and its scientific instruments were conducted at Building AN at the Cape Kennedy Air Force Station. During this period, tests of the RF link between the spacecraft and the Cape Kennedy DSS were performed. The Cape Kennedy DSS contained mission-independent and mission-dependent equipment (*Pioneer* ground operational equipment) functionally identical to that at the standard DSSs. This test was the first opportunity to validate the compatibility of the *Pioneer VI* communications subsystem with the DSN.

During countdown, the Cape Kennedy DSS received telemetry data from the spacecraft and monitored continuously the spacecraft communications subsystem performance and the compatibility of the subsystem with the DSN. The direction and status monitoring of the DSN were performed at the SFOF. Also, the performance of the spacecraft and scientific instruments was analyzed at the SFOF from spacecraft telemetry data teletyped from the Cape Kennedy DSS. These activities served as backup to similar tasks performed at Building AN.

The *Pioneer VI* spacecraft was launched on December 6, 1965. During the near-earth phase of the mission, the AFETR network tracked the launch vehicle and

received telemetry data from the spacecraft during the powered flight phase. The Cape Kennedy Air Force Station, stations at Grand Bahama Island and Antigua, and the *Coastal Crusader* Tracking Ship participated in the activities. The telemetry data were recorded on magnetic tape for later processing and analysis. The tracking data, excluding those from the ship, were teletyped immediately and continuously to the real-time computer facility at the Cape Kennedy Air Force Station, where the characteristics of the trajectory were calculated for predictions to be used for the initial DSN acquisition of the spacecraft. Similar activities were performed at the SFOF, using the AFETR tracking data.

Following the powered flight phase, the Johannesburg DSS made initial acquisition, starting the deep-space phase of the mission. This and all of the other DSSs supporting the *Pioneer VI* mission tracked, received telemetry data from, and transmitted commands to the spacecraft. Computing equipment at the SFOF processed the tracking data teletyped from each DSS during or immediately following a pass of the spacecraft for orbit determination, and calculated the predictions as an aid in subsequent acquisitions by the DSSs and by the 100-ft-diam transmitting antenna at Stanford University. As part of its radio propagation investigation, Stanford University transmitted 50- and 430-MHz signals to the two Stanford receivers on the spacecraft.

The SFOF mission support area was used for mission control during the initial phases of the mission, except for critical orientation maneuvers. For *Pioneer VI*, the initial acquisition and partial orientation were directed from the Johannesburg DSS, and the final orientation was controlled from the Echo DSS.

*d. Continuing DSN support of Pioneer VI mission.* During the cruise phase of the mission, principal support has been provided by the Echo, Tidbinbilla, and Johannesburg DSSs, since these are the only tracking stations equipped with mission-dependent ground operational equipment. A microwave system connecting the Echo DSS with the Pioneer and Mars DSSs provides a capability for utilizing the ground operational equipment at the Echo DSS in combination with the mission-independent equipment at the Pioneer and Mars DSSs. The Robledo and Woomera DSSs, also unequipped with mission-dependent ground operational equipment, have been used on an emergency backup basis.

The mission operations center has been located at Ames Research Center (ARC) during the cruise phase.

Both the SFOF mission support area and the ARC mission operations center receive, in near-real time by teletype from the tracking stations, sampled and processed telemetry data for use in monitoring the performance of the spacecraft and its scientific instruments and as an aid in planning mission operations. ARC also receives from the DSSs all spacecraft telemetry data recorded on 0.5-in. analog magnetic tape. All analog tapes are validated at the SFOF. Special- and general-purpose equipment at ARC is used to process the engineering and scientific data, which are then forwarded to the principal scientific investigators for study and assessment. The DSN also furnishes data packages on the orbits and view periods, as well as information on the light round-trip time between the spacecraft and the DSSs.

Every phase of the mission thus far has been successful, and all flight instruments are still operating. The DSN not only met all basic *Pioneer VI* support commitments, but also provided a large amount of additional tracking support from its 85-ft antenna network during the nominal mission period. This is illustrated in Fig. 4, which shows the DSN operational support rendered during the mission thus far. The Mars DSS began tracking the spacecraft approximately 7 mo after launch and is still tracking almost daily. However, since this is the only DSN advanced facility equipped with a 210-ft parabolic antenna, required hardware modification and testing at this station have sometimes interrupted the *Pioneer VI* regular tracking operations.

The only anomaly which has caused some operational problems during the past few months was erratic behavior of the voltage-controlled oscillator of the Channel 7 spacecraft receiver. Because of this instability, *Pioneer VI* now operates in a one-way mode using the auxiliary oscillator. The telemetry science and engineering information which is received is still satisfactory and has a low bit error rate. In fact, the bit error rate is lower than that in the two-way mode. The instability of the Channel 7 receiver has, however, impeded the celestial mechanics investigation by *Pioneer VI*, since precision two-way doppler tracking data are not available. Recent engineering telemetry data show some evidence that the difficulty is being resolved; if so, the spacecraft will be tracked in a two-way mode again.

The fixed earth-sun line heliocentric trajectory of *Pioneer VI* is shown in Fig. 5. The variable data transmission bit rate to the spacecraft made it a highly desirable monitoring platform. By sending proper commands from earth, the telemetry link could be switched to

operate on five discrete bit rates: 512, 256, 64, 16, and 8 bits/s. The bit rate was lowered as the earth-to-spacecraft distance increased in order to reduce the possibility of data errors. The higher bit rates provided science data with higher resolution.

When communications distance criteria required a low bit rate, the spacecraft could be commanded into a higher bit rate with onboard storage. The stored data could be read out later at the required lower bit rate. To assure the highest science and engineering data quality, the *Pioneer* Project specified a telemetry bit stream error limit of 1 error/ $10^3$  detected bits, with the stipulation that, in certain situations, a bit error rate of 1 error/ $10^2$  detected bits would be acceptable.

As the spacecraft's communications link range gradually increased, the telemetry bit rate was switched to the next lower level, as shown in Fig. 5. The 85-ft-antenna 8-bit/s telemetry threshold was reached in early-June 1966. The spacecraft was then tracked by the Mars DSS. The 210-ft-antenna's threshold at 8 bits/s is approximately 2 AU; therefore, the Mars DSS will be able to operate within the acceptable telemetry bit error rate during the next 3 yr.

The nominal power budget of the *Pioneer VI* telemetry link is given in Table 1. These data are compatible with the capabilities of the standard 85-ft-antenna stations. All DSN measurements during the first 180 days after launch showed excellent agreement with the data in Table 1. The practical deviations were well within the limits of measurement and calibration uncertainties.

Figure 6, which gives the carrier power levels recorded at the Echo and Mars DSSs, demonstrates that the design goals of the S-band communications link were met satisfactorily.

The telemetry bit error rates measured at the Echo DSS at the various bit-rate thresholds are shown in Fig. 7. As the communications link range increased (corresponding to the increasing pass numbers), the bit error rate during each pass also increased. The bit error rate during the middle portion of the tracking passes was quite uniform, but showed a tendency to increase at the beginning and end of each tracking period. This increase was caused by a degradation in telemetry signal-to-noise ratio, which, in turn, was caused by the fact that the system noise temperature of the antenna receiving system is lowest at high elevation angles but increasing at lower elevation angles.

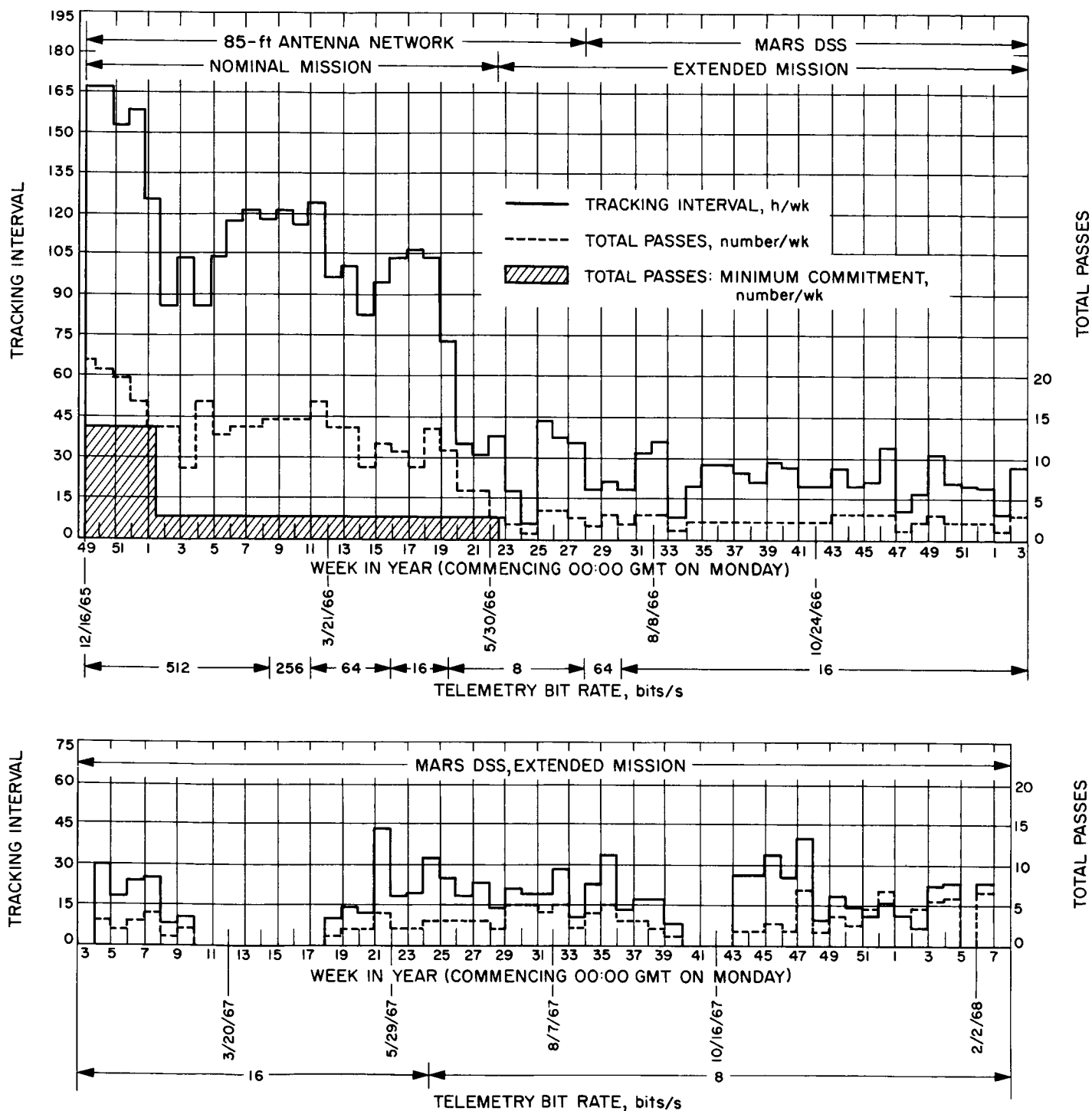


Fig. 4. DSN operational support of Pioneer VI mission: weekly tracking passes and hours and minimum commitment during the nominal mission

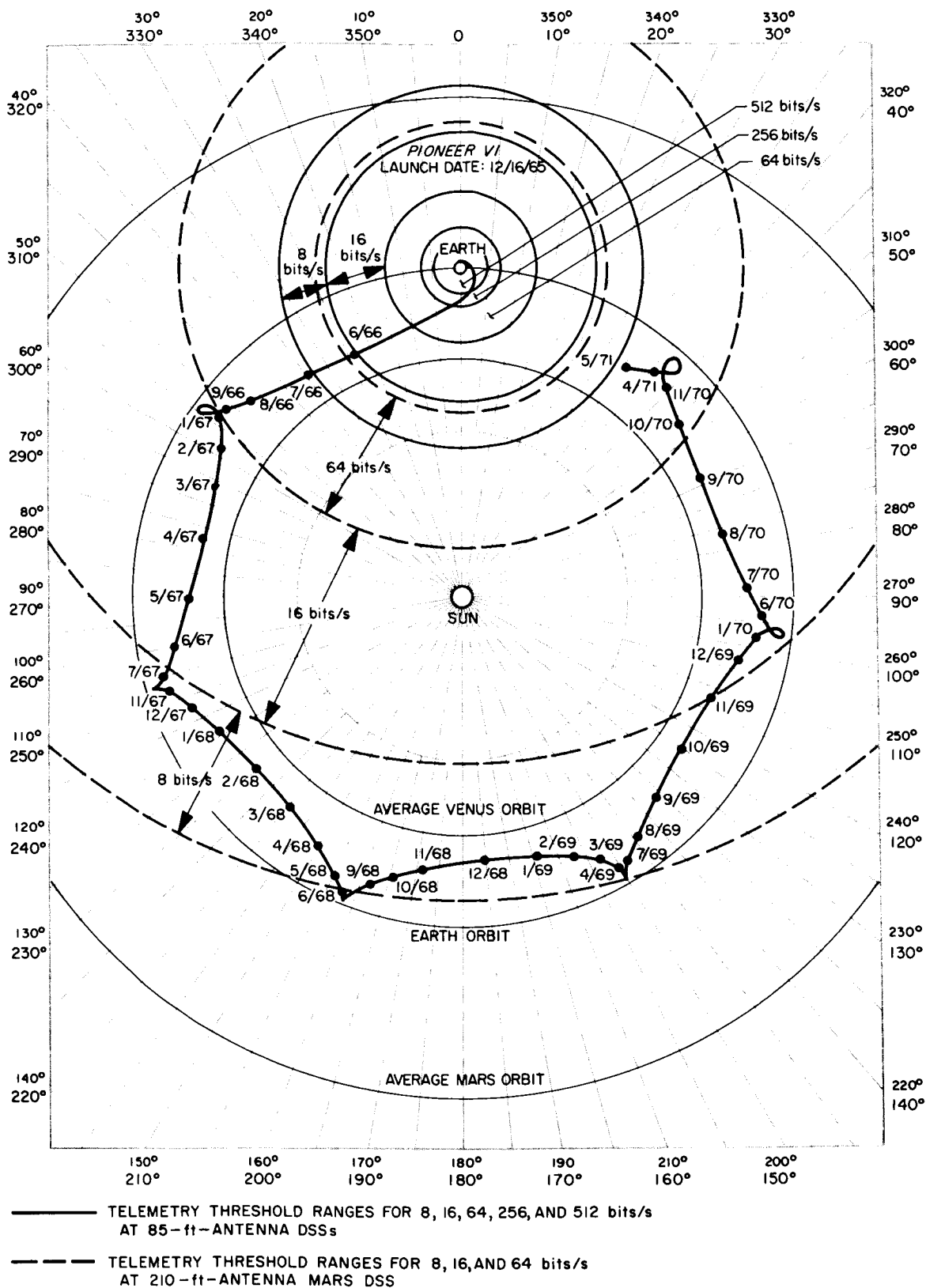


Fig. 5. Fixed earth-sun line heliocentric trajectory of Pioneer VI and telemetry threshold ranges

Table 1. Nominal power budget for the Pioneer VI/DSN telemetry link<sup>a</sup>

Parameter	Bit rate, bits/s				
	512	256	64	16	8
Total transmitter power, dBmW	38.4	38.4	38.4	38.4	38.4
Transmitting circuit loss, dB	1.6	1.6	1.6	1.6	1.6
Transmitting antenna gain, dB	11.0	11.0	11.0	11.0	11.0
Space attenuation (2292 MHz), dB	242.0	245.0	251.0	256.1	258.0
Polarization loss, dB	3.0	3.0	3.0	3.0	3.0
Receiving antenna gain, dB	53.4	53.4	53.4	53.4	53.4
Receiving circuit loss, dB	0.2	0.2	0.2	0.2	0.2
Total received power, dBmW	-144.0	-147.0	-153.0	-158.1	-160.0
Receiver noise spectral density (assumed system noise temperature = 45°K), dBmW/Hz	-182.1	-182.1	-182.1	-182.1	-182.1
Carrier performance					
Carrier modulation suppression (modulation index = 0.9 rad), dB	4.1	4.1	4.1	4.1	4.1
Received carrier power, dBmW	-148.1	-151.1	-157.1	-162.2	-164.1
Carrier automatic-phase-control noise bandwidth ( $2B_{LO} = 12$ ), dB	10.8	10.8	10.8	10.8	10.8
Threshold signal-to-noise ratio in $2B_{LO}$ , dB	6.0	6.0	6.0	6.0	6.0
Threshold carrier power, dBmW	-165.3	-165.3	-165.3	-165.3	-165.3
Carrier performance margin, dB	17.2	14.2	8.3	3.1	1.2
Data channel					
Subcarrier modulation suppression, dB	2.2	2.2	2.2	2.2	2.2
Received subcarrier power, dBmW	-146.2	-149.2	-155.2	-160.3	-162.2
Bit rate (1/T), dB	27.1	24.1	18.1	12.0	9.0
Required $ST/N$ ( $P_e = 10^{-3}$ ), dB	8.8	8.8	8.8	8.8	8.8
Receiver losses and degradation, dB	0	0	0	1.0	2.1
Threshold subcarrier power, dBmW	-146.2	-149.2	-155.2	-160.3	-162.2
Data performance margin, dB	0	0	0	0	0
Range, km $\times 10^6$	13.2	18.6	37.0	66.5	82.8
Time after launch, days	78.5	92.6	122.6	156.8	174.4
<sup>a</sup> The symbols used herein are defined as follows: $B_{LO}$ = carrier tracking loop bandwidth at threshold levels, Hz $T$ = time per information bit, s $S$ = signal power, W $N$ = noise spectral density, W/Hz $P_e$ = probability of data error					

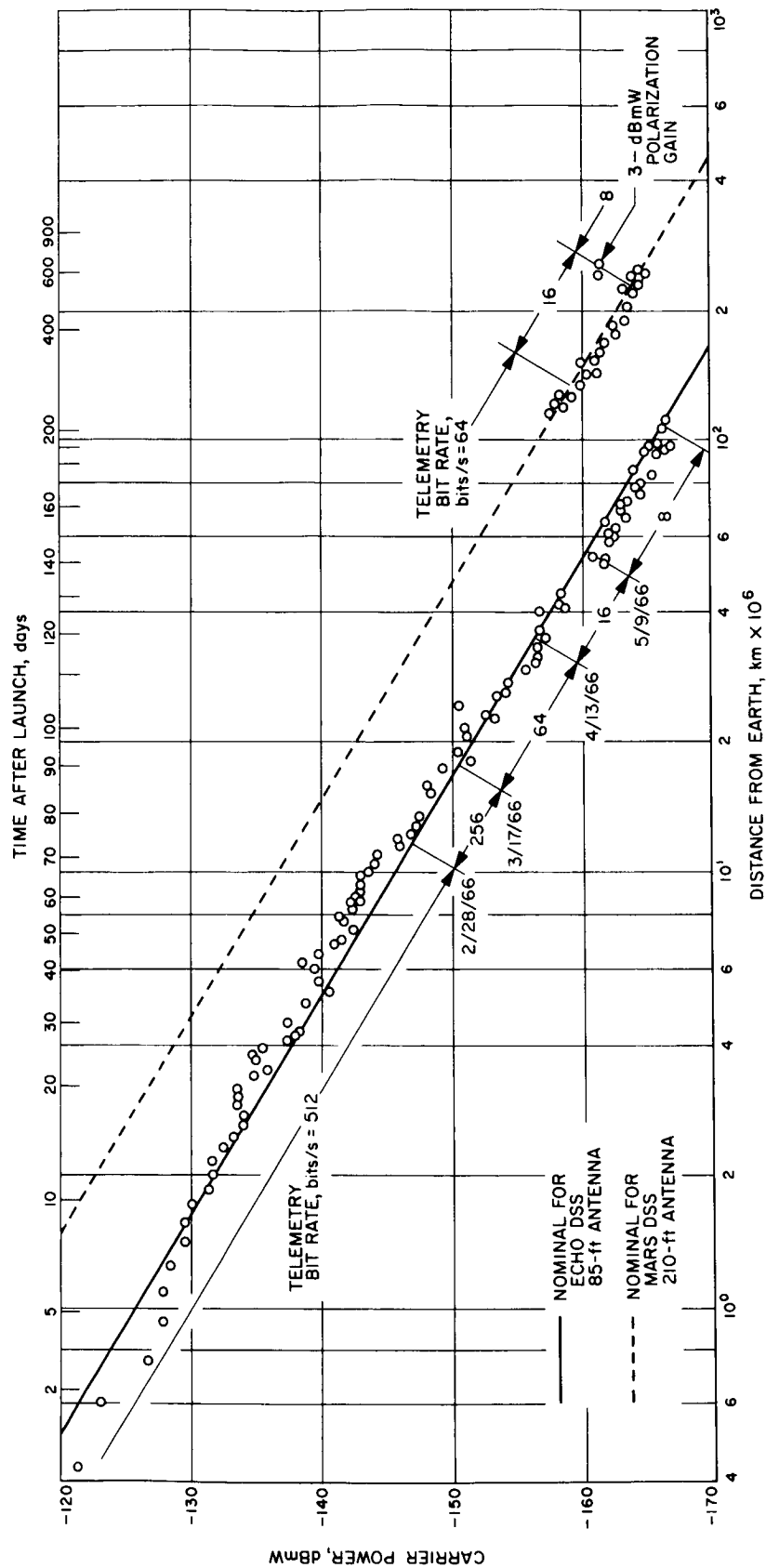


Fig. 6. Carrier power received from Pioneer VI from January 1966 to February 1968, as reported by the Echo and Mars DSSs

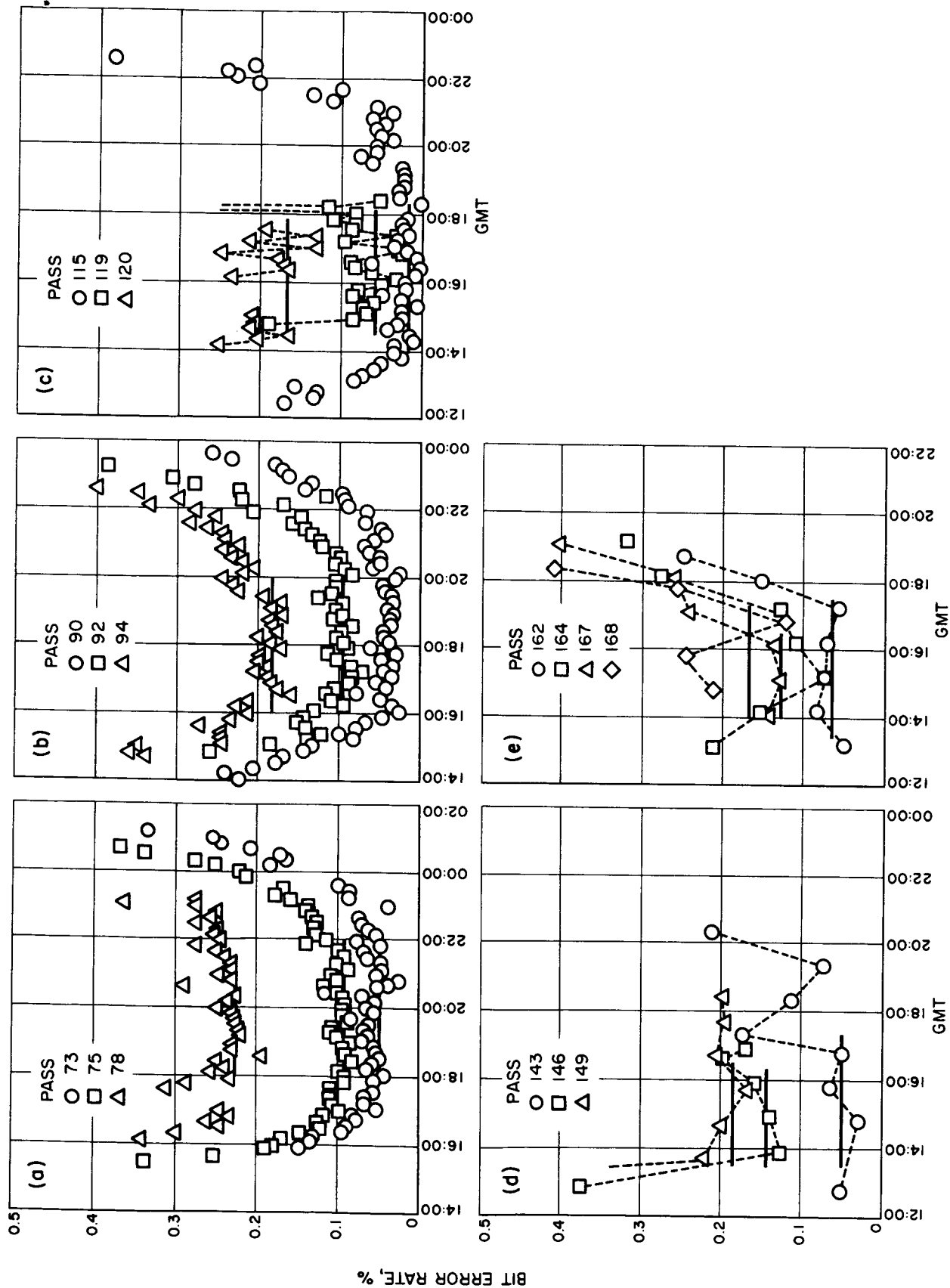


Fig. 7. Pioneer VI telemetry bit error rates estimated at the Echo DSS at the following bit rate thresholds:  
(a) 512, (b) 256, (c) 128, (d) 64, (e) 16, (f) 8 bits/s

Nearly  $3 \times 10^9$  bits of information have been collected by the DSN during the first 26 mo after the launch of *Pioneer VI*. This information may be categorized as follows:

Type of information	Number of bits, $\times 10^6$
Science data	2110
Engineering data	164
Parity check	386
Data identification	272
Unassigned	21
Total	2953

Throughout the flight, the spacecraft has operated primarily in the real-time data transmission mode. The spacecraft's duty-cycle storage mode generally used between tracking periods provided approximately 20% of the data coverage. However, due to intermittent data sampling, this mode contributed only about 0.06% of the total data received.

Based on its performance thus far, the estimated total lifetime of the *Pioneer VI* spacecraft is approximately 5 yr. During November 1968, the spacecraft will have a solar occultation, and *Pioneer* Project and DSN management personnel are presently coordinating preparations for the support of special experiments to be conducted at that time. The detection capability of the 85-ft-antenna network will again be reached by *Pioneer VI* during spring 1971.

#### Reference

1. *Pioneer VI Mission*. *Pioneer* Project Office, NASA Ames Research Center, Moffett Field, Calif., May 22, 1967.

### C. Planetary Flight Projects

#### 1. *Mariner Mars 1969 Mission Support*, K. W. Linnes

**a. Mission operations design.** Mission operations design for the *Mariner Mars 1969* Project is being accomplished in a closely coordinated effort by the MOS and TDS Managers. A joint MOS/TDS management plan has evolved which describes the method whereby the MOS and DSN personnel define mission operations. The plan follows the scheme shown in Fig. 3 (Section A) and describes the responsibilities of the mission operations, software, and DSN design teams (Fig. 2, Section A).

To ensure proper coordination of the MOS and TDS mission operations activities, the MOS and TDS Managers issue each month a revised joint master schedule. Progress on the current tasks is ascertained in a weekly meeting of these managers with the three design team leaders: the Space Flight Operations Director, the Software System Engineer, and the DSN Project Engineer. The principal benefit derived from this management approach is improved communication facilitating identification and solution of interface problems.

For the *Mariner Mars 1969* Project, the system-level functional requirements were formulated by the mission operations design team. From these requirements, that team formulated the space flight operations plan and preliminary versions of mission operations test plans. The software design team produced the functional specifications and most of the requests for programming (RFPs) for the software system. Working with the DSN systems engineers and managers, the DSN design team formulated configuration descriptions for each DSN system as it is to be used for the *Mariner Mars 1969* Project operations.

**b. Mission description.** The launch window for the *Mariner Mars 1969* mission will cover slightly more than 6 wk, beginning February 20, and will probably include not only the launch of both *Mariner Mars 1969* spacecraft, but the first midcourse maneuver of the first spacecraft. A second midcourse maneuver of the first spacecraft will be performed approximately 120 days after launch, although the actual date for this maneuver may change considerably. A period of intense activity will commence shortly before arrival of the first spacecraft at Mars about August 1 and will continue through the completion of playback by the second spacecraft about August 23. Continuous tracking data will be required starting 14 days before encounter. In the nominal mission, the far encounter sequence will commence 48 h prior to encounter for the purpose of obtaining more TV pictures (SPS 37-48, Vol. I, pp. 7-10). The end of the nominal mission will occur 90 days after encounter.

The near-earth phase of the missions will require support by the DSN, the AFETR, and the MSFN. Detailed plans for this support are being formulated. The deep-space phase of the missions will be almost entirely supported by the DSN.

**c. DSN support as outlined in the SIRD and NSP.** The requirements listed in the SIRD published in spring 1967 (presently being revised) are generally similar to those for previous planetary flight projects such as the *Mariner*



Venus 87 Project. However, the *Mariner Mars 1969* Project differs significantly in several areas:

- (1) The *Mariner Mars 1969* spacecraft will be launched by *Atlas/Centaur* vehicles in direct ascent; i.e., there will be no parking orbit, a feature which greatly simplifies the near-earth coverage problem.
- (2) Both missions will be presumed to have a high probability of success; therefore, provision must be made for tracking two identical planetary spacecraft on missions differing only slightly in time of launch and encounter. This requirement complicates mission operations, particularly utilization of the DSN, at launch and encounter.
- (3) The *Mariner Mars 1969* spacecraft will transmit approximately 30 times more encounter data than did *Mariner IV* ( $1.8 \times 10^8$  bits); also, higher rates of transmission will be required. For these reasons, the telecommunications subsystem will have a capability for a playback rate for the nominal mission of 270 bits/s. As a DSN research-and-development (R&D) project, a high-rate telemetry playback mode will be available for operation at 16,200 bits/s.

Two other project requirements cannot be met by the operational capability of the DSN and are, therefore, being supported as DSN R&D projects, i.e., on a limited basis. A tracking requirement for ranging data can be only partially met with a planetary ranging subsystem at the Mars DSS using R&D equipment. A requirement to meet a secondary objective of timing synchronization between the DSSs of 20  $\mu$ s cannot be met with operational equipment; however, some support can be given at this accuracy using an R&D timing synchronization subsystem.

The Echo, Mars, Woomera, Johannesburg, Cebreros, and Cape Kennedy DSSs have been committed to support of the *Mariner Mars 1969* Project in the NSP issued in the fall of 1967. The Pioneer, Tidbinbilla, and Robledo DSSs are committed to support of the *Apollo* Project and are therefore considered unavailable as prime stations for the *Mariner Mars 1969* Project. However, when available, these stations may be used to the extent that their capabilities permit.

As was provided for previous projects, the SFOF will provide areas for performing functions such as mission control and data processing.

The GCF support of the *Mariner Mars 1969* Project will consist primarily of utilization of the existing

NASCOM. Some changes will be made to the method whereby messages are handled on the high-speed data lines.

## D. Manned Space Flight Project

### 1. *Apollo* Mission Support, P. S. Goodwin

*a. Introduction.* Previous issues of the *Deep Space Network* SPS volume contained descriptions of specific equipment that the DSN was producing for the MSFN and the modifications being made to certain DSSs to support the *Apollo* Project. A series of articles on the overall DSN operational support for *Apollo* will be presented in this and subsequent issues of the SPS, Vol. II. A brief history of the aforementioned *Apollo* activity is also presented here.

*b. DSN equipment.* Following a decision to adopt the JPL-developed coherent tracking and telemetry technology for both the *Apollo* earth orbital and lunar missions, the Office of Tracking and Data Acquisition at NASA Headquarters directed JPL to provide the S-band equipment needed by the earth-based tracking stations. This equipment was to be supplied both to the MSFN and to the DSN. The DSN would, in turn, support the *Apollo* lunar missions by employing three of its 85-ft antennas as backup to three MSFN 85-ft antennas to be installed during the MSFN's upgrade from the *Gemini* Project to the *Apollo* Project.

The initial DSN-type design of the ground-station S-band receiver/exciter/ranging (RER) subsystem (2290- to 2300-MHz band) was known as the Block I S-band RER subsystem, as reported in previous SPSs. Of the 10 systems produced, several were aligned to *Apollo* frequencies (2270- to 2290-MHz band) to satisfy early MSFN and Manned Spacecraft Center (MSC) spacecraft/ground-station design and compatibility requirements.

The *Apollo* version of the RER subsystem was known as the MSFN Block II RER subsystem. The Block II design introduced several significant changes, such as four-frequency (quad) voltage-controlled oscillators, wider loop bandwidths, and a dual RER station capability. Since many of these features showed promise for DSN use and because future procurement would be simplified, the DSN adopted the Block II concept (except that the DSN subsystems would be aligned to DSN frequencies) for future subsystems, and agreed to a later upgrading of previously delivered Block I subsystems to the Block II design as hardware and operational schedules permitted. Though some retrofitting was necessary

on the early Block II subsystems, the Block II design was used for the 39 remaining subsystems produced.

As MSFN Block II subsystems became available and field experience was gained, it became apparent that certain refinements were desirable to meet the MSFN stations' operational needs for *Apollo*. An acquisition control kit was produced specifically to meet the need for rapid acquisition of telemetry and voice, rather than employing the DSN practice of ensuring early carrier acquisition for tracking data. Also, frequent coverage changes required between the command service module (CSM) and the lunar module (LM) necessitated manual rephasing of the ranging subsystem. To overcome the latter operational inconvenience, the constant-clock-frequency ranging subsystem modification was introduced as the Block II-B upgrade.

The degree of similarity between the MSFN and DSN versions of the S-band RF and ranging subsystems stimulated interest in a Block III version capable of operating

in either the MSFN or the DSN frequency bands with the proper performance characteristics. Several configurations, with varying flexibility and change-over time, were proposed as a Block III modification to the Block II RER subsystems. The "C" version was adopted, and Block III-C kits are presently being produced under JPL contract for use with all MSFN and DSN RER subsystems.

*c. DSN facilities.* The configuration to be employed at the DSN 85-ft-antenna *Apollo* backup stations was carefully studied. As *Apollo*'s lunar mission profile became defined, the term "backup" became somewhat of a misnomer: The beamwidth of an 85-ft antenna at S-band is such as to require two such antennas when *Apollo* is at the moon—one to cover the orbiting CSM and the other the landed LM (though, enroute to and from the moon, the second 85-ft antenna does serve as a true, redundant backup). Also, the projected DSN tracking schedules were quite full well into the expected *Apollo* time period.



Fig. 8. MSFN wing at Pioneer DSS

For the above reasons, it was decided to separate the *Apollo* activity from the other activities at the DSN back-up stations as much as possible to maximize the amount of parallel usage of these facilities. This was accomplished through the addition of MSFN wings to the Operations Buildings at the Pioneer, Robledo, and Tidbinbilla DSSs. Exterior and interior views of the MSFN wing at the Pioneer DSS are shown in Figs. 8 and 9.

The MSFN control rooms, when connected to the DSN 85-ft antenna and its associated equipment, constitute a complete, MSFN dual-type tracking station; however, for economy purposes, the *Apollo* mission-peculiar telemetry, voice, etc., are sent for demodulation by microwave link (Fig. 8) to the neighboring MSFN prime 85-ft-antenna

station. As may be seen in Fig. 9, an MSFN dual station contains two complete, independent, S-band receiving, transmitting, and ranging channels to permit simultaneous tracking and communications with both the *Apollo* CSM and LM whenever they are jointly within the antenna beamwidth. Since each *Apollo* spacecraft has two transmitting frequencies (one for coherent phase modulation and the other for frequency modulation), each MSFN dual station has the capability to simultaneously receive four frequencies (down-links) and transmit two frequencies (up-links), the latter with a capacity of 10 kW each at the 85-ft-antenna stations.

These operational *Apollo* requirements necessitated the addition of considerable MSFN-oriented equipment to



Fig. 9. Interior view of MSFN wing at Pioneer DSS

the declination-axis "wheel house" on the backup station's antennas. Besides a second maser and high-power klystron, four racks of MSFN receiver/exciter equipment and numerous MSFN/DSN transfer switching networks were added to the antenna. The latter are connected to an elaborate key-controlled interlock network which enables the station to be converted rapidly from DSN to MSFN service, and vice versa.

The design goal of maximum parallel activity in the two control rooms, except for antenna usage, has therefore been achieved. During *Apollo* activities, the DSN backup stations are staffed by MSFN personnel, with selected support from a limited number of DSN personnel to operate the common, inter-network subsystems, with the MSFN Maintenance and Operations Supervisor in charge. At other times, these stations, except for the MSFN control rooms, are under the direction of the DSN Station Director.

**d. Special support configurations.** It is not uncommon for a space flight project to require some form of special support from its tracking network to satisfy a mission constraint. Such a circumstance (discussed later) developed for the first two (unmanned) test flights of the *Saturn V* vehicle, AS-501 (*Apollo 4* mission) and AS-502, wherein both the MSFN and DSN 30-ft-antenna stations on Ascension Island (Fig. 10) were required for tracking. When originally implemented, these two stations were completely separate stations with equipment complements specific to each of the respective networks. The requirement to jointly support the AS-501 and AS-502 missions necessitated the addition of special interface equipment and the development of compatible operating procedures. Fortunately, sufficient time was available to accomplish both tasks prior to the AS-501 mission.

However, special support needs are not always evident enough in advance to enable a thorough engineering design of the interface equipment or the preparation of formal operating procedures; yet, the need must be met at least on a "best effort" basis. Such a situation which occurred for the Cape Kennedy DSS during the launch preparations for *Apollo 4* is discussed later.

#### **e. *Apollo* operations support**

*Apollo 4* (AS-501). Preparations for the Ascension Island DSS support of the *Apollo 4* mission (the first test of the 7,500,000-lb-thrust, *Saturn V* launch vehicle for the *Apollo* lunar missions) started in January 1967. Since the primary objective was to receive telemetry from, and



**Fig. 10. DSN and MSFN 30-ft antennas on Ascension Island**

to transmit commands to, the *S-IVB/IU* stage<sup>1</sup> after CSM separation, considerable engineering effort was expended by both the Goddard Space Flight Center and JPL in designing the telemetry and command interface between the MSFN and DSN stations on Ascension Island. The configuration chosen not only achieved all of the objectives, but utilized equipment available somewhere within the respective networks. The latter feature was significant, because there was insufficient lead-time to design and procure new equipment and still meet the original launch date for the spacecraft.

Sufficient time was available to develop and perfect the operational procedures to be used in this joint operation. The operational procedures and techniques used by the MSFN were different than those of the DSN, because they had been specifically tailored for manned orbital and lunar flights as opposed to unmanned lunar and planetary flights.

<sup>1</sup>Last stage of this series of *Saturn* launch vehicles and its associated instrumentation unit (IU), which includes the S-band transponder.

The first integrated tests in which the MSFN and DSN Ascension Island stations simultaneously tracked an instrumented aircraft (IAC) were performed in July 1967. In early-October, the Ascension Island DSS tracked *Lunar Orbiter V*, then in orbit about the moon, in an exercise of the station's ranging system. Besides providing additional training, a second IAC test provided experience in the rapid conversion of the Ascension Island DSS from a DSN configuration to an MSFN configuration.

On October 16, the station commenced configuration tests, which in this case were DSN procedures adapted for an MSFN configuration. During and following these tests, the station followed a series of MSFN checkout and training procedures specifically adapted for the Ascension Island DSS, including system tests, integrated system tests, station-readiness tests, and countdown demonstration tests.

On October 24, the DSN placed the Ascension Island DSS under configuration control, followed by a configuration freeze on October 28. Concurrently with the last item, the MSFN placed the Ascension Island DSS on mission status. This meant that henceforth, throughout the mission, this DSS would receive its operational directives from the MSC, which had project responsibility for the *Apollo 4* flight.

During the countdown demonstration test of the AS-501, a suspected multipath problem developed between the MSFN station on Merritt Island and the *Saturn V* vehicle on Pad 39A at the Kennedy Space Center. The DSN Cape Kennedy DSS, which is located directly on the Cape, was asked to convert to the *Apollo* frequency band and measure the stability of the AS-501 S-band signals in order to obtain measurements from a different location. Through a "make-shift" arrangement, the Cape Kennedy DSS was able to receive strong, stable signals from the spacecraft, providing confidence that the spacecraft's S-band system was in proper working order and that the launch preparations could continue.

The Cape Kennedy DSS also provided coverage during the terminal countdown, starting with a station countdown at 14:00 GMT on November 8. Continuous relay of the CSM telemetry and periodic signal strength and stability measurements were provided the MSFN station at the Kennedy Space Center throughout the countdown.

The AS-501 (*Apollo 4*) was successfully launched at 12:00 GMT on November 9. The Cape Kennedy DSS manually tracked (since it does not have autotrack capa-

bility) the *Apollo 4* CSM to the local horizon, with the received signal strength varying between  $-71$  dBmW at liftoff to  $-141$  dBmW at loss of signal, a period covering  $09^m07^s$ . One momentary out-of-lock occurred  $02^m20^s$  after liftoff, probably due to a spacecraft antenna null. Though not requested by the Goddard Space Flight Center, the Cape Kennedy DSS maintained operational status and passively tracked the *Apollo 4* CSM again at the end of its first orbital revolution. The received signal strengths during this tracking period of  $6^m44^s$  were in the range of  $-104$  to  $-110$  dBmW.

The Cape Kennedy DSS passively tracked the CSM a third time at the end of its second orbital revolution. Toward the end of this pass, the *S-IVB* stage of the *Apollo 4* launch vehicle ignited a second time to place the CSM in a high, earth-intersecting elliptical orbit with an apogee nearly 10,000 mi above the earth. The Cape Kennedy DSS track of the CSM lasted  $11^m46^s$ , with loss of signal at 15:20 GMT. The Ascension Island DSS had acquisition of signal on the *S-IVB/IU*  $2.5^m$  later. Both the CSM and the *S-IVB/IU* were programmed to reach apogee while in view of Ascension Island, prior to the CSM's planned re-entry test of its heat shield. During the apogee pass over Ascension Island, the two vehicles became sufficiently separated to necessitate the use of both the MSFN and DSN 30-ft antennas on Ascension Island (Fig. 10). (This situation will also arise during the AS-502 flight.) Some signal fluctuations experienced while the *S-IVB/IU* was near the Ascension Island DSS horizon were probably due to a combination of multipath effects and spacecraft antenna pattern variations.

During the early minutes of the pass, the Ascension Island DSS experienced a few dropouts, which were later attributed to up-range MSFN stations sweeping the *S-IVB/IU* transponder. When the elevation angle reached about 10 deg, the received signal stabilized in the vicinity of  $-100$  dBmW, and the preprogrammed sequence of ranging measurements and commands was followed without apparent anomaly. Due to the high apogee of the *S-IVB/IU* stage (roughly 1000 mi less than that for the CSM), the Ascension Island DSS track lasted  $3^h36^m5$ . It is of interest that the received signal was very strong at the end of the pass. The Ascension Island DSS reported  $-99$  dBmW at loss of signal, with a 0-deg elevation angle.

Post-flight analysis indicated that both the Cape Kennedy and the Ascension Island DSSs achieved their primary mission objective of providing reliable telemetry data to their counterpart MSFN stations. The only major anomaly occurred at the Ascension Island DSS, where a



faulty 100ths digit in the doppler counter resulted in a considerable number of bad data points. However, the Ascension Island DSS angle and range data appeared satisfactory. Difficulties experienced with the teletype circuit from the Goldstone DSCC system data analysis facility to the Ascension Island DSS prevented the station from receiving the planned real-time evaluation of its tracking data. It is doubtful, however, that the station could have corrected the doppler counter problem during the pass, since it was an intermittent problem.

The joint operating procedures developed for the MSFN and DSN Ascension Island stations were successful, though, as expected, experience with *Apollo 4* did disclose areas where relatively minor improvements could be made. Since the *Apollo 4* mission was so successful, it was an easy test of the new MSFN/DSN procedures and cross-support capabilities. For this reason, joint training exercises continued after the *Apollo 4* mission.

*Apollo 5* (AS-204/LM). The primary objective of the *Apollo 5* mission was to test the descent propulsion system and the ascent propulsion system of the LM. The flight plan called for the LM to be placed into earth orbit by an uprated *Saturn I* launch vehicle (S-IB first stage and S-IVB second stage). After several orbits, a series of engine firings was scheduled which would alter the LM's orbital parameters. According to the flight plan, Ascension Island would have spacecraft visibility starting on the third orbital revolution and lasting through the sixth orbital revolution.

There was no mission requirement for the Ascension Island DSS to track *Apollo 5*, but, since it would provide additional station training, the DSN obtained permission of the MSFN for the Ascension Island DSS to passively track the LM. The operational improvements resulting from the experience with *Apollo 4* were quickly introduced into the procedures so they could be flight-tested on this mission, planned for mid-January 1968 (only 2 mo after the *Apollo 4* mission). During this period, the MSFN automatic acquisition control kit modification was made to the Ascension Island DSS receiver/exciter subsystem.

Prepermission testing for the *Apollo 5* mission closely paralleled that for *Apollo 4*. On December 15, the station participated with the MSFN Ascension Island station in the final network readiness test prior to the MSFN going into mission status. From then until launch, the Ascension Island DSS passively participated in every MSFN scheduled prepermission test, with special emphasis

on the integrated system tests, during which the MSFN and DSN stations acted as a single Ascension Island facility. Configuration control over the Ascension Island DSS was established on January 3, and a configuration freeze was established on January 10.

Three special training exercises were performed in mid-January using the *Test and Training Satellite 1* (TATS-1). During the first two, the MSFN Ascension Island station was active, with the Ascension Island DSS tracking passively in the three-way mode. On the last TATS-1 exercise, the stations reversed roles, with the Ascension Island DSS establishing two-way lock and performing ranging measurements.

At the request of the Goddard Space Flight Center, the Cape Kennedy DSS participated in the premission countdown demonstration tests, using essentially the same configuration as that employed by the station for *Apollo 4*. The only significant difference was that the LM S-band transponder was activated only at specific times during the countdown, i.e., at 76<sup>h</sup> and 20<sup>h</sup> before liftoff, when the gantry was in place and a connection could be made to the S-band system. During launch, the LM was inside the vehicle shroud, which did not contain an S-band parasitic coupler antenna; thus, launch coverage was restricted to VHF. The Cape Kennedy DSS was on "stand-by" during launch, however, in the event that an abort caused a premature LM separation. If such a separation had occurred, the S-band signal would thus have become accessible.

The AS-204/LM (*Apollo 5*) was launched at 22:48 GMT on January 22, and was successfully inserted into earth orbit. The first pass over Ascension Island occurred on the third orbital revolution 2<sup>h</sup>19<sup>m</sup> after liftoff. The Ascension Island DSS passively tracked the LM in a three-way mode with the MSFN Ascension Island station for 4<sup>m</sup>17<sup>s</sup>. Composite telemetry provided to the MSFN station was not used, since that station had good signal lock on the spacecraft. The Ascension Island tracking data were successfully transmitted to, and processed by, the systems data analysis group at the Goldstone DSCC, which performs the tracking data validation function.

Between the third and fourth orbital revolution over Ascension Island, the LM was programmed to initiate the first burn of the descent propulsion system. An on-board system malfunction caused the engines to shut down after only a few seconds burn time, with the result that the LM was henceforth on a nonstandard trajectory.

As a result, neither Ascension Island station was able to obtain solid signal lock during the fourth orbital revolution.

By the time of the fifth orbital revolution pass, the MSFN had been able to process the post-burn tracking data from enough stations to permit the generation of a new acquisition message prior to the pass. This time both stations had successful tracks, and the data were handled in the same manner as for the third orbital revolution. Following the fifth pass over Ascension Island, the LM was commanded to execute the final ascent-propulsion-system burn to fuel depletion. However, the vehicle's attitude control subsystem's fuel supply was also depleted at this time, which resulted in spacecraft tumbling. The mission was declared completed shortly thereafter.

A post-flight analysis of the Ascension Island DSS activity during the *Apollo 5* mission showed that both the station performance and the upgraded procedures were satisfactory and that the experience gained should prove valuable for the AS-502 mission commitment. With the relaxation of the configuration freeze and control after the *Apollo 5* mission, a thorough investigation of the doppler counter problem was started, since this problem had recurred during the *Apollo 5* mission. The investigation disclosed that a wiring error made during the installation of the doppler resolver kit had created a logic problem in the counter, causing the 100ths digit to malfunction. Although no further doppler counter difficulties have been encountered since correction of the wiring error, this potential problem area is being observed carefully during the preparations for the AS-502 mission.

### III. Advanced Engineering

#### A. Tracking and Data Acquisition Elements Research

##### 1. Low Noise Receivers: Microwave Maser Development, Second Generation Maser Instrumentation, R. C. Clauss

*a. Introduction.* Normal operation of a wide bandwidth traveling-wave maser (TWM) can best be verified by a display of the entire TWM passband. An oscilloscope trace of power versus frequency may be obtained by use of a sweeping detector. Amplified input noise provides power for the display and no oscillators are used; therefore, the monitor may be used during tracking operations without interference to other receiver functions. The sweeping detector provides a display which can be used to properly adjust each of the electronic controls for the TWM.

*b. Detector description.* The sweeping detector is a very simple spectrum analyzer. It consists of a waveguide cavity, a capacitive rotor (driven by a synchronous 1800-rpm motor), and a diode detector (a 1N23E diode is used). The assembled device is shown in Fig. 1a.

Figure 1b shows the disassembled sweeping detector. Power is coupled into the cavity from a coaxial line with a probe. A loop provides the impedance transformation used for maximum power transfer to the diode. A loaded  $Q$  of approximately 1750 provides an instantaneous detector bandwidth of 1.3 MHz. The lucite rotor supports a

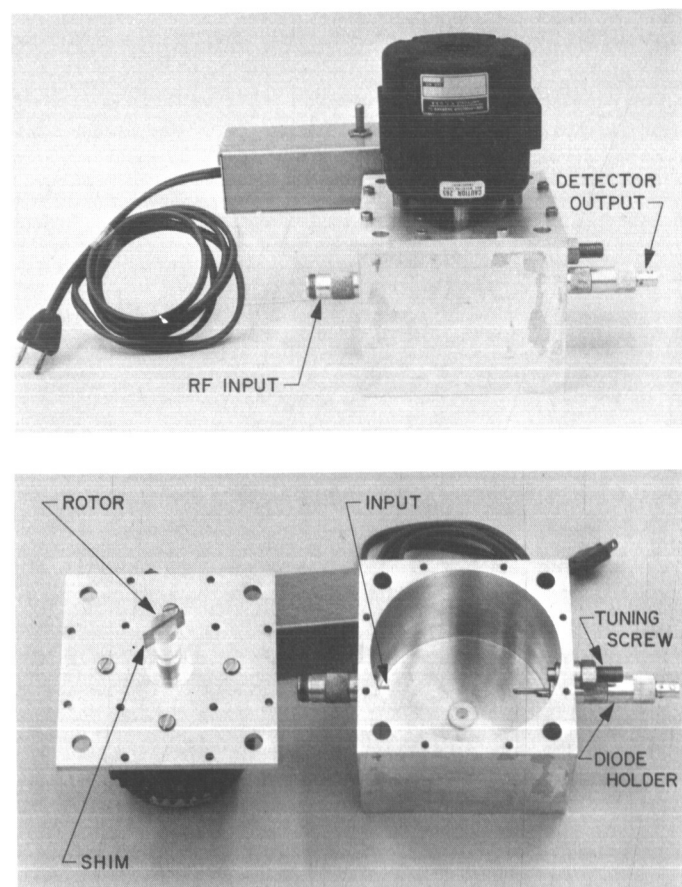
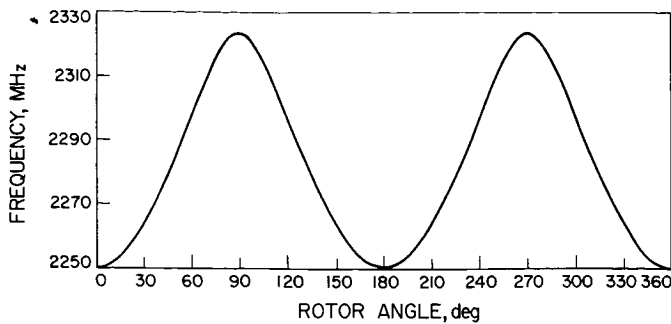


Fig. 1. Sweeping detector: (a) assembled, (b) disassembled





**Fig. 2. Detector frequency vs rotor position**

metal shim. Shim size determines the sweep width of the display. The rotor, a very light load, is supported by the motor shaft.

Figure 2 is a plot of detector frequency versus motor rotation (in degrees). The plot shows a wave shape which must be duplicated in the horizontal sweep voltage supply to obtain a linear frequency display. A phase variable circuit which approximates such a wave shape is in use.

Detector sensitivity is shown in Fig. 3. A square-law region exists up to  $-36$  dBm and provides sufficient dynamic range for the second-generation maser system. The lower limit, not shown on the figure, is determined by noise in the amplifier following the detector ( $10 \mu\text{V}$  peak to peak).

A microwave amplifier preceding the detector is used to amplify the maser output noise to a level which when detected is at least 10 dB above the postdetection amplifier noise level. The equivalent input noise temperature for a maser system may be as low as  $15^\circ\text{K}$ .

Gain requirements are determined by

$$P = kTBG \quad (1)$$

where

$$k = 1.38 \times 10^{-23} \text{ W/Hz}^\circ\text{K} \text{ (Boltzmann's constant)}$$

$$P = -51 \text{ dBm} (7.95 \times 10^{-9} \text{ W})$$

$$T = 15^\circ\text{K}$$

$$B = 1.3 \text{ MHz}$$

$$G = \text{microwave system net gain}$$

Solving Eq. (1) for  $G$  shows a net microwave gain requirement of 75 dB. Figure 4 shows the sweeping detector when used with a maser receiving system.

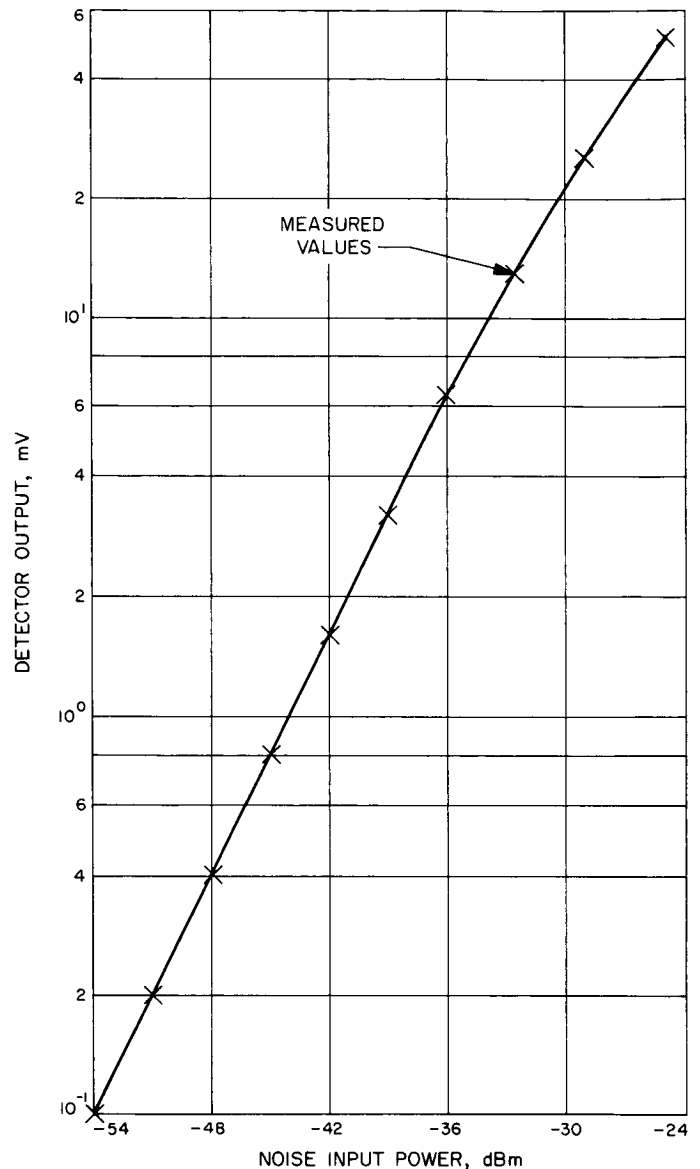


**Fig. 3. Detector sensitivity**

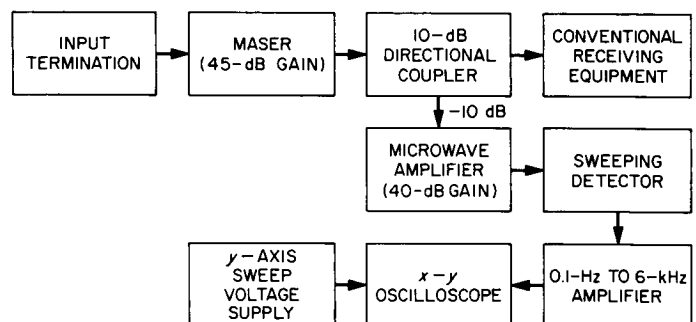


**Fig. 4. Maser system with sweeping detector**

The sweep range of the system is 75 MHz (from 2250 to 2325 MHz). The detector response is flat ( $\pm 0.2$  dB) within the range. The sweep range can be shifted with the tuning screw shown in Fig. 1b. The sweep range was observed to change 1 MHz when changing the cavity and detector temperature from 80 to 120°F.

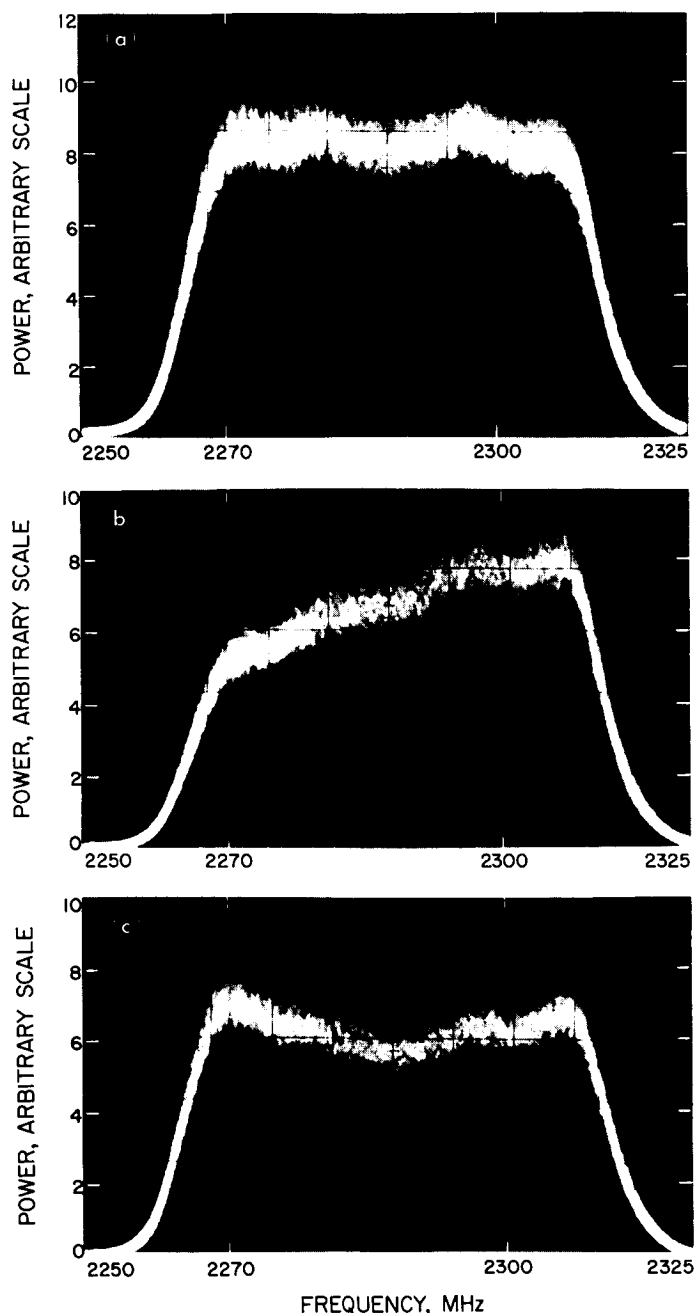


**Fig. 5. Oscilloscope traces: sweeping detector output with (a) normal TWM operation, (b) maser pump frequency detuned, (c) maser magnetic field shape coil detuned**

**c. Detector.** Use of the sweeping detector in the laboratory has provided excellent results. Figure 5a shows the oscilloscope display with normal TWM operation. The maser bandpass is flat ( $\pm 0.2$  dB) from 2269 to 2306 MHz at 46-dB net gain. Any change in electronic controls which affects maser operation (pump frequency, magnetic field shape, or strength) will result in a display change. Figure 5b shows the maser response with the klystron pump frequency set 6 MHz higher than in Fig. 5a. The square-law presentation shows 1.8-dB less gain at 2270 MHz and no change at 2300 MHz. The response shown in Fig. 5c is caused by excess current (a 10% increase) through the maser field shape coil. Oscilloscope displays observed while changing each of the maser control functions have demonstrated the need for a simple spectrum analyzer.

## 2. Solid State and Superconducting Electronics, R. W. Berwin

**a. Introduction.** Initial experiments using superconducting circuits for the purpose of measuring magnetic fields, voltages, and currents have begun. In this article, a brief introduction is given to the theory of the Josephson junction and the superconducting bridge, and the results of using superconducting quantum interference devices for detecting magnetic fields are presented.

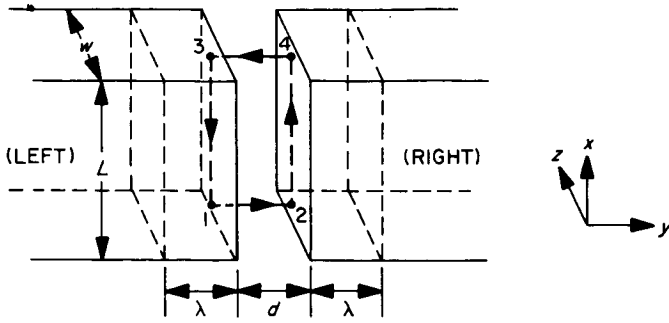
**b. Josephson junction and superconducting bridge.** A Josephson junction can be constructed by separating two superconductors with an insulating (non-superconducting) barrier sufficiently thin ( $\sim 10$  Å) that the exponentially decreasing wave functions for the ground state in the superconductors on either side of the barrier overlap across the barrier. The result is that the barrier acts as a weak superconductor and there is quantum mechanical tunneling of Cooper pairs from one Fermi surface to the other. The Cooper pair current density can be derived by a consideration of the relative phase values of the electron wave functions in the superconductors on both sides of the barrier.

Figure 6 shows a cross-sectional representation of a Josephson junction. The coherent tunneling current density of Cooper pairs through the barrier was predicted by Josephson (Ref. 1) as

$$J = J_0 \sin \phi(r, t) \quad (1)$$

where

$$\phi(r, t) = \theta_r - \theta_l - \frac{2e}{\hbar} \int_l^r \mathbf{A} \cdot d\mathbf{l}$$



**Fig. 6. Cross section of Josephson junction with barrier thickness  $d$ , length  $L$ , width  $w$ , and London penetration depth  $\lambda$**

the difference in the phases of the wave functions across the barrier.  $\theta_l$  and  $\theta_r$  are the respective values of the phases of the wave functions on the left and right sides of the barrier and

$$-\frac{2e}{\hbar} \int_l^r \mathbf{A} \cdot d\mathbf{l}$$

is the line integral of the vector potential across the barrier, which is a term included in the phase difference  $\phi(r, t)$  by Anderson (Ref. 2) to preserve gauge invariance of the phase for non-vanishingly small barrier thicknesses. In Eq. (1)  $J_0$  is equal to the quasi-particle current density when the junction is biased at a voltage of  $\pi\Delta_1\Delta_2/(\Delta_1+\Delta_2)$ , where  $\Delta_1$  and  $\Delta_2$  are half the energy gaps of the superconductors comprising the junction.

The phase difference between two points  $a$  and  $b$  in a superconductor is given by

$$\theta_b - \theta_a = \frac{1}{\hbar} \int_a^b (m^* \mathbf{v} + e^* \mathbf{A}) \cdot d\mathbf{l} \quad (2)$$

where  $\mathbf{v}$  = velocity of the Cooper pairs,  $m^* = 2m$ , twice the electron mass, and  $e^* = -2e$ , twice the electron charge. When an external magnetic field  $B_z$  is applied in the  $z$  direction, Eq. (1) can be put into a more convenient form by substituting Eq. (2) and integrating around the contour shown in Fig. 6. The result is that the current density at the coordinate  $x$  is

$$J(x) = J_0 \sin \left[ \delta(0) + \frac{2e}{\hbar} B_z (d + 2\lambda) x \right] \quad (3)$$

where  $\delta(0) = \theta_2(0) - \theta_1(0)$ , the phase difference at  $x=0$ , and  $d + 2\lambda$  is the extent of penetration by the field in the

junction. Note that  $B_z(d + 2\lambda)x = \Phi(x)$ , the flux across the junction up to the coordinate  $x$ .

Equation (1) shows that  $\phi$  is a function of  $r$  and  $t$ . To find the spatial dependence, one takes the derivative of  $\phi$  in Eq. (3):

$$\frac{\partial \phi}{\partial x} = \frac{2e}{\hbar} B_z (d + 2\lambda)$$

If this is carried through for  $\partial\phi/\partial z$  with the field in the  $x$  direction, the result is

$$\nabla \phi(r, t) = -\frac{2e}{\hbar} B_x \hat{j} \quad (4)$$

where  $\hat{j}$  is a unit vector in the  $y$  direction.

The time dependence is

$$\frac{\partial \phi}{\partial t} = \frac{d\delta(0)}{dt} = \frac{d}{dt} [\theta_2(0) - \theta_1(0)]$$

From quantum mechanics the phase of a wave function changes with time according to  $Et/\hbar$ , where  $E$  is the energy. If a voltage  $V$  is applied across the junction, then the energy difference of the Cooper pairs in tunneling from one side to the other is  $2eV$ . Therefore,

$$\frac{\partial}{\partial t} \phi(r, t) = \frac{2eV}{\hbar} \quad (5)$$

Equations (1), (4), and (5) are called the Josephson equations and describe completely the behavior of a Josephson junction.

The total current is found by integrating Eq. (3) over a junction whose length is  $L$ . Then

$$I = w \int_{-L/2}^{L/2} J(x) dx$$

Defining  $\Phi = B_z L(d + 2\lambda)$ ,

$$J = J_0 \frac{\sin \frac{\pi \Phi}{\Phi_0}}{\frac{\pi \Phi}{\Phi_0}} \sin \delta(0) \quad (6)$$

where  $\Phi_0$  is the quantum flux unit ( $2.1 \times 10^{-7}$  gauss-cm<sup>2</sup>). Equation (6) is analogous to the Fraunhofer diffraction

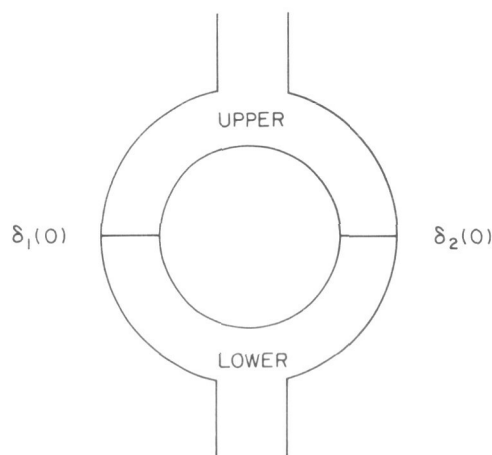


**Fig. 7. Josephson junctions connected in parallel by a superconducting path**

pattern obtained when coherent light passes through a narrow slit. The junction acts as a slit for coherent Cooper pairs. In analogy with a double slit arrangement in optics, it has been shown (Ref. 3) that when two Josephson junctions are in parallel and connected by a superconducting path as in Fig. 7, there is interference of the maximum current through the device. From a consideration of the phases in the upper and lower portions of the superconducting material comprising the parallel junctions, this current is

$$J = 2J_0 \frac{\sin \frac{\pi\Phi}{\Phi_0}}{\frac{\pi\Phi}{\Phi_0}} \cos\left(\frac{\pi\Phi_p}{\Phi_0}\right) \quad (7)$$

where  $\Phi_p$  is the flux linking the parallel circuit.

Equation (7) shows that there is an interference term modulated by a diffraction term. These well-behaved terms are based on the assumption that the two junctions are identical in performance. In practice this situation is difficult to obtain and the variation of the current with magnetic field can appear much distorted from the pattern given by Eq. (2).

Another phenomenon in which interference between Cooper pair current can occur is that of a superconducting bridge junction (Ref. 4). As yet, the detailed nature of this phenomenon is unknown. A typical  $I$ - $V$  characteristic of this type is shown in Fig. 8. The current through the bridge consists of two components: Cooper pairs and single electron conduction. At first, there is a current with

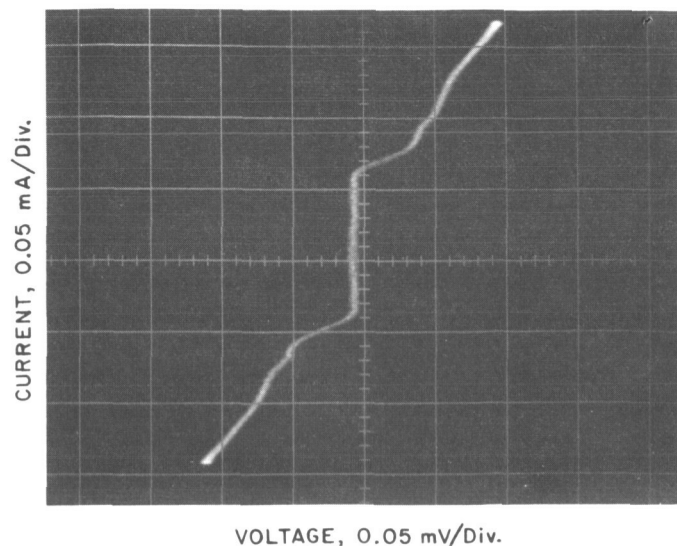


**Fig. 8.  $I$ - $V$  characteristics of a superconducting bridge**

no voltage appearing across the bridge. This is the superconducting state where the current is due to the conduction of paired electrons only. As the current is increased, a voltage continuously appears. This is the resistive-superconductive state which consists of paired and single electron conduction, and is attributed to the observation that the extrapolation of the resistive line to zero voltage leads to a finite current. This state is analogous to the behavior of a Type II superconductor. Dayem and Wiegand (Ref. 4) describe this conduction as the passing of vortices through the bridge at the rate of  $v = 2e/\hbar$  per second. These vortices are created by the current through the bridge and each contains one flux quantum. When two such superconducting bridges are in parallel and connected by a superconducting path, oscillations in the voltage occur across the junction and interference is observed in the resistive-superconductive state. A qualitative explanation of these voltage oscillations is given by Ouboter, et al. (Ref. 5), as follows: Let  $i_c$  be the observed critical current and  $i_c^0$  be the critical current when there is a whole number of flux quanta linking the parallel bridges (Fig. 9). When  $\Phi_{applied} = n\Phi_0$ ,  $i_c = i_c^0$ . When  $\Phi_{applied} \neq n\Phi_0$ , a persistent current  $i_p$  is set up in the loop such that a whole number of flux quanta links the bridges. The current in one bridge is  $i_c/2 + i_p$  and is  $i_c/2 - i_p$  in the other bridge. Since  $i_c + i_p$  must be equal to  $i_c^0$ , the observed critical current  $i_c$  is decreased. As the applied field is varied, the persistent current will vary in order to maintain an even number of flux quanta in the loop, thereby producing a fluctuating critical current. When the bridge current is greater than  $i_c$ , the resistive-superconductive state is reached and quantized vortices will pass through the bridges and be annihilated there.

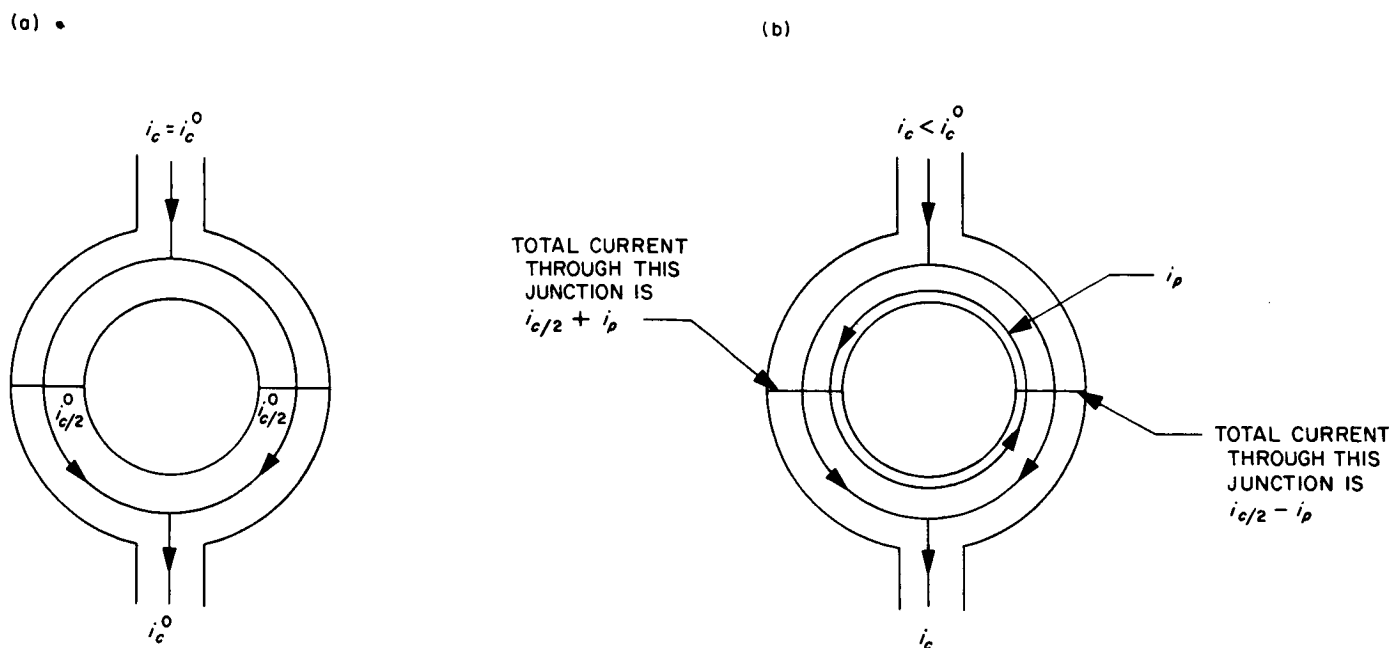


Fig. 9. Parallel bridge circuit illustrating persistent current when (a)  $\Phi_{\text{applied}} = n\Phi_0$  and (b)  $\Phi_{\text{applied}} \neq n\Phi_0$

The induction from the passing of the vortices will produce a voltage across the junction circuit and will oscillate as the external field is changed.

**c. Experimental technique and results.** In the initial experiments, an attempt was made to construct an interference device with superconducting bridges so that the voltage oscillations could be observed as a function of an applied magnetic field. The junctions were constructed much in the same manner as those by Clarke (Ref. 6). A 50% Pb-50% Sn solder droplet was melted and allowed to form a bead around a length of niobium wire (Fig. 10).

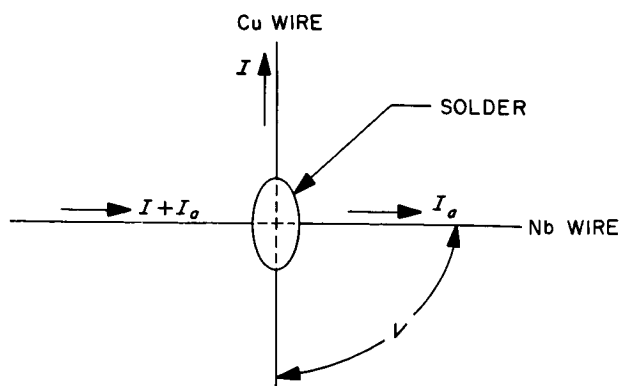
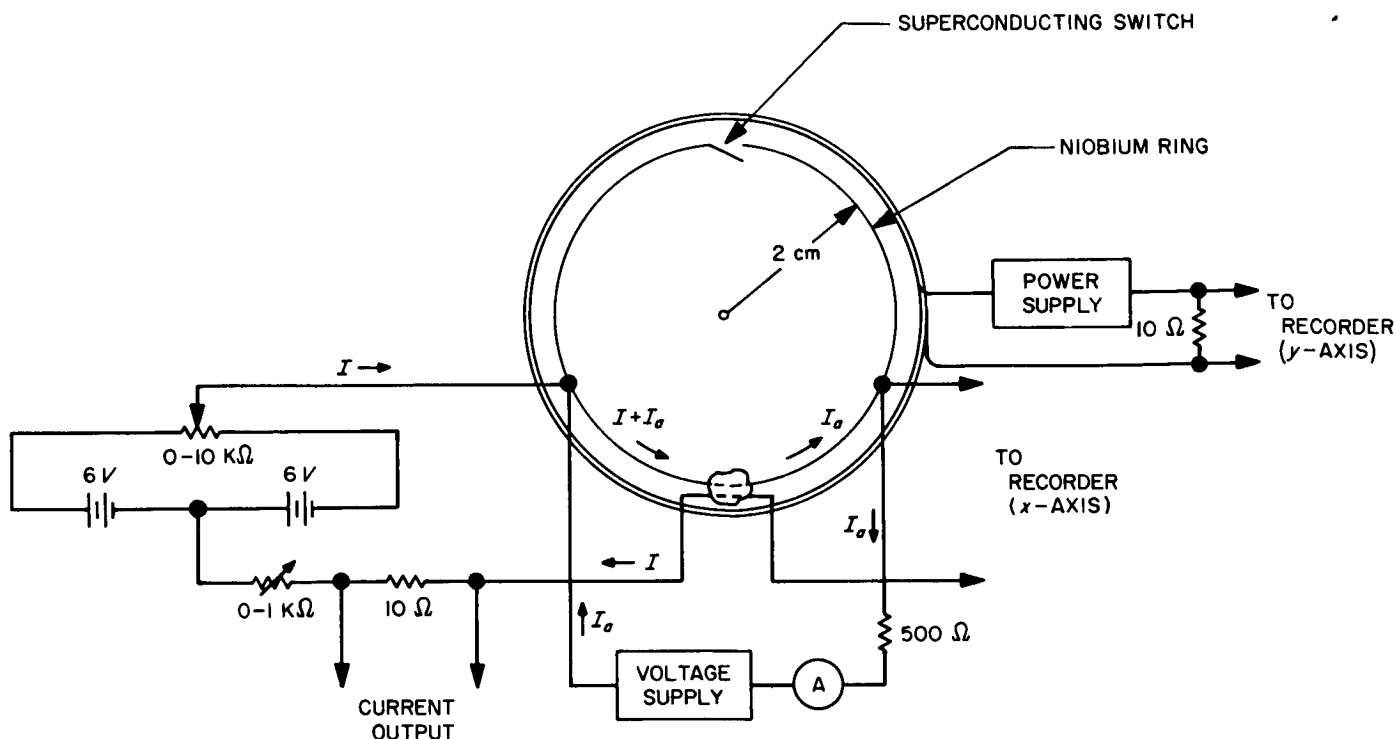


Fig. 10. Schematic of bridge junction used in the experiment for observing interference

Usually the solder covered about 4 mm of the wire. The natural oxide layer on the niobium wire served as the insulating barrier. A second wire, copper, was attached to the solder droplet to provide leads to the junction in a four-terminal arrangement, where two leads were used to drive current through the junction and two leads were used to measure the voltage across the junction.

It was found that voltage oscillations usually occurred across the junction when the room temperature resistance of the junction was between approximately 0.1 to 2  $\Omega$ . When the resistance was between 0.1 and approximately 1  $\Omega$ , Josephson tunneling was observed in some junctions and sometimes a combination of Josephson tunneling and a mixed resistive-superconducting state was observed in the same junction. Above 0.5  $\Omega$ , the  $I$ - $V$  characteristics were usually like those shown in Fig. 8. In this case, voltage oscillations were observed.

The applied magnetic field was produced in two ways: (1) by an additional current  $I_a$  through the niobium wire which produces a field  $B = \mu_0 I_a / 2\pi R$ , where  $R$  is the radius of the wire; and (2) by a Helmholtz coil which was immersed in the liquid helium. Figure 11 shows the arrangement of the junction. With the superconducting switch open, current  $I$  is increased through the junction until a voltage just appears. An additional current  $I_a$  is then sent through the niobium wire. The resulting magnetic field



**Fig. 11. Experimental arrangement used for obtaining voltage fluctuations across the junction as a function of externally applied magnetic fields produced by  $I_a$  or the Helmholtz coils**

changes the persistent current around the parallel junction circuit as explained before. Figure 12a shows the variation of the voltage as a function of  $I_a$  and the equivalent magnetic field.

When the superconducting switch is closed, a current  $I$  is increased until a voltage just appears, as before. In this case, the applied field is provided by the Helmholtz coil. Now the junction is much more sensitive to the magnetic field since the large area of the niobium ring contains a higher flux than there is around the parallel junction circuit. This type of behavior is possible, of course, since it takes much less change in the  $B$  field to produce a quantum unit of flux. Figure 12b shows the voltage variation across the same junction, with the niobium ring closed, as a function of the external magnetic field from the Helmholtz coil.

**d. Conclusions.** Figure 12b shows that by means of detecting the slope of the voltage versus field oscillations, microgauss changes in fields can be detected. Improved techniques in fabricating the bridges should improve the sensitivity by orders of magnitude to approximately  $10^{-9}$  G. A problem which requires further study is how to apply these results and phenomena in the absolute measurement of fields.

## References

1. Josephson, B. D., "Coupled Superconductors," *Rev. Mod. Phys.*, Vol. 36, No. 1, p. 216, Jan. 1964. Also Josephson, B. D., "Super-currents Through Barriers," *Advan. Phys.*, Vol. 14, p. 419, 1965.
2. Anderson, P. W., *Lectures on the Many-Body Problem*, Vol. 2. Academic Press, New York, 1964. Also Anderson, P. W., and Rowell, J. M., "Probable Observation of the Josephson Superconducting Tunneling Effect," *Phys. Rev. Lett.*, Vol. 10, No. 6, p. 230, Mar. 15, 1963.
3. Jaklevic, R. C., et al., "Quantum Interference Effects in Josephson Tunneling," *Phys. Rev. Lett.*, Vol. 12, No. 7, p. 159, Feb. 17, 1964.
4. Anderson, P. W., and Dayem, A. H., "Radio-Frequency Effects in Superconducting Thin Film Bridges," *Phys. Rev. Lett.*, Vol. 13, No. 6, p. 195, Aug. 10, 1964. Also Dayem, A. H., and Wiegand, J. J., "Behavior of Thin-Film Superconducting Bridges in a Microwave Field," *Phys. Rev.*, Vol. 155, No. 2, p. 419, Mar. 10, 1967.
5. Ouboter, R. De Bruyn, et al., "Oscillations in the Voltage Between Two Weakly Connected Current-Carrying Superconductors as a Function of the Applied Magnetic Field," *Physica*, Vol. 32, p. 1448, 1966.
6. Clarke, J., "A Superconducting Galvanometer Employing Josephson Tunneling," *Phil. Mag.*, Vol. 13, p. 115, 1966.

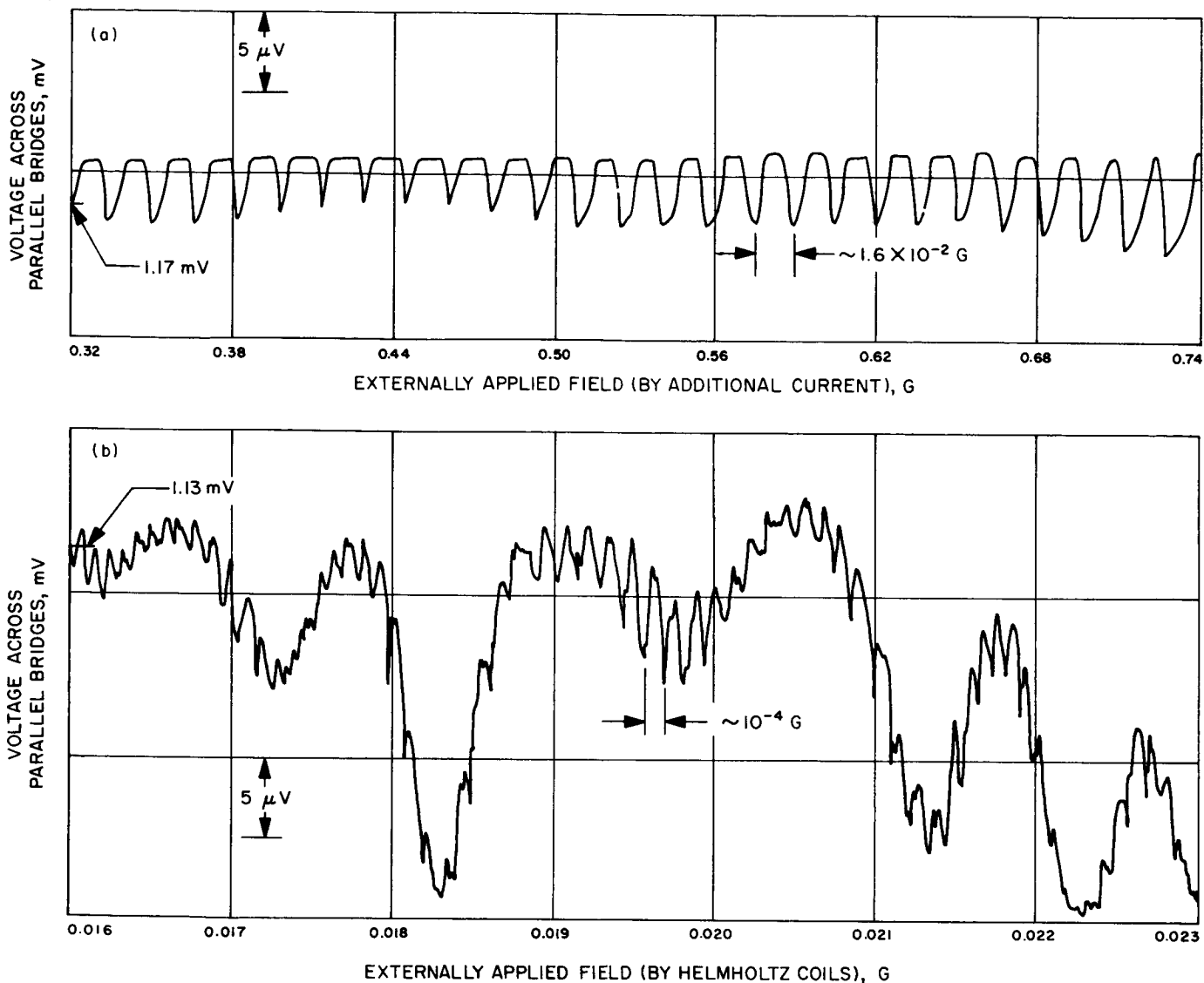


Fig. 12. Voltage oscillations vs magnetic field for parallel bridge circuit: (a) niobium ring open, (b) niobium ring closed

### 3. Improved RF Calibration Techniques: Receiving System

**Noise-Temperature Calibration,** C. T. Stelzried and T. Y. Otoshi

**a. Introduction.** Low-noise receiving system noise-temperature calibrations using the ambient load technique have been discussed in detail (SPS 37-42, Vol. III, pp. 25-32). The calibrations are made by switching the maser input between the antenna and an ambient termination. The principal advantage of this technique is the long-term stability and reliability of the ambient termination. Another advantage is that it is not necessary to evaluate the waveguide losses when the system temperature is defined at the maser input. This technique does depend on a previous calibration of the maser input noise tem-

perature; however, a 10% error in this parameter results in only about a 1% error in the system temperature measurement for a typical JPL low-noise installation.

**b. Results of noise-temperature calibrations.** The principal results of the noise-temperature calibrations that were made by using the ambient load measurement technique are presented in Table 1. The indicated errors are the standard deviation of the individual measurements and of the mean. These errors do not include bias errors such as those due to nonlinearity, etc. The system temperature averages  $T_{SA}$  were computed using only data with: (1) the antenna at zenith, (2) clear weather, (3) no RF spur in receiver pass band, and (4) the probable error

**Table 1. Summary of maser gain, follow-up contribution, and total system temperature parameters  
(Venus and Mars Deep Space Stations; Oct. 2, 1967 to Feb. 6, 1968)**

Deep Space Station	Cone	Frequency, MHz	Maser gain, dB	Follow-up contribution, °K	System temperature, °K
Venus	SCU on ground	2297	47.8 ± 0.16/0.05 9 data points	0.06 ± 0.005/0.002 8 data points	12.3 ± 0.05/0.02 8 data points
	SCU on antenna	2297	48.3 ± 0.10/0.04 8 data points	0.08 ± 0.005/0.002 7 data points	15.9 ± 0.17/0.07 7 data points
	SPR on ground	2388	39.6 ± 0.15/0.06 6 data points	0.52 ± 0.019/0.010 4 data points	18.9 ± 0.21/0.11 4 data points
	SPR on antenna	2388	38.0 ± 0.61/0.10 34 data points	0.73 ± 0.097/0.017 32 data points	22.7 ± 0.40/0.07 32 data points
	XCE on ground, maser mismatched	8448	35.4 ± 1.3/0.37 12 data points	0.95 ± 0.267/0.094 8 data points	31.5 ± 1.2/0.44 8 data points
	XCE on ground, maser matched	8448	34.4 ± 1.4/0.29 24 data points	1.53 ± 0.500/0.121 17 data points	33.3 ± 0.74/0.18 17 data points
Mars	SMF on antenna	2292	42.3 ± 1.2/0.18 47 data points	2.32 ± 0.188/0.036 28 data points	28.0 ± 1.6/0.30 28 data points
		2297	42.0 ± 0.52/0.10 25 data points	2.71 ± 0.317/0.082 15 data points	36.5 ± 0.77/0.20 15 data points
		2388	39.0 ± 0.79/0.19 17 data points	1.38 ± 0.166/0.059 8 data points	24.0 ± 1.1/0.40 8 data points
	XCE	8448	—	1.26 ± 0.013/0.006 5 data points	36.5 ± 0.35/0.16 5 data points

$PE_{T_{SA}}$  less than 0.30°K (from computer program printout CTS/20B). The maser gain is nominally optimized prior to each daily track measurement.

The 36.5°K system temperature measured for the S-band multifrequency (SMF) cone is higher in the diplexed mode of operation used when operating at 2297 MHz due to the added diplexer waveguide losses. The measured system temperature difference between ground and antenna operation at the Venus Deep Space Station is 3.6°K for both the S-band Cassegrain ultra (SCU) cone and the S-band planetary radar (SPR) cone. The follow-up contributions are subtracted from the system temperature measurements to minimize their effect.

Figure 13 shows a plot of the long-term system temperature variations for various cone/antenna configurations, that were obtained by using the ambient load measurement technique. Each horizontal bar represents the averaged temperatures obtained from the measurements taken during the indicated time period. There is considerable instability in the system temperature of the SMF cone operating at the Mars Deep Space Station.

The sources of this instability are from changes that were made in the cone waveguide plumbing (the waveguide switches have been changed), from maser match and noise temperature instabilities, and undoubtedly from some instability in the measurement technique. The SCU cone, which has a minimum of waveguide plumbing, has excellent repeatability for the two time periods indicated.

*c. X-band calibrations.* The X-band Cassegrain experimental cone (XCE) was installed on the 210-ft-diameter Mars Deep Space Station antenna on February 1, 1968 in order to perform antenna gain measurements. Prior to this installation, the cone was thoroughly checked out on the ground. These checks included maser temperature and match evaluations. The initial measurements of the maser temperature on the ground, using both the waveguide liquid helium and liquid nitrogen-cooled terminations in conjunction with the ambient termination, resulted in receiver temperatures considered to be too low (when compared to previous calibrations). It is felt that this was due largely to the high voltage standing-wave ratio (VSWR) of 1.36 at the maser input. The maser input was rematched to a VSWR of 1.02 on December 22,



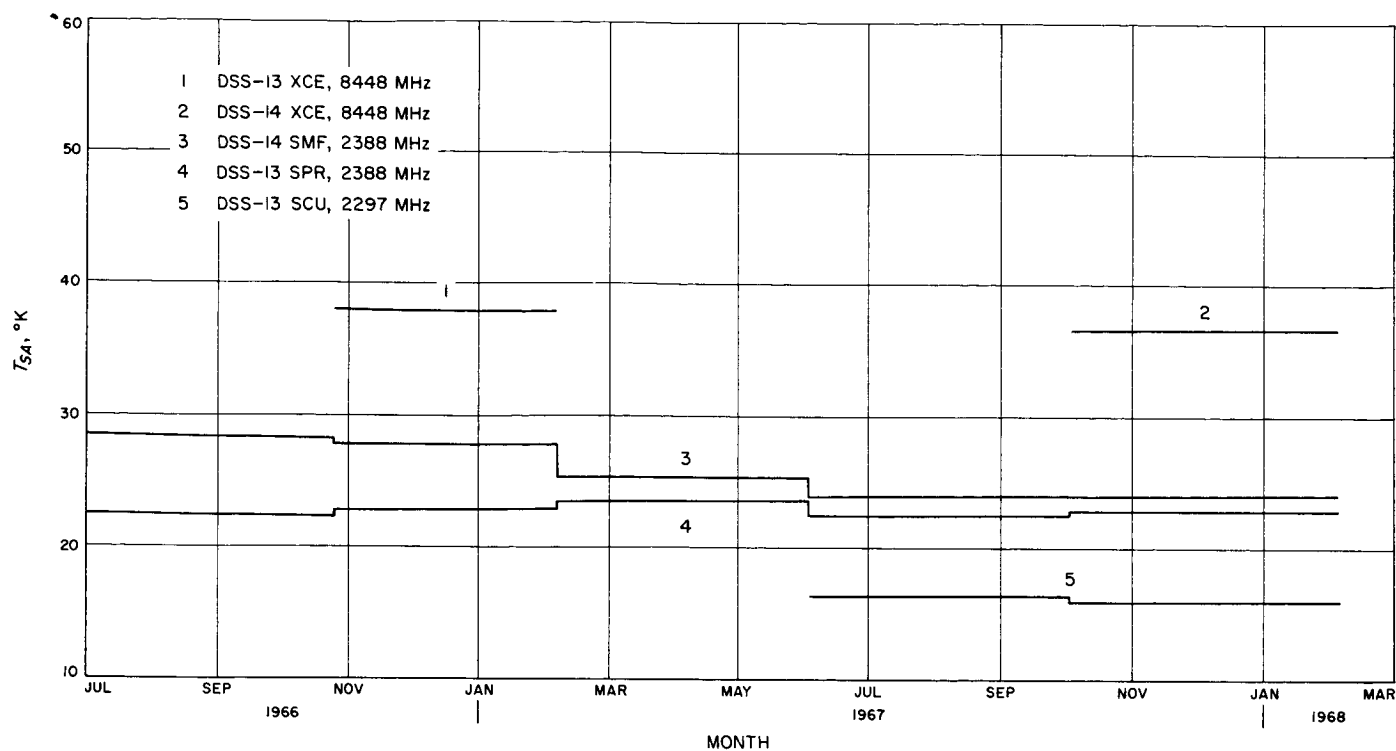


Fig. 13. Long-term system temperature variations for various antenna/cone configurations

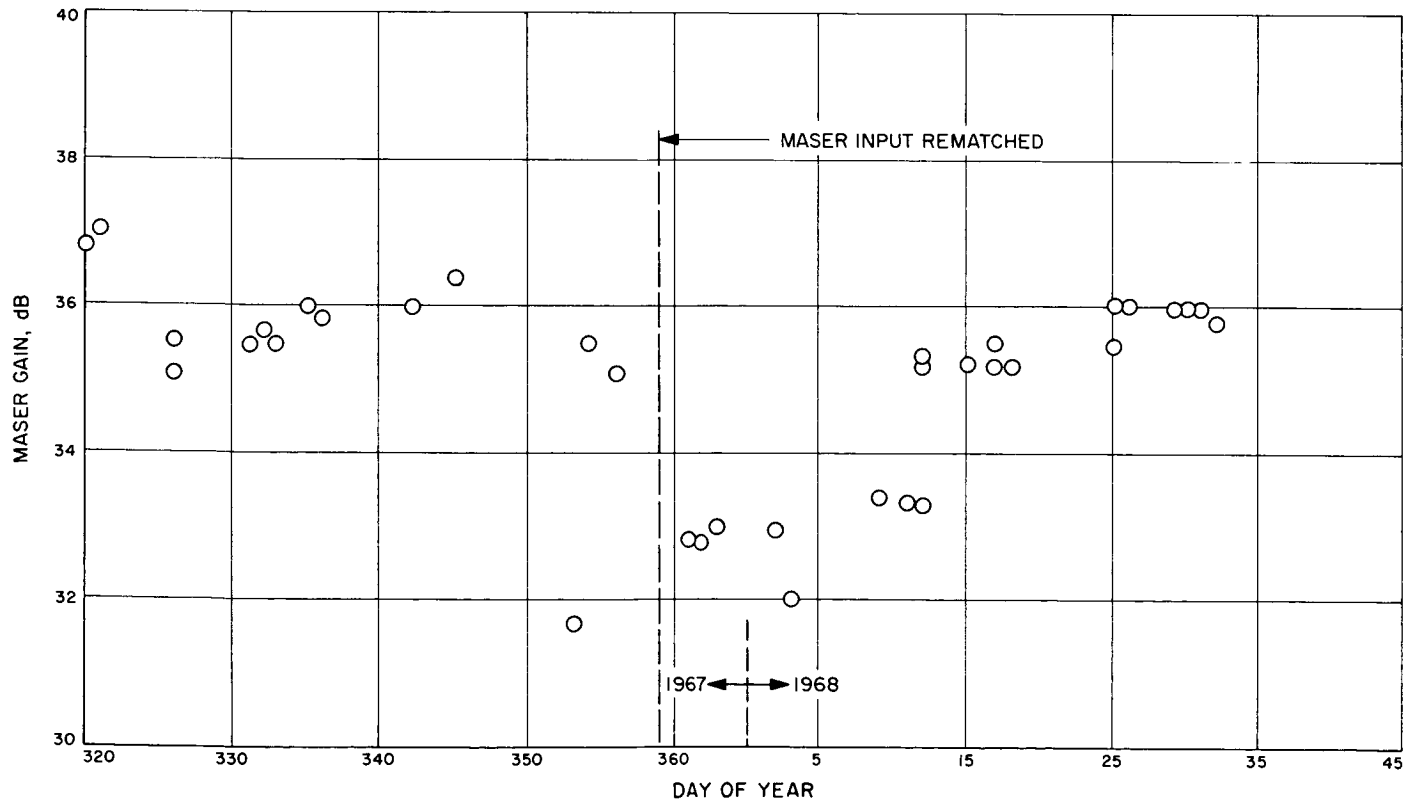


Fig. 14. X-band cone maser gain (Venus DSS XCE cone on ground)

1967. An error analysis indicates that the previous 1.36-VSWR mismatch causes a relatively small error in total system temperature calibrations, but can cause a significant peak error on the calibrated maser temperature. For

example, the effect of the mismatches between a 1.36-VSWR receiver and 1.03-VSWR ambient and liquid nitrogen-cooled thermal reference loads is to cause peak uncertainties of the order of  $\pm 2^\circ\text{K}$  on the measured receiver temperature value. When a 1.02-VSWR receiver is calibrated with these same loads, the peak uncertainties reduce to approximately  $\pm 1^\circ\text{K}$ . These peak uncertainties include the effects of the correlation between reflected and direct-wave receiver noise. If a 1.03-VSWR liquid helium-cooled load is used in place of the nitrogen load, the uncertainties are approximately  $\pm 1$  and  $\pm 0.7^\circ\text{K}$  when the receiver has a 1.36 and a 1.02 VSWR, respectively.

Figure 14 shows a plot of all the XCE cone maser gain measurements taken between November 16, 1967 and January 31, 1968. Figure 15 shows a strip chart recording of the X-band system gain stability obtained with the maser input connected to an ambient termination. The 0.1-dB calibration marks are equivalent to a temperature calibration of about  $0.8^\circ\text{K}$  (assuming a system temperature of  $37^\circ\text{K}$ ). This indicates an inherent radiometric measurement resolution of about  $0.1^\circ\text{K}$  (assuming the measurement is made on a time scale of seconds and neglecting additional instability due to the particular measuring scheme used). Figure 16 shows a recent system linearity check. This measurement indicates a satisfactory system gain level for the radiometer and that amplifier saturation problems do not exist for the range of required temperature measurements.

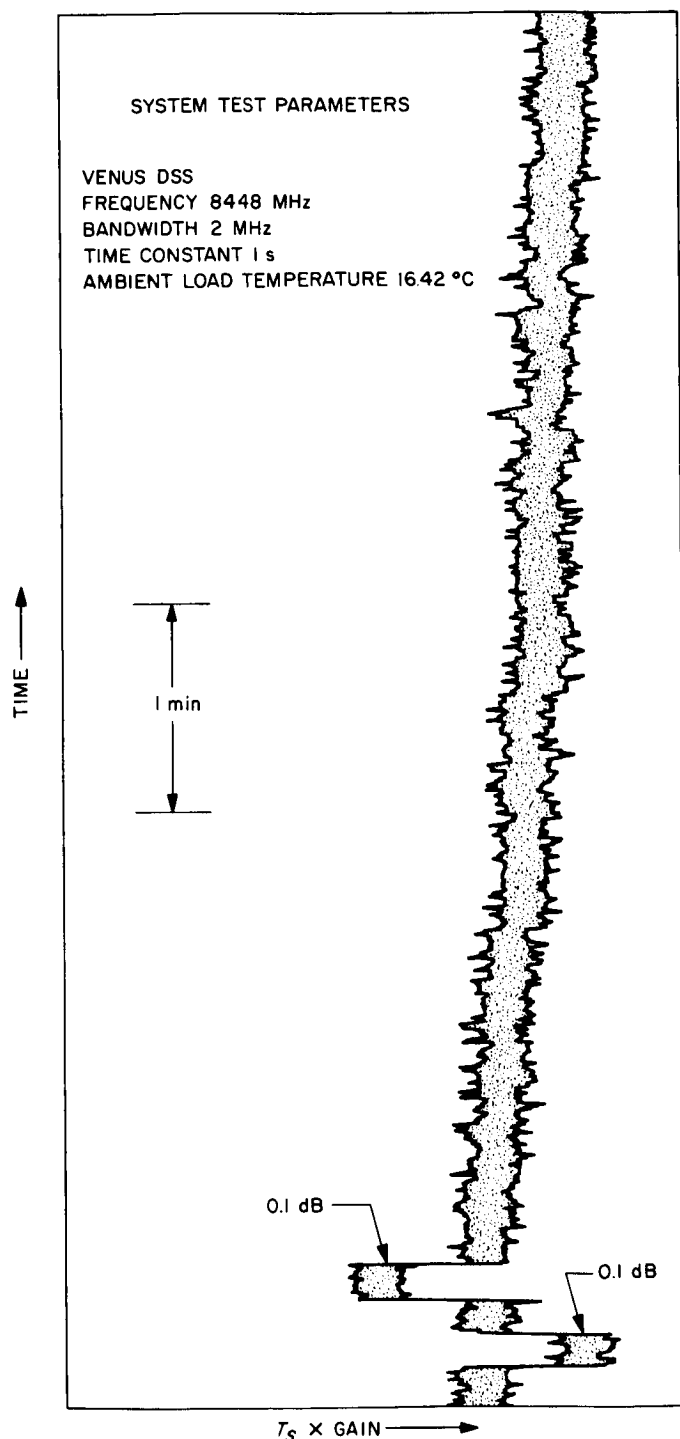


Fig. 15. Strip chart recording of X-band system gain stability (with maser on)

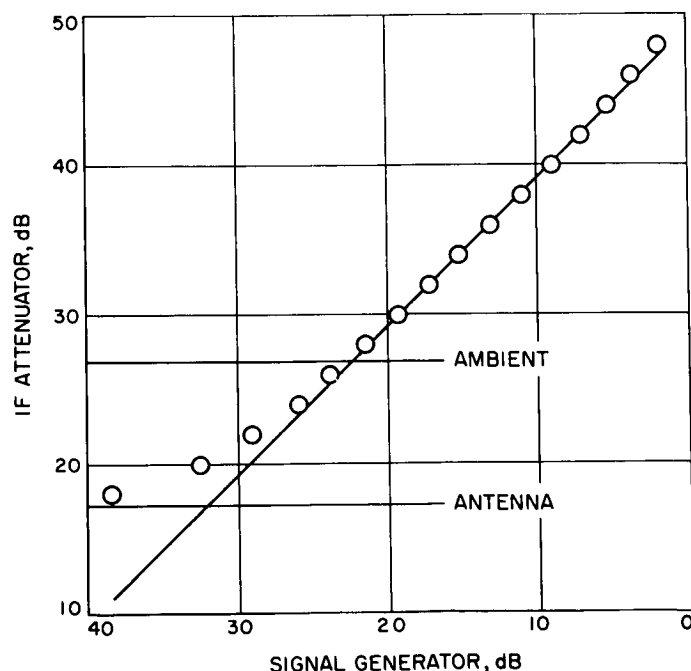


Fig. 16. X-band system linearity measurement

Table 2. XCE cone system noise-temperature calibrations (frequency = 8448 MHz)

DSS	GMT, day/h/min	Humidity, %	Temperature, °F	Clear weather	Reflectometer reading, dB		Gain, dB	$T_F$ , °K	$T_{SA}$ , °K	$PE_{TSA}$ , °K	Comments
					Ambient	Antenna					
Venus	320/19/20	30	69.5	No	20.0	42.3	29.2	1.06	33.06	0.27	Cone on ground
	321/21/10	33	69.0	Yes	39.0	41.0	37.0	0.93	31.53	0.26	Cone on ground
	326/17/08	43	51.1	No	40.0	38.0	35.5	1.23	31.74	0.26	Heavy rain previous day
	331/22/10	26	57.0	Yes	37.5	41.2	35.5	0.76	31.07	0.26	Cone on ground
	332/22/45	68	48.3	No	37.4	42.2	35.4	0.77	43.24	0.30	Cone on ground
	333/16/00	55	41.5	Yes	37.0	21.6	35.5	0.79	34.30	0.26	Clear, cold weather; cone on ground
	335/16/16	58	38.0	No	30.6	35.8	36.0	0.64	32.23	0.25	Hazy weather
	336/18/00	34	45.2	Yes	37.0	34.0	35.7	1.47	30.31	0.25	Cone on ground
	342/20/50	28	46.5	Yes	39.2	36.0	36.0	0.76	30.82	0.25	Cone on ground
	345/19/00	19	61.0	Yes	40.1	36.7	36.4	0.84	30.97	0.25	Cone on ground
	353/22/30	83	32.5	No	29.7	28.6	31.7	1.10	43.62	0.36	Cone on ground
	354/23/30	46	33.8	Yes	39.3	36.0	35.5	0.80	30.85	0.25	Cone on ground
	356/18/25 <sup>a</sup>	32	39.0	Yes	40.9	41.0	35.1	1.26	31.76	0.25	Cone on ground <sup>a</sup>
	361/14/10 <sup>a</sup>	36	59.0	Yes	36.2	35.4	32.8	1.99	34.41	0.27	Cone on ground <sup>a</sup>
	362/19/15	36	59.0	Yes	35.0	33.0	32.8	2.00	34.47	0.27	Cone on ground
	363/22/00	34	51.5	Yes	39.0	35.6	33.0	1.98	34.32	0.27	Cone on ground
	2/19/10	45	43.5	Yes	35.2	33.0	33.0	2.12	33.46	0.26	Cone on ground
	3/18/40	35	40.0	Yes	38.0	35.3	32.0	2.15	33.44	0.26	Clear weather
	4/21/40	24	49.0	Yes	40.0	36.0	33.0	1.91	32.83	0.44	Cone on ground
	5/20/50	25	49.6	Yes	41.6	42.7	33.1	2.06	33.77	0.28	Cone on ground
	8/22/30	23	45.6	No	37.0	36.0	33.0	1.92	33.53	0.26	Cone on ground
	9/22/37	27	49.5	No	41.1	37.5	33.4	1.98	33.75	0.27	Cloudy weather; cone on ground
	11/00/45	64	49.0	Yes	45.3	43.1	33.3	2.00	33.61	0.28	40-mph wind gusts
	12/02/15	30	40.0	Yes	42.9	38.9	33.3	1.97	33.55	0.26	Cone on ground
	12/19/30	21	48.0	No	38.0	35.0	35.3	1.15	32.95	0.26	Some clouds
	12/21/30	20	49.0	No	36.8	38.0	35.2	1.15	33.41	0.27	Cone on ground
	15/18/46	48	57.0	Yes	40.7	37.6	35.5	1.11	33.70	0.26	Cone on ground
	17/18/45	24	53.0	Yes	43.5	38.8	35.5	1.13	33.27	0.26	Cone on ground
	17/01/00	55	46.0	Yes	43.7	39.5	35.2	1.16	33.47	0.26	Prior to power off
	18/16/10	30	46.5	Yes	43.8	49.0	35.2	1.12	32.69	0.26	Cone on ground
	25/02/10	28	50.0	Yes	42.3	41.0	35.5	1.18	32.59	0.26	Cone on ground
	25/17/03	28	54.0	Yes	47.7	38.5	36.0	1.01	32.37	0.26	Cone on ground
	26/21/38	49	52.0	No	43.5	39.0	36.0	1.01	32.87	0.26	Cone on ground
	29/22/30	22	46.8	Yes	43.0	41.0	36.0	1.08	32.65	0.26	Cloudy weather
	30/17/08	42	43.0	No	38.8	36.1	36.0	1.00	31.76	0.25	Winds up to 40 mph
	31/21/30	60	50.0	Yes	38.0	37.0	36.0	0.85	32.27	0.26	Cone on ground <sup>b</sup>
	32/16/00 <sup>b</sup>	36	47.0	Yes	39.3	36.4	35.9	1.04	32.19	0.26	Checkout
	33/07/00	—	—	Yes	20.0	20.0	36.0	1.27	36.11	0.28	Checkout
	33/07/20	—	—	Yes	20.0	20.0	36.0	1.24	36.06	0.28	Checkout
	36/05/10	—	—	No	—	—	—	1.16	36.31	0.28	
	36/05/10	—	—	No	—	—	—	1.13	38.37	1.48	
	36/05/10	—	—	No	—	—	—	1.21	36.33	0.28	
	36/21/05	50	50.0	No	—	—	—	1.29	37.04	0.28	
	36/21/10	50	50.0	No	—	—	—	1.29	36.60	0.28	
	36/21/17	50	50.0	No	—	—	—	1.32	37.03	0.29	
	37/14/44	—	—	Yes	—	—	—	1.27	36.71	0.28	
	37/14/41	18	—	Yes	—	—	—	1.27	36.71	0.28	
	37/14/43	—	—	Yes	—	—	—	1.27	36.76	0.29	

<sup>a</sup>Maser input VSWR rematched at this time.  
<sup>b</sup>Cone installed on 210-ft-diam antenna at this time.

Table 2 and Fig. 17 show, respectively, a listing (from the computer) and a plot of all the total system temperature ( $T_{SA}$ ) calibrations that were taken pointed toward zenith on the ground at the Venus Deep Space Station between November 16, 1967 and February 1, 1968 and toward zenith on the antenna at the Mars Deep Space Station between February 1, 1968 and February 6, 1968.

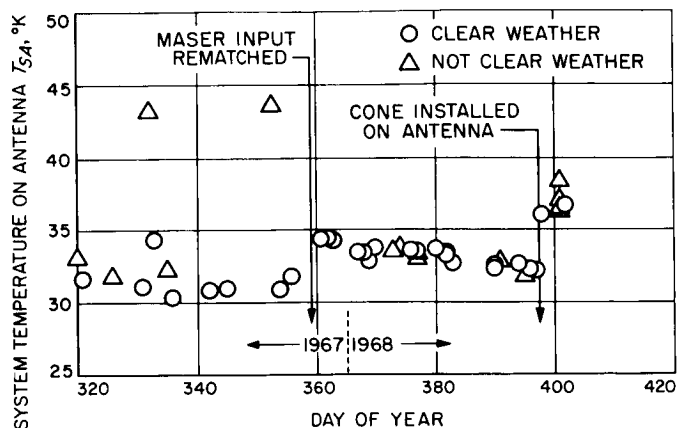


Fig. 17. XCE cone total system temperature measurements pointed toward zenith

The follow-up contribution to the system temperature, denoted by  $T_F$ , is shown in Fig. 18. The unweighted average of the system temperatures for the 8 runs taken with a higher maser VSWR was  $(31.5 \pm 1.2/0.44 \sigma)^\circ\text{K}$ . The 17 runs taken on clear days after rematching averaged  $(33.3 \pm 0.74/0.18 \sigma)^\circ\text{K}$ . Some of the  $1.3^\circ\text{K}$  difference (subtracting the follow-up contribution) is undoubtedly due to

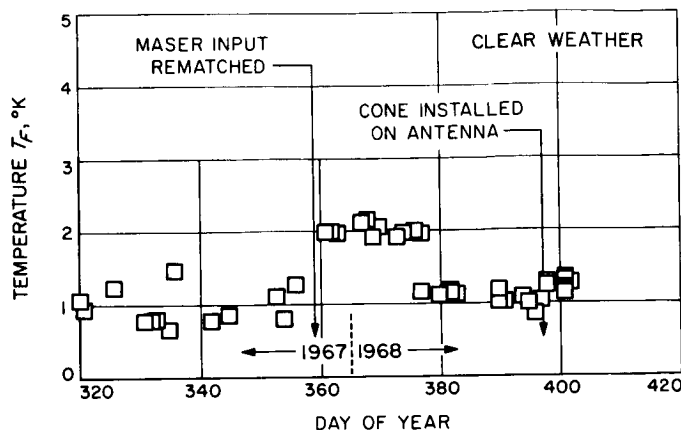


Fig. 18. Follow-up contribution to XCE cone total system temperature measurements pointed toward zenith

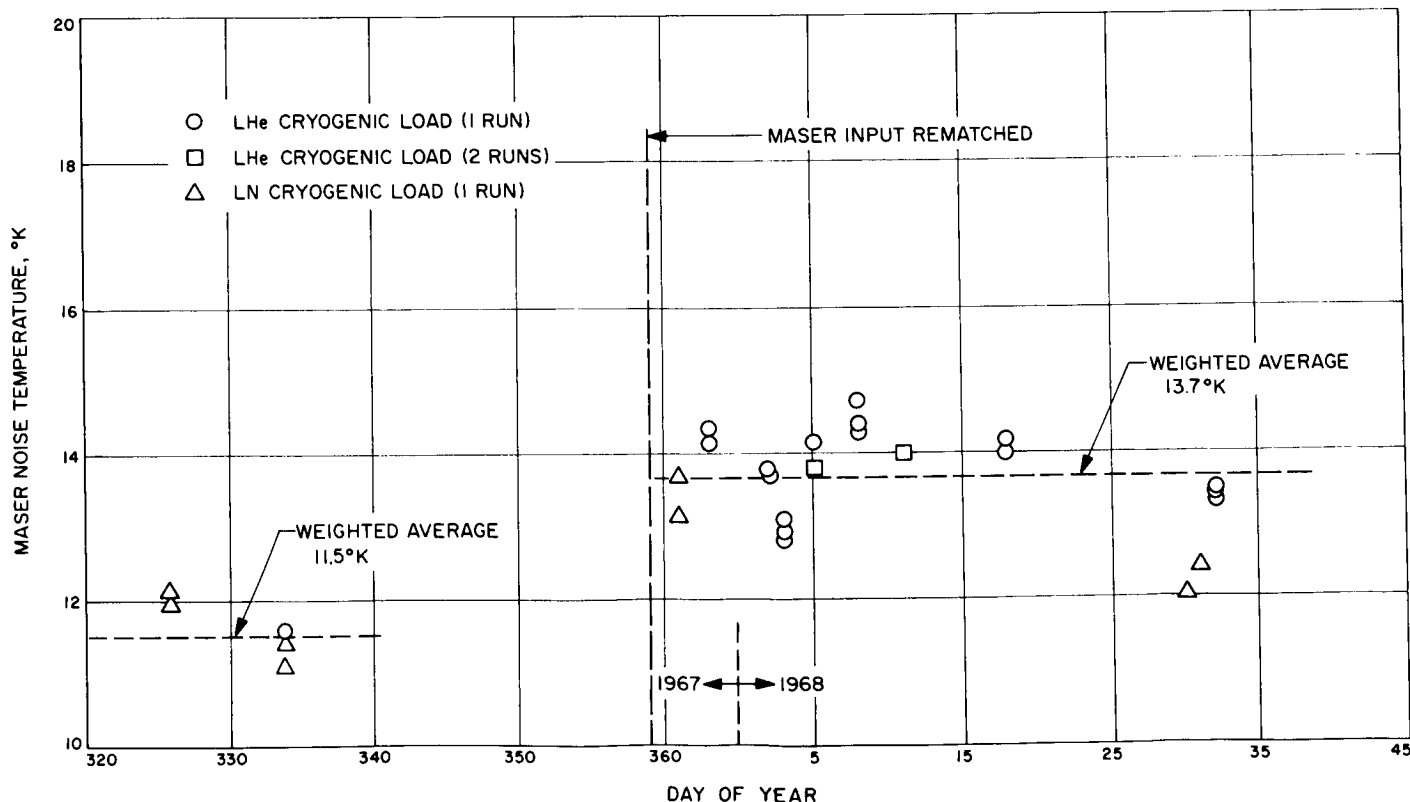


Fig. 19. X-band cone maser noise temperatures (Venus DSS XCE cone on ground)

measurement resolution, but a slight increase in measured system temperature can probably be attributed to measurement error corrected by rematching the maser input. The increase in system temperature between the ground and antenna is 3.4°K (again obtained by subtracting the follow-up contributions).

Figure 19 is a plot of the maser noise temperatures which were calibrated for the XCE cone from November 1967 through January 1968 by using cryogenic noise standards. The weighted averages for the maser temperature before and after maser rematching are respectively 11.5 and 13.7°K. The corresponding total probable error for each average is approximately 0.8°K, which includes a 0.1°K probable error due to dispersion of the data points.

Calibrations of the gas tube temperatures defined at the maser input reference flange are summarized in Table 3. The associated 3- $\sigma$  errors on these calibrations are approximately 5% of their reported value.

**Table 3. Summary of gas tube noise temperature calibrations**

Deep space station	Cone	Frequency, MHz	Low gas tube, °K	High gas tube, °K
Venus	SCU	2295	0.7	6.6
			13 data points	13 data points
	SPR	2388	4.5	44.7
			12 data points	12 data points
Mars	XCE	8448	3.7	38.9
			21 data points	21 data points
	SMF	2295	4.3	33.8
			37 data points	36 data points

#### 4. Radio Star Tracking at Mars Deep Space Station,

R. E. Cormack

**a. Introduction.** During the month of January 1968, a program of regular RF star tracking was initiated at the Mars Deep Space Station. While the reasons for this effort are many, the principal reasons are:

- (1) To improve knowledge of antenna performance.
- (2) To develop a better technique for both JPL and contractor operating personnel.

It is the purpose of this article to comment on the initial measurements that were made. These measurements give an overall system efficiency of approximately 59% at the

maser reference flange, which is in close agreement with the results of an independent method using the *Surveyor I* spacecraft.

**b. Initial measurements.** To determine one specific aspect of antenna performance, that of antenna efficiency, a fair amount of source temperature data was collected using 3C123 for observation because of its established behavior as a nearly point source of nonvariable nature. Observations of Cygnus A were also initiated, and it is intended to continue these for purposes of comparison with the 3C123 observations and with the large quantity of collected data obtained at the Venus Deep Space Station from observations of Cygnus A.

Table 4 shows indicated Mars Deep Space Station antenna efficiencies for various elevation angles as calculated for January 1968 source temperature measurements.  $F_{AT}$  is an atmospheric correction factor that takes into account oxygen and water vapor effects (SPS 37-43, Vol. III, pp. 63-68). The basis for  $T_S$  (100%) in each case is the output of the power curve fit program,<sup>1</sup> using selected radioastronomical input data. The data selection was based on measurements made at the 1420-MHz hydrogen line frequency and selected absolute measurements at 4080 MHz (Ref. 1).

The Mars Deep Space Station antenna efficiency as calculated from the *Surveyor I* lunar range gain test was

<sup>1</sup>Private correspondence from Boris L. Seidel, JPL.

**Table 4. 3C123 and Cygnus A source temperature observations<sup>a</sup>**

Elevation, deg	$T_S$ observed, °K	$F_{AT}$ , dB	$T_S$ corrected, °K	Efficiency, % <sup>b, c</sup>
<b>3C123</b>				
15	20.6	-0.104	21.1	57.9
45	21.3	-0.045	21.5	59.1
60	21.1	-0.037	21.3	58.5
85	20.7	-0.032	20.9	57.3
<b>Cygnus A</b>				
15	555	-0.104	569	57.3
45	576	-0.045	582	58.7
60	576	-0.037	581	58.5
85	554	-0.032	558	56.3
<sup>a</sup> Measurement frequency = 2295 MHz.				
<sup>b</sup> 3C123 efficiency based on $T_S$ (100%) = 36.46°K corrected for source width = 20" to $T_S$ (100%) = 36.41°K.				
<sup>c</sup> Cygnus A efficiency based on $T_S$ (100%) = 1027.9°K corrected for 2 point sources separated 118" to $T_S$ (100%) = 992.0°K.				

59.16% at the maser reference flange at an elevation angle of  $35 \pm 10$  deg and at a 2295-MHz frequency (SPS 37-44, Vol. III, pp. 100-105).

A rigorous error analysis of the *Surveyor I* gain test has been conducted and the January 1968 Mars Deep Space Station data reported here is in excellent agreement (order of 0.5%). A thoroughgoing error analysis of the latter has not been conducted because of the initial measurement nature of the data. A consistency check among five data points, however, shows a probable error, including assumed bias errors due to the technique used, of about 0.6% of the source temperature measured.

### Reference

1. Wilson, R. W., and Penzias, A. A., "The Flux of Six Radio Sources at 4.08 GHz," *Astrophys. J.*, Vol. 146, pp. 286-287, 1966.

## 5. Receiving System Noise-Temperature Performance at X-Band, D. A. Bathker

**a. Introduction.** The 85-ft az-el reflector at the Venus Deep Space Station (DSS 13) has been operated at X-band, 8448 MHz, using the X-band Cassegrain experimental (XCE) feedcone. Results obtained by observing Cygnus A during June 1967, in terms of excess system noise temperature on source, have been reported (SPS 37-49, Vol. II, pp. 65-67). In this reporting, all off-source system temperature measurements are given. The result is a system noise-temperature profile, including daily variations.

**b. Off-source system temperature measurements.** In SPS 37-49, Vol. II, pp. 65-67, approximately 370 measured excess system noise temperatures were given and plotted against elevation angle, for a selected fixed focus setting, which was optimum for elevation angles of 60-90 deg. The excess system noise temperature is defined as

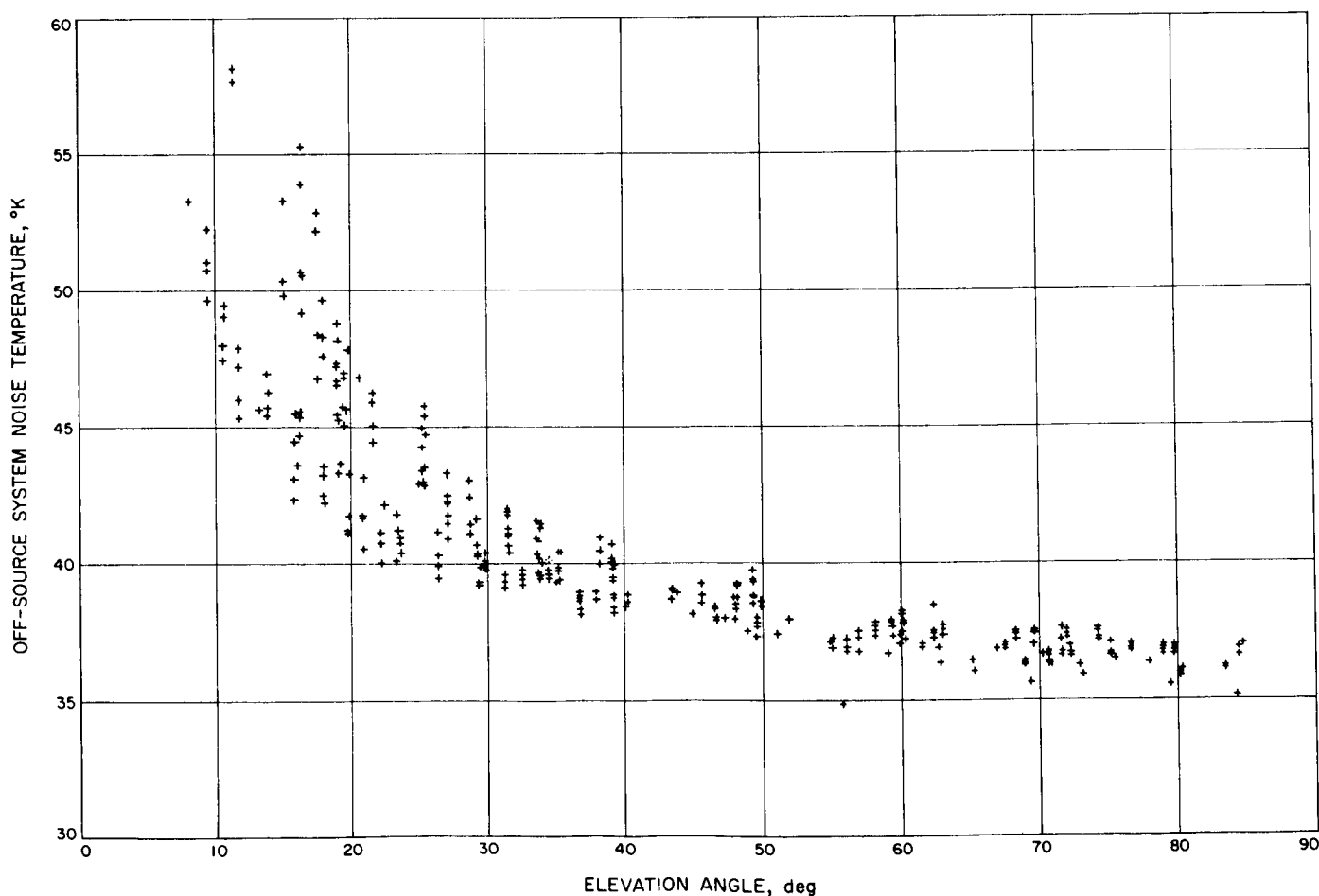


Fig. 20. Total system noise temperature vs elevation angle (VenusDSSXCE feedcone, 8448 MHz)

that increase in temperature observed at the maser reference flange when pointing at Cygnus over that measured on the adjacent cold sky. Figure 20 shows the corresponding cold sky measurements, taken between GMT days 160 and 175, 1967. Because all data were simply plotted without regard to day number or weather, it was first suspected the large spread among data at low elevation angles was due to weather. Closer examination of the raw data proved all low temperatures below 40-deg elevation occurred when looking approximately 90-deg azimuth, or east, and all high temperatures occurred when observing towards the west. The land mask at the Venus Deep Space Station is generally below 0.5-deg elevation when looking east but is always above 3 deg and as high as 13 deg between azimuths of 200 to 360 deg. It is clear that the high measured temperature portion of Fig. 20 is due to the land mask at the Venus Deep Space Station.

Of further interest in Fig. 20 is the increase in system noise from zenith to 10-deg elevation, which, for the favorable land mask direction, is only 13–14°K. This value is indicative of the high dry site of the Goldstone complex; a comparable value at S-band is 11°K (Ref. 1). Because antenna sidelobe, spillover, and blockage effects are of second-order importance, the increase in system noise temperature is nearly totally related to the main beam observing atmospheric extinction.

Table 5 gives the average temperatures  $T_{SA}$  and standard deviations of the data. Average temperatures and standard deviations below 30-deg elevation are qualified as including both sets of data (source rising and setting).

#### Reference

1. Potter, P. D., *The Design of a Very High Power, Very Low Noise Cassegrain Feed System for a Planetary Radar*, Technical Report 32-653. Jet Propulsion Laboratory, Pasadena, Calif., Aug. 24, 1964.

**Table 5. Off-source system noise temperatures (Venus DSS XCE feedcone, 8448 MHz)**

Elevation, deg	Average $T_{SA}$ , °K	Standard deviation, °K
82	36.53	0.45
74	36.78	0.43
64	37.14	0.61
57	37.18	0.57
46	38.52	0.54
35	39.84	0.93
25	41.95	1.92
16	47.04	3.62
9	51.38	—

## 6. Efficient Antenna Systems: X-Band Gain Measurements, D. A. Bathker

**a. Introduction.** The 85-ft-diameter az-el reflector at the Venus Deep Space Station was configured with the X-band Cassegrain experimental (XCE) feedcone on two occasions, during November 1966 and June 1967, for the purpose of evaluating antenna performance at extended frequency. Results obtained by observing Cygnus A (3C405) have been reported (SPS 37-45, Vol. III, pp. 42–48 and SPS 37-49, Vol. II, pp. 65–67). The Cygnus data indicate an overall system efficiency, i.e., aperture efficiency, including losses to the maser reference flange of  $(46.2 \pm 11.2\%)$ ,  $3\sigma$  for elevation angles of 40–70 deg.<sup>2</sup> The antenna gain stability is not outstanding; the RF beam pointing repeatability has been shown to be on the order of  $\pm 0.020$  deg and an observable degree of mechanical hysteresis and nonrepeatability of the paraboloid surface appears in both mechanical and RF tests (SPS 37-47, Vol. II, pp. 77–80). A somewhat smaller constraint in determining the efficiency more accurately is a 15%,  $3\sigma$  tolerance on the Cygnus flux density.

Using the Tiefort Mountain–Venus Deep Space Station collimation range, the system efficiency can be obtained independently by ground-based techniques. This article will discuss the ground-based method, which results in an overall system efficiency of  $(44.7 \pm 4.9\%)$ ,  $3\sigma$  for an elevation angle near 1 deg. The improvement in tolerance using the ground-based method is obvious; however, extension of this efficiency value to higher elevation angles cannot, at the present time, be done. The effective surface tolerance of the system, when looking at a 1-deg elevation angle, is 0.065 in. rms. A change of only 0.005 in. rms will change the system efficiency 2%.

**b. Ground-based measurement technique.** The method of gain measurement used is considered to be the most reliable among several alternative techniques. Briefly, a known flux is established at the transmitting site and the inverse square law is used to establish the flux at the receiving site. By so doing, serious questions concerning multipath propagation, which arise when using small comparison apertures at the receiving site, are avoided. Also avoided is the difficult matter of establishing an absolute flux. The flux established at the transmitter site is referenced to a full-scale instrument deflection. The received flux is similarly referenced to the same instrument deflection, causing absolutes to drop out. The

<sup>2</sup>The Cygnus flux density is taken to be  $S = (187.6 \pm 28.1) \times 10^{-26} \text{ W} \cdot \text{m}^{-2} \cdot \text{Hz}^{-1}$ ,  $3\sigma$ .

method of calibrating differences in power levels has been discussed in detail (SPS 37-43, Vol. III, pp. 61-63). A second requirement to establish the transmitter flux is the calibration of the transmitter antenna. A conical horn is used, an aperture having desirable properties from both a radiation pattern sense (suppressed sidelobes) and from an analytical sense. Calibration of the horn has been discussed in detail (SPS 37-44, Vol. III, pp. 94-100).

Another problem associated with the precise evaluation of a large ground antenna using ground-based techniques is that of removing the aperture under test sufficiently far from the exciting source so the phase front across the test aperture may be considered planar. An expression based on uniform illumination of a circular aperture relating the observed gain  $G$  to the true gain at infinity  $G_0$  is

$$\frac{G}{G_0} = \left( \frac{\sin x}{x} \right)^2 \quad (1)$$

where  $G_0 = 4\pi A/\lambda^2$ ,  $x = \pi D^2/8\lambda R$ , and  $D$ ,  $\lambda$ , and  $R$  are the aperture diameter, wavelength, and range, respectively (Ref. 1). A commonly accepted separation,  $R = 2D^2/\lambda$ , results in an observed gain  $G = 0.9872 G_0$ . For the Venus Deep Space Station to Tiefert Mountain evaluation range,  $R = 1.085 D^2/\lambda$  for the 85-ft reflector operated at X-band, 8448 MHz. This separation may be considered to lie in the quasi near-field inasmuch as the phase at the edge of the 85-ft aperture lags the central ray by 41.5 deg and the observed gain  $G = 0.9571 G_0$ . It is necessary for the system to remain focused at infinity for the observed gain to follow Eq. (1). Because of focusing difficulties previously discussed (SPS 37-49, Vol. II, pp. 65-67), it was decided to peak the antenna gain for the near-field tests by adjusting the hyperboloid. Peak gain occurred with the control room synchro indicator at -25 (Fig. 24, SPS 37-47, Vol. II, p. 78), which is consistent with a ray tracing analysis that indicated a near-field best fit focus would occur with the hyperboloid approximately 0.200 in. towards the apex of the paraboloid compared to the focus position at infinity.

Under the above conditions, the near-field observed gain will lie within the limits

$$0.9571 G_0 < G < 1.000 G_0$$

or the true gain at infinity,  $G_0 = (1.022 \pm 0.022 G), 3\sigma$ .

As an approximate cross check on the above, two cases were input to the radiation pattern program (Ref. 2),

which computes, among other things, axial gain loss as a function of aperture phase illumination. Using the actual rather than uniform amplitude illumination for cases having phase fronts excited from infinity and excited from Tiefert Mountain, a gain reduction of 0.9665 was obtained when excited from Tiefert Mountain. It therefore appears that the uniform illumination analysis is slightly conservative and will be adopted here.

On June 21, 1967, the Tiefert Mountain station was configured with the previously calibrated +29.510-dB gain standard horn excited with right-handed circular polarization by a turnstile junction polarizer. The horn was boresighted on the Venus Deep Space Station by means of an optical plummet and arranged to position all electronic equipment within the personnel shelter. The laboratory-calibrated portable thermistor power bridge was rechecked for linearity using dc substitution to an accuracy of 0.3%,  $3\sigma$  for a determination of a 20-dB change in power levels. The instrument was capable of resolving a few millidecibels because of an improved thermal design for the RF head and through the use of an integrating digital voltmeter readout. By use of two attenuators, each having greater than 20-dB range and one having precision resettability, the  $Z_0$  available power at the transmitter reference flange was determined to be +19.746 dB above full-scale indication of the instrument, nominally 10 mW. A second RF head, also of improved thermal design, was used as a monitor to detect possible long-term drifts in the carefully calibrated output. Because a separate amplitude levelling feedback loop was used, no drift more than a few millidecibels was detected for several hours in the transmitter output.

The calibrated portable bridge was then transported to the Venus Deep Space Station and attached to the maser reference flange within the XCE feedcone, shown on the 85-ft-diameter az-el reflector in Fig. 21. Propagation conditions over the 20-km Tiefert Mountain-Venus Deep Space Station path are seldom stable; however, during the gain test peak-to-peak fluctuations were about 0.5 dB, which is quite acceptable. By use of a 10-s integrating digital voltmeter, the fluctuations were averaged and the mean received power at boresight was determined by dc substitution to be 24.587 dB below full-scale indication of the instrument, or approximately -14.6 dBm. This power level is sufficiently above instrumental jitter and drifts such that these defects are negligible.

Table 6 shows measured and computed parameters used in obtaining the gain by ground-based techniques.



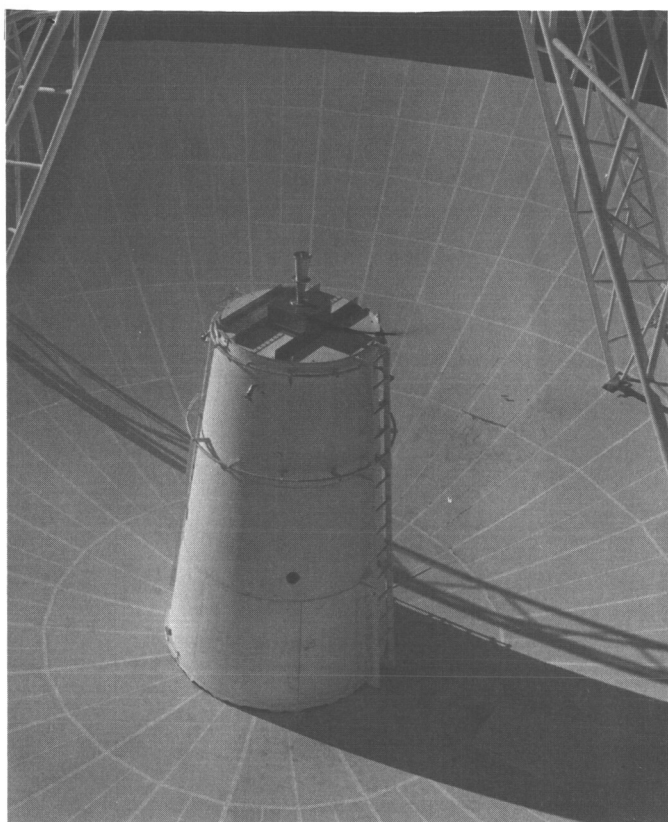


**Fig. 21. XCE feedcone installed on Venus Deep Space Station 85-ft-diameter az-el reflector**

It is clear that further effort towards improving tolerances should be devoted to the gain standard horn calibration.<sup>3</sup>

Because a dissipation loss of 0.150 dB occurs before the maser reference flange within the XCE feedcone, it is of interest to compare the measured aperture efficiency with the predicted efficiency, referenced to the antenna reference flange. Unfortunately, our knowledge of the surface tolerance is limited. We can, however, separate components of the efficiency and solve for the effective system surface tolerance at the elevation angle of the collimation station. Table 7 shows the method of computation; the efficiency balance of 0.715 is all attributed to the Ruze type loss, which leads to 0.065 in. rms.

The difficulty in extending the ground-based efficiency value to higher elevation angles, for the purpose of a direct determination of the Cygnus flux, can be seen in Fig. 22, which relates surface efficiency to surface tolerance for 8448 MHz. In Fig. 22, it will be seen that a very small change in the effective system surface tolerance will cause an appreciable change in system efficiency.

<sup>3</sup>Other possible sources of error, including multipath, polarization mismatch, antenna pointing, and possible wavefront decorrelation as indicated by 0.5-dB scintillations, have been examined and are considered small in comparison to the gain standard horn calibration error.

**Table 6. Ground-based gain measurements**

Parameter	Value, dB	1- $\sigma$ tolerance, dB	Comment
Transmitter power at transmitter reference flange	+ 19.746 (Ref.) <sup>a</sup>	$\pm 0.010^b$	By dc substitution
Insertion loss, transmitter reference flange to aperture	— 0.089	$\pm 0.020$	Estimated
Gain standard horn directivity	+ 29.510	$\pm 0.150$	Pattern integration (estimated)
Effective radiated power	+ 49.187 (Ref.) <sup>a</sup>	—	—
Path loss, Venus Deep Space Station to Tiefert Mountain	— 137.226	$\pm 0.013$	Inverse square (estimated)
Path absorption, Venus Deep Space Station to Tiefert Mountain	— 0.165	$\pm 0.020$	Theoretical <sup>c</sup>
Expected received power for isotropic aperture	— 88.204 (Ref.) <sup>a</sup>	—	—
Received power level at maser reference flange	— 24.587 (Ref.) <sup>a</sup>	$\pm 0.010$	By dc substitution
Observed gain G/isotropic	+ 63.617	$\pm 0.154$	At maser reference flange
Near-field correction	0.095	$\pm 0.032$	—
Far-field gain $G_0$	+ 63.712	$\pm 0.158$	At maser reference flange
Gain for 100% $\eta$	+ 67.210	—	—
Efficiency at maser reference flange	(-3.498 $\pm$ 0.158 dB), 1 $\sigma$		(44.69 $\pm$ 1.63%), 1 $\sigma$

<sup>a</sup>Reference is 10 mW, nominal.  
<sup>b</sup>Includes mismatch error.  
<sup>c</sup>Based on 0.89 atmospheric pressure, 20°C, and 4-g/m<sup>3</sup> H<sub>2</sub>O vapor (Ref. 3).

**Table 7. Effective system surface tolerance computation**

Parameter	Efficiency	1- $\sigma$ tolerance, dB	Comment
Aperture integration	0.7388	$\pm 0.002$	Estimated
Quadripod blocking	0.8755	$\pm 0.008$	80 to 120% opacity times physical area
Measured	0.4626	$\pm 0.0163$	At antenna reference flange
Balance	0.7152	$\pm 0.0141$	
Effective system surface tolerance (at 0.8-deg elevation) = 0.065 $\pm$ 0.002-in. rms (Fig. 22).			

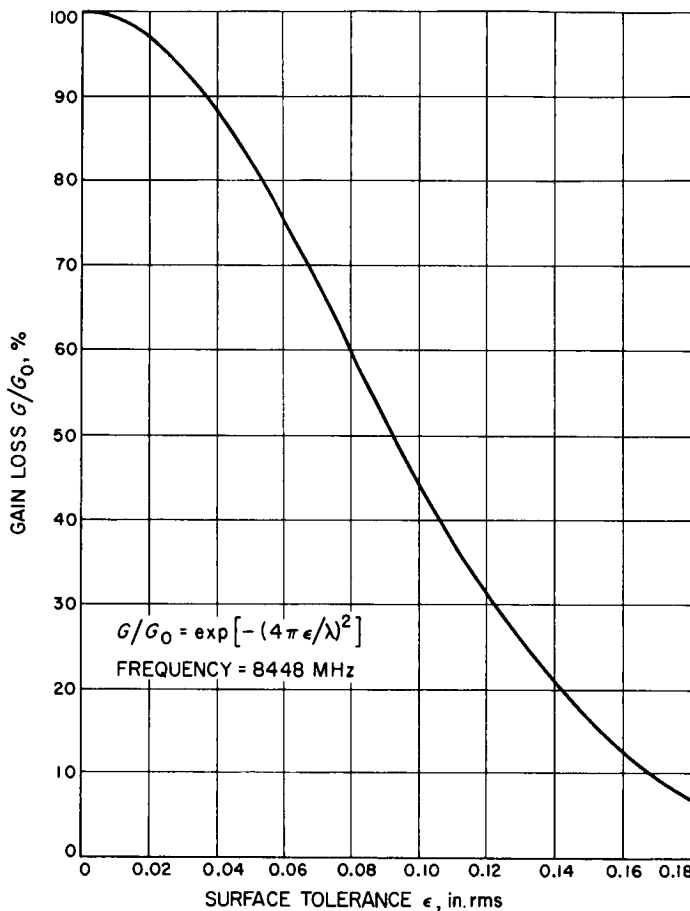


**Fig. 22. Gain loss as a function of surface tolerance**

**c. Conclusion.** The 85-ft-diameter az-el aperture efficiency at X-band has been evaluated by independent methods; the results are in good agreement. Based on a selected value of flux density for Cygnus A, a high elevation angle result has been obtained; and based on an independent ground-based method, the gain has been obtained near a 1-deg elevation angle. Table 8 gives the final results. Although the results are consistent with expectations of a better system surface tolerance at high elevation angles (the surface was originally set optimally

**Table 8. Independent methods of efficiency determination**

Method	Efficiency at maser reference flange	Comment
Radioastronomical	$(46.2 \pm 11.2\%)$ , 3 $\sigma$	Applicable for 40–70-deg elevation
Ground-based	$(44.7 \pm 4.9\%)$ , 3 $\sigma$	Applicable for 0.8-deg elevation

at a 45-deg elevation angle), it is felt further analysis would be subjective.

## References

1. *Microwave Antenna Theory and Design*, MIT Radiation Laboratory Series, Vol. 12. Edited by S. Silver. McGraw-Hill Book Co., Inc., New York, 1949.
2. Ludwig, A., *Computer Programs for Antenna Feed System Design and Analysis*, Technical Report 32-979. Jet Propulsion Laboratory, Pasadena, Calif., Apr. 15, 1967.
3. Bean, B. R., and Dutton, E. J., *Radio Meteorology*. U.S. Department of Commerce, National Bureau of Standards, Mar. 1, 1966.

## 7. Low- and Medium-Rate Telemetry, M. H. Brockman

**a. Introduction.** Analysis of the subcarrier demodulator was presented in SPS 37-49, Vol. II, pp. 100–113. This article provides information on subcarrier phase noise and its resultant degradation of  $ST_B/N_0$  for low- and medium-rate *Mariner Mars 1969* telemetry.

**b. Subcarrier demodulator.** The low- and medium-rate telemetry for *Mariner Mars 1969* will be uncoded and will use data rates of 8½, 33½, 66½, and 270 bits/s. Operation of the subcarrier demodulator on its narrow bandwidth ( $BW_{scl_0} = 0.03$  Hz) will accommodate these data rates. The resultant subcarrier phase noise  $\sigma_{\phi n}$  is shown in Fig. 23 as a function of  $ST_B/N_0$  for 8½, 33½, 66½, and 270 bits/s with  $\tau_D/T_B = \frac{1}{3}$  and a 50% probability that the data bit stream switches on successive bit periods (SPS 37-49, Vol. II). The symbols used here are defined as follows:  $S$  = signal power,  $T_B$  = time per information bit,  $N_0$  = one-sided noise spectral density, and  $\tau_D$  = time constant of data waveform filter.

Degradation in  $ST_B/N_0$  due to rms phase noise error in the subcarrier tracking loop is (from SPS 37-48, Vol. II, pp. 125–129):

$$\frac{\text{Demodulated } \frac{ST_B}{N_0}}{\text{Input } \frac{ST_B}{N_0}} = \left[ 1 - \left( \frac{2}{\pi} \right)^{\frac{1}{2}} \sigma_{\phi n} \right]^2 \quad (1)$$

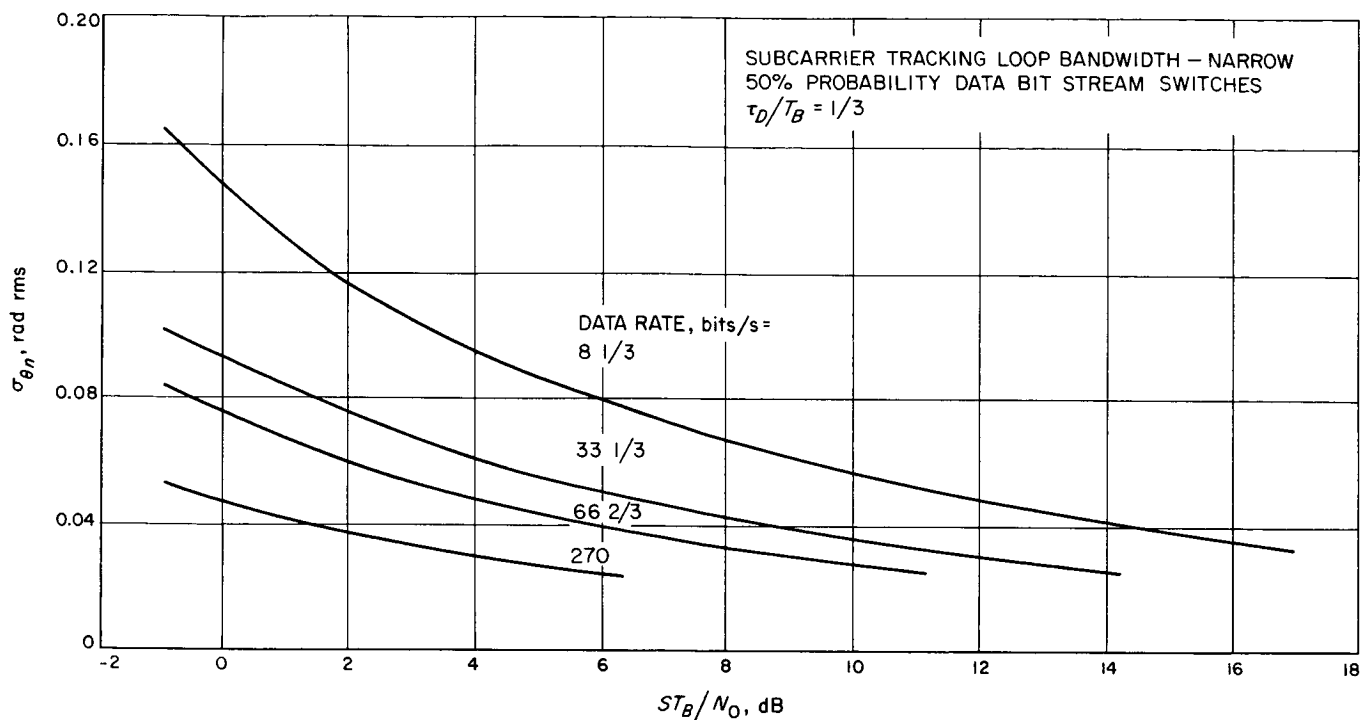


Fig. 23. Subcarrier demodulator rms phase noise error vs ratio of signal energy per bit to noise spectral density

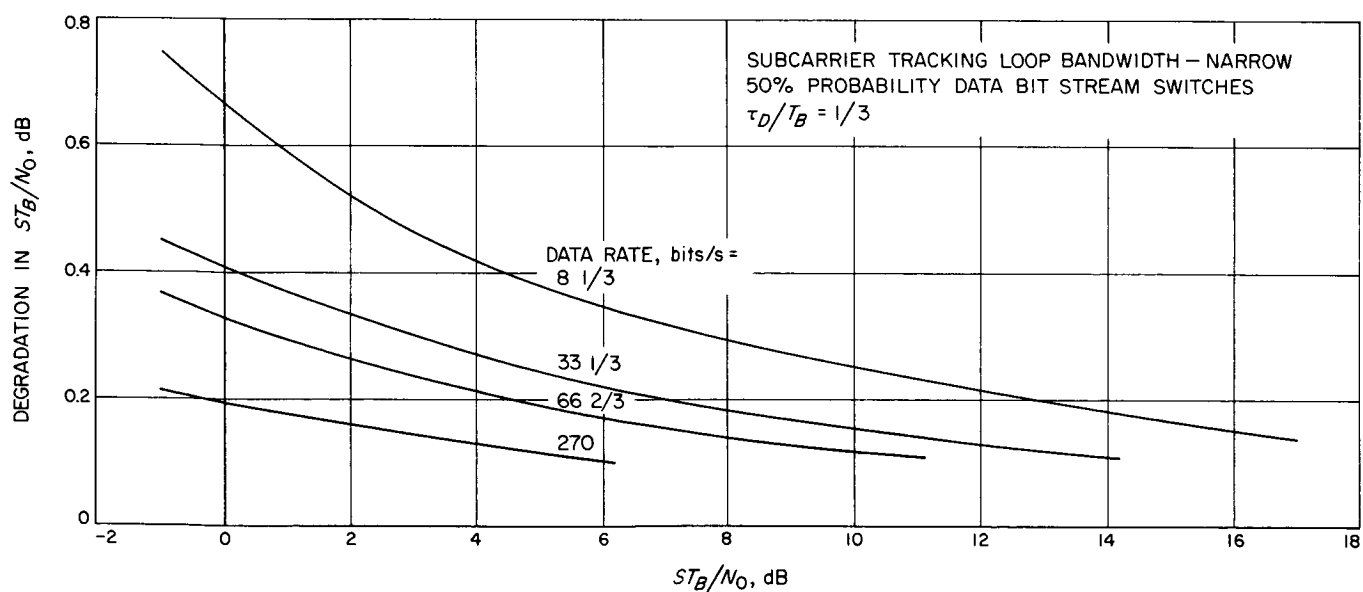


Fig. 24. Degradation in  $ST_B/N_0$  due to phase noise error vs ratio of signal energy per bit to noise spectral density

The resultant degradation in  $ST_B/N_0$  due to subcarrier phase noise is shown in Fig. 24 as a function of  $ST_B/N_0$  for data rates of 8½, 33½, 66½, and 270 bits/s.

## B. Communications System Research

### 1. Mariner Venus 67 Ranging System Digital Processing

Design, W. A. Lushbaugh and L. D. Rice

**a. Introduction.** This article describes the design of the digital processing portion of the *Mariner Venus 67* ranging system. For a discussion of the entire ranging system, see SPS 37-42, Vol. III, pp. 52-56. A general functional description of the system is given in the following Paragraph b.

The use of a digital computer for correlation and decision functions greatly enhances the flexibility of the ranging system. However, it also introduces a number of problems due principally to the discrete nature of the information involved in the range measurement, and to the different time scales upon which the computer and the various subsystems operate. This article discusses several specific problems, and their various solutions, encountered in the design of the digital hardware/computer software interface. For a detailed description of the digital and software portions of the system, see the following two articles, subsections B-2 and B-3, respectively.

**b. Ranging system functional description.** Figure 25 shows that the system consists of a number of RF, digital, and computer software subsystems that interact to perform the functions of range and range-rate calculations. Received signal, reference tones, and an RF doppler signal pass from the DSIF receiver to the analog portion of the system where the product of the received signal with the ranging system receiver coders is generated and filtered. The signals then pass through the digital interface equipment to the SDS 920 computer, which computes the correlation and acts to systematically align each of the six code components with the code contained in the received signal. While the correlations are being performed, the RF doppler signal is counted and used to correct the receiver coders for rate variation in the incoming signal. Once the receiver coders are aligned with the code in the received signal, the rate variations in the incoming signal are tracked by means of the code correlation itself. The range and range-rate are thenceforth available for output.

**c. Programming problem areas.** The ranging system, as seen by the computer program, is essentially a number of

distinct but related tasks that must be managed simultaneously. Because the digital computer is a sequential machine, the main problem is the establishment of correct timing relationships between system component operation and computer program execution.

The most critical problem, with respect to timing considerations, is that of maintaining phase-locked synchronization of the doppler-aided tracking loop with the clock doppler frequency, which is centered around  $100 \pm 70$  Hz. Thus, the loop must be phase-locked over this frequency range. This is accomplished by checking the phase relationship once each cycle and updating the cycle time of the number-controlled oscillator (NCO) to maintain the correct phase. The two routines that check the phase relationship (PHDINT) and control the NCO (NCOINT) are described in the article by D. L. Rice appearing in this volume. Controlling the timing of the NCOINT routine is accomplished by an interrupt signal generated each time the NCO counts down one cycle. The phase-detector counter is also started at this time. The counter is stopped on the next cycle of the clock doppler frequency, which also generates an interrupt to execute the PHDINT routine. The phase-detector counter is then read and reset by PHDINT.

A difficulty arises from the possibility that if the loop frequency and the clock doppler frequency are not identical, two successive cycles of one frequency can occur before the next cycle of the other frequency. In one case, the counter will be read before it has been started by the NCO, and in the other case, the counter will be restarted before it has been read and reset. Either case results in an erroneous count.

This problem is solved by disarming the PHDINT phase-detector routine inside itself so that once it has been executed, the interrupt will not respond until it has been rearmed. This rearming is done in the NCO routine so that the PHDINT routine will be active only once after each execution of NCOINT. Making the NCOINT a higher priority than the PHDINT assures that any phase shift input to the NCO will be entered into the loop only once.

Another timing problem is related to the use of the typewriter under interrupt control so that main program operation is delayed for the shortest possible time. A queue is established by setting a flag corresponding to each output message desired. These flags are checked once each second to determine whether any messages are waiting to be typed. An alternate method is to construct a list of waiting messages and type from this list if it is

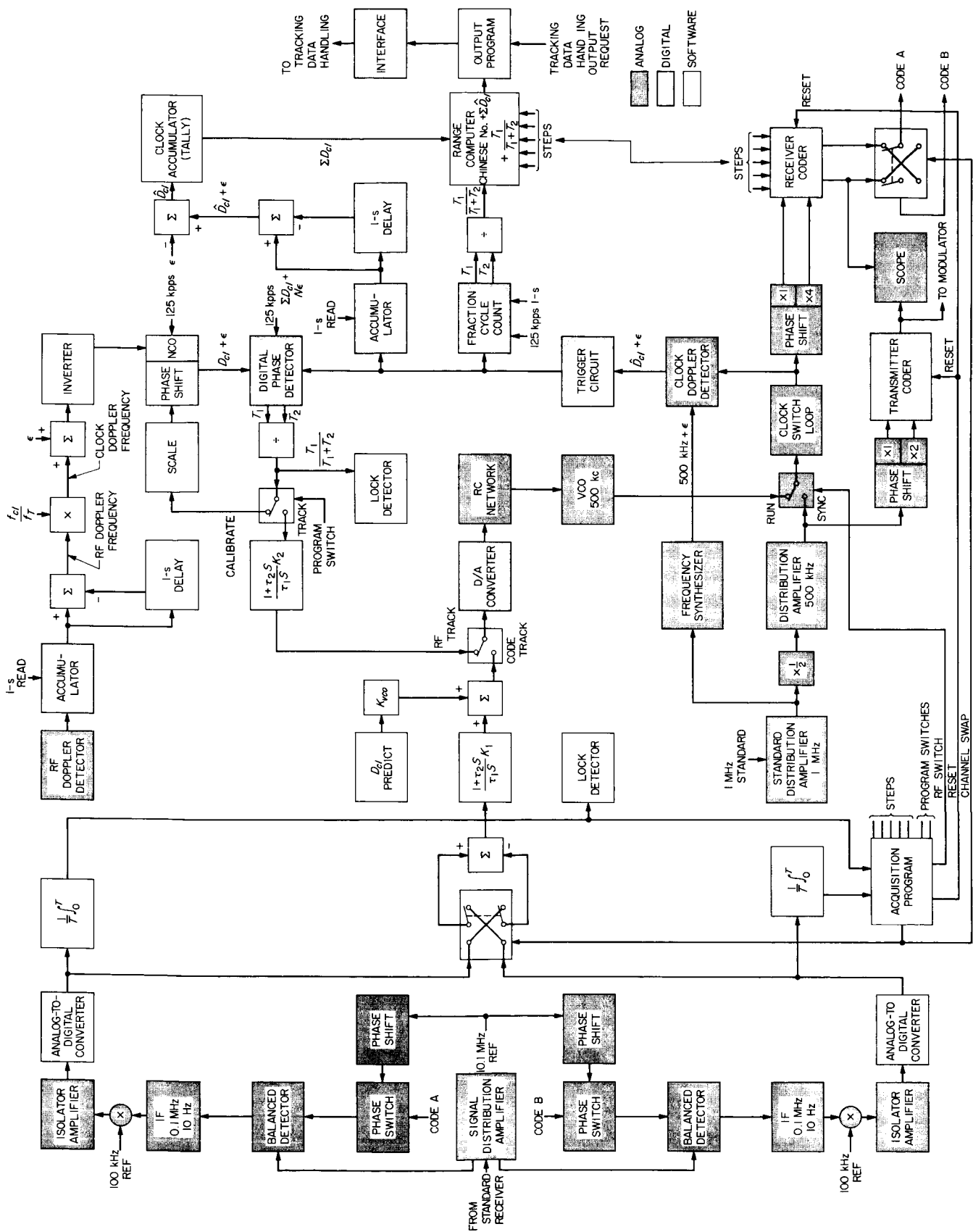


Fig. 25. Mariner Venus 67 ranging equipment

non-empty. This system requires either a much more elaborate memory allocation scheme than is used, or an absolute limit to the number of messages waiting for type-out. In the latter case, if the list is full, a message may be ignored entirely. In the system as used, a message request may be ignored if the corresponding flag is already set, but each message requested will eventually be typed at least once. When a message is set up for typing, its flag is reset and it may then be requested again.

**d. Hardware synchronizing problem.** The SDS 920 is a synchronous machine with a basic timing cycle of  $8 \mu\text{s}$ . The special-purpose digital equipment added to it for the *Mariner Venus 67* ranging experiment was tied to a 1-MHz standard clock or the 500-kHz plus clock doppler frequency. The synchronizing problem was two-fold since both the computer and digital rack command each other at various times in the ranging operation. A special synchronizing circuit was developed for each of these timing problems (refer to the article by W. A. Lushbaugh appearing in this volume).

**e. Hardware/software optimization.** In a few instances, the close cooperation of the logic designer and programmer led to a system simplification. For example, each of the various binary counters in the digital rack had to be frozen at the 1-s time tick and read into the computer. It was thought originally that two counters would be needed in each case with each used on alternate seconds. By proper arrangement of interrupt priorities, however, it was arranged to have only a small auxiliary counter to count events while the computer was reading the main counters (see the article by W. A. Lushbaugh appearing in this volume).

Another interesting hardware/software trade-off was made in the design of the NCO. During the design of this oscillator, it became obvious that a saving of hardware would result if an extra clock period was used to develop the transfer of the desired number from its hold register to the binary counter. Doing this and re-interpreting the definition of binary *one* in the hold register meant that the programmer could use *two's* complement for the desired period. Since programming the desired period in *two's* complement form was easily introduced, this format was adopted.

## 2. Mariner Venus 67 Ranging System Digital Rack,

W. A. Lushbaugh

**a. Introduction.** The *Mariner Venus 67* ranging system (see Ref. 1 and SPS 37-42, Vol. IV, pp. 198-200) uses a

rack of special-purpose digital equipment to relieve the computer of some necessary bookkeeping functions. This equipment is in addition to an SDS 920 computer, an RF rack, and digital-to-analog and analog-to-digital converters (see SPS 37-48, Vol. II, pp. 63-67). The digital rack was constructed with standard modules and comprises approximately eight rows of 25 modules each. The digital rack is actually a set of subsystems that fit into various parts of the tracking loop.

The main blocks are as follows:

- (1) Computer output interface
- (2) Transmitter and receiver code generators
- (3) Receiver coder output control
- (4) One-second interrupt time routine
- (5) Clock doppler counter
- (6) Fractional cycle counter
- (7) Number-controlled oscillator (NCO)
- (8) Digital phase detector
- (9) Ultra-high frequency (UHF) doppler counter

This article discusses each of these digital blocks.

**b. Computer output interface.** Since the basic purpose of the digital rack is to extend the capabilities of the SDS 920 computer, there is a great deal of communication between the two devices. Communication between the two systems is via the standard parallel input (PIN) connector, the parallel output (POT) connector, as well as various interrupts, and the  $\bar{S}_{sc}$  line (SKS instruction test line). The computer commands the digital rack by going through an EOM instruction followed by either a PIN or POT instruction while the digital rack commands the computer via the interrupt lines.

A block diagram of the computer interface is shown in Fig. 26. The various  $C_i$  and SYS signals shown are the C-register signals from the computer POT connector buffered through a power amplifier. EOMs of the form 0023XX37 were assigned to the ranging system (see SPS 37-39, Vol. III, pp. 54-65 for details of EOM structure). Octal digits 5 and 6 of this instruction are the function digits, and EOMs will be described by these octal digits in the remainder of this article. Actually, only five of the six function bits were decoded with  $C_{12}$  being left out. The decoding was done in the standard two-level fashion with  $C_{15}$ ,  $C_{16}$ ,  $C_{17}$  being completely decoded with 8 three-input power amplifiers and  $C_{14}$  and  $C_{13}$  with four

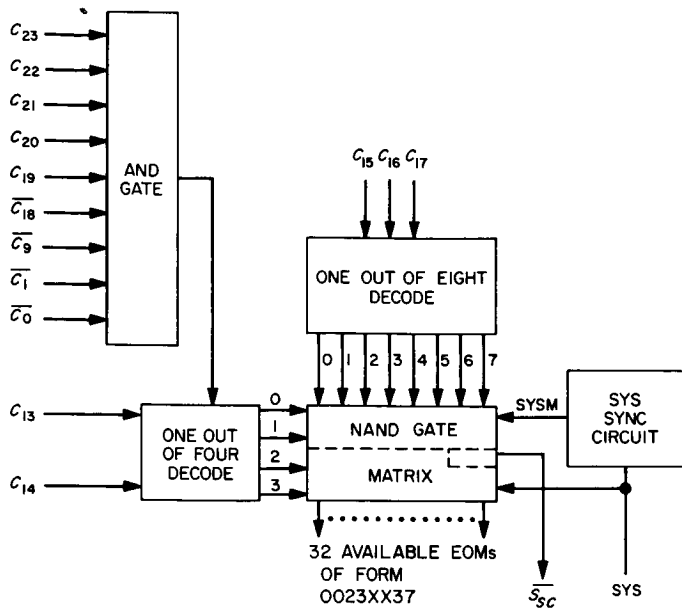


Fig. 26. Computer output interface

power amplifiers. The third input term of the  $C_{13}$   $C_{14}$  gates was supplied with the AND function of the constant terms of the ranging system EOMs, i.e.,  $C_{23}$ ,  $C_{22}$ ,  $C_{21}$ ,  $C_{20}$ ,  $C_{19}$ ,  $\overline{C_{18}}$ ,  $\overline{C_9}$ ,  $\overline{C_1}$  and  $\overline{C_0}$ . The NAND gate matrix consists of thirty-two gates with one of each of the  $C_{15}$  to  $C_{17}$  and  $C_{13}$   $C_{14}$  terms on two of its inputs. The third leg needs the SYS signal from the computer to separate an EOM from an SKS instruction. The lower half of the matrix is supplied with SYS directly from the computer while the upper half is supplied with a SYS derived signal called SYSM. SYSM is a pulse that appears during the 4- $\mu$ s SYS period but reduced to the width of, and synchronous with, the receiver clock.

Two gates of the NAND gate matrix have no SYS signal supplied and are used for SKS instructions. These are

gates 26 and 27 (octal) used to interrogate the *RF doppler loop in lock relay* and the *run-sync switch in run*, respectively. The outputs of these two gates are collector ORed and supplied to the  $\overline{S}_{sc}$  line.

**c. Transmitter and receiver code generators.** The transmitter code generator is clocked by a 1.000200-MHz sine wave standard from the synthesizer. The sine wave is converted to a digital clock in the shaper (see SPS 37-48, Vol. II, pp. 63-67) before clocking the coder register. The ranging sequence has five pseudo-noise components (of lengths 7, 11, 15, 19 and 23) and a clock component. Table 9 lists the feedback functions that generate each component. Note that the feedback functions for the lengths 19 and 23 components are developed in complementary form. For more detail concerning these component sequences see Ref. 2.

These five components are combined in the code function box the output of which is added modulo 2 to the clock component and delivered to the precision 50-ohm line driver (see SPS 37-48, Vol. II, pp. 63-67).

The coder function has been chosen to optimize the correlation jumps. Table 10 shows the truth table of this function of the five variables. Notice that the lengths 7 and 15 components have been developed in their complementary form. A majority function column has been added to show that there are only four discrepancies between the two truth tables. This function minimizes to

$$f = \overline{X}_{22} \overline{X}_{42} X_{62} + \overline{X}_{22} \overline{X}_{42} X_{52} + \overline{X}_{22} X_{32} X_{52} \\ + X_{32} \overline{X}_{42} X_{62} + X_{32} X_{52} X_{62} + \overline{X}_{42} X_{52} X_{62}$$

which, when factored for minimum gate count and put in the form needed for implementation by standard modules,

Table 9. Shift register feedback functions for ranging code components

Component length	Shift register length	Feedback function	Sequence
2	1	$X_{12} = \overline{X}_{11}$	01
7	3	$X_{24} = X_{22} \oplus X_{21}$	01011 10
11	5	$X_{36} = \overline{X}_{32} \overline{X}_{35} + \overline{X}_{31} \overline{X}_{41} + X_{31} X_{32} \overline{X}_{33}$	11011 10001 0
15	4	$X_{45} = X_{42} \oplus X_{41}$	10001 00110 10111
19	5	$\overline{X}_{56} = X_{51} \overline{X}_{52} X_{53} + \overline{X}_{61} X_{52} \overline{X}_{53} \\ + X_{51} X_{53} \overline{X}_{54} + \overline{X}_{51} \overline{X}_{53} X_{54} \\ + X_{52} X_{54} X_{55}$	11001 11101 01000 0110
23	7	$\overline{X}_{68} = \overline{X}_{62} X_{63} X_{65} + \overline{X}_{63} X_{64} \overline{X}_{65} \\ + X_{62} X_{64} X_{67} + \overline{X}_{61} X_{63} X_{67} \\ + X_{61} X_{62} \overline{X}_{68}$	11111 01011 00110 01010 000

Table 10. Ranging function truth table

Length 7	Length 11	Length 15	Length 19	Length 23	Ranging function	Majority function
$\bar{X}_{22}$	$X_{32}$	$\bar{X}_{42}$	$X_{52}$	$X_{62}$		
0	0	0	0	0	0	0
0	0	0	0	1	0	0
0	0	0	1	0	0	0
0	0	0	1	1	0	0
0	0	1	0	0	0	0
0	0	1	0	1	0	0
0	0	1	1	0	0	0
0	0	1	1	1	1	1
0	1	0	0	0	0	0
0	1	0	0	1	0	0
0	1	0	1	0	0	0
0	1	0	1	1	1	1
0	1	1	0	0	0	0
0	1	1	0	1	1	1
0	1	1	1	0	0	1
0	1	1	1	1	1	1
1	0	0	0	0	0	0
1	0	0	0	1	0	0
1	0	0	1	0	0	0
1	0	0	1	1	0	1
1	0	1	0	0	0	0
1	0	1	0	1	1	1
1	0	1	1	0	1	1
1	0	1	1	1	1	1
1	1	0	0	0	0	0
1	1	0	0	1	0	1
1	1	0	1	0	1	1
1	1	0	1	1	1	1
1	1	1	0	0	0	1
1	1	1	0	1	1	1
1	1	1	1	0	1	1
1	1	1	1	1	1	1

becomes

$$f = \bar{X}_{42} X_{62} (\bar{X}_{22} \bar{X}_{32} \bar{X}_{52}) + \bar{X}_{22} X_{32} X_{52} + \bar{X}_{22} X_{42} X_{52} + X_{32} X_{52} X_{62}$$

Other factorizations are possible but do not further reduce the gate count.

The output of the coder function is a sequence of length 1,009,470 with a period of slightly over 1 s at the transmitter clock rate. Sequences of such length are extremely difficult to verify and a malfunction of one of the gates in this function could quite easily go undetected until a critical time in a ranging operation. It is for this reason that special care was given to the factoring of the ranging function and the addition of a code function test circuit.

The test circuit consists of five switches and an AND gate capable of selecting any of the possible thirty-two combinations that the five components can assume and delivering a true level when the selected combination appears. This signal then interrogates the coder function output modulo-2 added to the selected phase of the clock component and records the answer in a flip-flop. With everything working properly, this flip-flop should remain in one state for a given switch setting and can be checked via the observation light.

A more sophisticated version of this test circuit was designed but not installed, due to space limitation, in the digital rack. This scheme replaces the switches with a digital switch and a binary counter which runs through the thirty-two states in sequence, advancing states with the 1-s time tick. The observed function bit is then transferred to the computer which compares it to a list and



signals the operator via the typewriter if a malfunction occurs. In such a scheme, each component sequence could also be monitored by the computer at the cost of one more hold register.

A series of word detectors for each component is supplied which, when ANDed together, give a sync position on the complete ranging code. This output is supplied in the receiver coder only for test purposes, but is used for coder synchronization in the transmitter.

Upon receipt of EOM 10, a flip-flop in the coder-sync control is set which allows the *next* transmitter coder word detector pulse to reset the receiver coder to the then known state of the transmitter coder. Even though this may take up to one full cycle of the sequence, it is still the most desirable method since the transmitting sequence is never interrupted and thus avoids long round-trip time delays to distant spacecraft being ranged.

It is important for the two coders to be running on the same clock when they are synchronized. For this reason, a run-sync control is provided. In the *run* position, both coders are allowed to run on their respective clocks. When synchronization is desired, however, EOM 14 sends a relay closure to the RF portion of the system which then slaves the two clocks together. EOM 13 returns the system to its normal state.

*d. Receiver coder output control.* This portion of the receiver coder differs from that of the transmitter since, during an acquisition, each of the six components of the full code must be correlated to the incoming sequence. Since there are seven different selections to be made, it was decided to have seven individual flip-flops, of which only one may be true at any time. Each of the seven *select* flip-flops has its set and reset inputs connected to a bit of the computer C-register and all clocks are commoned to the POT 2 signal from the computer after receipt of EOM 00. The method for selecting a desired

component, then, is for the program to deliver the correct EOM followed by a POT of the correct combination of C-register bits to do the desired selection. Table 11 gives the numbers to be outputted for each of the possible selections.

The ranging algorithm involves computing the correlation of each component for all its possible phases and then choosing the phase with the highest correlation as being correct. This function is performed by providing EOM 7 as a shift command. Upon receipt of this EOM, the component selected at that time has one clock pulse deleted, thereby dropping the phase of that component by one with respect to the received sequence. After all phases of a component have been correlated, the computer must deliver EOM 7 for *n* machine cycles, where *n* is the difference of the resulting and correct phase of the selected component.

Two phases of the selected component are supplied, one to each of the two correlator channels. These two phases, called the early and late codes, differ by one clock pulse. The two correlator channels have been designated channel 0 and channel 1. Due to the physical impossibility of constructing two identical gain correlator channels, the early and late codes are periodically switched between them to average out their differences. Two EOMs have been supplied for this purpose: EOM 11 selecting the early code for channel 0, and EOM 12 selecting the late code.

The signals delivered to the two channels of the correlator during component acquisition are  $F = C_i \oplus CL$  and  $F' = (C_i \oplus CL)^{-1} = C_i^{-1} \oplus CL$  where  $C_i$  and  $C_i^{-1}$  are the selected component and the selected component delayed by one, respectively, and CL is the clock component. However, these equations must be changed when the clock component itself, or the composite code, is the selected component. When the clock component is selected, the signals delivered to the two channels are

Table 11. Receiver coder component select table

Selected component	C-register bits														C-register in octal							
	C <sub>10</sub>	C <sub>11</sub>	C <sub>12</sub>	C <sub>13</sub>	C <sub>14</sub>	C <sub>15</sub>	C <sub>16</sub>	C <sub>17</sub>	C <sub>18</sub>	C <sub>19</sub>	C <sub>20</sub>	C <sub>21</sub>	C <sub>22</sub>	C <sub>23</sub>								
Clock	0	1	1	0	1	0	1	0	1	0	1	0	1	0	7	7	5	5	2	5	2	
Length 7	1	0	0	1	1	0	1	0	1	0	1	0	1	0	7	7	6	3	2	5	2	
Length 11	1	0	1	0	0	1	1	0	1	0	1	0	1	0	7	7	6	4	6	5	2	
Length 15	1	0	1	0	1	0	0	1	1	0	1	0	1	0	7	7	6	5	1	5	2	
Length 19	1	0	1	0	1	0	1	0	0	1	1	0	1	0	7	7	6	5	2	3	2	
Length 23	1	0	1	0	1	0	1	0	1	0	0	1	1	0	7	7	6	5	2	4	6	
Composite code	1	0	1	0	1	0	1	0	1	0	1	0	0	1	7	7	6	5	2	5	1	

$F = CL$  and  $F' = (CL)^{-1} = \overline{CL}$ . When the composite is selected, the two channels receive  $F = C \oplus CL$  and  $F' = (C \oplus CL)^{-1} = C^{-1} \oplus \overline{CL}$ .

It can be seen from these last two sets of equations that, in these cases, the equation for the late flip-flop is simply its complement for the other cases (i.e., the true output of the early flip-flop). Thus, the function of the late code control box is to make the late flip-flop copy the early flip-flop, or its complement, as a function of the selected component.

**e. One-second interrupt time routine.** The remainder of the digital rack consists of special purpose counters to record events in parallel and relieve the computer from performing this duty via the interrupt lines. These counters either count or are synchronized to a third clock in the digital rack: the 500-kHz reference derived from the 1-MHz standard. This clock is delivered as a sine wave and immediately shaped to a square wave in a shaper. This digital clock is then divided by 2 to supply the basic 500-kHz signal used to control the counters and to allow any of the four quadrature phases of 500 kHz to be developed. The falling edge of the 1 MHz starts phases 1 and 3, while the falling edge of the 500 kHz defines the beginning of phase 1. The 1-s time tick from the frequency and timing subsystem (FTS) is the main source of time reference for the computer and also defines phase 1 of the four phases of the 500 kHz by the direct-set line of the 500-kHz flip-flop. The 1-s time tick is shaped and level-shifted in the shaper (see SPS 37-48, Vol. II, pp. 63-67) and also synchronized with the computer clock to serve as a correctly shaped interrupt for the computer. The 1-s time tick also freezes the counters in the digital rack, and the interrupt derived from it signals the computer to read these counters via the PIN connector.

This 1-s subroutine of the computer takes several hundred microseconds, and, if the clock doppler and UHF doppler counters are to be frozen during this time, some means must be found for counting these events during this special period. It was decided to supply both of these counters with a small auxiliary counter that accepts counts only during the 1-s time routine. This involved developing a control flip-flop, called the SEC flip-flop, that is set by the 1-s time tick at phase 1. This flip-flop remains set, then, until the computer delivers the last EOM-PIN sequence of its subroutine. This last EOM is EOM 31, *read the clock doppler counter*, and the PIN signal that follows initiates the final SEC period sequence. This sequence of pulses consists of a *phase 3 reset main*

*counter pulse* and a *phase 4 transfer auxiliary counters* signal, followed by the resetting of the SEC flip-flop coincident with phase 1.

**f. Clock doppler counter.** The clock doppler counter receives the clock doppler as a sine wave and shapes it in the shaper (see SPS 37-48, Vol. II, pp. 63-67). The rising edge of this output is then synchronized with phase 1 to develop a 0.5- $\mu$ s clock doppler signal to be sent to various counters in the digital rack. An interrupt that is synchronous with the computer clock is also developed and sent to the computer.

The phase 1 clock doppler pulse enters the 9-bit clock doppler counter via the control unit which steers it either to the main or auxiliary counter, depending upon the condition of the SEC signal. During the 1-s routine, the clock doppler counter is disabled and awaits EOM 31, which causes its output to be parallel-read into the computer via one set of PIN gates.

**g. Fractional cycle counter.** The fractional cycle counter reads the time interval between the receipt of the last clock doppler pulse and the 1-s time tick to the nearest 2  $\mu$ s. This is mechanized by having each clock doppler pulse reset the 15-bit fractional cycle counter (except during the 1-s routine when its value is held to be read by EOM 34).

**h. Number-controlled oscillator.** The NCO is a 15-bit counter with a hold register of the same length. This counter counts the 500 kHz until it reaches the *all one* state, at which time it requests reloading from the hold register. This request, called the NCO output, occurs at phase 3. The NCO hold register itself is capable of being loaded from the computer. Upon receipt of EOM 20, the hold register awaits the POT signal from the computer. The load command for the hold register must be synchronized with the 500-kHz clock to avoid trying to load both registers simultaneously. Thus, the POT 2 signal from the computer enters the POT synchronizer and develops two output signals at phases 1 and 2.

The first of these signals resets the hold register so that only single terms need be supplied to the hold register. If this were not done, one inverter per hold register bit would be needed as a reset signal for these flip-flops. The second of these signals is the clock that strobes-in the new number. Since the NCO has an output only at phase 3, interference between the loading of the hold register and loading the main counter is impossible.

An interesting minimization used in the transfer network from the hold register to the counter resulted in a requirement to program the NCO in *two's* complement form. Since the hold register is loaded into a register wired as a binary counter, the loading is done by means of the *direct set* and *direct reset* lines. However, if the binary counter is in the *all zero* position, new information can be transferred into it only via the direct set line since no carry propagations can be generated in this state. This saves the gate needed to develop the otherwise needed complementary term for the direct reset line. Waiting for the up-counter to recycle to the all zero state, however, adds one unit of time to the count; this unit can be accounted for by programming the NCO with a *two's* complement number and interpreting the proper side of the hold register as being a binary *one*.

The POT control unit merely separates the two EOM signals and delivers the POT-derived signals to the proper register.

**i. Digital phase detector.** The digital phase detector is a counter used to give the time measurement of the phase difference between the NCO output and the clock doppler to the nearest  $2 \mu\text{s}$ . The counter is started with the receipt of a clock doppler pulse and stopped with the next NCO output. The NCO output and clock doppler pulses were chosen with different phases to avoid the simultaneous starting and stopping of this counter. Once stopped by the NCO, the digital phase detector remains off until it is read into the computer by EOM 33. After being read, the counter is reset and the control unit is allowed to await the next clock doppler pulse to repeat the cycle.

**j. Ultra-high frequency doppler counter.** Except for size, the UHF doppler counter is identical to the previously described clock doppler counter.

A sine wave UHF doppler signal is shaped and synchronized to phase 1. This UHF doppler signal is delivered to an 18-bit main counter or a 4-bit auxiliary counter, depending upon the status of the SEC signal. The counter is read by EOM 26, reset at the end of the SEC period by a phase 3 signal, and the auxiliary counter is then transferred to the main counter by a phase 4 signal.

The UHF doppler signal is supplied in two quadrature phases for the purpose of determining the sign of the doppler signal. The 90-deg doppler signal is shaped in

the shaper and fed to the input of a flip-flop clocked by the 0-deg doppler signal. Thus, it is determined whether the 90-deg signal is leading or lagging the 0-deg doppler, thereby determining the sign: if it leads the reference, the doppler sign is positive. This sign bit is calculated on each transition of the 0-deg doppler signal, and the constant answer is read into the computer when the magnitude is read each second. Tolerances, here, are very important. Since the maximum UHF doppler signal rate was designed to be on the order of 66 kHz, the quadrature UHF doppler signal at this rate would change within  $4 \mu\text{s}$  of the 0-deg doppler. Since it was necessary to have a phase 1 UHF doppler pulse in other parts of the system, it was decided to use this signal as a clock for the sign determination flip-flop. However, it may take as long as  $2 \mu\text{s}$  to develop this phase 1 signal after the 0-deg UHF doppler has made its transition; the  $4\text{-}\mu\text{s}$  safety factor between these two signals is reduced in worst-case to  $2 \mu\text{s}$ . This method does, however, guarantee the highest noise immunity possible in the circuit by avoiding clocking the sign flip-flop directly from the output of the shaper.

If it is felt that this 100% safety factor is not sufficient, the UHF doppler synchronizer can be duplicated with the 500-kHz input being replaced by 1 MHz, thus reducing the delay to a maximum of  $1 \mu\text{s}$ . Space limitations, however, precluded this alternative.

**k. Conclusions.** The complete digital rack described above has been operating since June 1967 as a part of the *Mariner Venus 67* ranging system at the Goldstone Mars Deep Space Station. To date, all equipment has operated satisfactorily with no failures attributable either to the modules or to the design.

The various minimizations mentioned in this article were extremely desirable because of (1) the added reliability that results from fewer circuits, and (2) the large savings of circuits that was needed to meet the space allotment of one SDS 920 computer rack.

As a summary, Table 12 lists all of the EOMs used in the system.

## References

1. Titsworth, R. C., *Optimal Ranging Codes*, Technical Report 32-411. Jet Propulsion Laboratory, Pasadena, Calif., Apr. 15, 1963.
2. Golomb, S. W., *Digital Communications with Space Applications*, p. 169. Prentice-Hall, Englewood Cliffs, N.J., 1964.

**Table 12. EOMs of form 0023XX37 used for digital rack**

EOM number, octal	Function	PIN/POT
00	Alert code select	POT
07	Shift selected component	—
10	Sync coders	—
11	Select early code for channel 0	—
12	Select late code for channel 0	—
13	Run/sync switch to run	—
14	Run/sync switch to sync	—
20	Alert NCO	POT
21	Alert 16 most significant bits, TDH hold register	POT
22	Alert 16 least significant bits, TDH hold register	POT
31	Alert clock doppler counter (last EOM of 1-s routine)	PIN
32	Alert UHF doppler	PIN
33	Alert digital phase detector	PIN
34	Alert fractional cycle counter	PIN
26 <sup>a</sup>	Test RF doppler in-lock relay	— <sup>a</sup>
27 <sup>a</sup>	Test run/sync switch	— <sup>a</sup>

<sup>a</sup>SKS rather than EOM type instructions.

### 3. Mariner Venus 67 Ranging System Program, L. D. Rice

**a. Introduction.** A research and development ranging system was designed and built to accomplish the celestial mechanics experiment associated with the *Mariner Venus 67* mission. The ranging system consists of a SDS 920 digital computer interfaced to a rack of digital logic modules and a rack of RF analog equipment. The computer control program for the ranging system consists of the main ranging program and the receiver alignment test program in addition to several short check-out routines to perform diagnostic checks on the various input and output interfaces to the computer. This article describes the structure of the main ranging program and the receiver alignment test program.

**b. Ranging program structure.** The ranging program is written in SDS 920/930 symbol language to allow the coding efficiency needed to meet the system's timing requirements. Several of the SDS programmed operator (POP) library routines are used with the restriction that no POPs are called within any of the interrupt routines. This is done to avoid POP re-entrance problems.

The program is segmented along functional lines so that, wherever possible, each segment contains the coding for a specific functional task. In most cases, this coding is in one actual subroutine and, in a few cases, the segment contains three or four individual subroutines associated

with the functional task of that segment. Figure 27 is a flow chart of the entire ranging program showing the function of each segment and the calling relationships between segments.

All temporary storage and data locations used by only one subroutine are contained within that segment. All temporary and data cells used by routines in more than one segment are located in the DATA AND TABLES segment.

Physically, the paper-tape version of the ranging program includes the binary main program, preceded by both the SDS universal binary loader and a patch, to zero the loading relocation bias, followed by a POP library consisting of those POP routines called by the ranging program.

**c. Description of ranging program segments.** A brief description is given here of the function of each segment and how that segment interrelates with the rest of the program under operating conditions.

*Begin Mariner Venus 67 ranging program (BEGIN).* The first segment controls execution of the rest of the ranging program according to breakpoint switch settings and the program mode switch setting. Breakpoint (BPT) switch settings for the ranging program are as follows:

BPT	Up (reset)	Down (set)
1	Execute PARAM if in ranging mode	Skip PARAM routine
2	Pause in SYNC to check coder 1 MHz	Skip 1-MHz check pause
3	Execute SCURVE routine	Skip SCURVE routine
4	Type out range in decimal format	Type out range in octal format

*Initialization routine (INIT).* The INIT segment, after arming the manual interrupts, enabling the interrupt system, and checking all error flags, calculates the program parameters depending on data input in the PARAM segment. In the *calibrate* mode, calibration values are substituted for the input data for signal level and noise temperature. The acquisition parity bit is flipped to INIT on each entry to assure a change of parity indicated for each reacquisition.

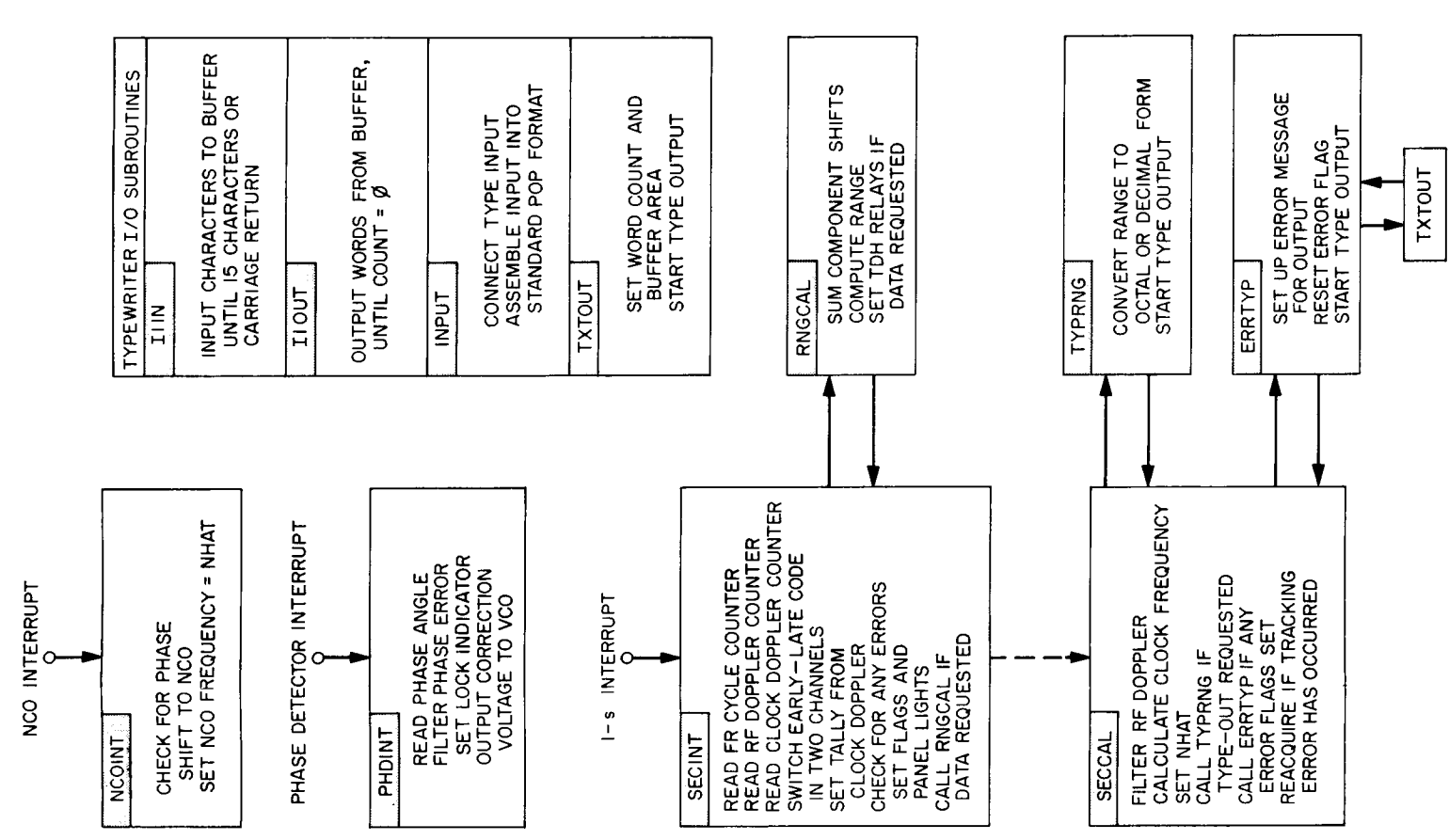
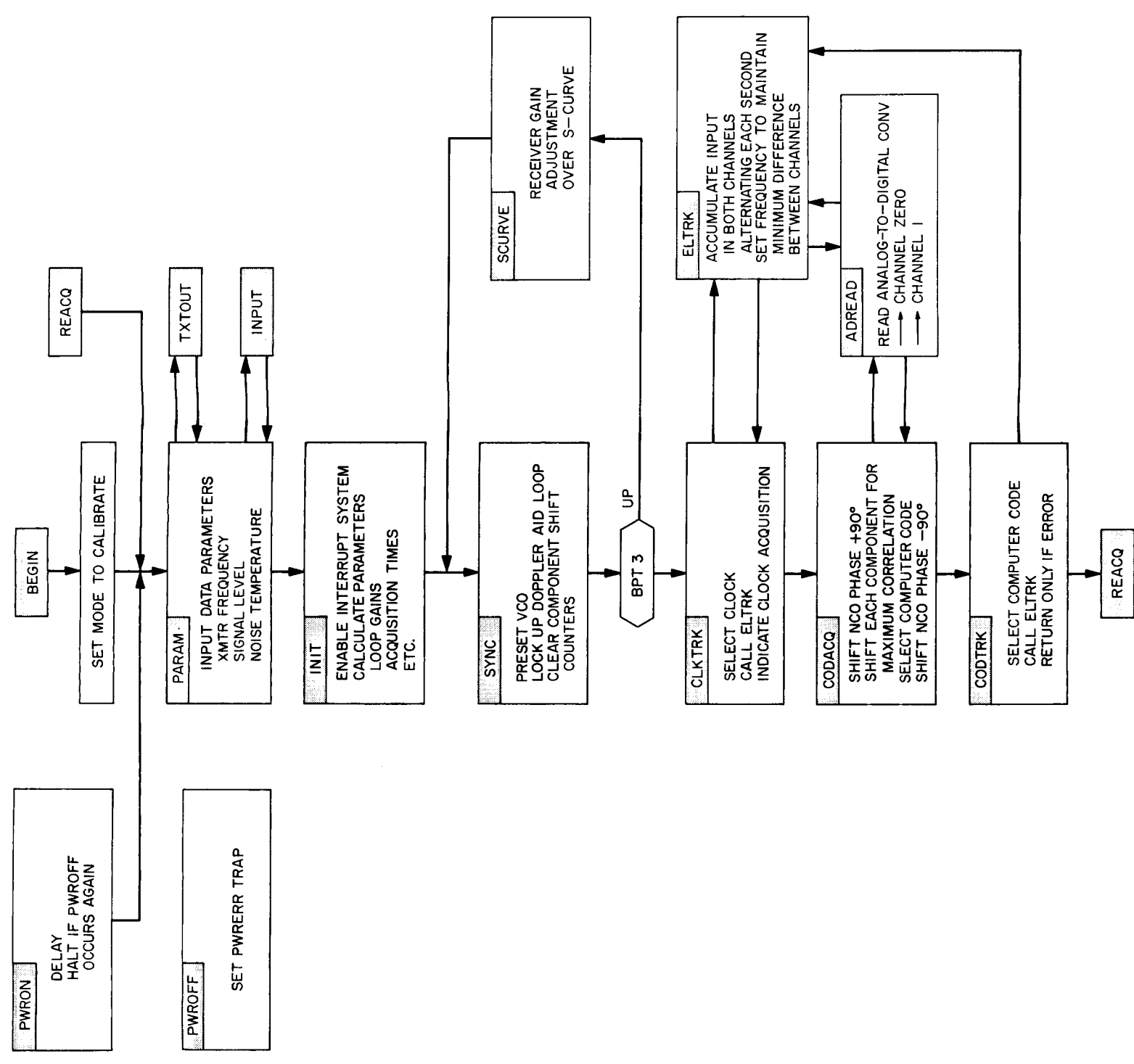


Fig. 27. Main ranging system program

*Code sync routine (SYNC).* This segment locks the doppler-aid phase-locked loop. First, the voltage-controlled oscillator (VCO) is pretuned as a third-order function of the clock doppler frequency. If BPT 2 is reset, a pause occurs until it is set to allow checking the synchronization of the 1-MHz coder inputs. After the operator sets BPT 2, a 2-s delay allows any transients to die out, the EOM command to sync the coders is given, and the number-controlled oscillator (NCO) interrupt is armed so that the doppler-aid loop can lock (see the descriptions under NCOINT and PHDINT). After lock is achieved, the DOPPLER-AID LOCK panel light is turned on.

*S-curve adjustment routine (SCURVE).* This segment, if called, shifts the NCO phase by  $1/500$  cycle per cycle so that receiver gain can be checked at the maximum and minimum points of the response curve knee (S-curve adjustment). The NCO continues to drift at  $1/500$  cycle per cycle until BPT 3 is set by the operator.

*Clock track routine (CLKTRK).* This segment selects the clock component from the receiver-coder output and then calls the ELTRK segment which tracks the clock component until the time computed in INIT has elapsed. ELTRK then returns to CLKTRK, which sets a flag to indicate that the clock has been acquired, and then turns on the CODE LOCK panel light.

*Code acquisition routine (CODACQ).* The CODACQ segment has the function of stepping through the components of the code and shifting each component until the maximum correlation is obtained. The amount of shift or delay required for each component is recorded and the composite code selected. Before beginning code acquisition, the doppler-aid loop phase is shifted by 90 deg, and when the composite code is acquired, it is shifted back 90 deg.

*Code tracking routine (CODTRK).* The CODTRK segment calls ELTRK to track the composite code. A LP1FLG flag is set equal to  $-1$  to indicate to ELTRK that the composite code is being tracked. In this case, ELTRK does not return control to CODTRK; rather, the correlation voltage is checked against a threshold value. If the correlation falls below the threshold level, and more than 60 s have elapsed since ELTRK was called, the TRKERR error flag is set and a new acquisition cycle is started.

*Early-late gate tracking routine (ELTRK).* This segment is called as a subroutine by CLKTRK and CODACQ to track either the clock component alone or the composite code, depending on the setting of the LP1FLG

flag. The correlation inputs from the two channels are summed in the early and late gate accumulators by alternating channels each second. The average difference between the accumulated values is filtered and used to set the doppler-aid loop frequency. When ELTRK is called by CLKTRK to track the clock component, it returns control to CLKTRK when the tracking time has elapsed. When called by CODTRK, an exit occurs only in the case of an abnormal condition causing the tracking loop to fall out of lock. In this case, a TRKERR flag is set and a new acquisition cycle is started.

*Number-controlled oscillator interrupt routine: location 0200 (NCOINT).* This routine is connected to the NCO interrupt which fires once per NCO cycle. On entry to this routine, all registers are saved and then restored, as is the overflow condition, prior to exit. This routine's function is to calculate the NCO frequency from the NHAT and PHASE variables, and output the cycle time to the NCO register. In order to prevent new data from being stored in the location of the PHASE variable before the present value has been used in the calculation of the NCO frequency, the phase detector interrupt is prevented from firing twice without an NCO interrupt having occurred (see PHDINT routine, below). This is accomplished by disarming the phase detector interrupt inside the PHDINT routine and arming this interrupt within NCOINT.

*Tracking data handling interrupt routine: location 0201 (TDHINT).* This segment sets the TDHFLG flag to  $-1$  when the tracking data handling (TDH) interrupt occurs. It must be assigned to a higher priority interrupt than the 1-s time tick so that the flag will be set before completion of the 1-s interrupt routine (the TDH interrupt occurs concurrently with the 1-s tick).

*One-second interrupt routine: location 0202 (SECINT).* The 1-s time tick freezes the three hardware registers: the fractional cycle counter, the RF doppler counter, and the clock doppler counter. The first action of the 1-s interrupt routine is to read the contents of these three registers. On reading the last one (clock doppler), the registers are released to resume normal operation. If either the fractional cycle counter or the clock doppler counter contain the value 0, an error is indicated by setting the corresponding FCYERR or CLDERR flags. A 0 read for the fractional cycle count is ignored and the previous fractional cycle count is used in the computation.

The SECINT routine also selects alternate channels each second for the early and late gate code input. If

TFLAG is  $-1$ , it is set to 0 and the late code is input to channel 0 while the early code is input to channel 1. If TFLAG is 0, it is set to  $-1$  and the early and late gates are exchanged in the two channels.

Also in SECINT, the clock doppler cycle accumulator, TALLY, is updated. TALLY contains the number of cycles the clock frequency has slipped and is used to determine the range figure in RNGCAL.

Finally, before returning control to the main program, several error conditions are checked and the corresponding lights on the ranging system front panel are turned either *off* or *on* as the error condition indicates. If none of the errors that would result in erroneous range data are set, the DATA CONDITION panel light is turned *on* and the data condition flag is set to indicate good data.

If the TDH request flag is negative (see TDHINT), the subprogram RNGCAL is executed. Two flags are set (SECFLG to  $-1$  and NHFLAG to 0) indicating completion of the SECINT routine (see SECCAL). The elapsed time counter cell is incremented and all registers and the overflow condition are restored. Control is then returned to the main program.

*One-second computation routine (SECCAL).* The SECCAL segment is functionally a part of the 1-s interrupt routine. It is separate from the interrupt routine so that POP calls can be used without the problem of re-entrance. As much of the arithmetic computation needed on the 1-s tick as possible is located in SECCAL so the POP calls can be used efficiently. Separating the SECCAL routine from SECINT requires SECINT to set a flag on completion. This flag must be regularly checked in the main program in order to determine when to execute SECCAL. Actually, two flags are set (see SECINT), one to  $-1$  and one to 0, for maximum convenience in the main program. The flag checks are located in the acquisition and tracking routines so that a flag is checked approximately every 10 to 20 ms. When a flag indicates that SECINT is completed, a branch to SECCAL is executed. The normally negative NHFLAG flag is set to 0 in SECINT and reset to  $-1$  in SECCAL.

The RF doppler count read in SECINT is smoothed over several seconds and used to calculate the new NCO NHAT frequency.

If the TYPFLG flag is non-negative (set), the TYPRNG routine is executed (see TYPRNG). The error flag table is checked for non-negative (set) flags and the ERRTYP

routine is executed when the first non-negative flag is found (see ERRTYP). If either the tracking routine fails to track the code or an error has occurred in the clock doppler counter, SECCAL exits immediately to REACQ. Otherwise, it restores the saved registers and returns to the calling point in the main program.

*Phase-detector interrupt routine: location 0203 (PHDINT).* The phase-detector routine, together with NCOINT, keeps the doppler-aid loop locked at the desired frequency. The phase-detector interrupt is disarmed inside PHDINT to prevent two consecutive executions of PHDINT without NCOINT having been executed. After the phase-detector counter has been read, the input count is used to calculate the dynamic phase error, which then is filtered to obtain the phase correction angle. This angle is converted to the correction voltage for the VCO. The routine then restores all registers and returns control to the main program.

*Calibrate reacquire interrupt routine: location 0204 (CALINT).* This segment, connected to the REACQUIRE CALIBRATE manual interrupt button, sets the mode switch to 0 (*calibrate mode*) and exits to REACQ. The mode-change flag is also set if the mode switch is not already set to 0 (see BEGIN). All registers are saved and restored.

*Ranging reacquire interrupt routine: location 0205 (RNGINT).* This segment, connected to the REACQUIRE RANGING manual interrupt button, sets the mode switch to  $-1$  (*ranging mode*) and exits to REACQ. The mode-change flag is also set if the mode switch is not already set to  $-1$  (see BEGIN). All registers are saved and restored.

*Range type-out interrupt routine: location 0206 (TYPINT).* This segment is connected to the TYPE OUTPUT manual interrupt button. Its function is to set the TYPFLG flag to 0. All registers are saved and control is returned to the main program.

*Range computation routine (RNGCAL).* The RNGCAL segment uses the component delay table and the FRACO, FRACCY, and TALLY variables to compute the range data. If the TDH request flag is set, the range data is immediately output to the TDH relay bank. Because this segment is called inside the SECINT interrupt routine, it has the same restriction regarding the use of POPs. As a result, several double-precision operations are coded within the segment.

Initially, the component delays are multiplied by the "chinese" numbers from the FACTOR table. In one case, M5, the product could overflow if M5 is large enough. That case is detected and M5 is reduced by nine leaving the corresponding value in the accumulated sum. The products are then added together and reduced modulo 1009470. This result, added to the contents of TALLY and the difference FRACO - FRACCY, is multiplied by the ratio of transmitter frequency to clock frequency to give the range data.

If the mode switch is set to CALIBRATE, the data condition bit is set to indicate bad data.

*Range data type-out routine (TYPRNG).* This subprogram, like all those using the typewriter, begins with a buffer test, and if the buffer isn't ready, the subprogram exits immediately. This segment is called from SECCAL only if the TYPFLG flag is set. An immediate exit does not change this flag, and the segment will be called repeatedly until the buffer is ready. The range data can be typed in either octal or decimal format depending on the setting of BPT 4. When the range data has been converted to the desired output format, the word count and text location are set in the type-output interrupt routines and the typewriter is connected to the output buffer. Typing of the range data is done at 1 character/word instead of the 4 characters/word of all other type output. The TYPFLG calling flag is reset and the routine exits, returning control to SECCAL, while the typewriter continues to type the range data.

*Typewriter input/output subroutines (IIIN, IIOUT, INPUT, TXTOUT).* Two different interrupt routines (IIIN and IIOUT) are connected to the end-of-word (I1) interrupt for typewriter input and output, respectively. On input, a character is input from the buffer and checked to see if it is a carriage return. If so, the typewriter is disconnected from the buffer. In any case, the character is stored in the input storage area, located in this segment in the ASSEM subroutine, and the character count is decremented by one. If the character count is now zero, the typewriter is disconnected (if it has not been already) and the routine exits.

On output, the IIOUT routine outputs one word from the output storage area to the buffer. The word count is decremented by one and, if it is zero, the instruction to terminate output is given; however, the typewriter continues typing the present word and the routine exits. On both input and output, the end-of-record (I2) interrupt is connected to a do-nothing routine that exits immediately.

Two other routines, INPUT and TXTOUT, are used for input and output to set up the character count or word count and to connect the proper I1 interrupt routine. INPUT sets the character count to fifteen, connects IIIN to the I1 interrupt, and executes a 40-ms pause before connecting the typewriter. After connecting the typewriter, a buffer test is made repeatedly while the input continues under interrupt control until the typewriter has been disconnected. The characters in the input storage area are then reassembled into the format needed for POP conversion to binary form. On output, the routine TXTOUT sets the word count (from the A-register), sets up the output text storage location (from the B-register), and connects IIOUT to the I1 interrupt. The typewriter is started at 4 characters/word and the routine exits immediately so that program operation is not held up for typewriter output operations.

*Power failure subroutines (PWRON, PWROFF).* In the event of a power failure and subsequent restart, no attempt is made to continue tracking in the current acquisition. Rather, a reacquisition is attempted using the current mode and parametric data. Thus, no data is considered vulnerable to power failure and nothing is saved and restored by these routines. If the power fails, a PWRERR flag is set and the computer waits until the voltage is down. When the voltage comes back up, a 100-ms delay is executed to prevent the restarting of the program by a short voltage transient. If power is still on at the end of the delay, the routine exits to REACQ for a new acquisition. The error flag that was set is checked in INIT so that the error message PWRERR can be typed and acquisition continue.

*Parameter input routine (PARAM).* The PARAM segment is a series of calls to the typewriter input and output subroutines which alternately output a data header and then input the desired data. The input data is converted to binary floating-point format and stored in the appropriate location in the DATA AND TABLES segment. BPT 1 must be set before exiting this routine. Since this routine is skipped during acquisition if BPT 1 is set, this routine is normally entered only once unless the operator specifically wishes to change the stored value of one of the parameters. In that case, the operator must raise BPT 1 and reacquire in the ranging mode.

*Error type-out subroutine (ERRTYP).* This segment is called in INIT or SECCAL if any of the error flags have been set. The flags are checked in an indexed loop so that, on entry to ERRTYP, the index register indicates



which flag is set. The buffer is checked, and if the typewriter is busy, the routine exits immediately without resetting the error flag. Thus, ERRTP will be called once each second from SECCAL, or on each reacquisition from INIT, until the typewriter is free. The indexed message is stored in the text output location, the indexed error flag is reset (a negative value stored there), and TXTOUT is called to start the typewriter. The error message table is located in this segment, while the error flag table is in DATA AND TABLES since other routines need access to the error flags in order to set them. Twelve locations are reserved in both tables although only ten error messages are used in the present system. (See DATA AND TABLES for error message listing.)

**DATA AND TABLES.** This segment consists of all the data and temporary storage locations accessed by more than one segment in the ranging system. The segment is divided into four sections: (1) array variables, (2) error flag array, (3) constants and variables, and (4) program flags and indicators. The program flags and error flags are described in the comment field in the program listing of this segment, and all other data cells are described in the comments at the head of each segment accessing that data.

Ten error flags are used in the present system. The messages typed and faults indicated are as follows:

Message	Fault
EPSERR	Clock bias frequency setting wrong
ADCERR	Analog-to-digital converter read error
TRKERR	Code tracking failure
PHDERR	Phase detector counter read error <sup>a</sup>
FCYERR	Fractional cycle counter read error <sup>a</sup>
RFDERR	RF doppler counter read error <sup>a</sup>
CLDERR	Clock doppler counter read error <sup>a</sup>
LP2ERR	Doppler aid loop lock failure
TIMERR	Component acquisition time too large
PWRERR	Power failure

<sup>a</sup>Read errors are judged to have occurred if the read-in of the number is 0. For FCYERR and RFDERR this may not be an actual failure.

*Analog-to-digital converter read routine (ADREAD).* Two versions of this segment are available, one of which changes the sign of the converted numerical data in both channels. This is equivalent to inverting the polarity of the voltage at the analog-to-digital converter input terminals. In this way, the program is made compatible with

the ranging code, whether or not it is inverted during retransmission in the spacecraft, by using the system with a normal or inverting ADREAD, as required.

Initially on entry, the channel number is set to 0 and the ready test is executed. The ready test is a subroutine that delays 50  $\mu$ s, issues the command to convert, delays another 50  $\mu$ s, then checks to see if the converter is ready. If it is not, the ADCERR error flag is set. The data is then read from channel 0 and the channel number is stepped to 1. Again, the ready test is executed thereby converting the data in channel 1. Channel 1 is read, the inverting routine negates the data in both channels, the registers used are restored, and the routine exits.

**d. Receiver alignment test program.** This program provides a step-by-step method of setting up the receiver alignment adjustments prior to acquisition of the ranging code. The alignment procedure is output on the typewriter one step at a time. Each step is followed by a pause for checking or setting each adjustment and logging any settings or data read as a record of the alignment activity. Entering a carriage return ends the pause and initiates the next step in the procedure.

The tests accomplished with the receiver alignment test program are as follows:

- (1) TDH interface checkout: Four different bit patterns are sent to the TDH readout and compared with the typed data.
- (2) Frequency check of 10-MHz reference frequency.
- (3) Frequency check of ranging switch loop.
- (4) VCO voltage-frequency calibration curve: Three voltage levels are input to the VCO: -10, 0, and +10 V. The oscillator frequency is logged for each input voltage.
- (5) 1-MHz reference loop-lock test.
- (6) Digital counter and doppler-aid loop check. The doppler-aid loop is locked at 1/1000 the frequency read from the RF doppler counter; the clock doppler and fractional cycle counters are then read to check the loop frequency. An error message is typed if the loop frequency fails to match the input frequency within 0.001 Hz.
- (7) Ranging pad adjustment.
- (8) 10.1-MHz phase shifter adjustments on both channels.

- (9) Modulation pad adjustment.
- (10) Transmitter and receiver-coder phase shifter adjustments.

Entering a negative sign and a *carriage return* following the digital counter and doppler-aid loop check causes the loop-lock sequence to be repeated.

If a negative entry is made for the channel 1 detector output voltage during the 10.1-MHz phase shifter adjustments, the operator is instructed to shift the channel 0 phase by 180 deg and then repeat the step.

The final typed instruction tells the operator to load the main ranging program and obtain a reading for the calibration range. If this value is near 504,634,000, the alignment program should be reloaded and the short program executed, completing the last three steps of the full alignment program, beginning with the 10.1-MHz phase shifter adjustments. The short program is entered by executing a BRU 2 instruction after loading the alignment program tape.

#### 4. Programmable RF Attenuator, S. Fisher

**a. Introduction.** A need exists for an accurate, stable, remotely controllable S-band RF attenuator. It would be used, initially, to facilitate Deep Space Network (DSN) receiver sensitivity calibration. Later, it would be incorporated into the DSN automatic performance monitoring and simulation equipments.

Although an insertion-loss stability and repeatability of 0.5 dB would be comparable to presently attainable performance, a goal of 0.1 dB is being pursued in order to facilitate system upgrading.

A dynamic range of from 100 to 120 dB is desirable because it would provide extra flexibility with different receiver preamps, although 85 to 90 dB could be used satisfactorily.

A device which may have promise for this application is the PIN diode attenuator. Tests of its stability and repeatability are described herein.

**b. PIN diode attenuator.** The PIN diode is a semiconductor device having a layer of intrinsic semiconductor material between its P and N regions. The minority carrier storage time in the intrinsic region is long compared to an RF signal period at frequencies above a few hundred

megahertz. At S-band, consequently, the diode, when forward-biased, looks like a resistor whose magnitude is dependent upon dc bias current. In a suitable circuit, this device can be used as an RF attenuator. Such an attenuator is made by the Hewlett-Packard Company. Their Model 8732B is designed to operate in the frequency range 1.8 to 4.5 GHz.

A typical plot of attenuation as a function of bias voltage and current is shown in Fig. 28. Temperature sensitivity is such that temperature compensation and/or control would be necessary for system use.

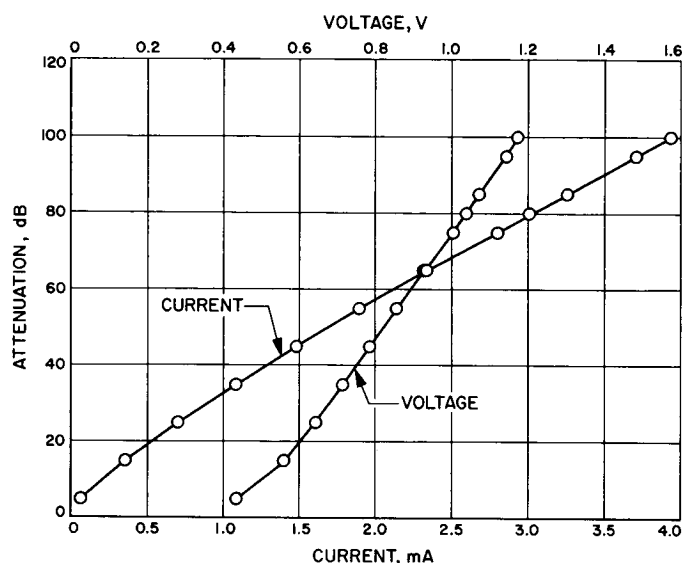


Fig. 28. PIN attenuator insertion loss at 2282.5 MHz as a function of bias voltage and current

**c. Test procedure.** The test circuit used is shown in Fig. 29. Here, the signal from a stable source is split and passed through two channels. One contains a precision attenuator and a variable-length, constant-impedance line used as a phase shifter; the other contains a PIN diode attenuator isolated by input and output pads. The signals from the two channels are summed in a hybrid and applied to the input of a receiver tuned to 2282.5 MHz. The amplitudes and phases of the signals in the two channels are adjusted to produce an output null. The null signal can provide a sensitive indication of changes in PIN diode attenuator characteristics when precautions are taken to stabilize the other channel.

**d. Results.** A representative measurement of null depth versus time is shown in Fig. 29. The nominal attenuator insertion loss is 40 dB. It can be seen that, over a 12-min

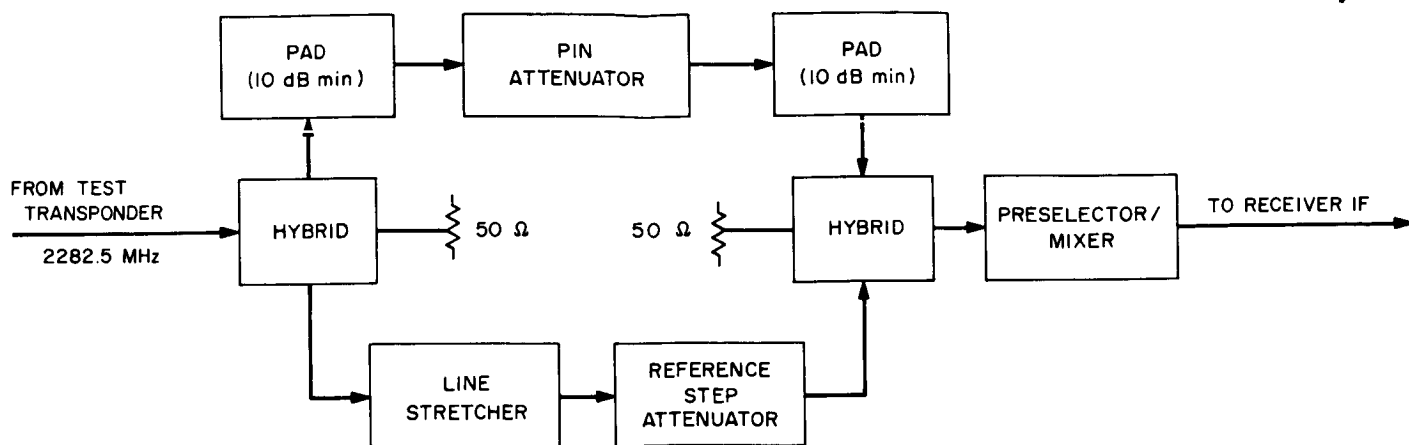


Fig. 29. Test setup

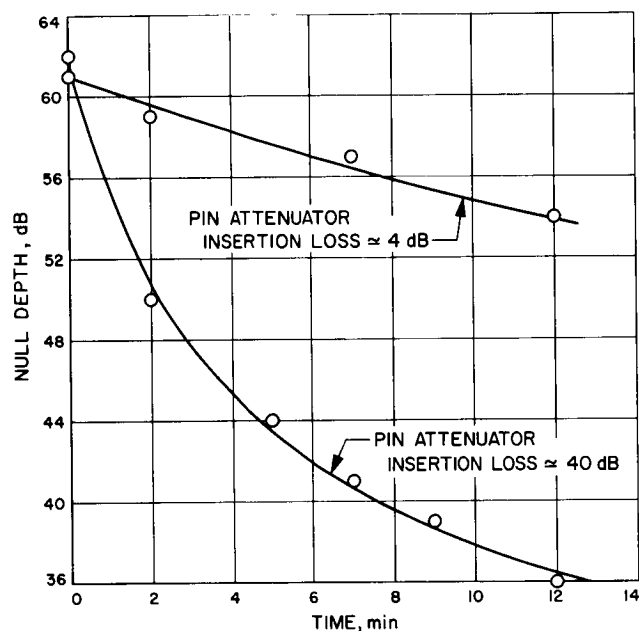


Fig. 30. Null depth as a function of time

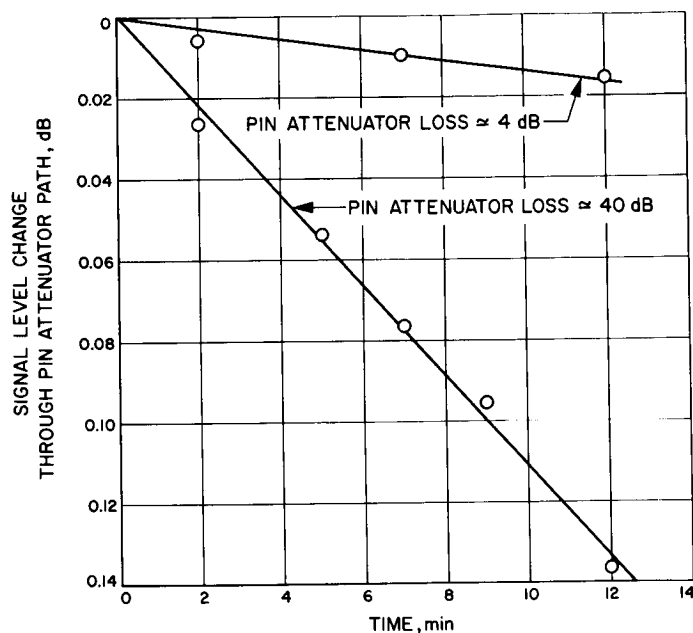


Fig. 31. Change in PIN attenuator insertion loss as a function of time

period, the receiver input signal rose from a level of  $-138$  to  $-112$  dBmW, corresponding to a change in null depth from 62 to 36 dB. Plotted in the same figure is the curve of null depth versus time obtained when the PIN diode attenuator insertion loss was reduced to approximately 4 dB, and fixed coaxial attenuators were used to raise overall attenuation in this channel to its previous value. The difference in measured null depth versus time is, consequently, attributable to PIN diode attenuator drift.

**e. Conclusion.** The change in insertion loss corresponding to the change in null depth (see Fig. 30) is plotted

in Fig. 31. (Tests were made to verify that the observed change in null depth was due primarily to insertion-loss drift and not to phase-shift drift.) It is evident that this insertion-loss stability is inadequate to meet initial project goals.

Discussion of these results with Hewlett-Packard led to the return of the 8732B attenuator and substitution of passivated PIN diodes for the non-passivated components in the original model. Preliminary measurements made on the modified unit indicate improvement in insertion-loss stability. More extensive tests will follow.

## 5. System Design of a Sequential Decoding Machine,

W. A. Lushbaugh and J. W. Layland

**a. Introduction.** Convolutional encoding and sequential decoding are currently receiving considerable attention for use in spacecraft telemetry systems (Ref. 1). The properties of the codes and the decoding algorithm are discussed in detail in Ref. 2. Up to the present, most sequential decoding has been performed using general-purpose computers programmed according to the Fano algorithm. This article describes the preliminary design of a special purpose hardware decoder for binary convolutional codes based upon this algorithm.

**b. The Fano algorithm and convolutional codes.** The convolutional encoder consists of a  $K$ -bit shift register coupled with  $V$  parity check adders, each of which is connected to a distinct subset of the bits in the shift register. Typically, the code is systematic and complementary; i.e., one adder receives only the most recent bit, and this bit is connected to all adders. After each data bit is shifted into the register, the  $V$  check symbols are sampled in turn and transmitted. These  $V$  symbols form one branch of the tree code which is generated. To synchronize and block the data, the encoder is set to a known state at the beginning of each  $L$ -bit block of data, and following the transmission of these  $L$  bits, a known sequence, or tail, of at least  $K$  bits is encoded and transmitted.

The decoder for this code consists of a buffer to hold received symbols, a copy of the encoder, and equipment to measure the merit of the output of this encoder relative to the received symbol sequence. This metric is used sequentially and systematically to estimate and/or correct the local data sequence. The metric is computed branch-by-branch and compared to a threshold. Whenever a threshold violation occurs, the local data sequence is searched backwards for a probable cause and then corrected. The estimation and backward searching are controlled according to the Fano algorithm in such a way that no looping is possible; i.e., given enough time and very unfavorable circumstances, all  $2^L$  possible local data sequences could be examined by the decoder. The basic flow diagram of the Fano algorithm is shown in Fig. 32.

**c. Design aims.** Although design and construction of the sequential decoder are scheduled for readiness at the launch of *Pioneer D*, a significant factor in its design is the requirement that the decoder be capable of decoding all "reasonable" convolutional codes and data formats. Reasonable has been defined to include all systematic and complementary codes of constraint length

32 or less, block size 2048 or less, having 5 or fewer symbols per branch, and having a tail of length 64 or less. The decoder must perform in a near-optimal manner and with a computation rate which is significantly faster than that obtainable by using presently available general-purpose machines under program control.

**d. Computational format.** In order to simplify the description of the decoder to follow, it is convenient to describe here the items which are computed by the decoder at each step. These are defined as follows:

$M_p$  = global metric after  $p$ th branch of code

$r_{i,p}$  =  $i$ th received quantized symbol on  $p$ th branch

$R_p$  =  $p$ th branch received data

$M(x)$  = metric value of the symbol  $x$

$BM_p(x)$  = branch metric using  $p$ th branch data assuming  $p$ th bit was  $x$

$b_p$  = estimated best bit at  $p$ th branch

$b_p = 1$  if  $BM_p(1) \geq BM_p(0)$

$d_p$  = local data bit selected for  $p$ th branch

$c_{i,p}$  =  $i$ th local coder check symbol on  $p$ th branch

The branch metric,  $BM_p(x)$  is further defined by

$$BM_p(x) = M_0 + \sum_{i=0}^{v-1} M(x * c_{i,p} * r_{i,p})$$

where the operation  $*$  denotes multi-bit exclusive-or; i.e., each bit in the binary expansion of  $x * c_{i,p} * r_{i,p}$  is the modulo 2 sum of  $x$ ,  $c_{i,p}$ , and the corresponding bit of  $r_{i,p}$ .

Assume that the decoder has just completed a forward step onto the  $p$ th branch.  $M_p$  and certain other recent metric terms are available from previous computation. To determine the next step, the decoder computes the following four items:

$$M_{0,p+1} = M_p + BM_{p+1}(0) \quad (1)$$

$$M_{1,p+1} = M_p + BM_{p+1}(1) \quad (2)$$

$$\Delta_{1,p+1} = \sum_{i=0}^{v-1} [M(c_{i,p+1} * r_{i,p+1}) - M(1 * c_{i,p+1} * r_{i,p+1})] \quad (3)$$

$$\Delta_{2,p+1} = \sum_{i=1}^{v-1} [M(c_{i,p+1} * r_{i,p+1}) - M(\delta_i * c_{i,p+1} * r_{i,p+1})] \quad (4)$$

where  $\delta_i = 1$  if  $d_p$  enters into  $c_{i,p+1}$ .

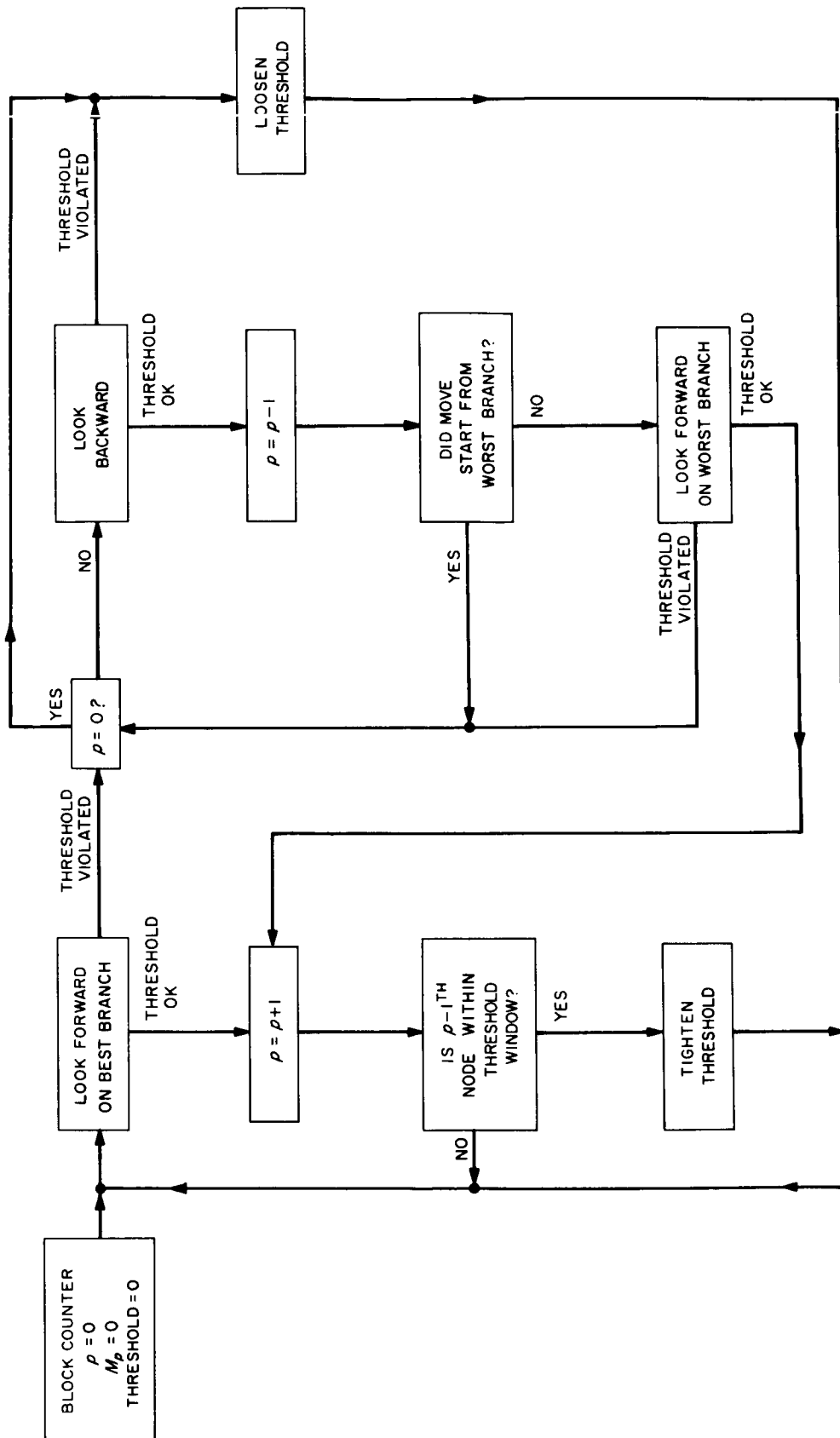


Fig. 32. Basic flow diagram for the Fano algorithm

If  $\Delta_{1,p+1}$  is positive, then  $b_{p+1} = 0$ , and  $M_{0,p+1}$  corresponds to the best branch after the  $p$ th; otherwise  $b_{p+1} = 1$  and  $M_{1,p+1}$  is best.  $\Delta_{2,p+1}$  is used if and when it becomes necessary to examine the metrics on the  $p$ th branch after complementing  $d_p$ . Let primes denote these metrics. Then

$$\Delta'_{1,p+1} = \Delta_{1,p+1} - 2 * \Delta_{2,p+1}$$

$$M'_{0,p+1} = M_{0,p+1} - (-1)^{b_p} \Delta_{1,p} - \Delta_{2,p+1}$$

$$M'_{1,p+1} = M_{1,p+1} - (-1)^{b_p} \Delta_{1,p} + \Delta_{2,p+1}$$

and the new terms are generated with two additions instead of the  $V + 1$  that were required to generate the initial terms.

Decoder action after the computation phase depends upon a subset of the stored metrics. The decoder may step backward, accept

$$M_{b_{p+1}, p+1}$$

and step forward, or require examination of the primed terms before stepping backward, or accepting

$$M'_{b_{p+1}, p+1}$$

and stepping forward.

The metrics available after the forward computation phase are shown schematically in Fig. 33. Solid lines refer to metrics retained from the previous step, while dashed lines refer to metrics just computed. The computation profile for a backward step is similar to Fig. 33 with two exceptions: (1) the  $p + 1$  terms are retained (along with  $M_p$ ) from the previous step, and the  $M_{p-1}$ ,

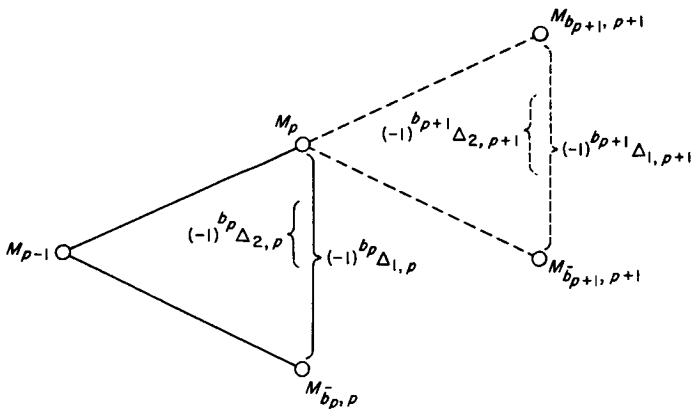


Fig. 33. Forward computation profile

$M_{d_{p,p}}$ , and  $\Delta_{1,p}$  and  $\Delta_{2,p}$  are computed, and (2)  $M_p$  may be less than  $M_{d_{p,p}}$ , in which case the decoder has stepped backward to a worst branch and will execute another backward step immediately. The array of metrics available to the decoder after either the forward or reverse computation phase permit the decoder to perform in one step, via a simple decision-gating network, operations which appear to be performed in two, three, or more steps in the flow chart of Fig. 32. A functional diagram of this decision gating is shown in Fig. 34.

**e. Decoder operation.** A basic block diagram of the decoder is shown in Fig. 35. The symbols as received are quantized into three bits packed into a four-bit segment of the packing buffer. When this buffer is full, it is written into the random access memory (RAM) and the next word, containing old symbols and decoded data, is read out. Transmission of the decoded data from the decoder is clocked by the received data, and it lags the initial receipt of that data by  $N$ -symbol times (where  $N$  is the RAM size in symbols). When symbols are needed by the decoding unit, they are transferred from the slow, magnetic core RAM to the high-speed buffer where they are available, symbol-by-symbol, for the computations described in paragraph *d* above. This symbol-oriented organization is a critical factor in allowing flexibility in  $V$ , the number of symbols per branch. The fourth bit assigned to each symbol in the memory is used by the decoder for two purposes. The decoded data bit from the last stage of the coder,  $d_{p-33}$ , is placed into the fourth bit of  $r_{0,p}$  on a forward step, and retrieved on a backward step. Simultaneously with the forward computation of the metrics at  $p + 1$ , the local encoder calculates the check-digits

$$\left\{ c_{i,p+2} \right\}_{i=1}^{V-1}$$

as if  $d_p = d_{p+1} = 0$ , and places them into the fourth bit of the associated

$$\left\{ r_{i,p+2} \right\}_{i=1}^{V-1}$$

This precomputation allows a much longer effective time to compute each  $c_{i,p}$  while still allowing full flexibility, as  $d_p$  and  $d_{p+1}$ , and only these bits, are changeable during the step following a step onto the  $p$ th branch. The stored check digits, therefore, remain valid into the past, and need not be computed on a backward step.



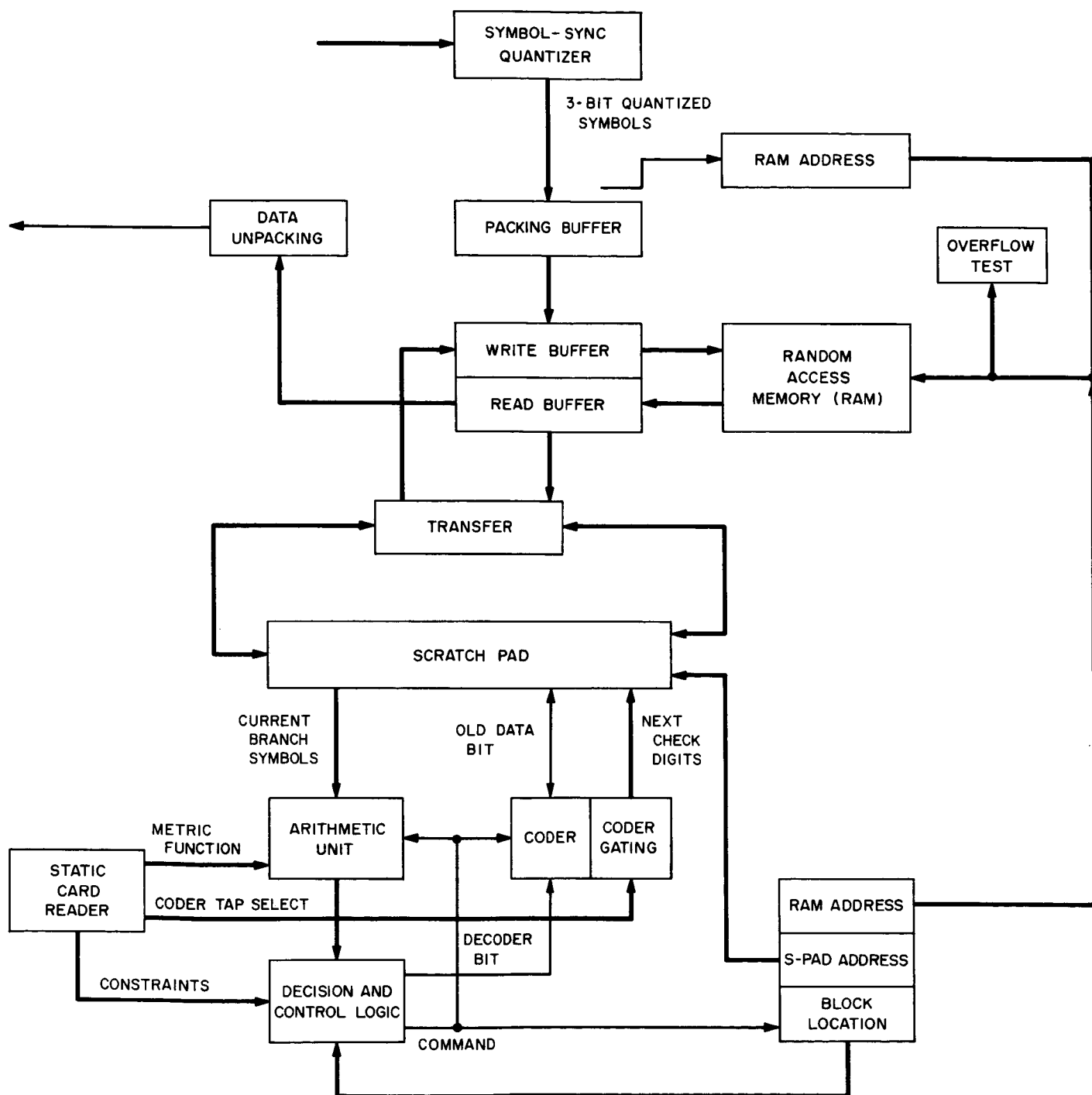


Fig. 35. Basic block diagram of sequential decoder



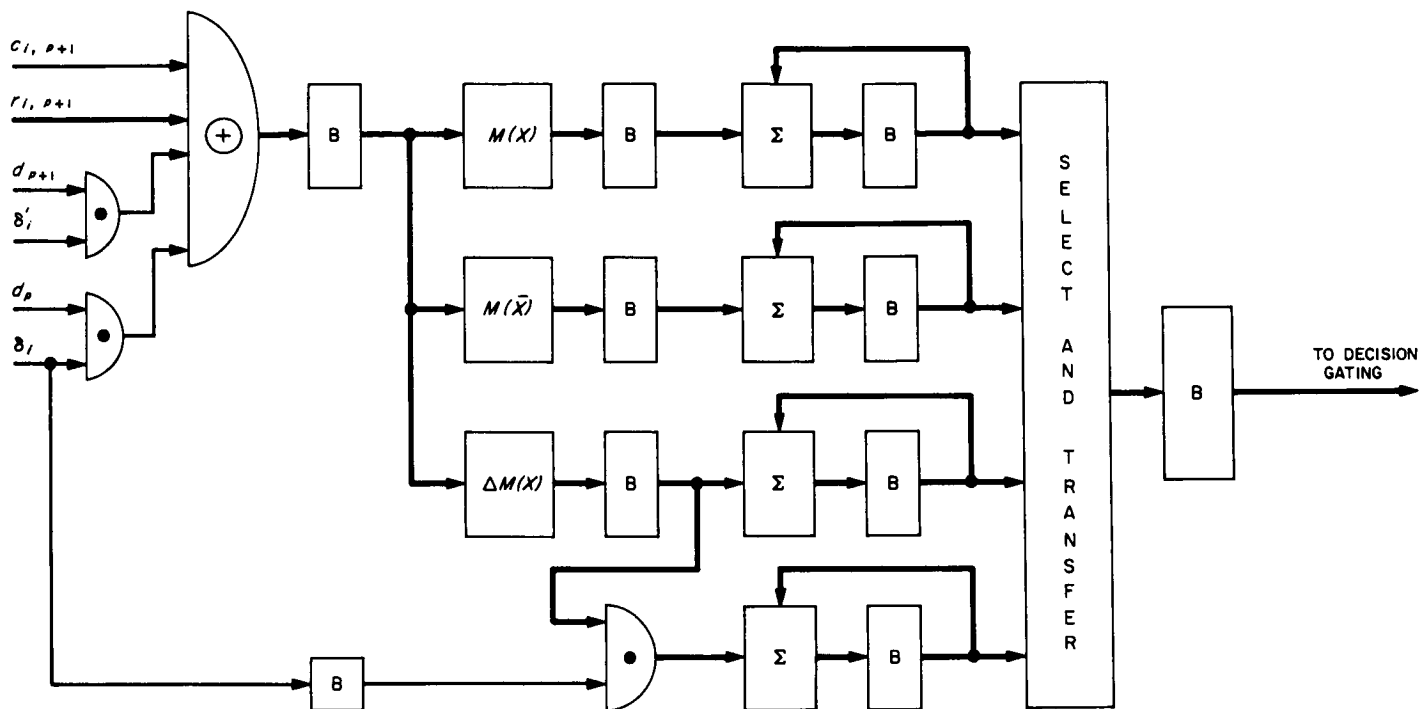


Fig. 36. Simplified block diagram of decoder arithmetic unit



A simplified diagram of the decoder arithmetic unit is shown in Fig. 36. The intermediate buffering shown serves to reduce the amount of time a given element of the arithmetic unit stands idle and, hence, to increase the effective computation speed. For a code with  $V$  symbols per branch, the time from the initiation of a forward step to the completion of the succeeding computation phase is estimated to be  $4 + V$  minor cycles, and the subsequent decoding may take 1 to 3 cycles, depending upon whether or not the primed metrics must be generated. A minor cycle should fall somewhere in the range 100 to 150 ns.

The static card reader (see Fig. 35) is an essential element in providing the desired decoder flexibility. As a simple, changeable, read-only memory, it defines such things as the coder taps, block size, the sync or forcing sequence, and the metric function. One of the possible card formats is shown in Fig. 37. While the present decoder is to be assembled for a maximum of four check symbols, or a  $V$  of five symbols per branch, little redesign would be necessary to expand this to perhaps  $V = 9$  other than expanding the gating on the coder segment of the static card reader.

### References

1. Jacobs, I. M., "Sequential Decoding for Efficient Communication from Deep Space," Paper 19TP67-937, *IEEE Trans. Commun. Technol.*, Vol. 15, No. 4, pp. 492-501, Aug. 1967.
2. Wozencraft, J. M., and Jacobs, I. M., *Principles of Communication Engineering*. John Wiley & Sons, Inc., New York, 1965.

### 6. Subroutines to Permit SDS FORTRAN II to Handle Magnetic Tapes With Arbitrary Formats, W. B. Kendall

**a. Introduction.** It is frequently desirable to use SDS FORTRAN II computer programs to process data recorded in some nonstandard format. To do this, it is necessary to have special subroutines to handle magnetic tapes, since the magnetic-tape handling routines of FORTRAN require tapes in a specific format. Furthermore, FORTRAN is basically a "one-file" system; it has no provisions for skipping files or taking automatic action when an end-of-file (EOF) mark is encountered on magnetic tape. (It does, however, have the ability to write an EOF.) For these reasons, a set of subroutines has been written to enable a FORTRAN program to handle magnetic tapes in arbitrary formats.

**b. The subroutines.** There are three separate subroutines in the set. These are as follows:

- (1) A magnetic tape reading routine (TAPE).

- (2) A routine for skipping records (or files), either forward or backward (SPACE).
- (3) One of the standard SDS magnetic tape handlers (MTAPE—catalog numbers 040004 or 540001).

All actual tape movement is done by MTAPE. The TAPE and SPACE routines simply provide for communication with FORTRAN and, when necessary, for format conversion.

**c. Use of the TAPE subroutine.** One record from a magnetic tape can be read by the FORTRAN statement

```
CALL TAPE (IWDCNT, LOC, MODE,
           IUNIT, ICHR, IERR, IOCNT)
```

where the arguments have the following significance.

IWDCNT is the number of words to be read from the record. If the record contains more than IWDCNT words, all extra words will be discarded. If fewer than IWDCNT words are in the record, then only the number of words actually in the record will be read. This will be indicated by the value returned in IOCNT.

LOC is an array to receive the words read.

MODE is a number that indicates whether the tape-read operation is to be in binary or binary-coded decimal mode. If MODE is even (i.e., its least-significant bit is zero), then the read will be in binary-coded decimal mode; otherwise, it will be in binary mode.

IUNIT is the tape unit number. If this is from 10 through 17 (decimal), then unit 0 through 7, respectively, on channel Y will be used. Otherwise, the least significant three bits of IUNIT are used as a unit number for channel W. In other words, if IUNIT is 0 through 7, then units 0 through 7 on channel W will be used.

ICHR is the number of characters per word on the tape. This can be from one through four. If it is less than four for a binary-coded decimal read, the characters read will be right justified in the computer words and the unfilled portions of the words will be unpredictable. (These right-justified words can easily be output in FORTRAN by using the R-format.) If ICHR is one or two for a binary read, the characters will be right justified with the sign bit (most significant bit read) extended to fill the left end of the words (i.e., standard two's complement form). Three-characters-per-word for a binary read is a special case. This is the format produced by JPL's analog-tape

digitizing facility, but with negative numbers recorded in *one's* complement form. The TAPE routine assumes any three-characters-per-word binary tape to be produced by this facility, and, thus, after right justifying and extending the sign of the characters read, TAPE adds one to all negative numbers to convert them from *one's* to *two's* complement form.

IERR is a word to receive the status of the requested tape-read operation. The significance of the value of IERR returned by TAPE is as follows:

IERR = 0 Read was successful

IERR = 4 End-of-tape encountered during read

IERR = 8 End-of-file mark read

IERR = 16 Unrecoverable read error

If more than one of these conditions is encountered, IERR will be the sum of the appropriate values; e.g., IERR = 12 signifies end-of-tape and end-of-file both encountered. If an end-of-file is encountered, the tape will be positioned *after* the file mark by current versions of MTAPE.

IOCNT is a word to receive the number of words actually transferred by TAPE. If the number of words in the record read was less than the number requested by IWDCNT, then IOCNT will be set equal to the number of words in the record. However, if the record contained as many *or more* words than requested, then IOCNT will be set equal to IWDCNT. Thus, if it is desired to check that a record contains a specified number of words, IWDCNT should be set equal to at least one more than the number of words expected so that long records will cause IOCNT to exceed the expected record length.

*d. Use of the SPACE subroutine.* Spacing over magnetic tape records can be accomplished with FORTRAN by the statement

```
CALL SPACE (ICOUNT, IUNIT, IERR, IOCNT)
```

where the arguments have the following significance.

ICOUNT is the number of records to skip. If ICOUNT is positive, skipping will be forward; if negative, skipping will be in reverse; if zero, no action will be taken.

IUNIT is the tape unit number: 0 through 7 for channel W, 10 through 17 for channel Y (the same as TAPE).

IERR is a word to receive the status of the requested spacing operation. The significance of its value (returned by SPACE) is as follows:

IERR = 0 No unusual conditions encountered

IERR = 2 Encountered beginning-of-tape

IERR = 4 Encountered end-of-tape

IERR = 8 Encountered end-of-file

If more than one of these conditions is met, IERR will be set to the sum of the appropriate values. If end-of-file is encountered, then the tape will be stopped just beyond the file mark. This means that it will be after the file mark for forward spacing, and in front of the file mark for reverse spacing.

IOCNT is a word to receive the number of records actually skipped. Its sign has the same significance as that of ICOUNT. Unless end-of-file or beginning-of-tape is encountered, IOCNT will be set equal to ICOUNT.

*e. Use of SPACE to skip files.* The SPACE routine can conveniently be used to skip files in FORTRAN. For example, if it is desired to skip *N* files, where *N* may be positive (for forward), zero (for no action), or negative (for reverse), the following statements are used:

```
L = 8388607
```

```
IF(N) 6, 40, 10
```

```
6 N = -N
```

```
L = -L
```

```
10 DO 20, I = 1, N
```

```
12 CALL SPACE (L, IUNIT, IERR, IOCNT)
```

```
IF (IERR-8) 15, 20, 15
```

```
15 IF (IERR) 40, 12, 40
```

```
20 CONTINUE
```

```
IF (L) 30, 40, 40
```

```
C SPACE FORWARD OVER EOF
```

```
30 CALL SPACE (1, IUNIT, IERR, IOCNT)
```

```
40 CONTINUE
```

## 7. Digital Processing of the Mariner Venus 67 Occultation Data—Frequency Shifting and Filtering, W. B. Kendall

**a. Introduction.** The basic signal processing operation required for the Mariner Venus 67 occultation experiment was the continuous estimation of the frequency of the spacecraft's RF carrier as the spacecraft moved behind Venus and the received signal passed deeper and deeper through the Venus atmosphere (Ref. 1). Up to a certain point, this was done in real time by the phase-locked receivers at the DSN Mars and Venus DSSs. However, the occultation data were also recorded in analog form for later nonreal-time processing. This later processing enabled the signal to be followed for an additional 3 min, during which its strength fell to approximately 20 dB below the threshold of the DSN receivers. Nonreal-time processing consisted of the operations discussed below.

*Digitizing and digital recording of the analog data.* The analog data had a bandwidth of over 100 kHz, and were recorded, along with a 320-kHz timing reference tone, on a 60-in./s analog recorder. This recording was slowed to 3.75 in./s (a factor of 16) for playback. Its output bandwidth was then about 7 kHz. This was low-pass filtered to about 3500 Hz, sampled at a 20-kHz rate derived from the timing reference tone, and written on SDS 930 computer seven-track digital tape units.

*Frequency shifting and digital filtering of the digitized data.* This was done to reduce the amount of data to be processed further, and also to hold the frequency of the observed RF carrier as nearly constant as possible. A nearly constant frequency was desirable since the optimum processor for such a signal is much easier to synthesize in a computer than is the processor for a signal whose frequency changes. A compression of the data was necessary so that all the data from long segments of time could be held in the computer's memory at one time for further processing.

*Digital spectrum analysis of the filtered and shifted data.* This was done because a spectrum analyzer is the optimum estimator for the frequency of a constant-frequency sine wave of unknown phase in additive gaussian noise. Initially, power spectra of the spacecraft's signal from successive short-time intervals were used to estimate its frequency variation as a function of time. Each individual spectrum was based on a short time interval, so the frequency was effectively constant for each spectrum. Such a short time could be used only for

data from the early stages of occultation, since only then was the signal strong enough to be detectable from a short observation. As the signal became weaker and weaker due to the effects of the Venus atmosphere, it was necessary to use more and more data for each spectrum. This, in turn, required that the signal's frequency be constant to a specified tolerance for a longer time. This was accomplished by starting with the spectra obtained when the signal was strong, and fitting a quadratic function of time to the observed change in the signal's frequency. This quadratic frequency variation was then used in the frequency-shifting program to preprocess the data from the next segment of time. This preprocessing of the data allowed an even longer time to be used for each subsequent spectrum, so that the signal could still be detected at the now decreased SNR. This, in turn, allowed the quadratic approximation of frequency versus time to be updated to fit this latter data. The new approximation was then used in the frequency shifting program to preprocess the following segment of data, and so forth. This "bootstrapping" operation was used to follow the signal deeper and deeper into occultation until the signal was so weak that instabilities in the spacecraft's crystal oscillator prevented sufficiently long times from being used for the individual spectra.

*Processing the filtered and shifted data in a digital phase-locked loop.* This was done to produce a running estimate of the signal's amplitude and its frequency deviation from the quadratic frequency versus time approximation. Once the frequency of the signal had been made very nearly constant by the frequency-shifting and spectrum programs, the effective bandwidth of the digital phase-locked loop could be made very narrow, and the loop could then track at the very low SNRs present deep into occultation.

**b. Frequency shifting.** Shifting the frequency of the digital data is done in a way that is completely analogous to the use of a programmed local oscillator (PLO) in an analog system. In fact, the results are exactly the same that would have been obtained if an analog PLO had been used before the data were digitized. The advantage of doing the shifting digitally is that then it can be done for different frequency-versus-time functions without repeating the digitization process.

*Interference considerations.* If we represent the analog signal from the receiver by  $x(t)$  and its samples by

$$x_j = x(t_j) = x(j\Delta)$$

where  $t_j$  is the time of the  $j$ th sample and the sampling times are  $\Delta$  sec apart, then the frequency shifting operation consists of simply replacing  $x(t)$  by

$$y(t) = \cos[2\pi f_{lo}(t)t] x(t)$$

where  $f_{lo}(t)$  is the frequency of the PLO at time  $t$ . Since this is a memoryless operation, it can be done either before or after sampling.

In the frequency domain, the effect of this (analog) operation is, roughly speaking, to shift half of the energy in the spectrum of  $x(t)$  up in frequency by  $f_{lo}(t)$ , and the other half of the energy down in frequency by  $f_{lo}(t)$ . (We assume here that  $f_{lo}(t)$  is effectively constant for a time much longer than the reciprocal of the bandwidth of  $x(t)$ . If the frequency of the expected signal is  $f_s(t)$ , its "upper side-band" will appear at frequency  $f_s(t) + f_{lo}(t)$  and will not suffer interference from the "lower side-bands" of any of the higher-frequency noise if

$$f_s(t) + f_{lo}(t) > W - f_{lo}(t)$$

or

$$f_{lo}(t) > \frac{1}{2} [W - f_s(t)]$$

where  $W$  is the (one-sided) bandwidth of  $x(t)$ .

It is also necessary to choose  $f_{lo}(t)$  so that, after sampling, no noise will be aliased down to the new signal frequency  $f_s(t) + f_{lo}(t)$ . If the data are sampled (or have been sampled) at a rate of  $s$  samples/s, the effective bandwidth of the sampled data is (Ref. 2)

$$f_{\max} = \frac{s}{2} = \frac{1}{2\Delta}$$

and some aliasing will take place if

$$f_{lo} + W > f_{\max}$$

The aliasing will interfere with the signal *unless*

$$f_s(t) + f_{lo} < f_{\max} - [f_{lo}(t) + W - f_{\max}]$$

or

$$f_{lo}(t) < f_{\max} - \frac{1}{2} [W + f_s(t)]$$

The constraints on  $f_{lo}(t)$  are thus

$$\frac{1}{2} [W - f_s(t)] < f_{lo}(t) < f_{\max} - \frac{1}{2} [W + f_s(t)]$$

which can always be satisfied if  $W < f_{\max}$ .

Of course, the purpose of frequency shifting is not simply to change the signal's frequency, but to remove its time variation. In other words,  $f_{lo}(t)$  is to be chosen so that

$$f_{lo}(t) + f_s(t) = f_c$$

where  $f_c$  is the constant frequency at which the signal will be detected. Assume that the frequency range over which the signal varies is from  $f_1$  to  $f_2$  so that

$$0 \leq f_1 \leq f_s(t) \leq f_2 \leq W$$

Then we have

$$\frac{1}{2} [W + f_s(t)] < f_{lo}(t) + f_s(t) < f_{\max} - \frac{1}{2} [W - f_s(t)]$$

This lower bound can be as large as  $1/2 (W + f_2)$  and the upper bound as small as  $f_{\max} - 1/2 (W - f_1)$ , so that, to avoid interference, we must have

$$\frac{1}{2} (W + f_2) < f_c < f_{\max} - \frac{1}{2} (W - f_1)$$

This is possible if

$$f_2 - f_1 < 2(f_{\max} - W)$$

Almost all of the frequency shifting for the *Mariner Venus 67* occultation experiment was done on data sampled at 320,000 samples/s so  $f_{\max} = 160$  kHz. The bandwidth  $W$  was about 55 kHz, and the signal frequency was shifted to  $f_c = 80$  kHz. Note that, in this case

$$2(f_{\max} - W) = 210 \text{ kHz} > W$$

so there was no restriction on the frequency range ( $f_1, f_2$ ) over which the signal could be followed.

*The frequency-versus-time profile.* For the occultation data, the variation of signal frequency with time could be well approximated by a quadratic function of time

$$f_s(t) = a + bt + ct^2$$

This required that the programmed local oscillator (PLO) frequency  $f_{lo}(t)$  be

$$\begin{aligned} f_{lo}(t) &= f_c - f_s(t) \\ &= f_c - a - bt - ct^2 \end{aligned}$$

The phase of the PLO (in cycles) was made to vary according to

$$\phi(t) = f_o t + \frac{1}{2} R t^2 + \frac{1}{6} \dot{R} t^3$$

so that

$$f_{lo}(t) = \frac{d\phi}{dt} = f_o + R t + \frac{1}{2} \dot{R} t^2$$

from which it follows that

$$f_o = f_c - a$$

$$R = -b$$

$$\dot{R} = -2c$$

The time rate of change of the PLO frequency can be seen to be

$$\frac{df}{dt} = R + \dot{R} t$$

The phase of the PLO had to be calculated for the times  $t = n\Delta$  for  $n = 0, 1, 2, \dots$ , where

$$\Delta = \frac{1}{s} = \frac{1}{2f_{\max}}$$

and the origin  $t = 0$  was taken to be the time of the first data point to be processed. The phase increment  $\phi(n\Delta) - \phi[(n-1)\Delta]$  can be seen to be

$$\begin{aligned} \phi(n\Delta) - \phi[(n-1)\Delta] &= f_o \Delta + \frac{1}{2} R \Delta^2 (2n-1) \\ &\quad + \frac{1}{6} \dot{R} \Delta^3 (3n^2 - 3n + 1) \\ &= a_i + a_r n + a_a n^2 \end{aligned}$$

where

$$a_i = f_o \Delta - \frac{1}{2} R \Delta^2 + \frac{1}{6} \dot{R} \Delta^3$$

$$a_r = R \Delta^2 - \frac{1}{2} \dot{R} \Delta^3$$

$$a_a = \frac{1}{2} \dot{R} \Delta^3$$

For the frequency-shifting portion of the computer program, the coefficients  $a_i$ ,  $a_r$ , and  $a_a$  were precomputed from the values of  $f_o$ ,  $R$ , and  $\dot{R}$  entered into the program. Then, after each input data point was multiplied by the cosine of the PLO phase, the PLO phase was incremented by  $a_i + n(a_r + na_a)$ . After each input record was processed, the value of  $n$  was reset to one, and the values of  $a_i$  and  $a_r$  were changed to compensate for this. Letting  $l$  denote the number of data points in each input data record is equivalent to replacing  $n$  by  $m = n - l$ . The phase increment can then be expressed as

$$\begin{aligned} \phi[(m+l)\Delta] - \phi[(m+l-1)\Delta] &= a_i + a_r(m+l) \\ &\quad + a_a(m+l)^2 \\ &= (a_i + a_r l + a_a l^2) \\ &\quad + (a_r + 2a_a l)m \\ &\quad + a_a m^2 \end{aligned}$$

Thus, each time  $n$  was reduced by  $l$ , the coefficient  $a_i$  was increased by  $l(a_r + la_a)$  and the coefficient  $a_r$  was increased by  $2la_a$ .

**c. Filtering.** Once the occultation data had been processed so that the signal from the spacecraft appeared at a known nearly-constant frequency, it was no longer necessary to keep such a wide-band representation of the data. Therefore, the data were (digitally) filtered to a narrow bandwidth, and the time interval between data points increased (i.e., the number of data points was systematically reduced) to correspond to this narrower bandwidth.

**Filters used.** In the continuous-time (analog) domain, the relationship between the signal  $y(t)$  to be (linearly) filtered and the output  $z(t)$  of the filter is

$$z(t) = \int_{-\infty}^{\infty} y(t - \tau) h(\tau) d\tau$$

where  $h(\tau)$  is the weighting function of the filter. In the frequency domain, this becomes (Ref. 2)

$$Z(f) = Y(f) H(f)$$

where  $Z(f)$ ,  $Y(f)$ , and  $H(f)$  are the Fourier transforms of  $z(t)$ ,  $y(t)$ , and  $h(t)$ , respectively, defined by

$$Z(f) = \int_{-\infty}^{\infty} z(t) \exp(-2\pi i f t) dt$$

$$z(t) = \int_{-\infty}^{\infty} Z(f) \exp(2\pi i f t) df$$

and similarly for  $Y(f)$  and  $H(f)$ . The object here is to choose a filter frequency function  $H(f)$  that is zero outside the desired frequency range and constant inside this range. It is convenient to choose  $H(f)$  to be a real and even function of frequency  $f$  (it need not represent a physically realizable filter). In that case we have simply

$$h(\tau) = 2 \int_0^{\infty} H(f) \cos(2\pi f \tau) df$$

and

$$h(-\tau) = h(\tau)$$

Two forms for  $H(f)$  provided in the computer program<sup>4</sup> are shown in Figs. 38 and 39. The resulting expressions for  $h(\tau)$  are

$$h(\tau) = \frac{2[\cos\pi(F_2 + F_3)\tau][\sin\pi(F_3 - F_2 + \delta)\tau](\sin\pi\delta\tau)}{\pi^2 \delta \tau^2}, \quad (\text{band-pass})$$

and

$$h(\tau) = \frac{[\sin\pi(2F_3 + \delta)\tau](\sin\pi\delta\tau)}{\pi^2 \delta \tau^2}, \quad (\text{low-pass})$$

It is convenient to have  $h(\tau)$  expressed as a product of well-behaved functions, as it is here, since calculations done in this form are relatively immune to round-off error.

<sup>4</sup>It was also possible to completely bypass the filtering portion of the program.

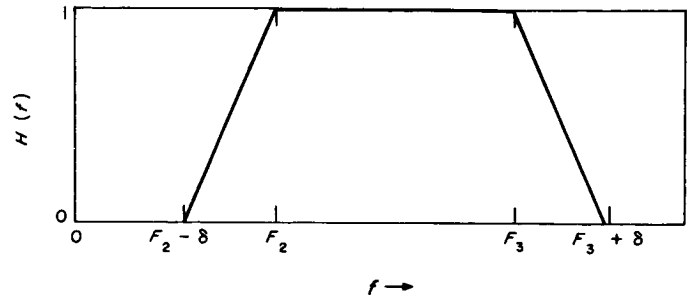


Fig. 38. Band-pass filter frequency function form

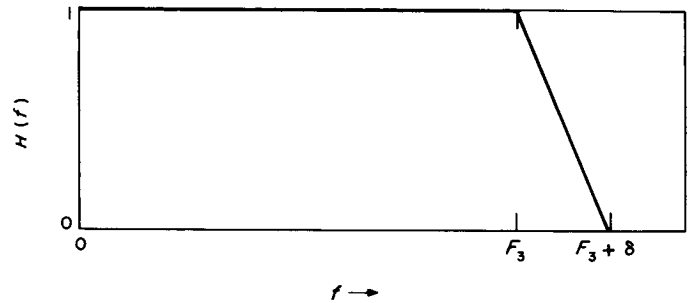


Fig. 39. Low-pass filter frequency function form

*Digital implementation.* The continuous signal  $y(t)$  can be represented in terms of its samples by

$$y(t) = \sum_{n=-\infty}^{\infty} y_n \text{sinc}(s\tau - n)$$

where

$$\text{sinc}(x) = \frac{\sin \pi x}{\pi x}$$

and

$$y_n = y(n\Delta)$$

and the samples are taken at a rate  $s = 1/\Delta$  samples/s. This representation is exact if  $y(t)$  is bandlimited to a bandwidth less than  $f_{\max} = s/2$ . Similarly, if the filter frequency function  $H(f)$  is zero outside the range  $|f| < f_{\max}$  (which it will be here), its weighting function can be represented as

$$h(\tau) = \sum_{j=-\infty}^{\infty} h_j \text{sinc}(s\tau - j)$$

where

$$h_j = h(j\Delta)$$



The filter's output at the sample times  $t = k\Delta$ ,  $k = 0, \pm 1, \pm 2, \dots$ , can thus be expressed as

$$\begin{aligned} z_k &= z(k\Delta) = \int_{-\infty}^{\infty} y(k\Delta - \tau)h(\tau) d\tau \\ &= \sum_j \sum_n h_j y_n \int_{-\infty}^{\infty} \text{sinc}(k - n - s\tau) \text{sinc}(s\tau - j) d\tau \\ &= \Delta \sum_j h_j y_{k-j} \\ &= (\Delta h_0)y_k + \sum_{j=1}^{\infty} (\Delta h_j)(y_{k-j} + y_{k+j}) \end{aligned}$$

where we have made use of the orthogonality relation

$$\int_{-\infty}^{\infty} \text{sinc}(x - m) \text{sinc}(x - n) dx = \begin{cases} 1, & m = n \\ 0, & m \neq n \end{cases}$$

*Truncation error.* Of course, in the computer it is not possible to sum over an infinite set of  $h_j$ . Instead, the summation is terminated at some finite  $j = K$ . This is equivalent to assuming that  $h_j = 0$  for  $|j| > K$ , which, in turn, is equivalent to replacing the weighting function  $h(\tau)$  by  $h^*(\tau)$  where

$$h^*(\tau) = \begin{cases} h(\tau), & |\tau| < K\Delta \\ 0, & \text{otherwise} \end{cases}$$

The filter frequency function actually realized will then be  $H^*(f)$  [the Fourier transform of  $h^*(\tau)$ ].

If we let  $E$  denote the normalized rms difference between  $H^*(f)$  and the desired  $H(f)$ , we have<sup>5</sup>

$$E^2 = \frac{\int_{-\infty}^{\infty} [H^*(f) - H(f)]^2 df}{\int_{-\infty}^{\infty} [H^*(f)]^2 df}$$

The numerator of this expression is

$$\begin{aligned} \int_{-\infty}^{\infty} [H^*(f) - H(f)]^2 df &= \int_{-\infty}^{\infty} [H^*(f)]^2 df \\ &\quad - 2 \int_{-\infty}^{\infty} H^*(f)H(f) df \\ &\quad + \int_{-\infty}^{\infty} [H(f)]^2 df \end{aligned}$$

<sup>5</sup>This error criterion was suggested by S. Zohar of JPL.

$$\begin{aligned} &= \int_{-\infty}^{\infty} [h^*(t)]^2 dt \\ &\quad 2 \int_{-\infty}^{\infty} h^*(t) h(t) dt \\ &\quad + \int_{-\infty}^{\infty} [H(f)]^2 df \\ &= \int_{-\infty}^{\infty} [H(f)]^2 df - \int_{-\infty}^{\infty} [h^*(t)]^2 dt \end{aligned}$$

where we have made use of Parseval's theorem and the fact that we are dealing with real, even functions. Now, by writing  $h^*(t)$  as

$$h^*(t) = \sum_{j=-K}^K h_j \text{sinc}(s\tau - j)$$

it is easy to see that

$$\int_{-\infty}^{\infty} [h^*(t)]^2 dt = \Delta \sum_{j=-K}^K h_j^2 = \Delta h_0^2 + 2\Delta \sum_{j=1}^K h_j^2$$

For the filters we are considering, we can let

$$\begin{aligned} Q &= \frac{\Delta}{2} \int_{-\infty}^{\infty} [H(f)]^2 df = \Delta \int_0^{\infty} [H(f)]^2 df \\ &= \begin{cases} \Delta(F_3 - F_2 + \frac{2}{3}\delta), & \text{(band-pass)} \\ \Delta(F_3 + \frac{1}{3}\delta), & \text{(low-pass)} \end{cases} \end{aligned}$$

and then express the rms error as

$$E = \left[ \frac{Q - S}{S} \right]^{1/2}$$

where

$$S = \frac{1}{2} (\Delta h_0)^2 + \sum_{j=1}^K (\Delta h_j)^2$$

In the computer program, the coefficients  $\Delta h_j$  were calculated from the relations

$$A_0 = \Delta h_0 = \begin{cases} \frac{2(\delta + F_3 - F_2)}{s}, & \text{(band-pass)} \\ \frac{\delta + 2F_3}{s}, & \text{(low-pass)} \end{cases}$$

and

$$A_j = \Delta h_j = \left( \frac{C_1}{j^2} \right) (\cos C_2 j) (\sin C_3 j) (\sin C_4 j)$$

where

$$\left. \begin{aligned} C_1 &= \frac{2s}{\pi^2 \delta} \\ C_2 &= \frac{\pi(F_2 + F_3)}{s} \\ C_3 &= \frac{\pi(\delta + F_3 - F_2)}{s} \\ C_4 &= \frac{\pi \delta}{s} \end{aligned} \right\} \text{(band-pass)}$$

$$\left. \begin{aligned} C_1 &= \frac{s}{\pi^2 \delta} \\ C_2 &= 0 \\ C_3 &= \frac{\pi(\delta + 2F_3)}{s} \\ C_4 &= \frac{\pi \delta}{s} \end{aligned} \right\} \text{(low-pass)}$$

The number of these coefficients to be calculated was determined by adding the square of each term as it was calculated to a running sum  $S$  until either

$$S \geq \frac{Q}{1 + e^2}$$

where  $e$  is the desired rms error entered into the program, or 800 terms had been calculated. The quantity  $Q$  was computed from the filter parameters entered into the program. The actual filtering was then done by a machine-language high-speed subroutine which calculated

$$z_k = A_0 y_k + \sum_{j=1}^K A_j (y_{k-j} + y_{k+j})$$

**d. Decimation.** Once the bandwidth of the occultation data had been reduced by filtering, it was possible to increase the time between adjacent data samples (i.e., to decrease the sampling rate) without degrading the quality of the data. This data compression was necessary before the spectrum program, which was to use the data further, could hold data from sufficiently long segments of time to

detect the signal. (All data for each time segment had to be in core at one time.) The filters used in the computer program were chosen so that the sampling rate could be decreased by simply keeping only every  $d$ th filtered data point and discarding all the rest. Of course, the summation that gave the filter outputs was not performed for output points to be discarded.

The effect of keeping only a set of data samples separated by  $d\Delta$ , where  $\Delta$  is the time between the undecimated samples, is to first divide the original frequency range,  $(0, f_{\max})$  into  $d$  contiguous frequency ranges of width  $f_{\max}/d$ , and then to alias the power in each of these into the frequency range  $(0, f_{\max}/d)$ . In other words, power which, in the undecimated data, appears at frequency  $f$ , where

$$\frac{(l-1)f_{\max}}{d} \leq f \leq \frac{l f_{\max}}{d}$$

for integer  $l$  in the range  $1 \leq l \leq d$ , will, after decimation, appear at frequency

$$f - \frac{(l-1)f_{\max}}{d}, \quad l \text{ odd}$$

$$\frac{l f_{\max}}{d} - f, \quad l \text{ even}$$

In order for this aliasing not to degrade the filtered occultation data, it was necessary to choose the filter so that almost all of the power in its output was confined to a single frequency range  $\{(l-1)f_{\max}/d, l f_{\max}/d\}$ . This was accomplished by first choosing the amount of decimation  $d$  such that  $f_{\max}/d$  was slightly larger than the desired undistorted bandwidth of the output data. Commonly used values were  $f_{\max} = 160$  kHz and  $d = 101, 201$ , and  $401$ . Next, the frequency  $f_c$ , to which the signal was to be shifted, was chosen so that it was in the center of one of the contiguous frequency ranges, i.e.,

$$f_c = \frac{(l-1/2)f_{\max}}{d}$$

Most of the occultation data were shifted to  $f_c = f_{\max}/2$ , which was satisfactory for any  $d$  satisfying  $d = 2l - 1$ , i.e., for any odd  $d$ . The frequency range containing  $f_c$  then extended from  $[(1-1/d)f_{\max}]/2$  to  $[(1+1/d)f_{\max}]/2$ .

The (band-pass) filter's pass band  $(F_2, F_3)$  was chosen to be symmetrical about the frequency  $f_c$  (see Fig. 40) and somewhat narrower than  $f_{\max}/d$ . The roll-off range  $\delta$  was then chosen so that aliasing would not extend into the frequency range  $(F_2, F_3)$ , i.e., so that

$$\delta < 2 \left\{ \left[ \frac{\left(1 + \frac{1}{d}\right) f_{\max}}{2} \right] - F_3 \right\}$$

For low-pass filtering of data it was necessary to choose  $\delta$  such that

$$\delta < 2 \left\{ \left( \frac{f_{\max}}{d} \right) - F_3 \right\}$$

so that aliasing would not affect the passband  $(0, F_3)$  (see Fig. 41). The low-pass mode was used only for initial quick looks at the data. Actual signal detection was done on data that had been shifted to  $f_{\max}/2$  and band-pass filtered.

**e. Conclusion.** The effect of the processing described above was to take input data sampled at a rate of 320,000 samples/s and containing a signal frequency that varied approximately quadratically with time, and producing

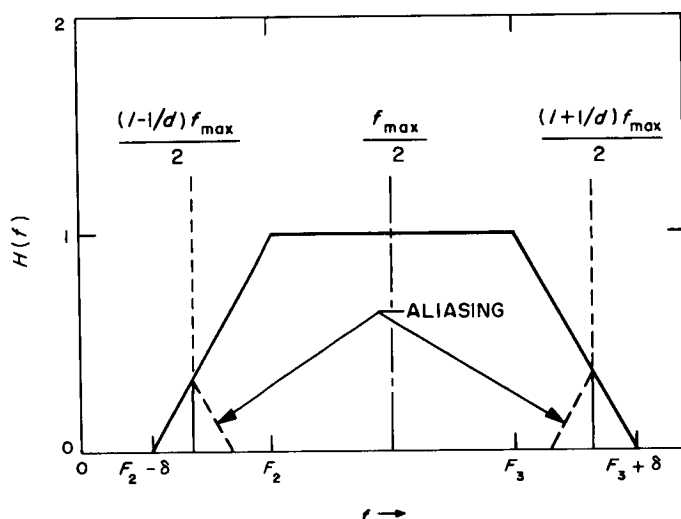


Fig. 40. Band-pass filter parameters used with decimation

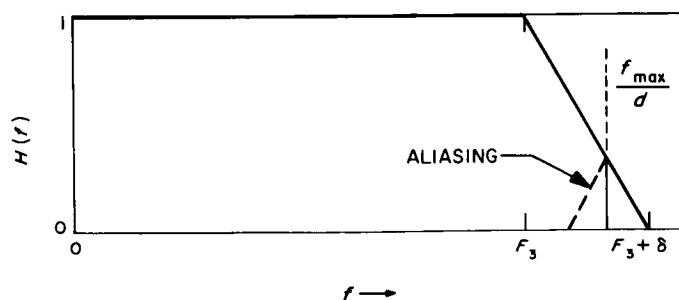


Fig. 41. Low-pass filter parameters used with decimation

from it output data sampled at rates down to 800 samples/s containing a signal frequency that was very nearly constant. Before processing, each 2400-ft reel of magnetic tape contained 28 s of data. After processing, one reel of tape could hold over 50 min of data. Besides facilitating handling of the data, this compression was essential before the spectrum program, which used this output data, could process data from sufficiently long segments of time to be able to detect the signal.

A block diagram of the computer program that accomplished the frequency shifting and filtering described in this article is shown in Fig. 42. This program is written in the SDS FORTRAN-II language and will run in any SDS 920 or 930 computer with 16,000 words of core. The program could also be run in an SDS 910 computer if its machine-language subroutines were modified. The numbers on the blocks in Fig. 42 refer to FORTRAN statement numbers.

This program is also available in a form that will run on an IBM 7094 computer system. The conversion from the original language to the much more restrictive IBM FORTRAN-IV was carried out by D. L. Nixon of JPL.

## References

1. Kliore, A., Levy, G. S., and Cain, D. L., "Atmosphere and Ionosphere of Venus from the Mariner V S-Band Radio Occultation Measurement," *Science*, Vol. 158, pp. 1683-1688, Dec. 1967.
2. Woodward, P. M., *Probability and Information Theory, with Applications to Radar*, Chap. 2, Pergamon Press Ltd., London, 1953.

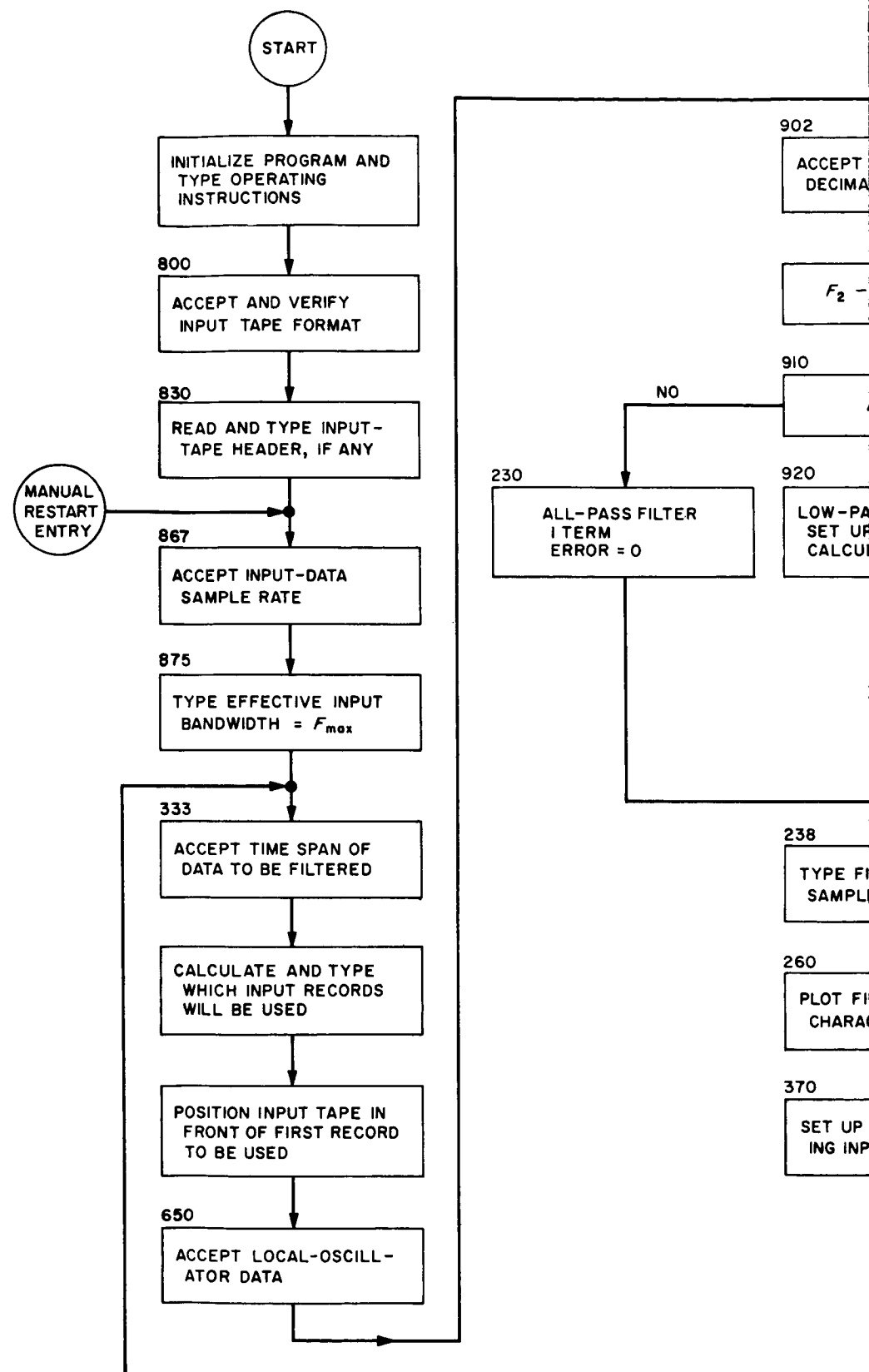
## C. Tracking and Navigational Accuracy Analysis

### 1. DSN Inherent Accuracy Project, T. W. Hamilton and D. W. Trask

The DSN Inherent Accuracy Project was formally established by the DSN Executive Committee in July 1965. The objectives of the project are:

- (1) Determination (and verification) of the inherent accuracy of the DSN as a radio navigation instrument for lunar and planetary missions.
- (2) Formulation of designs and plans for refining this accuracy to its practical limits.

Achievement of these goals is the joint responsibility of the Telecommunications Division (33) and the Systems Division (31) of JPL. To this end, regular monthly meetings are held to coordinate and initiate relevant activities. The project leader and his assistant (from Divisions





31 and 33, respectively) report to the DSN Executive Committee, and are authorized to task project members to (1) conduct analyses of proposed experiments, (2) prepare reports on current work, and (3) write descriptions of proposed experiments. The project is further authorized to deal directly with those flight projects using the DSN regarding data-gathering procedures that bear on inherent accuracy.

The various data types and tracking modes provided by the DSIF in support of lunar and planetary missions are discussed in SPS 37-39, Vol. III, pp. 6-8. Technical work directly related to the Inherent Accuracy Project is presented in SPS 37-38, Vol. III, and in subsequent *Deep Space Network* SPS volumes, and is continued in the following subsections of this volume.

The power of radio tracking data to determine the orbits of deep space probes has been discussed in a series of articles. These include a discussion of the "velocity parallax" versus "position parallax" contributions by J. Light (SPS 37-33, Vol. IV, pp. 8-16), the extension of the "velocity parallax" concept in an article on the information content of a single pass of doppler data by Hamilton and Melbourne (SPS 37-39, Vol. III, pp. 18-23), and a discussion of the critical navigational accuracy parameters for a deep space probe during the planetary encounter phase by Hamilton, Grimes, and Trask (SPS 37-44, Vol. III, pp. 4-11). Subsection 2 extends these concepts and describes an analytical procedure for determining the approximate navigation accuracy obtainable from two-way doppler tracking of a deep space probe during the early stages of planetary encounter when the effect of the target planet's gravity is still negligible. This solution is found to produce a remarkably accurate approximation of the results obtained from more time-consuming orbit determination programs. The ability to rapidly compute such navigation accuracy estimates considerably simplifies the study of guidance requirements for future missions.

The next two subsections discuss tropospheric refraction corrections to the doppler data. Subsection 3 describes the current model being used to process DSIF radio tracking data, compares the data corrections predicted from this empirical model to those derived from actual measurements of the refractivity profile versus altitude, gives an example of the sensitivity of the doppler refraction corrections versus the change in the assumed surface refractivity  $N_0$ , and for each DSS recommends the best  $N_0$ . Subsection 4 analyzes the effect of these tropospheric correction changes for the postmidcourse phase of the *Lunar Orbiter II* translunar trajectory. A

change of up to 2 m in the distance between the DSS and the earth's spin axis results from these tropospheric correction changes. This is significant when compared to the goal of determining the DSS locations on the order of 1 m to provide the navigational accuracy requirements being considered by future projects.

In recent years, it has become increasingly important to be able to calculate accurately the long-term evolution of the orbit of an artificial satellite about its central body. Straightforward methods, such as the standard Cowell-type numerical integration, not only deteriorate rapidly when the accuracy is a function of the number of the orbits integrated but are also expensive in computer time. Subsection 5 describes the integrator currently being developed at JPL which uses an algorithm that allows the integration of these orbits in multirevolution steps. This approach makes use of a trajectory program, such as DPTRAJ (Khatib, SPS 37-49, Vol. II, pp. 52-56), as a "black box" for very accurately computing increments in the orbital elements over one revolution. The degree to which these changes are "well behaved" from orbit to orbit determines the number of orbits which may be extrapolated over without the necessity of doing detailed calculations. Although these detailed calculations must be performed over the region where radio tracking exists, this method is particularly attractive where large time gaps exist between successive blocks of tracking data.

The next three articles report results based on the real-time tracking of space missions. Subsection 6 describes the determination of the selenographic location of *Surveyor VI* and the geographic location of the DSSs from the utilization of the tracking data obtained during the postlunar touchdown phase of this mission and the sensitivity of these solutions as a function of the recent lunar ephemeris improvements. In the case of the selenographic locations, a favorable comparison is obtained between the locations obtained from postlanding tracking data and those obtained from the translunar tracking data. Although a significant improvement in fitting the observational data has resulted from the recently upgraded lunar ephemeris, significant trends still appear in the residuals (observed data-predicted data). Two remaining inadequacies are known to exist in the lunar ephemeris (Mulholland, SPS 37-49, Vol. II, pp. 4-6) and a further improved lunar ephemeris is being produced. In addition, other model limitations, including tropospheric refraction model errors and the omission of ionospheric charged particle effects, can cause systematic effects in the residuals of the observed magnitude and work is also progressing in these areas.

Subsection 7 reports on the real-time cruise and encounter orbit determination results with particular emphasis placed on the variation in physical constant solutions that occurred throughout the mission. In particular, the lunar mass derived from the *Mariner V* tracking data is consistent with that obtained from the *Mariner II* Venus and *Mariner IV* Mars missions but is significantly higher than that obtained from the *Ranger VI-IX* lunar flights (Vegos and Trask, SPS 37-44, Vol. III, pp. 11-28). During the encounter operations, the estimated closest approach distance of the spacecraft to the planet remained relatively invariant while a variation of  $\pm 435$  km took place along the direction normal to the spacecraft-planet line. This is a critical parameter for the *Mariner Mars 1969* mission, which requires a  $3\sigma \leq 250$  km. The spread in *Mariner Venus 67* results is mainly due to numerical noise in the DSS location solutions. This error source scaled to the *Mariner Mars 1969* conditions results in a  $\pm 100$ -km excursion. The decrease is mainly due to the increased probe declination during *Mariner Mars 1969* encounter.

Subsection 8 discusses the successful attainment of the *Pioneer VIII* trajectory which closely matched the pre-flight nominal. The value of a relatively close match is discussed in terms of the needs for the orientation maneuvers and the pertinent trajectory parameters as they relate to the scientific objectives of the mission.

## 2. An Approximate Solution to the Estimate of Navigational Accuracy for a Deep Space Probe During the Planetary Encounter Phase,

L. Kingsland, Jr., and W. E. Bollman

**a. Introduction.** This article describes an analytical procedure for determining the approximate navigation accuracy obtainable from two-way doppler tracking of a deep space probe during the early stages of planetary encounter, when the effect of the target planet's gravity is still negligible. The solution is found to produce a remarkably accurate approximation of the results obtained from more time-consuming orbit determination programs. The capability to rapidly compute such estimates of navigation accuracy may considerably simplify the study of guidance requirements for future missions.

**b. Background.** The analytical determination of navigational accuracy from the two-way doppler tracking of a distant spacecraft has been the subject of several previous SPS articles. Hamilton and Melbourne (SPS 37-39, Vol. III, pp. 18-23) discussed the information content of a single pass of doppler data and derived an approxi-

mate equation which very accurately describes the observed instantaneous range rate of a distant spacecraft:

$$\dot{\rho} = \dot{r} + \omega r_s \cos \delta \sin \omega (t - t_0) \quad (1)$$

where

$\rho$  = distance from the tracking station to the spacecraft

$r$  = distance from the center of the earth to the spacecraft

$r_s$  = distance of the tracking station off the earth's spin axis

$\omega$  = mean rotation rate of the earth of date

$\delta$  = geocentric equatorial declination of the spacecraft

$t$  = time of the observation

$t_0$  = time of maximum elevation (zenith)

The determination of declination and right ascension was found to be highly dependent on station location uncertainty and data noise.

A later article (SPS 37-44, Vol. III, pp. 4-11) discussed the combined effects of "velocity parallax," caused by tracking station motion, and "position parallax," due to the relative motion of the earth and spacecraft. The difficulties arising from the limited accuracy of the current JPL single precision orbit determination program (SPODP) were described and a simplified procedure for estimating the semimajor axis (SMAA) of the dispersion ellipse in the aiming plane was presented. The results agreed within a few percent with those computed by SPODP, confirming that data noise and station location were indeed the major sources of navigation uncertainty during the planetary approach phase.

Unfortunately, the simplified procedure used to obtain the SMAA estimate becomes indeterminate when the spacecraft is near zero geocentric declination. A more recent article by Anderson (SPS 37-48, Vol. II, pp. 22-23) pointed out that this indeterminacy is a characteristic of the first-order terms used in the simplified procedure, whereas the exact orbit determination calculations in SPODP do not result in such indeterminacy. Furthermore, the procedure is severely limited in that it can, at best, estimate only the uncertainty in geocentric range rate, declination, and right ascension. In order to determine a complete description of the expected uncertainty in all six encounter parameters ( $\mathbf{B} \cdot \mathbf{T}$ ,  $\mathbf{B} \cdot \mathbf{R}$ ,  $T_e$ ,  $C_3$ ,  $\mathbf{S} \cdot \mathbf{T}$ ,

and  $\mathbf{S} \cdot \mathbf{R}$ ) it has, until now, been necessary to obtain such values from SPODP. The use of SPODP to perform guidance studies, however, is limited by the precision with which such computations can be made and by the expense of running the time-consuming computations required. Clearly, there is a need for a general analysis procedure which can more efficiently and effectively provide the estimates required for navigation accuracy studies. This article described an approximate method of solution which has been developed to fulfill that need.

**c. Method of solution.** Except for certain significant simplifications, the proposed procedure is essentially the same as that presently used in JPL orbit determination programs to produce an estimate of navigation accuracy. The elements of this procedure can be summarized:

(1) Obtain the partial derivatives of the observable  $\dot{\rho}$  with respect to the  $n$  parameters to be estimated:

$$\phi_{i_t} = \frac{\partial \dot{\rho}}{\partial Q_1}, \dots, \frac{\partial \dot{\rho}}{\partial Q_n} \quad (n \times 1 \text{ vector})$$

(2) Generate the mapping matrix  $(U_{t_0, t})$  and use it to project the state variables to the solution time (generally the time of encounter):

$$\phi_{i_0} = U_{t_0, t} \phi_{i_t}$$

(3) Multiply the vector of partials by itself and by a weighting matrix  $\omega_i^{-1}$  to form the matrix:

$$J_i^* = \phi_{i_0} \omega_i^{-1} \phi_{i_0}^T$$

(4) Add  $J_i^*$  to the accumulated matrix

$$J^* = J_1^* + J_2^* + \dots + J_{i-1}^*$$

(5) Given an *a priori* covariance matrix  $\tilde{\Gamma}$  of the parameters to be estimated, obtain the estimated covariance matrix:

$$\Gamma = (J^* + \tilde{\Gamma}^{-1})^{-1}$$

In order to simplify several of the steps described above, a number of assumptions are made:

(1) The spacecraft is sufficiently far out on the incoming asymptote that the gravitational effect of the target planet is negligible. Therefore, the trajectory of the spacecraft can be considered to be a heliocentric conic, eliminating the need for integrated trajectory information.

(2) The state variables to be estimated are the encounter parameters expressed in the  $\mathbf{B}$  system:

$$\mathbf{B} \cdot \mathbf{T}, \mathbf{B} \cdot \mathbf{R}, T_e, C_3, \mathbf{S} \cdot \mathbf{T}, \mathbf{S} \cdot \mathbf{R}$$

(3) The approximate data equation (Eq. 1) is a sufficiently accurate representation of the observable to be used in the calculation of partial derivatives.

(4) The accumulated matrix  $J_i^*$  can be approximated by "compressing" the data content of a daily pass of tracking data.

Under the assumptions described above, the following approximate solution procedure can then be used:

(1) Calculate the partials of the observable  $\dot{\rho}$  with respect to the state variables  $\mathbf{X}$  and  $\dot{\mathbf{X}}$ , as well as any other parameters to be estimated, such as station location. The approximate data equation (Eq. 1) is used to obtain these partials, producing terms of the form:

$$\frac{\partial \dot{\rho}}{\partial Q_j} = \alpha_j + \beta_j \cos \omega(t - t_0) + \gamma_j \sin \omega(t - t_0)$$

(2) Obtain the mapping matrix to project the state variables forward to the time of encounter. The mapping matrix is generated under the assumption of heliocentric conic motion, and the "projected" state variables  $\mathbf{X}_0$  and  $\dot{\mathbf{X}}_0$  will, therefore, be those which would result if the planet were not present. These "projected" state variables have no real meaning in themselves, but they can be transformed directly into the  $\mathbf{B}$  encounter parameters by a simple rotation of coordinates:

$$\begin{pmatrix} \Delta x_0 \\ \Delta y_0 \\ \Delta z_0 \\ \Delta \dot{x}_0 \\ \Delta \dot{y}_0 \\ \Delta \dot{z}_0 \end{pmatrix} = \begin{pmatrix} l_{tx} & l_{rx} & l_{sx} & 0 & 0 & 0 \\ l_{ty} & l_{ry} & l_{sy} & 0 & 0 & 0 \\ l_{tz} & l_{rz} & l_{sz} & 0 & 0 & 0 \\ 0 & 0 & 0 & l_{sx} & l_{rx} & l_{tx} \\ 0 & 0 & 0 & l_{sy} & l_{ry} & l_{ty} \\ 0 & 0 & 0 & l_{sz} & l_{rz} & l_{tz} \end{pmatrix} \begin{pmatrix} \Delta \mathbf{B} \cdot \mathbf{T} \\ \Delta \mathbf{B} \cdot \mathbf{R} \\ V_\infty \Delta T_e \\ \Delta C_3 / 2V_\infty \\ V_\infty \Delta \mathbf{S} \cdot \mathbf{R} \\ V_\infty \Delta \mathbf{S} \cdot \mathbf{T} \end{pmatrix}$$



where the elements  $l_{ij}$  are the direction cosines between the  $\mathbf{R} \cdot \mathbf{S} \cdot \mathbf{T}$  and the heliocentric cartesian coordinate systems.

The partial derivatives of  $\dot{\rho}$  can then be obtained from the chain multiplication of partials:

$$\left(\frac{\partial \dot{\rho}}{\partial \mathbf{B}}\right) = \left(\frac{\partial \dot{\rho}}{\partial \mathbf{X}}\right) U_{t_0, t} L_{ij}$$

Since the above operation is linear, the partial derivatives with respect to the  $\mathbf{B}$  system parameters will also be of the form:

$$\frac{\partial \dot{\rho}}{\partial B_j} = a_j + b_j \cos \omega(t - t_0) + c_j \sin \omega(t - t_0)$$

(3) The  $J_i^*$  matrix is calculated, using a weighting matrix  $\omega_i^{-1} = \sigma_{\dot{\rho}}^{-2} I$ . Each term of the  $J_i^*$  matrix will have the form:

$$\begin{aligned} (J_i^*)_{jk} = & [a_j a_k + (a_j b_k + a_k b_j) \cos \omega(t - t_0) \\ & + b_j b_k \cos^2 \omega(t - t_0) + (a_j c_k + a_k c_j) \sin \omega(t - t_0) \\ & + (b_j c_k + b_k c_j) \cos \omega(t - t_0) \sin \omega(t - t_0) \\ & + c_j c_k \sin^2 \omega(t - t_0)] / \sigma_{\dot{\rho}}^2 \end{aligned}$$

The effect of adding each term of the  $J_i^*$  matrix to the accumulating  $J^*$  matrix can be approximated by assuming that the coefficients  $a_j$ ,  $b_j$ , and  $c_j$  will be very nearly constant through the tracking pass. The data can then be "compressed" by integrating over the duration of the tracking pass:

$$(J_c^*)_{jk} \cong \frac{1}{\omega} \int_{\omega t_l}^{\omega t_F} [J_i^*(t)]_{jk} d\omega(t - t_0)$$

If the pass is symmetrical ( $t_F = -t_l \equiv \Psi/\omega$ ), the expression for "compressed"  $(J_c^*)_{jk}$  can be written:

$$\begin{aligned} (J_c^*)_{jk} = & \left[ (a_j a_k + c_j c_k)(t_F - t_l) + \frac{(a_j b_k + a_k b_j)}{\omega} \right. \\ & \left. \times \int_0^{\Psi} \cos \eta d\eta + \frac{(b_j b_k - c_j c_k)}{\omega} \int_0^{\Psi} \cos^2 \eta d\eta \right] / \sigma_{\dot{\rho}}^2 \end{aligned}$$

where  $(t_F - t_l)$  is the duration of the daily tracking pass.

(4) The compressed  $J_c^*$  matrix is added to the accumulated  $J^*$  matrix.

(5) The estimated covariance matrix is obtained as before:

$$\Gamma = (J^* + \tilde{\Gamma}^{-1})^{-1}$$

**d. Mariner Venus 67 example.** An estimate of navigation accuracy was calculated for conditions corresponding to an encounter orbit accuracy study performed for Mariner Venus 67.<sup>6</sup> The nominal trajectory studied was for a June 17, 1967 earth launch and an October 19, 1967 Venus encounter. The following *a priori* uncertainties were assumed:

$$\begin{aligned} \sigma_x, \sigma_y, \sigma_z &= 1000 \text{ km} \\ \sigma_{\dot{x}}, \sigma_{\dot{y}}, \sigma_{\dot{z}} &= 1 \text{ km/s} \\ \sigma_{\text{stn rad}} &= 24 \text{ m} \\ \sigma_{\text{stn lon}} &= 0.0005 \text{ deg} \end{aligned}$$

The encounter parameters were:

$$\begin{aligned} B &= 25,000 \text{ km} \\ V_{\infty} &= 3.113 \text{ km/s} \\ \theta &= -32 \text{ deg} \end{aligned}$$

Two stations tracking from  $E - 9$  days and a data noise of  $\sigma_{\dot{\rho}} = 0.005 \text{ m/s}$  were assumed. The results of the approximate solution are plotted in Figs. 43 and 44 for comparison with those obtained from SPODP. Calculation of the estimate was performed on an IBM 1620 computer in double precision. Total required computation time for the data shown was about 30 min.

**e. Conclusion.** The approximate solution technique described above may be of considerable value in the study of navigational accuracy during the planetary encounter phase. The solution remains determinate at zero declination and produces an estimate of all six encounter parameters. The speed of computation and the capability to produce realistic estimates present a very attractive alternative to the use of the more complex and time-consuming orbit determination programs for navigation accuracy studies.

The method of solution described in this article is valid only if the gravitational effect of the target planet is negligible. As the spacecraft nears the target planet, this effect will no longer be negligible and must be considered in any estimate of navigation accuracy. A future

<sup>6</sup>G. E. Pease, *Mariner Venus 67 Orbit Determination Characteristics and Accuracy*, June 9, 1967 (JPL internal document).

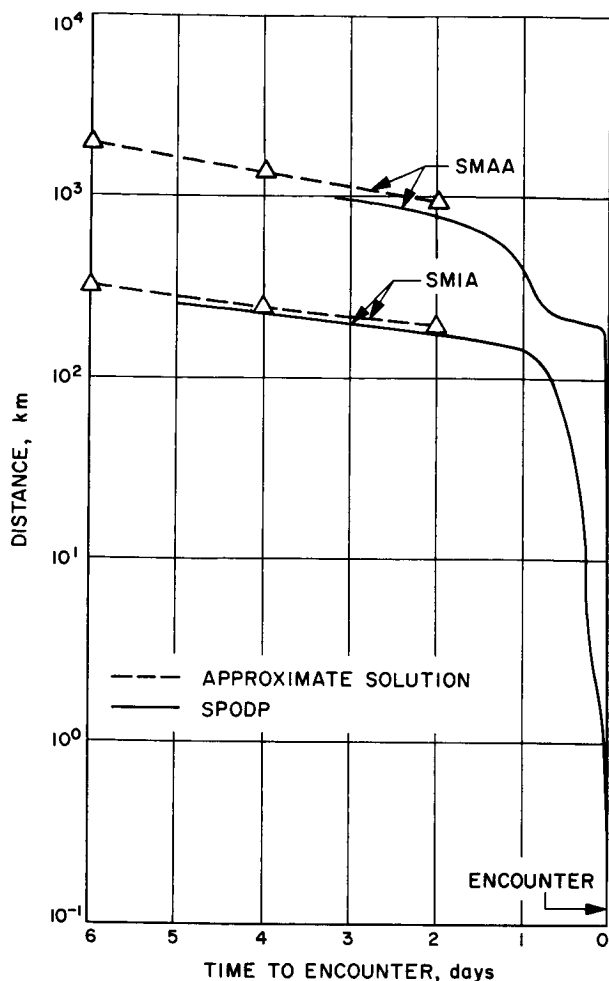


Fig. 43. Semimajor axis (SMAA) and semiminor axis (SMIA) determined from doppler tracking

article will discuss how the effect of the target planet's gravity can be incorporated into the approximate solution, permitting an accurate estimate of navigational accuracy throughout the planetary encounter phase.

### 3. Recent Changes to the Tropospheric Refraction Model Used in the Reduction of Radio Tracking Data From Deep Space Probes, A. Liu

**a. Introduction.** A major consideration in the reduction of tracking data is the effect of the intervening medium between the tracker and the spacecraft, the presence of which causes the speed of the propagated wave to differ from the speed of light. The atmosphere causes a delay in the transmission time of both the doppler and range signal. Calculations have been made to determine the various range differences caused by differing assump-

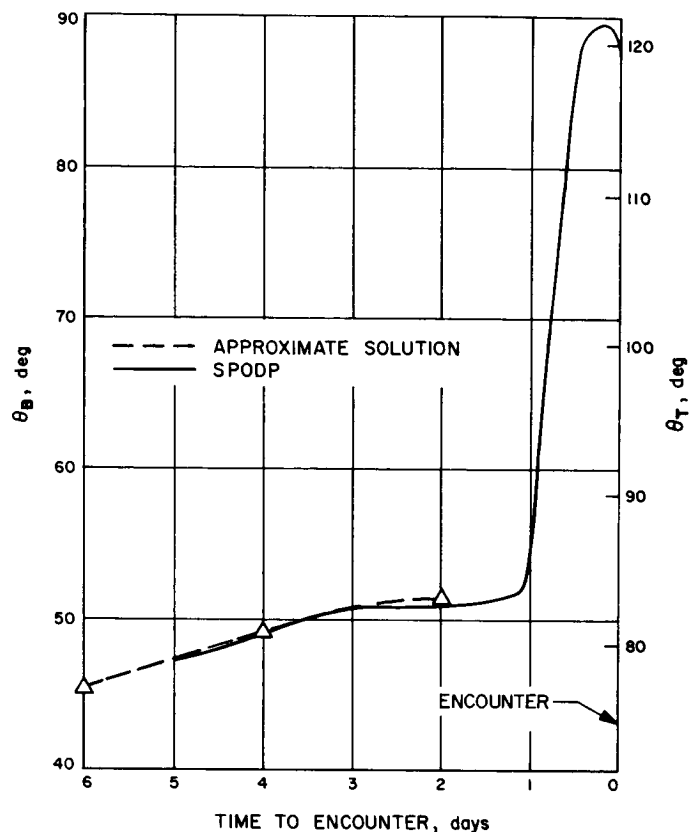


Fig. 44. Orientation of semimajor axis to B and T determined from doppler tracking

tions of the atmosphere, as well as the effect upon doppler data due to an error in the assumed surface refraction.

**b. Model atmospheres.** It is usually assumed that the refractivity  $N$  decreases exponentially with height  $h$  above sea level, i.e.,

$$N = N_0 \exp(-Bh) \times 10^{-6} \quad (1)$$

where  $N_0$  is the surface refractivity, and  $B$  is the inverse scale height in  $\text{km}^{-1}$ .

Three atmospheric models are considered here. Model 1, illustrated by Fig. 45 and taken from Ref. 1, shows an atmosphere based upon radiosonde weather data of Las Vegas, San Diego, and Yuma on July 14-15, 1965. The best fit to these data corresponded to values of  $N_0 = 349$  and  $B = 0.1326 \text{ km}^{-1}$  for altitudes above 6 km.

Model 2, illustrated by Fig. 46 and taken from Ref. 2, represents radiosonde data of Las Vegas, San Diego, and Point Arguello on October 18-19, 1967. The best fit for these data corresponded to  $N_0 = 285$  and  $B = 0.109 \text{ km}^{-1}$

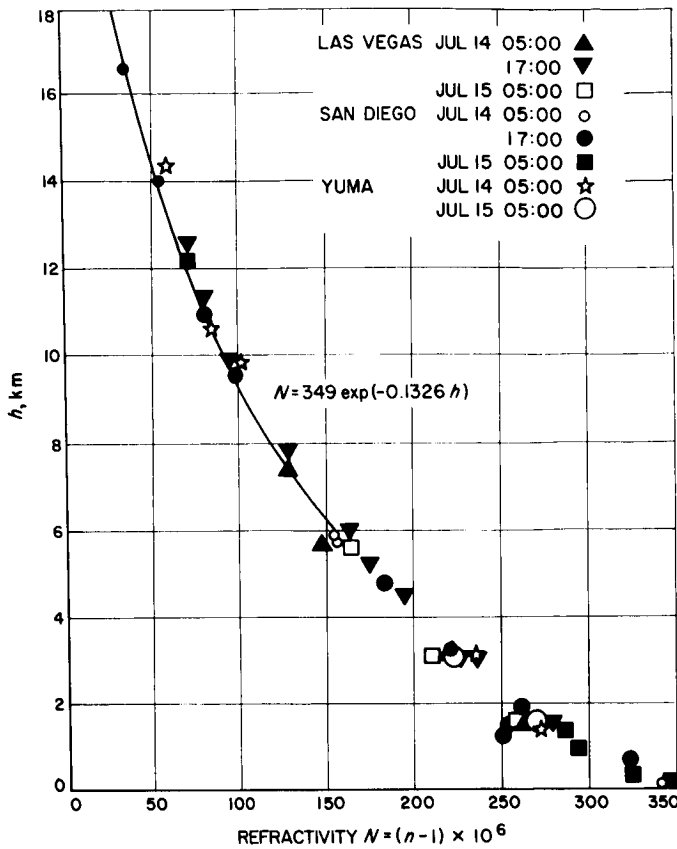


Fig. 45. Index of refraction vs altitude

for  $1.1 \leq \text{altitude} \leq 10.6$  km, and  $N_0 = 400$  and  $B = 0.142$   $\text{km}^{-1}$  for altitudes  $> 10.6$  km. The represented model consists of two layers of differing scale heights.

The present model (Model 3), which was used in correcting the received tracking data, consists of only one layer with the associated parameters of  $N_0 = 340$  and  $B = 0.142 \text{ km}^{-1}$  for all altitudes.

**c. Data correction.** Model 3 was used to compute a set of tabular corrections for range  $\Delta \rho$  and range-rate  $\Delta \dot{\rho}$  against elevation angle  $\gamma$ . The tabular solution was fitted to obtain the following expressions, which are currently being used and have been used to correct for refraction (Ref. 3).

$$\Delta \rho = \frac{N_{0i}}{340} \left[ \frac{A}{(\sin \gamma + B)^{1.4}} \right] \quad (2)$$

$$\Delta \dot{\rho} = \left( \frac{N_{0i}}{340} \right) \left( \frac{A}{\tau} \right) \left[ \frac{1}{(\sin F + B)^{1.4}} - \frac{1}{(\sin G + B)^{1.4}} \right] \quad (3)$$

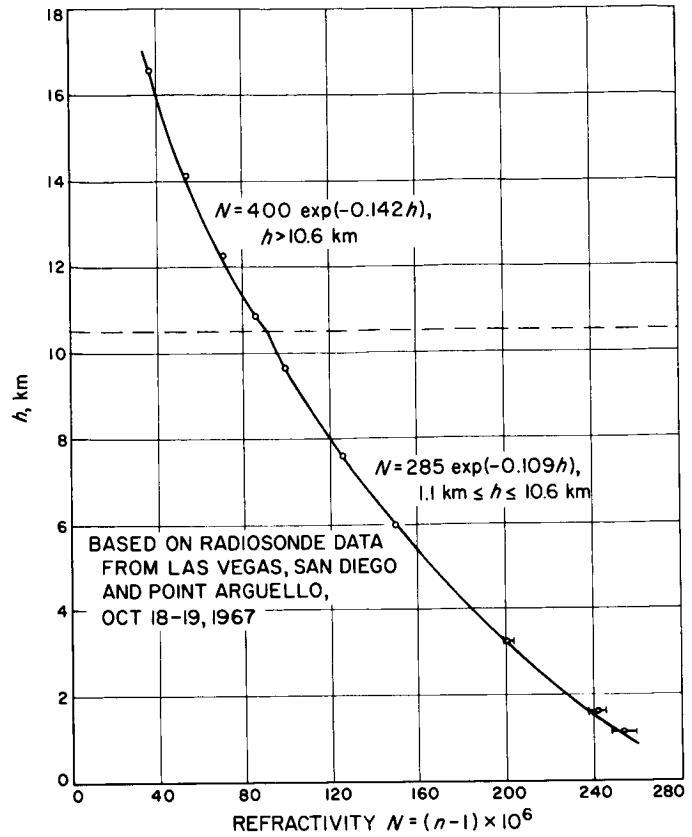


Fig. 46. Average refractivity profile

where  $A$  and  $B$  are found empirically to be:

$$A = 0.0018958$$

$$B = 0.06483$$

and

$\gamma$  = elevation angle in degrees

$N_{0i}$  = refractivity of station  $i$

$\tau$  = doppler averaging time in seconds

$$F = \gamma + (\tau/2) \dot{\gamma}$$

$$G = \gamma - (\tau/2) \dot{\gamma}$$

Model 2, which is a two-layered model, was used to compute a set of tabular corrections for range and range-rate for the Goldstone Deep Space Communications Complex. This solution was then compared against  $\Delta \rho$  and  $\Delta \dot{\rho}$  by Eqs. (2) and (3) for two values of  $N_{0i}$  ( $N_{0i} = 340$  and  $N_{0i} = 253$ ). Figure 47 is a plot of range correction versus elevation angle for  $N_{0i} = 340$ , labeled ODP (340),  $N_{0i} = 253$ , labeled ODP (253), and the two-layered model 2, labeled RAY-TRACE (253,400).

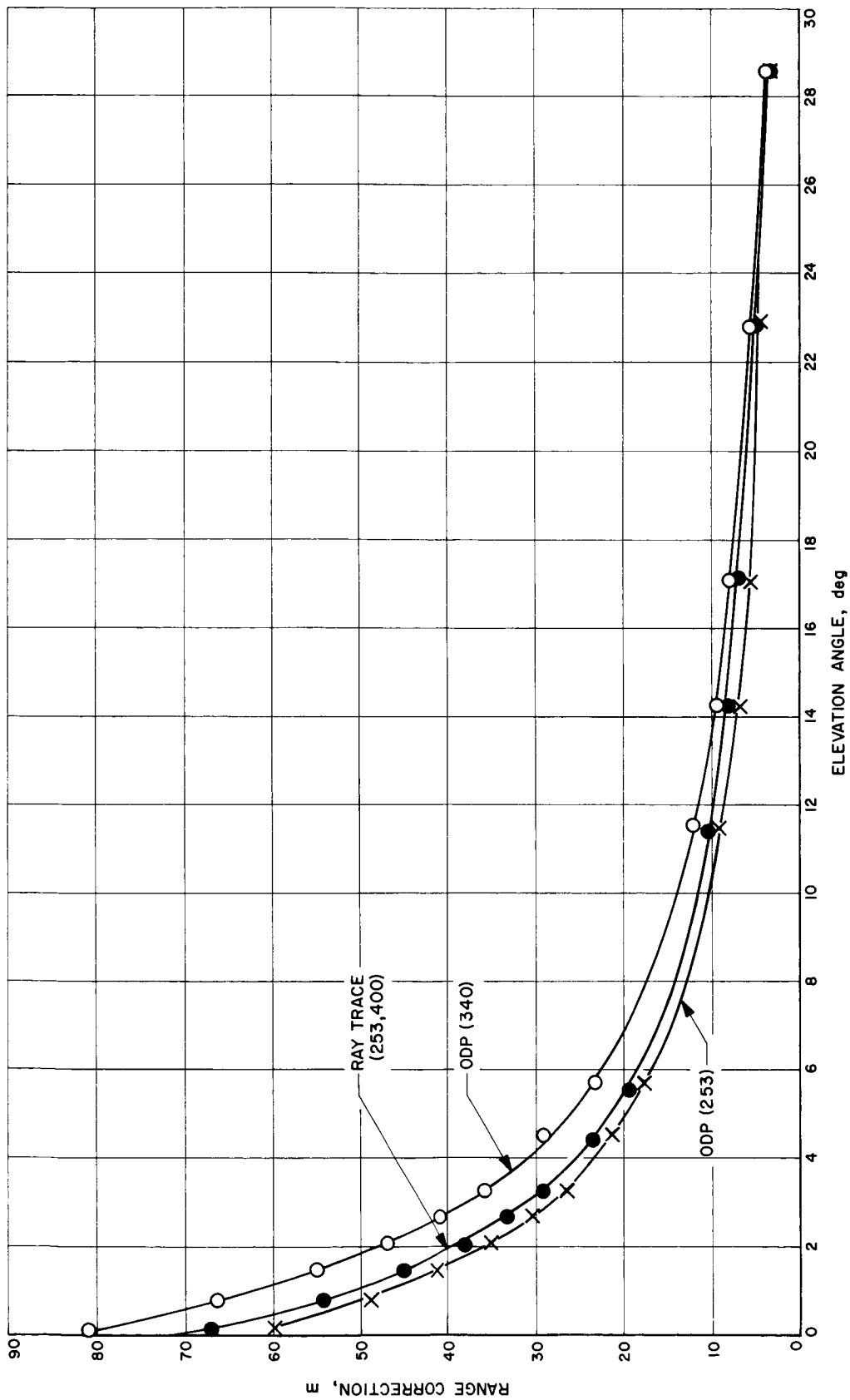


Fig. 47. Range error with various model atmospheres vs elevation angle

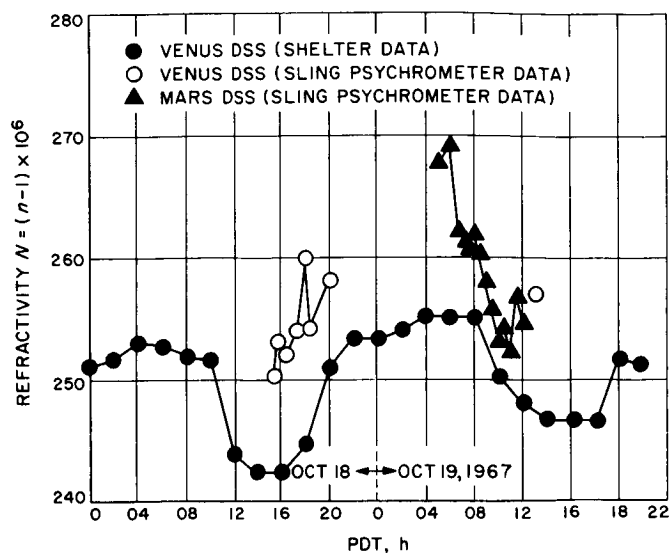


Fig. 48. Surface refractivity at Goldstone

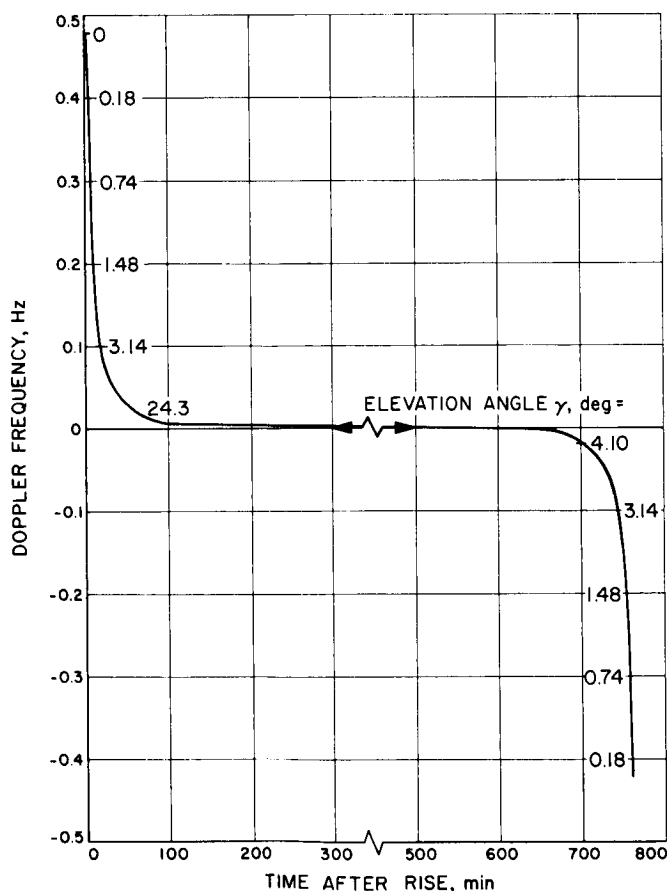


Fig. 49. Doppler correction for 100  $N_0$  units

The value of  $N_{0i} = 253$  for Goldstone was selected on the basis of Fig. 48, taken from Ref. 2. The average diurnal value of surface refractivity for that date (which was also probably the seasonal average) was 253.

SPS 37-45, Vol. IV, pp. 270-276 shows the average seasonal surface refractivity at Edwards Air Force Base to be 280. The refractivity was based upon daily measurements, and the difference between refractivity measured at Goldstone in Ref. 2 and that measured at Edwards Air Force Base is possibly due to differing weather conditions.

The value of  $N_{0i} = 340$  was selected for the final computation because at present the standard practice in data reduction is to apply refraction correction with that surface refractivity for tracking stations.

The differences in correction can be seen to be quite large for low elevation angles, especially between ODP (340) and ODP (253). The differences between RAYTRACE (253,400) and ODP (253) are less and are due to the different value of the inverse scale height of the two models (model 2 and model 3). Based on Eq. (3), Fig. 49 illustrates the doppler error in cycles per second for a change of 100 units of surface refractivity for a typical pass over Goldstone. At low elevation angles, a change of 100 units of  $N_0$  causes a difference of nearly 0.5 Hz of doppler.

Table 13. Average refractivity

Deep Space Station	Height above sea level, km	Refractivity source			Recommended refractivity
		Yearly average <sup>a</sup>	Tracking data <sup>a</sup>	Model 3	
Pioneer, Echo (Goldstone)	1.2	253	240	286	240
Woomera	0.1	NA	340	336	340
Tidbinbilla	0.64	NA	NA	310	310
Johannesburg	1.5	NA	NA	275	240
Robledo, Cebreros (Madrid)	0.75	NA	300	306	300

<sup>a</sup>NA = not available.

Table 13 lists a preliminary set of refractivity values for each of the DSN stations, and the refractivity from various sources.

**d. Conclusion.** The range and doppler errors are quite noticeable at low elevation angle. For this reason it is important that a refractivity value appropriate for each

tracking station be used in the reduction of tracking data. A good value of refractivity is arrived at, as suggested in Ref. 4, by measuring a number of surface refraction indices and profiles, and averaging over the collection of these models. The major part of errors due to the atmosphere is thus removed.

## References

1. Smyth, J. B., and Cashman, L. B., *Final Report, Radio Meteorology at JPL Goldstone Pioneer Station, July 14, 1965*, Final Report No. SRA-462. Smyth Research Associates, San Diego, Calif., July 1965.
2. Smyth Research Associates staff, *Effects of the Earth's Atmosphere on the Phase of the Mariner V Venus Probe Signal During Occultation*, Final Report No. SRA-632. Smyth Research Associates, San Diego, Calif., November 1967.
3. Warner, M. R., and Nead, M. W., *SPODP-Single Precision Orbit Determination Program*, Technical Memorandum 33-204. Jet Propulsion Laboratory, Pasadena, Calif., Feb. 15, 1965.
4. Bean, B. R., and Thayer, G. D., "Comparison of Observed Atmospheric Radio Refraction Effects with Values Predicted Through the Use of Surface Weather Observations," *Radio Science Journal Research NBS/USNC-URSI 67D*, No. 3, p. 273, 1963.

## 4. Effect of New Tropospheric Corrections on Lunar Orbiter II Cruise Solution Vector, N. A. Mottinger

**a. Introduction.** The spacecraft orbit and physical constants estimated from radio tracking data are influenced by changes in the tropospheric refraction corrections applied to the doppler and ranging data as recommended in Subsection 3. The effect of these recommended changes is given for the tracking data, the spacecraft orbit, and the deep space station locations for the case of the post-midcourse maneuver phase of the *Lunar Orbiter II* trans-lunar orbit. (This is the same tracking data discussed by N. A. Mottinger and W. L. Sjogren in SPS 37-46, Vol. III, pp. 19-23.) Although changes to the spacecraft orbit are not important in this case, the deep space station loca-

tions changed up to 2 m, which is significant compared to the 1-m accuracy required to meet the navigational accuracy goals being considered for future planetary missions.

**b. Discussion.** Doppler residuals obtained at low elevation angles when using the SPODP (Single Precision Orbit Determination Program, Ref. 1) to reduce the post-midcourse portion of the cruise data (doppler and range) of *Lunar Orbiter II* are shown in Figs. 50, 51, and 52. Those labeled nominal troposphere residuals were obtained using the nominal index of refraction ( $N_0 = 340$ ) in the SPODP, which corrects the range and doppler data for refraction using Eqs. (2) and (3) of A. Liu's article in Subsection 3. These residuals were obtained for the tracking at the Echo, Woomera, and Robledo Deep Space Stations at either the beginning or ending of a pass of tracking, a time when the elevation is less than 20 deg (approaching 5 deg in some instances). Table 14 summarizes the elevation angles for each deep space station by pass for the postmidcourse phase under consideration. This information is graphically displayed in Figs. 53, 54, and 55, which show the elevation angle as a function of time for a typical pass. Indicated on each curve is the time when doppler data were being received and used in the reduction. One can note that the station with the lowest elevation angle (Robledo DSS) also shows the highest residual (0.016 Hz or about 1 mm/s, Fig. 52). Data for the other stations were taken at higher elevation angles and do not show as large a residual.

Residuals of this nature are also present in other probe analyses. For example, see Subsection 6 in which residual plots for doppler data from a landed *Surveyor* are shown [in Fig. 64 (pass 4 for the Pioneer DSS and pass 4 for the Robledo DSS) this phenomenon is also present]. Although the *Lunar Orbiter* residuals were only 1 mm/s at most, this would account for at least one half of some of these residuals from the *Surveyor*.

Table 14. Parameter summary

DSS	Postmid-course pass	Pass interval			Number of data points used in fit		Elevation angle, deg			$\Delta N_0$	Effect of $\Delta N_0$	
		Day at start of pass	GMT of data interval, day:h:min				$\gamma_{start}$	$\gamma_{max}$	$\gamma_{end}$		$\Delta f_s$ , m	$\frac{\Delta \lambda}{1 \times 10^{-5}}$ deg
			Start	End	Doppler	Range						
Echo	1	Nov. 9, 1966	09:14:33	09:22:04	433	117	23	44	16	100	1.6	1
	2	Nov. 10, 1966	10:13:48	10:20:25	393	56	17	46	36			
Woomera	1	Nov. 8, 1966	08:21:48	09:05:31	455	133	42	69	22.5	0	0.1	1
	2	Nov. 9, 1966	09:22:12	10:05:24	413	130	43	68	26			
Robledo	1	Nov. 9, 1966	09:05:39	09:14:23	477	163	6	38	15	40	2.1	1
	2	Nov. 10, 1966	10:05:44	10:13:37	364	57	7	40	24			

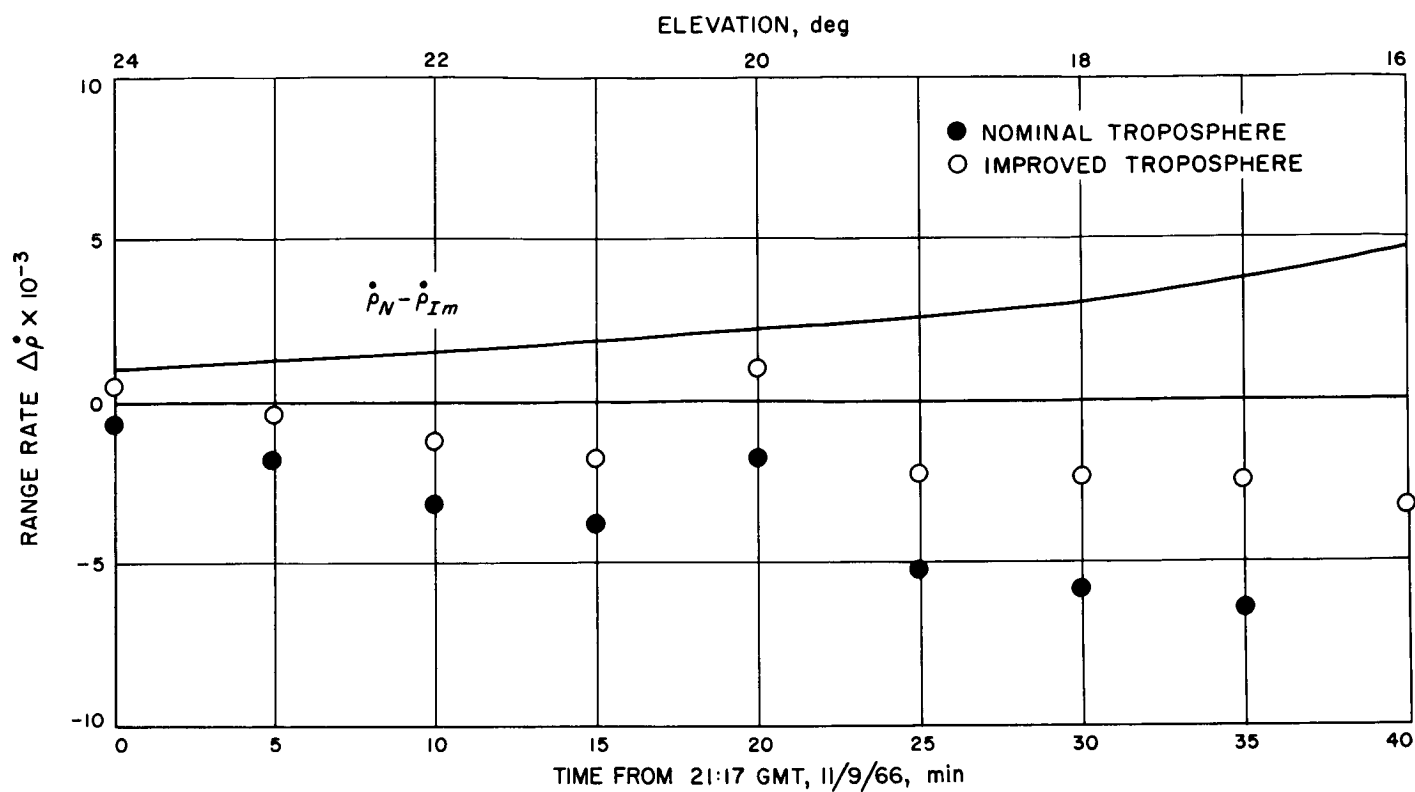


Fig. 50. Lunar Orbiter doppler residuals (Echo DSS)

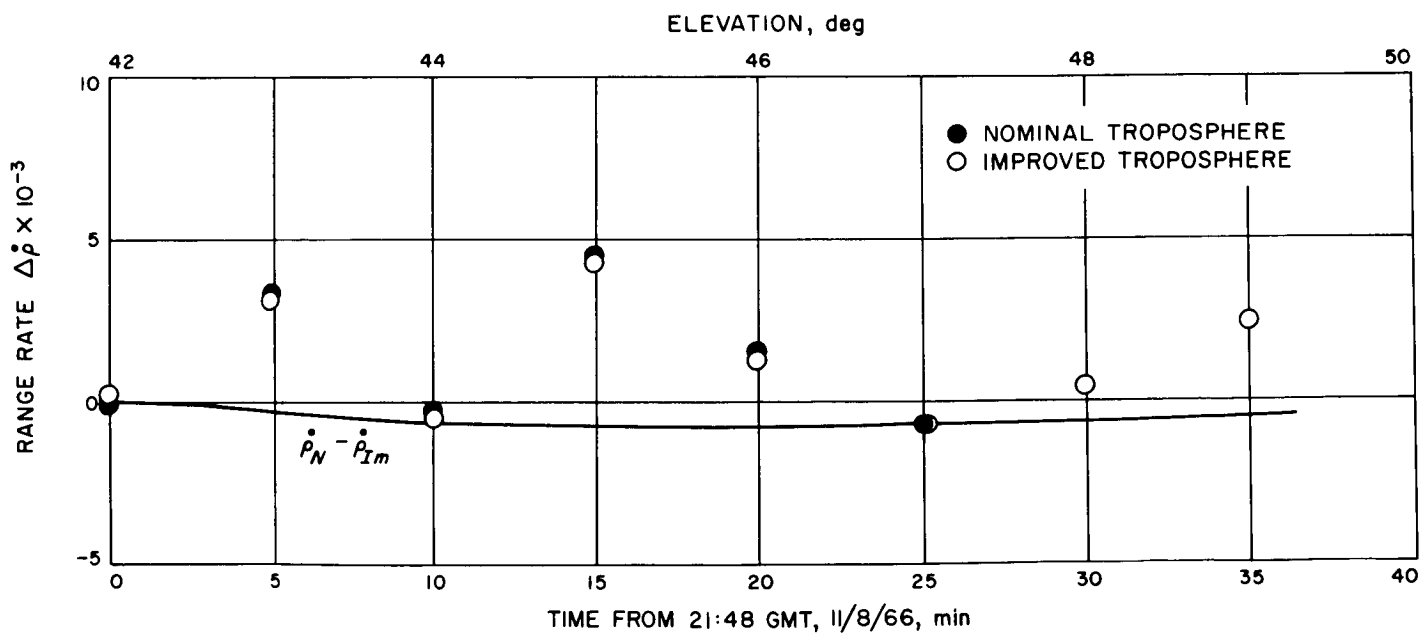


Fig. 51. Lunar Orbiter doppler residuals (Woomera DSS)

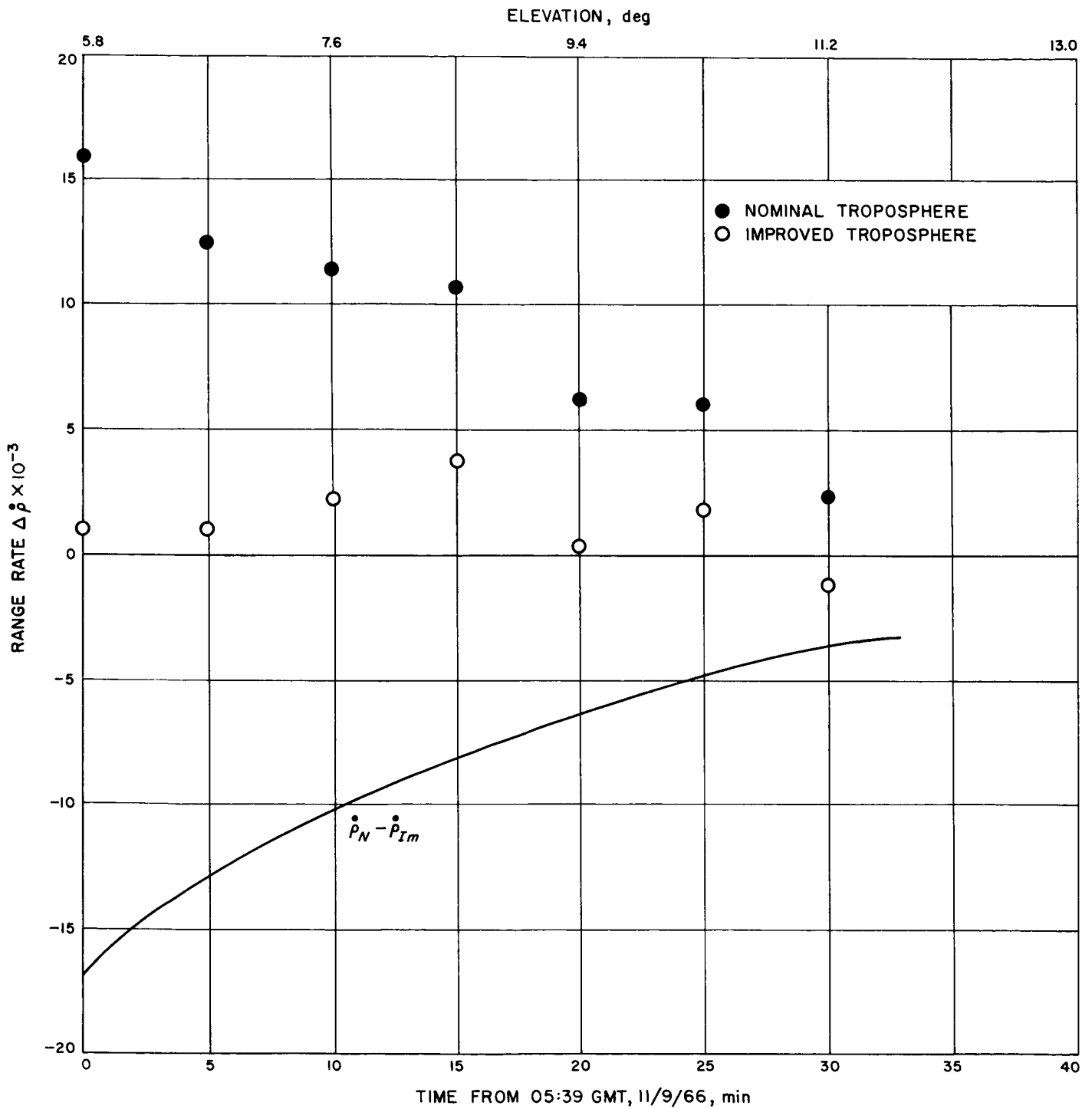


Fig. 52. Lunar Orbiter doppler residuals (Robledo DSS)



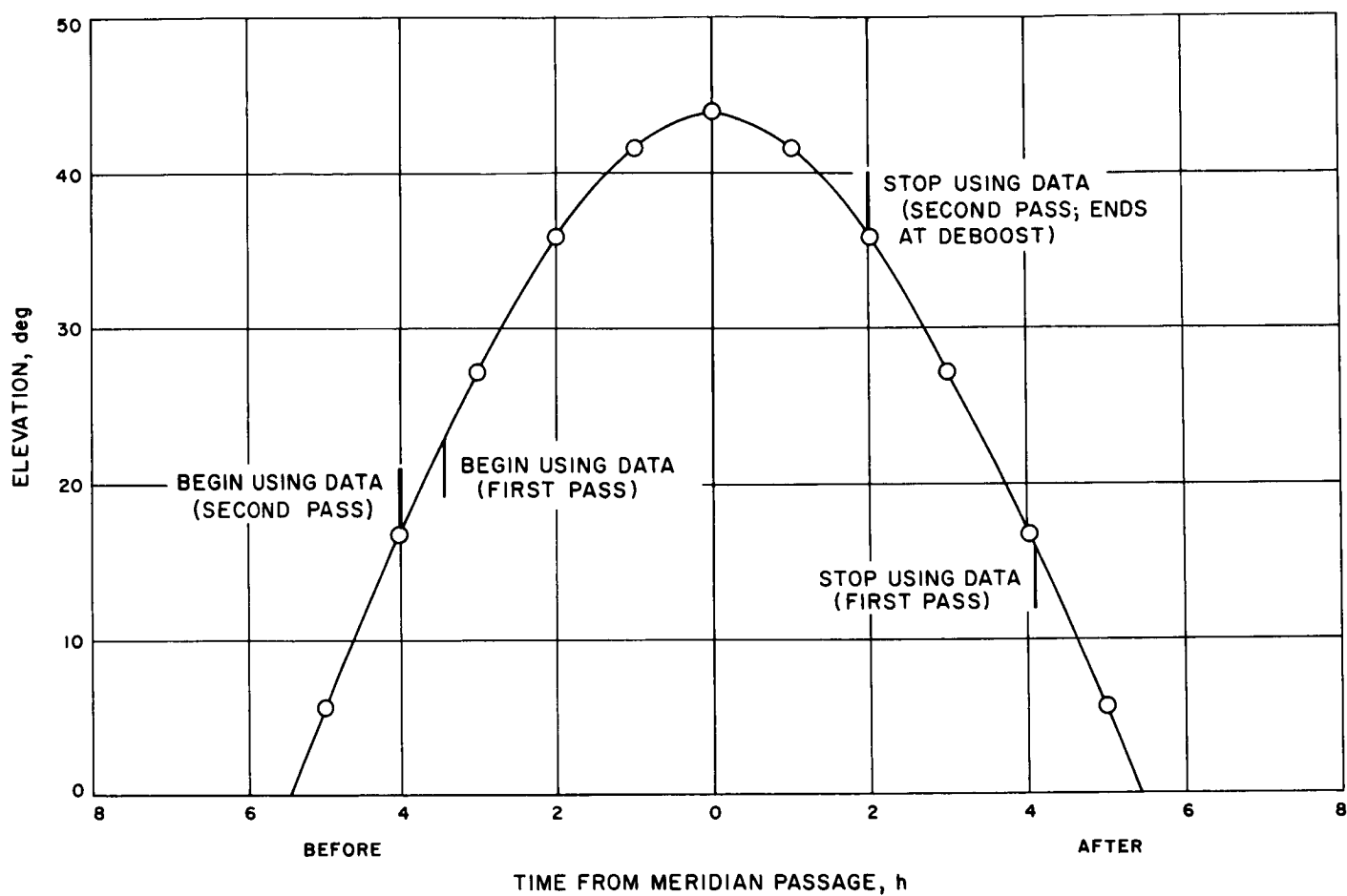


Fig. 53. Elevation probe vs time from meridian passage (Echo DSS)

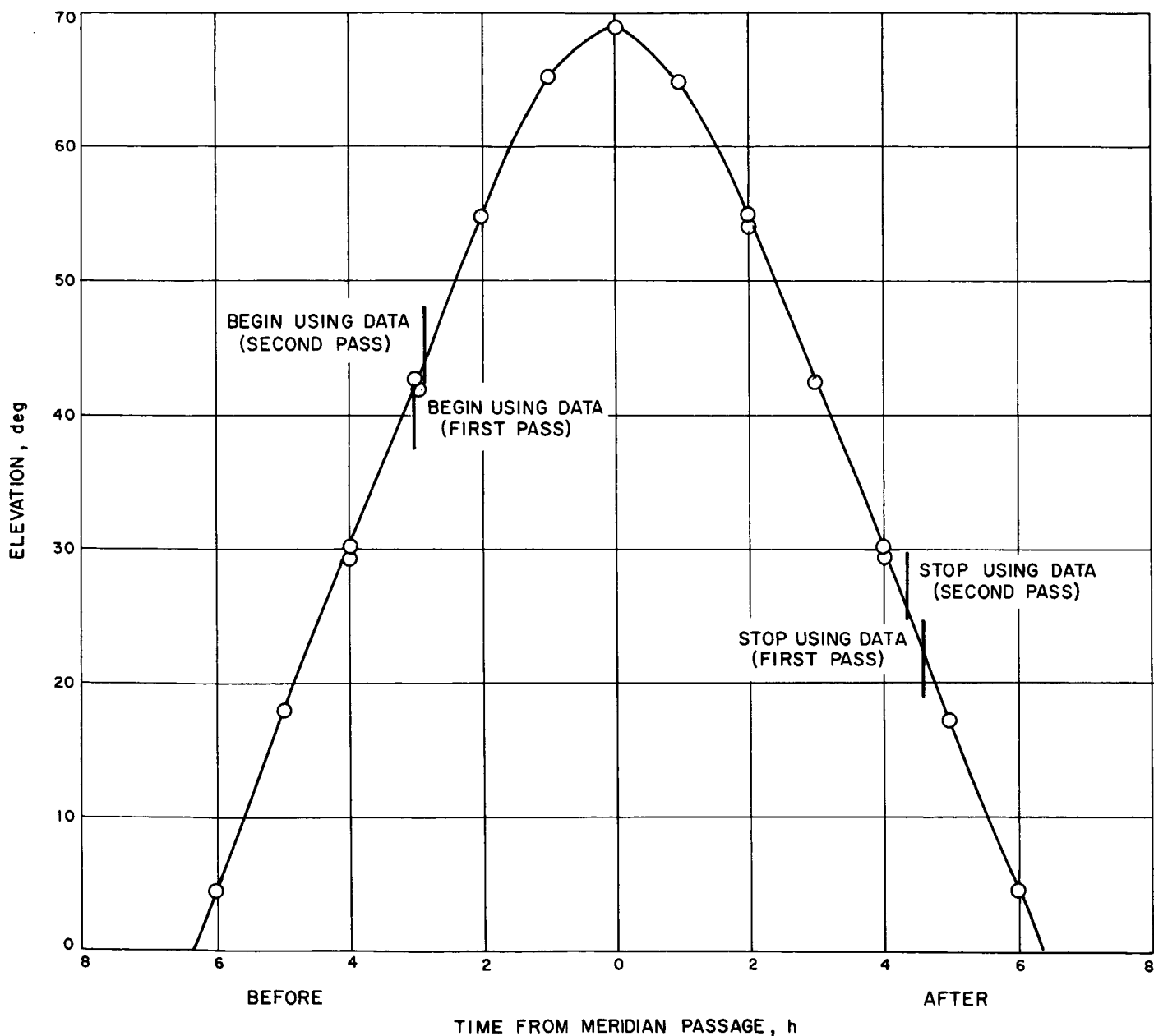


Fig. 54. Elevation of probe vs time from meridian passage (Woomera DSS)

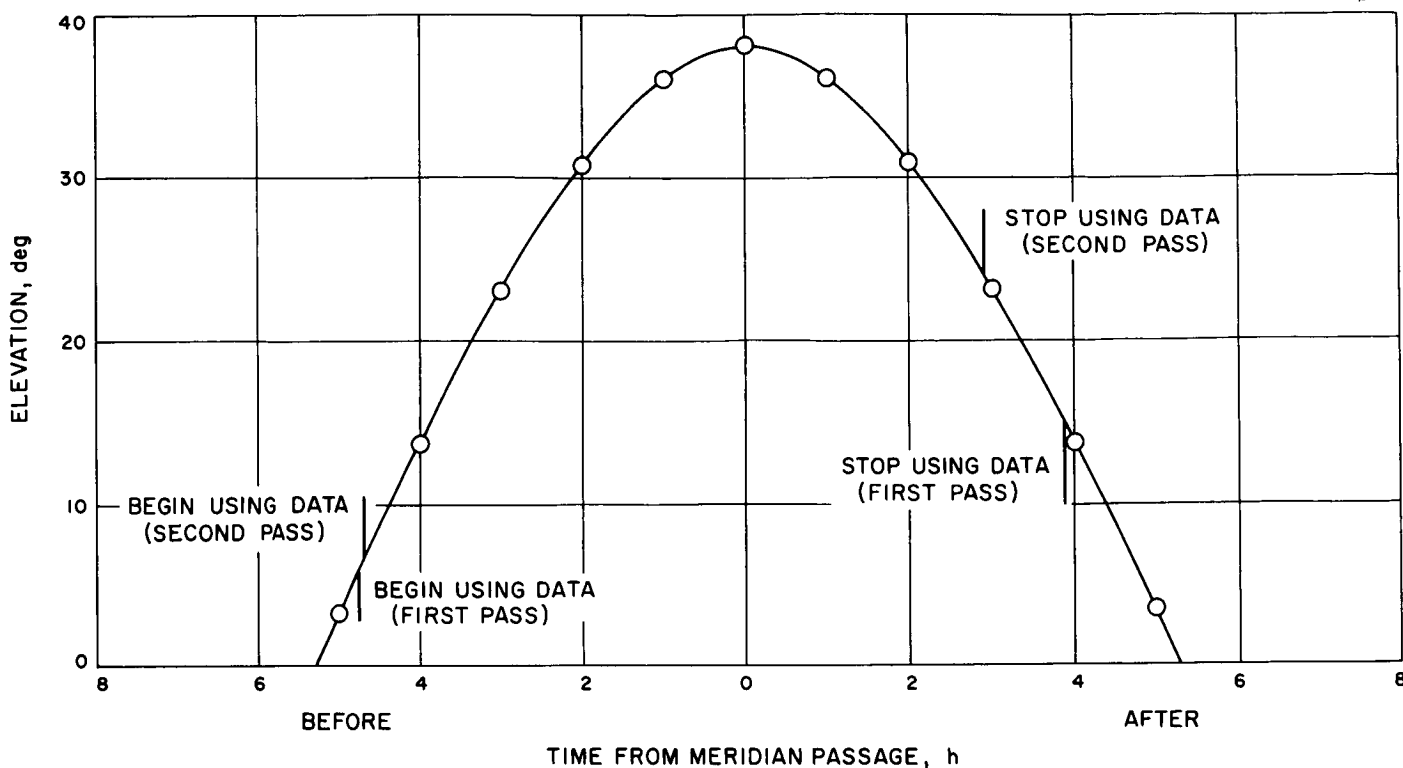


Fig. 55. Elevation of probe vs time from meridian passage (Robledo DSS)

The residuals obtained for *Lunar Orbiter*, using a new model of the troposphere as recommended in Subsection 3, Table 13, also appear in Figs. 50, 51, and 52 and are marked improved troposphere residual. The Robledo DSS shows the largest decrease. Those for the Echo DSS, which were received when the probe was 15 deg above the horizon, also show a noticeable improvement; but due to the higher elevation, the changes are not as great as for the Robledo DSS, even though the changes in the index are greater for the Echo DSS than for the Robledo DSS. The small changes present for the Woomera DSS are on the order of the value of the least significant bit for the single-precision observable computation of the SPODP. The change in the doppler refraction correction due to the change in the index of refraction is also shown.

The changed tropospheric refraction corrections not only result in a better fit to the tracking data, but also affect the solution vector. In line with the simplified model proposed by T. W. Hamilton and W. G. Melbourne (SPS 37-39, Vol. III, pp. 18-23) deep space station location changes are correlated with probe position changes. In particular, the changed tropospheric correction will cause changes in  $b$  and  $c$  (two of the "naturally" determined quantities from a pass of doppler data) as follows:

$$\frac{\Delta b}{\omega_{\oplus}} (\sim \text{m}) = \Delta r_s \cos \delta - r_s \sin \delta \Delta \delta$$

$$\frac{\Delta c}{\omega_{\oplus}} (\sim \text{m}) = [\Delta \alpha - \Delta \lambda] r_s \cos \delta$$

where

$r_s$  = distance between earth's spin axis and the deep space station

$\lambda$  = longitude

$\delta$  = declination of spacecraft, deg

$\alpha$  = right ascension of spacecraft, deg

$\omega_{\oplus}$  = angular rotation rate of earth

However, with this situation in which six passes of data have been reduced together, the  $\Delta b/\omega_{\oplus}$  and  $\Delta c/\omega_{\oplus}$  terms cannot accurately be calculated on a per pass basis. It can be noted, from Fig. 56, which shows the difference in  $\alpha$  and  $\delta$  of the spacecraft as a function of changes induced due to correcting the tropospheric index of refraction, that at deboost the location of the spacecraft was

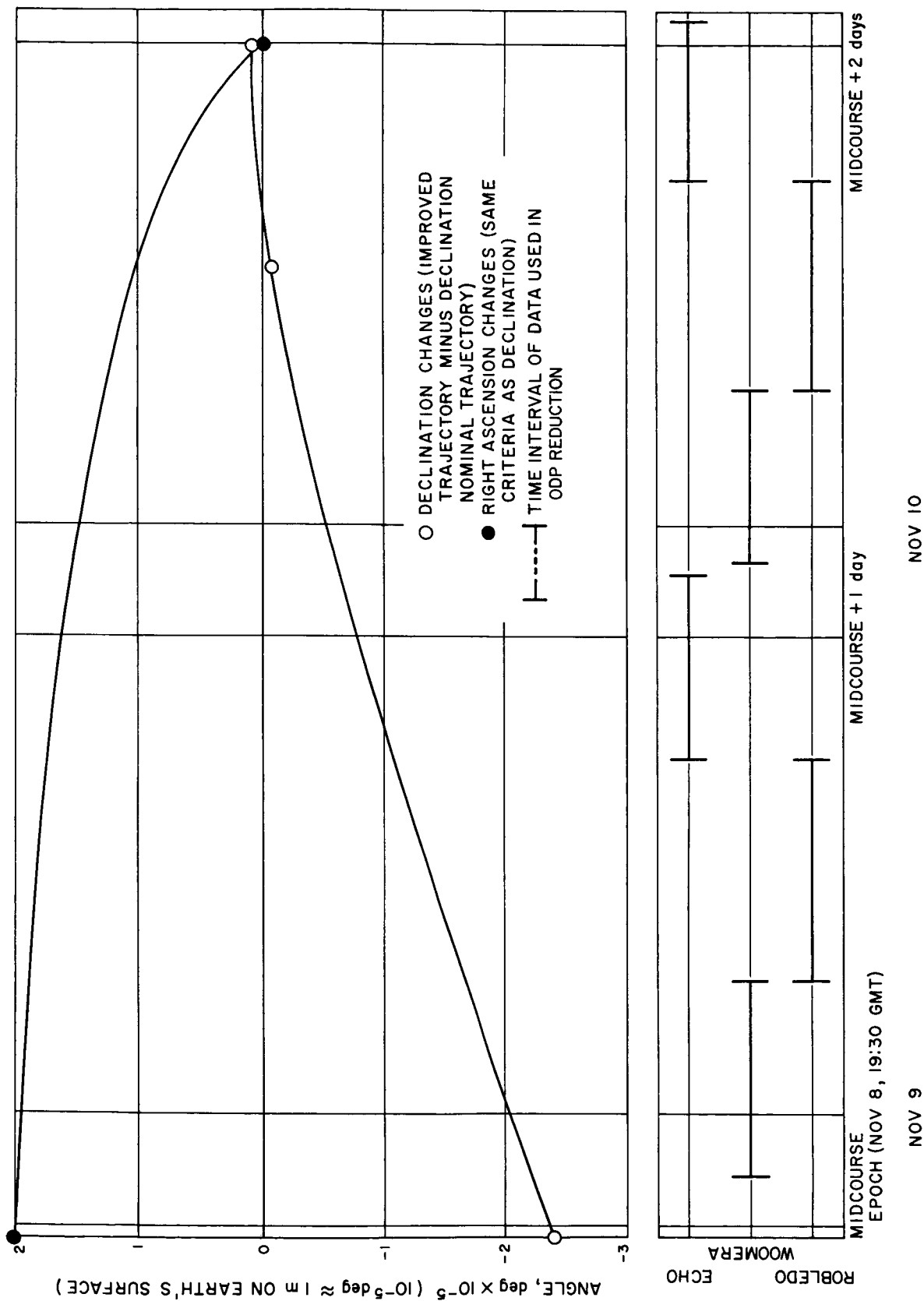


Fig. 56. Changes in  $\alpha$  and  $\delta$  as a function of tropospheric model change

not changed. This would be expected since this is determined by the physical location of the moon, which has not been changed. Were one to assume that  $\Delta b$  and  $\Delta c$  could be calculated for individual passes based upon the final  $\Delta r_s$  and  $\Delta \lambda$  observed for the entire postmidcourse block, the results would indicate that since the declination is small and  $\Delta \delta$  is very small then the  $\Delta b/\omega_\oplus$  terms reflect only the change in  $r_s$  while  $\Delta c/\omega_\oplus$  shows only the change in longitude.

It should also be noted that the  $\Delta r_s$  for the individual deep space station does not correlate with  $\Delta N_0$  (Table 14). This is due to the lower elevation angles during the tracking span at the Robledo DSS than at the Echo DSS and hence the larger correction to the doppler data (Figs. 50-52). This is true even though the doppler data is off-weighted in proportion to the size of the total tropospheric correction. For this analysis, the following empirical weighting scheme was used.

$$\sigma_{\dot{p}_{weight}} = \sigma_{\dot{p}_{(\gamma=0)}} \left\{ 1 + \frac{18}{[1 + \gamma(\text{deg})]^2} \right\}$$

**c. Conclusion.** Improving the relationship between the real universe and its model in the SPODP by changing the indices of refraction to more representative values for the various deep space stations has been reflected in a better fit to the data taken and at the same time has shown significant changes in the solutions for station locations. As was shown, even though the position of the probe is correlated with the station locations, the changes observed show that for this case the greatest effect of this improvement has been on these locations. Studies applying these improvements to other spacecraft analyses will be observed to see what changes occur.

## Reference

1. Warner, M. R., and Nead, M. W., *SPODP-Single Precision Orbit Determination Program*, Technical Memorandum 33-204. Jet Propulsion Laboratory, Pasadena, Calif., Feb. 15, 1965.

## 5. An Algorithm for Integrating Lifetime Orbits in Multirevolution Steps, D. Boggs

**a. Introduction.** In recent years, it has become increasingly important to be able to calculate accurately the long-term evolution of the orbit of an artificial satellite about its central body. As demonstrated by the *Lunar Orbiter* missions, precise long-range predictions of the positions of future orbiters about the planets and the moon will be required. The computation of these predictions is synonymous with the calculation of the "lifetime"

trajectory—the computation of the satellite's path over hundreds and perhaps thousands of orbits.

Standard Cowell-type numerical integration of the equations of motion in Cartesian coordinates is usually unsatisfactory for solving the lifetime trajectory problem for two reasons:

- (1) The accuracy of the numerical solution yielded by classical predictor-corrector difference integration techniques deteriorates rapidly as a function of the number of orbits integrated because of the large number of integration steps required per orbit, even when double-precision arithmetic (IBM 7094 double precision  $\approx 16$  significant decimal digits) is used.
- (2) The computer time necessary to integrate a typical lifetime trajectory is overwhelming—more than one minute per orbit for a typical lunar orbiter case.

These difficulties led several investigators to study special numerical techniques which compute many-orbit trajectories without actually integrating every revolution about the primary. With these methods, the change in the Keplerian orbital elements during one revolution is determined by conventional numerical integration; this secular change in turn serves as the basis for a multirevolution integration step. The multirevolution integration step then advances the orbital elements  $m$  revolutions forward with the result that only one out of every  $m$  orbits is integrated with a standard stepwise integrator. The essential difference in the methods is the manner in which they extrapolate the state elements forward in the  $m$ -revolution jump. In any case, the solution to the system of nonlinear differential equations describing the motion over a long interval of time reduces to a two-stage algorithm: an external integration (or extrapolation) with respect to the argument  $k$  (the number of revolutions) and an internal integration using standard methods to integrate one revolution.

The first approach to the problem, reported by Taratynova in 1958 (Ref. 1), treats the secular change during one orbit as a derivative with respect to revolution number and then numerically integrates with respect to this independent variable. The approximation of the derivative of the elements with respect to revolution number by the increments of these elements over one orbit introduces a systematic error which becomes larger as  $m$  (the number of orbits jumped) decreases. Taratynova later reports (Ref. 2) that greater accuracy was obtained

by using modified Runge- and Adams-type formulas derived (apparently by her) specifically to solve a difference equation of the form  $\Delta \mathbf{a} = f(\mathbf{a}, k)$  instead of the differential equation  $\dot{\mathbf{a}} = f(\mathbf{a}, k)$ . These formulas are each derived individually and are of order four or less. The derivations are quite complex and apparently cannot be systematized, so that formulas of order higher than four probably cannot be found. Thus, the generality of this approach is limited.

In 1960, Mace and Thomas (Ref. 3), in a refinement of the Taratynova method, derived a backward-difference multirevolution predictor formula for extrapolating the state elements  $m$  orbits forward; they applied it to a somewhat simplified example, obtaining encouraging numerical verification. Subsequently, Cohen and Hubbard (Ref. 4) derived an analogous corrector formula and analyzed the accumulation of round-off error, but did not report any computational tests. In all of these efforts, the approach was somewhat specialized for application purposes, e.g., fixed order of integration for the external  $m$ -orbit step, fixed jumping index  $m$  (Mace-Thomas), and no discussion of the computation of the current trajectory time, which is a dependent variable.

This article describes a more generalized, yet programmable, algorithm for calculating long-term orbital trajectories based on an orbit-skipping technique. The existence of the Laboratory's Double-Precision Trajectory Program (DPTRAJ),<sup>7</sup> a generalized trajectory program capable of performing the single-orbit integrations very accurately using a Gauss-Jackson backward-difference method, was a prime motivation for this effort. Clearly, the accuracy of any similar orbit-skipping method depends completely on the accuracy of the internal single-orbit integrator. An important feature of this approach is that it allows the use of a trajectory program, such as DPTRAJ, as a "black box" for computing the quantity  $\Delta \mathbf{a}$ . Thus, any change in the mathematical/physical model incorporated into the trajectory program is automatically incorporated into the lifetime program.

In any orbit-skipping technique, the increments in the orbital elements over one revolution,  $\Delta \mathbf{a}$ , must be sufficiently "smooth" functions of the revolution number  $k$  so that the functions  $f(\mathbf{a}, k) = \Delta \mathbf{a}$  can be adequately represented by polynomials of fixed degree over a substantial range of values of  $k$ . Then, with successive revolutions being closely similar, for example, so that successive peri-

foci are close together, one may probably extrapolate forward somewhere between two and several hundred orbits. This corresponds physically to the assumption that perturbing forces vary smoothly and slowly from orbit to orbit. Thus, an orbit-skipping technique may not adequately account for perturbing forces (such as the gravitational effect of a fast-rotating nonspherical central body) which are not near-periodic with respect to the orbital period of the probe. This, however, appears to be a difficulty to any lifetime trajectory computational method.

Following is the derivation of an all-purpose backward-difference formula and a description of its use as a basis for a multirevolution integration algorithm. The formula is in the "summed" form, i.e., the first sum is used in predicting, correcting, and interpolating. Three modes of performing the multirevolution integration are developed: predict only (P), predict-pseudo correct (P-PC), and predict-correct (P-C). A suitable starting procedure for the integration, which makes use of the orbit-skipping method on a smaller scale, is described. Also derived is a method for calculating the current running trajectory time with accuracy consistent with the computation of the state elements. This calculation is necessary because one does not automatically obtain the trajectory time involved in a multirevolution integration step, since  $m - 1$  orbits are skipped and the orbital period varies. Finally, an interpolation procedure for computing the state elements at an intermediate orbit not calculated during a large integration step is developed.

**b. Derivation of the basic difference formula.** In Fig. 57, the fine grid lines indicate the ending and beginning of successive orbits about the central body. While these grids could represent nearly any reference point on the orbit, it is assumed they correspond to perifocal passage. The distance between the large grid lines corresponds to the multirevolution integration step size; in this case,  $m = 5$ . The term  $\mathbf{a}_{nm}$  is the orbital element state vector

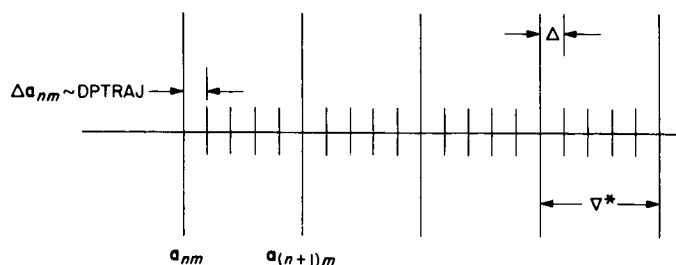


Fig. 57. Schematic of multirevolution integration step

<sup>7</sup>Warner, M. R., et al., *Double Precision Orbit Determination Program*, June 1967 (JPL internal document).

at the  $n$ th large integration step ( $\mathbf{a} = [a_1, a_2, a_3, a_4, a_5, a_6]$ ) and  $\mathbf{a}_{(n+1)m}$  is the state one large step later. Note that the subscript  $nm$  represents the product  $n \cdot m$ ; it is *not* a double subscript. The increment  $\Delta \mathbf{a}$  in the elements over one orbit is defined as the forward difference

$$\Delta \mathbf{a}_{nm} = \mathbf{f}_{nm} \equiv \mathbf{a}_{nm+1} - \mathbf{a}_{nm} \quad (1)$$

It is assumed that this increment is computed by a conventional integration over one revolution at the completion of each  $m$ -revolution step. Thus, it is calculated for the orbit immediately following each large grid.

Define the operators  $E$ ,  $\Delta$ ,  $E^*$ , and  $\nabla^*$  by

$$\left. \begin{aligned} E f_{nm} &= f_{nm+1} \\ \Delta f_{nm} &= f_{nm+1} - f_{nm} = (E - 1) f_{nm} \\ \nabla^* f_{nm} &= f_{nm} - f_{(n-1)m} \\ E^* f_{nm} &= f_{(n+1)m} = (1 - \nabla^*)^{-1} f_{nm} \end{aligned} \right\} \quad (2)$$

Thus, the asterisked operators are defined over the large grid width and the unmarked operators are defined over the fine grid. The two types of operators are connected by the relation

$$E^m = E^* \quad (3)$$

Assume that  $\mathbf{a}_{nm}$ ,  $\Delta \mathbf{a}_{nm}$ , and the increments at large grids preceding the  $nm$  grid are known. Further, assume that from the backward-difference (asterisked) line on

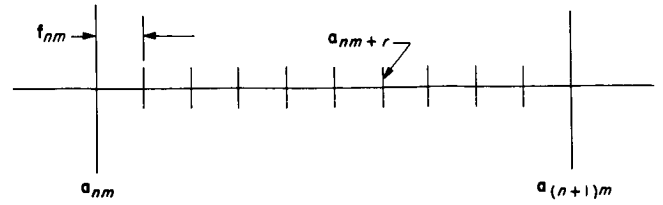


Fig. 58. One multirevolution step with  $m = 10$

these increments one wishes to extrapolate  $r$  orbits forward (Fig. 58) to obtain the state at the  $nm + r$  grid,  $\mathbf{a}_{nm+r}$ , where  $r$  can be any positive or negative integer, or zero. A difference formula which can be used for this calculation is now derived following C. L. Lawson. Since  $\Delta \mathbf{a}_{nm} \equiv \mathbf{f}_{nm}$ , then

$$\begin{aligned} \mathbf{a}_{nm} &= \Delta^{-1} \mathbf{f}_{nm} = (E - 1)^{-1} \mathbf{f}_{nm} = \frac{1}{E^{*1/m} - 1} \mathbf{f}_{nm} \\ &= \frac{1}{(1 - \nabla^*)^{-1/m} - 1} \mathbf{f}_{nm} \end{aligned}$$

so that

$$\begin{aligned} \mathbf{a}_{nm+r} &= E^r \mathbf{a}_{nm} = E^{*r/m} \mathbf{a}_{nm} = (1 - \nabla^*)^{-r/m} \mathbf{a}_{nm} \\ &= \frac{(1 - \nabla^*)^{-r/m}}{(1 - \nabla^*)^{-1/m} - 1} \mathbf{f}_{nm} \end{aligned}$$

By expanding the above equation,

$$\begin{aligned} \mathbf{a}_{nm+r} &= \frac{1 - \left(-\frac{r}{m}\right) \nabla^* + \frac{1}{2} \left(-\frac{r}{m}\right) \left(-\frac{r}{m} - 1\right) \nabla^{*2} - \frac{1}{6} \left(-\frac{r}{m}\right) \left(-\frac{r}{m} - 1\right) \left(-\frac{r}{m} - 2\right) \nabla^{*3} + \dots}{-\left(-\frac{1}{m}\right) \nabla^* + \frac{1}{2} \left(-\frac{1}{m}\right) \left(-\frac{1}{m} - 1\right) \nabla^{*2} - \frac{1}{6} \left(-\frac{1}{m}\right) \left(-\frac{1}{m} - 1\right) \left(-\frac{1}{m} - 2\right) \nabla^{*3} + \dots} \mathbf{f}_{nm} \\ &= \frac{m}{\nabla^*} \frac{1 - \left(-\frac{r}{m}\right) \nabla^* + \frac{1}{2} \left(-\frac{r}{m}\right) \left(-\frac{r}{m} - 1\right) \nabla^{*2} - \dots}{1 - \frac{1}{2} \left(-\frac{1}{m} - 1\right) \nabla^* + \frac{1}{6} \left(-\frac{1}{m} - 1\right) \left(-\frac{1}{m} - 2\right) \nabla^{*2} - \dots} \mathbf{f}_{nm} \\ &= \frac{m}{\nabla^*} \frac{\sum_{s=0}^{\infty} b_s \nabla^{*s}}{\sum_{t=0}^{\infty} c_t \nabla^{*t}} \mathbf{f}_{nm} \quad (4) \end{aligned}$$

where

$$\left. \begin{aligned} b_s &= (-1)^s \binom{-r/m}{s} \\ c_{t-1} &= m(-1)^t \binom{-1/m}{t} \end{aligned} \right\} \quad (5)$$

and where

$$\binom{-r/m}{s} \text{ and } \binom{-1/m}{t}$$

are binomial coefficients.

Now the quotient of two infinite sums of this form (with leading coefficients equal to 1) can easily be computed to be another sum of the same form: thus,

$$\mathbf{a}_{nm+r} = \frac{m}{\nabla^*} \cdot \sum_{s=0}^{\infty} d_s \nabla^{*s} \cdot \mathbf{f}_{nm} \quad (6)$$

where

$$\left. \begin{aligned} d_0 &= 1 \\ d_1 &= b_1 - c_1 \\ d_2 &= b_2 - (c_1 d_1 + c_2) \\ d_3 &= b_3 - (c_1 d_2 + c_2 d_1 + c_3) \\ &\vdots \\ d_s &= b_s - \sum_{\beta=2}^{s+1} c_{\beta-1} d_{s+1-\beta}, \quad s \neq 0 \end{aligned} \right\} \quad (7)$$

Eqs. (5) and (7) yield

$$d_s = (-1)^s \binom{-r/m}{s} - \sum_{\beta=2}^{s+1} (-1)^\beta m \binom{-1/m}{\beta} d_{s+1-\beta} \quad (8)$$

for  $s \neq 0$ . If Eq. (6) is written in the form

$$\mathbf{a}_{nm+r} = \sum_{s=-1}^{\infty} c_s \nabla^{*s} \mathbf{f}_{nm} \quad (9)$$

and coefficients of like powers of  $\nabla^*$  are equated,  $md_{i+1} = e_i$  for  $i = -1, 0, 1, 2, \dots$ . Hence, from Eq. (8)

$$\frac{e_s}{m} = (-1)^{s+1} \binom{-r/m}{s+1} - \sum_{\beta=2}^{s+2} (-1)^\beta m \binom{-1/m}{\beta} \frac{e_{s+1-\beta}}{m}$$

or

$$e_s = (-1)^{s+1} m \binom{-r/m}{s+1} - m \sum_{\beta=2}^{s+2} (-1)^\beta \binom{-1/m}{\beta} e_{s+1-\beta} \quad (10)$$

for  $s \neq -1$  with  $e_{-1} = md_0 = m$ .

Expand the binomial coefficients in Eq. (10) and add the indices  $m$  and  $r$  to the coefficients  $e_s$  to denote functional dependence on these parameters, then the final form becomes

$$e_s^{m,r} = \frac{r(r+m)(r+2m) \cdots (r+sm)}{m^s (s+1)!} - \sum_{\beta=2}^{s+2} \frac{(1+m)(1+2m) \cdots [1+(\beta-1)m]}{m^{\beta-1} \beta!} e_{s+1-\beta}^{m,r} \quad (11)$$

for  $s \neq -1$  with  $e_{-1}^{m,r} = m$ .

Truncate the infinite sum in Eq. (9) at  $s = N$ , and the final difference equation for computing the state  $\mathbf{a}_{nm+r}$ , using the  $N$ th order difference line on the increments  $\mathbf{f}_{nm}$ , is

$$\mathbf{a}_{nm+r} = \sum_{s=-1}^N e_s^{m,r} \nabla^{*s} \cdot \mathbf{f}_{nm} \quad (12)$$

The coefficients in Eq. (12) are calculated by using Eq. (11) for any integral values of the indices  $m$  and  $r$ . The difference operator  $\nabla^{*-1}$  that appears in Eq. (12) is the first sum and is defined by the relation

$$\nabla^{*-1} \mathbf{f}_{nm} = \nabla^{*-1} \mathbf{f}_{(n-1)m} = \nabla^{*0} \mathbf{f}_{nm} = \mathbf{f}_{nm} \quad (13)$$

The predict-only (P) multirevolution integration mode, taken through one complete step, requires the following successive calculations (assuming previous integration up to the  $nm$  grid):

- (1) A Cowell short-step integration (DPTRAJ) over one orbit using  $\mathbf{a}_{nm}$  as initial conditions, resulting in the increment  $\mathbf{f}_{nm} = \mathbf{a}_{nm+1} - \mathbf{a}_{nm}$ .



- (2) Computation of the difference line  
 $\nabla^{*-1} \mathbf{f}_{nm}, \nabla^{*1} \mathbf{f}_{nm}, \nabla^{*2} \mathbf{f}_{nm}, \dots, \nabla^{*N} \mathbf{f}_{nm}.$
- (3) Prediction (extrapolation) forward to obtain the state  $\mathbf{a}_{(n+1)m}$ , using Eq. (12) with  $r = m$ .

The predict-pseudo correct (P-PC) mode requires the following calculations for one multirevolution step:

- (1), (2), (3) Same as above.
- (4) Same as (3) except set  $r = m + 1$  to obtain the predicted value of  $\mathbf{a}_{(n+1)m+1}$ .
- (5) Compute  $\mathbf{f}_{(n+1)m} = \mathbf{a}_{(n+1)m+1} - \mathbf{a}_{(n+1)m}$ .
- (6) Form new difference line at  $(n + 1)m$ :

$$\nabla^{*-1} \mathbf{f}_{(n+1)m}, \nabla^{*1} \mathbf{f}_{(n+1)m}, \dots, \nabla^{*N} \mathbf{f}_{(n+1)m}$$

- (7) Use Eq. (12) with  $r = 0$  to get the corrected state  $\mathbf{a}_{(n+1)m}$ .

Note that in this mode DPTRAJ is used only once per cycle.

A complete cycle in the true predict-correct (P-C) mode requires the following steps:

- (1), (2), (3) Same as (P-PC) mode.
- (4) A DPTRAJ integration over one orbit using  $\mathbf{a}_{(n+1)m}$  as initial conditions.
- (5), (6), (7) Same as (P-PC) mode.

The important difference here is that DPTRAJ is used twice per cycle, once for predicting and once for correcting. For most purposes the (P-PC) mode would probably be used, since most of the computer time per cycle is taken by the DPTRAJ integration. Thus, the (PC) part of the (P-PC) cycle would be a relatively inexpensive bonus over the (P) mode. The (P) and (P-C) modes would probably be used mostly as investigative tools. Every step in each of the integration modes described above has an analogy in conventional predictor-corrector integration as employed by DPTRAJ. For example, the calculation of the increment  $\Delta \mathbf{a}_{nm}$  with DPTRAJ as a function of  $\mathbf{a}_{nm}$  and  $nm$  is analogous to the evaluation of the acceleration vector  $\ddot{\mathbf{r}}$  performed at each integration step by DPTRAJ, as a function of the Cartesian position  $\mathbf{r}$  and the time  $t$ .

**c. Starting procedure.** The  $N$ th order integration procedure just described requires that the increments in the state elements be known at  $N$  large grid points preceding the  $nm$  grid. Thus, a starting procedure is required for advancing the state elements from the given initial

conditions  $\mathbf{a}_0$  through  $Nm + 1$  orbits. From this point an initial difference line can be computed and the normal integration procedure can then continue.

Starting with the initial conditions  $\mathbf{a}_0$  (they are assumed to correspond to the first perifocal passage),  $2N + 1$  consecutive orbits are integrated with DPTRAJ. This is just far enough to allow the computation of the  $N + 1$  increments  $\Delta \mathbf{a}_0, \Delta \mathbf{a}_2, \dots, \Delta \mathbf{a}_{2N}$ , as pictured in Fig. 59. Here, the temporary orbit-skipping index  $m'$  is equal to 2. Now  $2N$  orbits are integrated forward (to grid  $4N + 1$ ), using a multirevolution integration mode described above with  $m = 2$ . Thus, half of these  $2N$  orbits are integrated with DPTRAJ, and half are skipped. This integration is  $N$ th order and is done in the same mode that is to be used in the integration after the starting procedure has finished, i.e., (P), (P-PC), or (P-C). In this way, the starting procedure is commensurate with the ensuing integration. Next, the temporary jumping index is doubled so that  $m' = 4$ . Then, having computed the increments  $\Delta \mathbf{a}_0, \Delta \mathbf{a}_4, \dots, \Delta \mathbf{a}_{4N}$ , the previous cycle is repeated, this time integrating  $4N$  orbits out to grid  $8N + 1$ . Of these  $4N$  orbits,  $N$  have again been integrated directly with DPTRAJ. After further doubling, the starting procedure is complete when the multirevolution integration during a cycle carries the state elements to grid  $Nm + 1$ , where  $m$  is the permanent orbit index for the ensuing integration.

This proposed starting method is a compromise between machine time efficiency, adaptability to programming, and numerical precision. Perhaps a more accurate method for advancing the state  $Nm + 1$  orbits initially would be to integrate them all with DPTRAJ. However, typical parameter values might be  $N = 10$  and  $m = 100$ , in which case 1001 orbits would have to be computed by DPTRAJ just to start the integration. This method of starting would therefore be highly impractical. An important feature of the above starting algorithm is that it

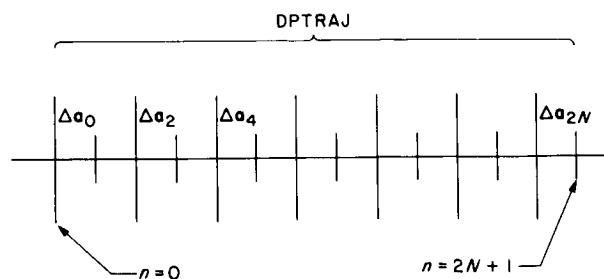


Fig. 59. First cycle in starting procedure  
 $(m' = 2, N = 6)$

requires little programming beyond that already necessary for implementing the overall integration algorithm. Finally, the numerical precision retained by the method is at least as great as that associated with the continuing integration. The number of orbits  $J$  computed by DPTRAJ during this starting process is equal to  $Ns + 1$ , where  $s$  is the smallest integer such that  $2^{s-1} \geq m$ . Thus, for the case  $N = 10$ ,  $m = 100$ , we have  $J = 81$ .

From Eq. (13), it is seen that the first sum is computed at the  $nm$  grid point by  $\nabla^{*-1} \mathbf{f}_{nm} = \mathbf{f}_{nm} + \nabla^{*-1} \mathbf{f}_{(n-1)m}$ . Thus, each first sum is a function of the first sum at the preceding (large) grid. The initial first sum  $\nabla^{*-1} \mathbf{f}_{2N}$  is computed during the starting procedure and is a function of the initial conditions  $\mathbf{a}_0$ . Set  $r = -2N$  in Eq. (12) and obtain

$$\mathbf{a}_0 = \sum_{s=-1}^N e_s^{m, -2N} \nabla^{*s} \mathbf{f}_{2N}$$

Then solve for  $\nabla^{*-1} \mathbf{f}_{2N}$ , using  $e_{-1}^{m, -2N} = m$ :

$$\nabla^{*-1} \mathbf{f}_{2N} = \frac{\mathbf{a}_0}{m} - \frac{1}{m} \sum_{s=0}^N e_s^{m, -2N} \nabla^{*s} \mathbf{f}_{2N} \quad (14)$$

Thus, after the difference line  $\nabla^* \mathbf{f}_{2N}$ ,  $\nabla^{*2} \mathbf{f}_{2N}$ ,  $\dots$ ,  $\nabla^{*N} \mathbf{f}_{2N}$  has been computed at grid  $2N$ , the initial first sum is calculated by Eq. (14).

**d. Trajectory time calculation.** For any practical application of the proposed multirevolution integration algorithm, it is necessary to know the current time  $t$  associated with the state elements at any grid point. Since the orbital period of the perturbed trajectory is not constant and since not every orbit is computed by DPTRAJ, the time, like the orbital elements, must be computed as a function of the independent variable  $k$ , the revolution number. However, because the time increases nearly linearly with  $k$ , it violates the smoothness requirement of the  $\Delta$ 's, and thus cannot be integrated directly as are the elements. The following scheme for the calculation of  $t$  is consistent with the integration of the other dependent variables. Define the variable  $v$  as follows:

$$v_{nm} \equiv t_{nm} - t_0 - nmP_0 \quad (15)$$

where  $t_{nm}$  = time at  $nm$  grid,  $t_0$  = initial epoch time, and  $P_0$  = initial orbital period. Then, from Eq. (15),

$$v_0 = 0$$

$$\Delta v_{nm} = \Delta t_{nm} - P_0 \quad (16)$$

Since the orbital period  $\Delta t_{nm} = t_{nm+1} - t_{nm}$  is a function of the semimajor axis of the orbit,  $\Delta v_{nm}$  is a function that is "smooth" in the same sense as the increments in the orbital elements. Thus, letting the element vector consist of five Kepler elements and  $v, \mathbf{a} = (a, e, i, \Omega, \omega, v)$ , the variable  $v$  is obtained at the required grid points by integrating  $\Delta v$  forward in the same mode used for the increments in the Kepler elements. Apply the operator  $\nabla^*$  to  $v_{(n+1)m}$  and use Eq. (15), then

$$t_{(n+1)m} = t_{nm} + mP_0 + v_{(n+1)m} - v_{nm} \quad (17)$$

The computation of the time over one  $m$ -orbit integration step in the (P) mode then requires the following calculations (assuming previous integration up to grid  $nm$  so that  $v_{nm}$  and  $t_{nm}$  are known):

- (1) Integrate one orbit with DPTRAJ, using  $a_{nm}$ ,  $e_{nm}$ ,  $i_{nm}$ ,  $\Omega_{nm}$ ,  $\omega_{nm}$ , and  $t_{nm}$  as initial conditions, resulting in the increment  $\Delta t_{nm} = t_{nm+1} - t_{nm}$  (time is the independent variable for DPTRAJ).
- (2) Compute  $\Delta v_{nm}$ , using Eq. (16).
- (3) Compute the difference line on  $\Delta v_{nm}$ .
- (4) Predict forward using (P) mode integration to obtain  $v_{(n+1)m}$ , using Eq. (12) with  $r = m$ .
- (5) Calculate  $t_{(n+1)m}$  by Eq. (17).

Similar time calculation algorithms are easily developed for the (P-PC) and (P-C) integration modes.

**e. Interpolation.** The utility of the multi-orbit integration procedure would be enhanced by the capability for computing the state vector at grid points intermediate to the large grids. This clearly implies an interpolative procedure, since integration up to these intermediate grids would negate the efficiency of the orbit-skipping algorithm. The following scheme makes use of existing computational machinery [Eqs. (11) and (12)] and yields an  $N$ th order interpolation—the same order as used by the integration. Assume that the integration has been completed up to the  $nm$  grid and that the state is required at grid  $nm - p$ , where  $p$  is an integer in the range  $1 \leq p < m$ . Setting  $r = -p$  in Eq. (12) immediately yields the state elements  $\mathbf{a}_{nm-p}$  as a function of the difference line at the  $nm$  grid. The associated time  $t_{nm-p}$  must then be calculated from  $v_{nm-p}$ ; another application of Eq. (15) yields the needed relationship:

$$t_{nm-p} = t_{nm} - pP_0 + v_{nm-p} - v_{nm}$$

It is clear that this (or any) interpolation is *not* valid for computing the state at points between the fine grids by allowing  $p$  to be a non-integer number: the functions  $f_{nm} = \Delta a_{nm}$  are not defined between fine grid points. To compute the state at such intermediate times, DPTRAJ would have to integrate to these times from the nearest preceding fine grid point (perhaps after an interpolation to this point).

**f. Conclusion.** This multirevolution integration algorithm appears to be worthy of numerical investigation. User flexibility would allow experimentation with the accuracy-dependent variables  $m$ , integration order  $N$ , and integration mode, for various types of orbits. Hopefully, an interrelationship between these variables could be found. To this end, an IBM 7094 double-precision program based on this algorithm and using DPTRAJ as the "inner" integrator is currently being developed.

### References

1. Taratynova, G. P., "The Motion of an Artificial Satellite," *The Russian Literature of Satellites, Part I*, pp. 71-85. International Physical Index, Inc., New York, 1958.
2. Taratynova, G. P., "Methods for the Numerical Solution of Finite Difference Equations and Their Application to Computations of Satellite Orbits," *Artificial Earth Satellites, Vol. 3-4-5*, pp. 254-287. Edited by L. V. Kurnosova. Plenum Press, New York, 1961 (JPL Library No. 629.13882, k, Vol. 3-4-5).
3. Mace, D., and Thomas, L. H., "An Extrapolation Formula for Stepping the Calculation of the Orbit of an Artificial Satellite Several Revolutions Ahead at a Time," *Astron. J.*, Vol. 65, No. 5, pp. 300-303, June 1960.
4. Cohen, C. J., and Hubbard, E. C., "An Algorithm Applicable to Numerical Integration of Orbits in Multirevolution Steps," *Astron. J.*, Vol. 65, No. 8, pp. 454-456, Oct. 1960.

### 6. Preliminary Surveyor VI Postlanded Tracking Data Analysis, F. B. Winn

**a. Introduction.** This article describes the postlunar-touchdown *Surveyor VI* tracking data acquired by the DSIF and the utilization of that data to determine the selenocentric location of the probe and the geocentric locations of the DSSs, used in the tracking operations. The discussion relating to data utilization encompasses the application of data rejection techniques and the relative weighting of observables and parameters.

The lunar ephemerides employed in the data reduction are identified, and the associated influences of each ephemeris on the solution are discussed.

The parameter solutions are presented in tabular form with the formal standard deviation specified. The probe's position as determined from *Lunar Orbiter IV* photographs and the cruise data reduction are presented for comparison. The terrestrial tracking positions as calculated from land surveys, *Ranger* spacecraft, and *Mariner* spacecraft are presented in the company of the *Surveyor VI* reductions for comparison.

**b. Tracking data acquisition.** To maximize the effectiveness of the tracking data sample which could be acquired, the following data acquisition policy was requested:

- (1) All tracking data collection periods should be a minimum of 30 min.
- (2) Tracking data collected during the course of one lunar day are to be equally distributed throughout the mean lunar pass as opposed to being collected at the same points or portions during each pass.

An extensive effort was made to create these data characteristics, and the resultant coverage is shown in Fig. 60. Due to the desire to conduct video-oriented research over the Pioneer DSS (Goldstone, California), the Tidbinbilla DSS (Canberra, Australia) and the Robledo DSS (Madrid, Spain) frequently transferred spacecraft control over to the Pioneer DSS as soon as it became possible. The lunar rise of the Tidbinbilla DSS and the lunar set of the Robledo DSS, as a consequence, were infrequently observed. Obligation to video activities precluded the Pioneer DSS from taking tracking data to the extent that the Tidbinbilla DSS and the Robledo DSS did, even though the latter two stations had their view periods truncated.

**c. Tracking data validity and weighting.** The data acquisition procedures and the associated influences on the solutions are reflected in the weighting techniques. The tracking data (coherent two-way doppler) as acquired contained some blunder points, systematic bias, and trends. The detection of these characteristics was accomplished by using the raw data in the single-precision orbit determination program (SPODP, Ref. 1) to perform a recursive least-squares fit and by inspecting the "observed minus computed" ( $O - C$ ) residuals. These initial residual sets adequately demonstrate any pronounced irregularities in the data sample (Figs. 61-63).

The most outstanding data feature revealed in the raw data residual sets was a consistent bias of the Robledo

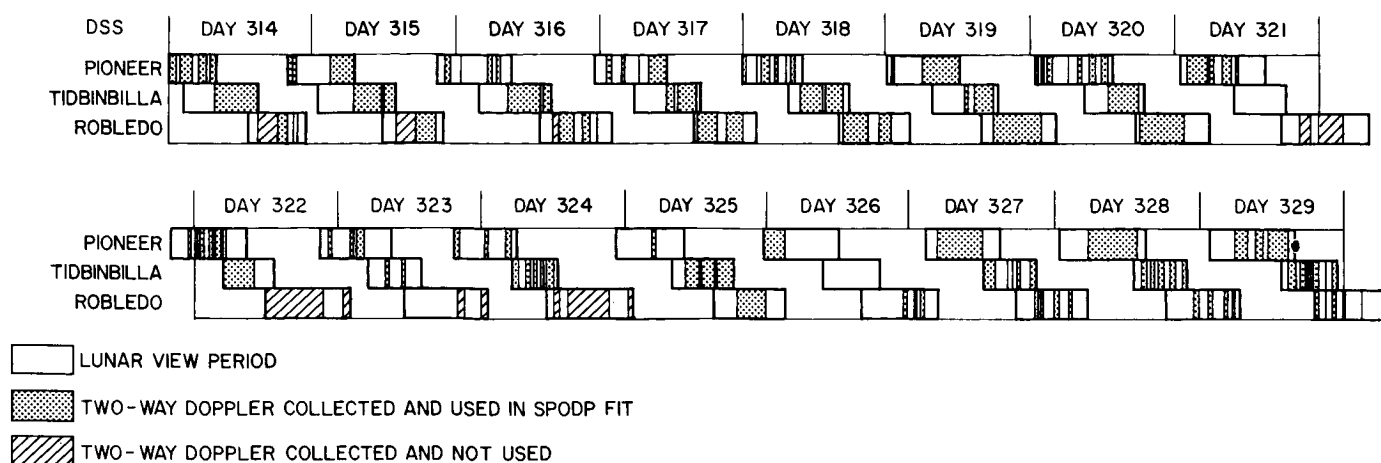


Fig. 60. Tracking data acquisition times

DSS tracking data on four consecutive days. The Robledo DSS data on days 322 to 325 exhibited a bias of approximately 2 mm/s (0.03 Hz). The 1291 data points collected by the Robledo DSS during this period were removed from the solution. This data condition is unique to the Robledo DSS. In order to inspect the finer noise characteristics of the bias passes and compare them to the unbiased passes, the solution was executed without the biased data, and then, using a better resolution on the abscissa scale, the O - C residuals were plotted for all data points—the unbiased and biased data. No difference in the noise spectrum is apparent (Fig. 64). At this time, the bias cause is unknown.

Another data feature associated with the Robledo DSS was a series of blunder points resulting from improper incrementing of the least-significant digits of the doppler cycle counter. Examination of Fig. 63 shows such an occurrence on days 315, 316, and 325. These points were deleted from the fit.

Another type of blunder point, normally resulting from teletype communication line noise or other hardware sporadic noise sources, was experienced by all stations. Four such points are pictured on the Tidbinbilla DSS raw data residual plot (Fig. 62). The preponderance of these blunder points does not fall within the bounds of the residual plots represented in Figs. 61, 62, and 63 because the rejection sigma assigned to all coherent two-way doppler data points is 0.1 Hz (6.6 mm/s).

The tracking data were acquired at the rate of 1 data point/min. To facilitate computer processing and to reduce the data's associated high frequency noise, the surviving valid data is compressed into 5-min normalized

data points. One normalized point is comprised of 5 consecutive sample time (1/min) points. If a sample point is missing or deleted from the point-per-minute sequence, the compression point under construction is abandoned and a new compression point is initialized. It is this compression process that resulted in a Pioneer DSS data point loss of 14.5%. This data loss was recovered in a subsequent data reduction (mentioned earlier in connection with the Robledo DSS biased data analysis) in which the data sample input to the SPODP was comprised of 1 data point/min.

The number and percentage of data points which had the described traits and were utilized are depicted in the data usage summary table (Table 15).

In the noncompressed data reduction, each data point is assigned a standard deviation of 0.33 mm/s (0.05 Hz). The assignment of this weight reflects model limitations and "known" data noise. The compressed data point weight is

$$\sigma_{\text{compressed point}} = \frac{\sigma_{\text{individual point}}}{(\text{number of points per normal point})^{1/2}}$$

**d. A priori parameter constraints.** It is possible to constrain the terrestrial tracking station position parameters in the SPODP tracking data reduction to those of some previous determination. However, such a constrained solution can lead to systematic distortion. There are many time-dependent variables incorporated in the theoretical model, e.g., E. W. Brown's lunar theory, lunar librations, terrestrial diurnal rotation, ionosphere, space plasma effects, etc. There is a series of models used to provide values for some of these time-dependent parameters, and

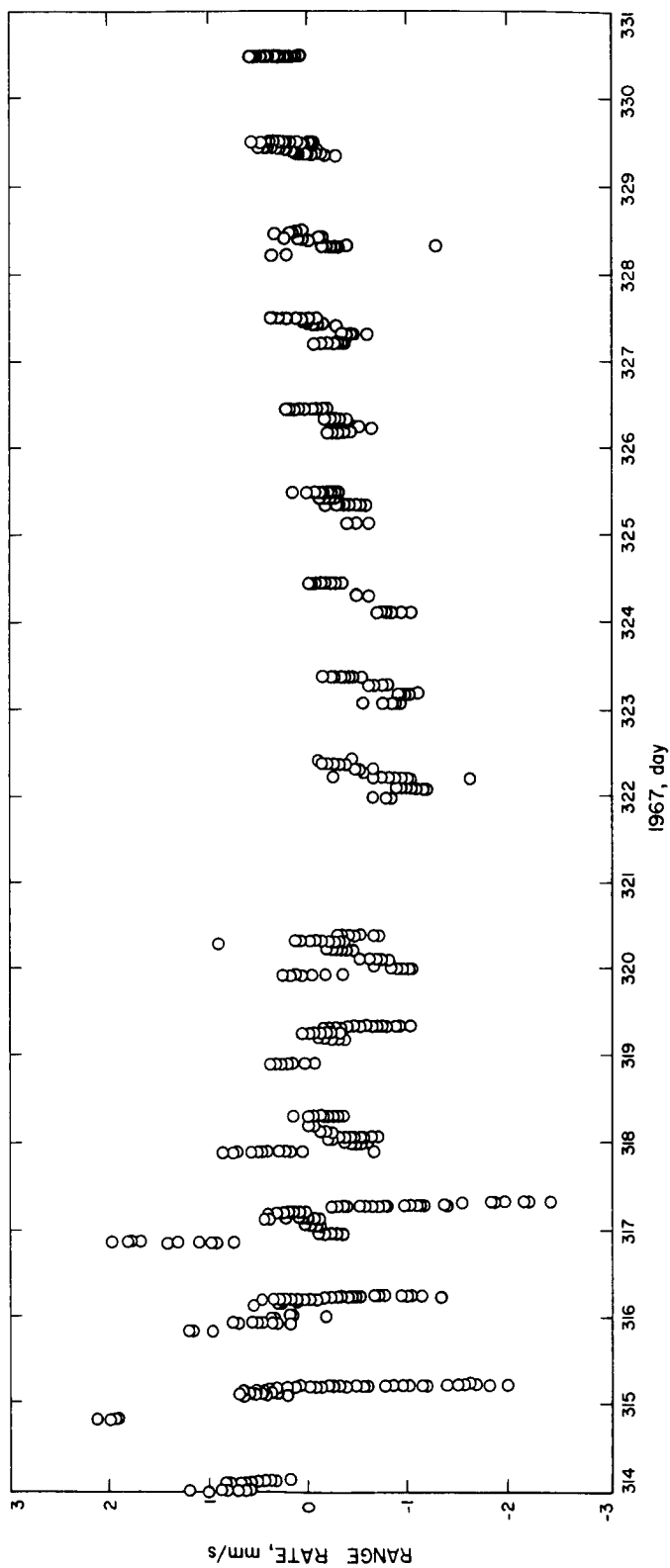


Fig. 61. Pioneer DSS O — C raw data residual set (Surveyor VI, first lunar day, DE 29/LE 5, one data point/min)

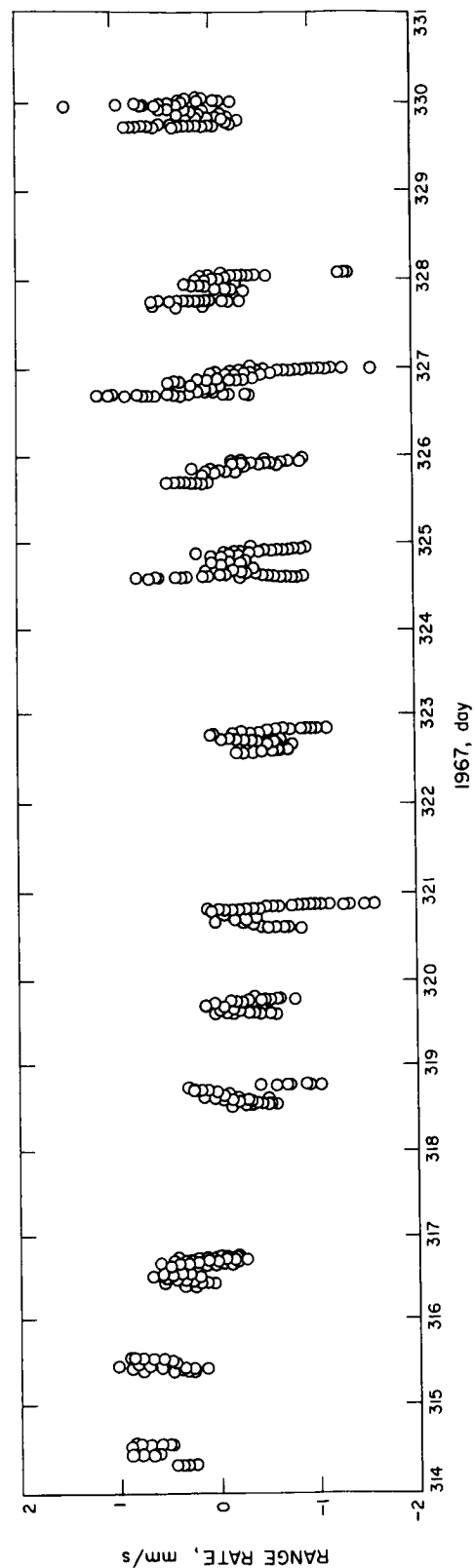


Fig. 62. Tidbinbilla DSS O — C raw data residual set (Surveyor VI, first lunar day, DE 29/LE 5, one data point/min)

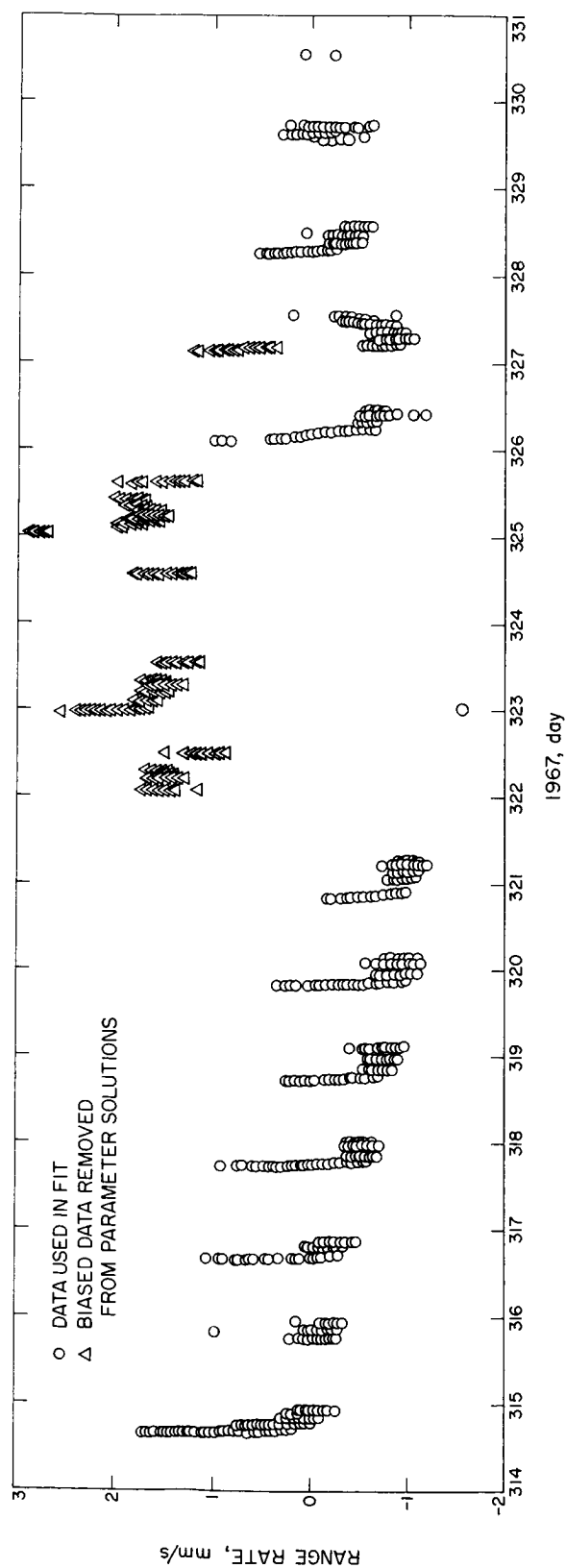


Fig. 63. Robledo DSS O - C raw data residual set (Surveyor VI, first lunar day, DE 29/LE 5, one data point/min)

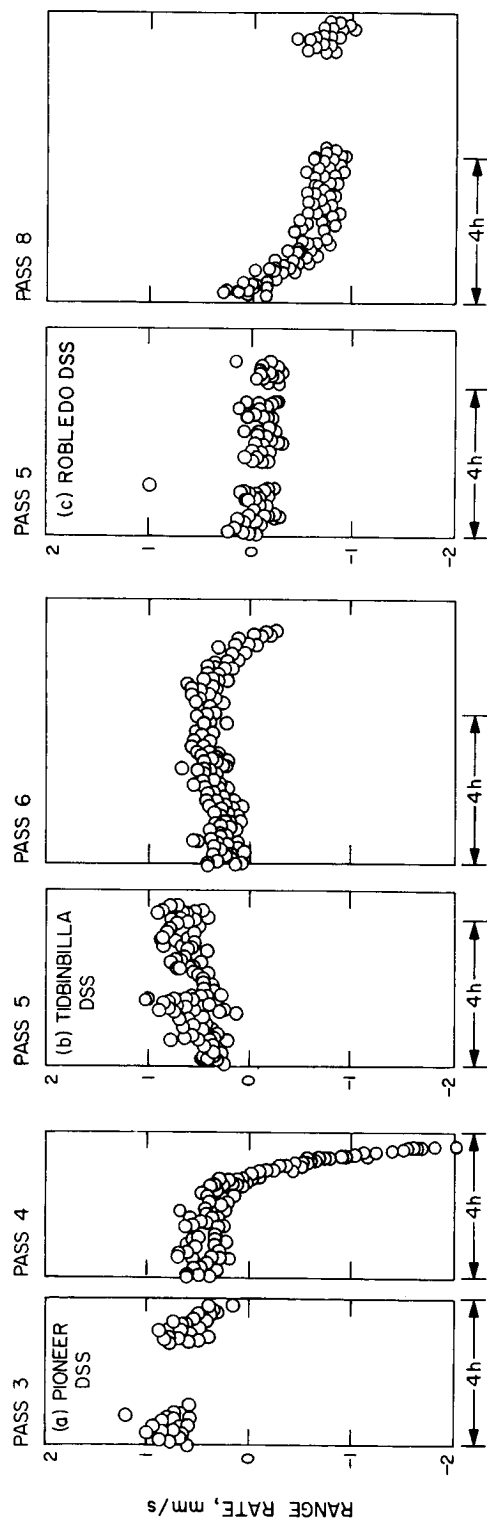


Fig. 64. DSS tracking passes of unbiased and biased data: (a) Pioneer DSS, (b) Tidbinilla DSS, (c) Robledo DSS

**Table 15. Surveyor VI postlanded data utilization summary (coherent 2-way doppler data, 1-min data points)**

DSS	Data points received		Data points used		Biased data points		Blunder data points		Data points lost in compression	
	Number	%	Number	%	Number	%	Number	%	Number	%
Pioneer	1863	100	1585	85.1	0	0	8	0.4	270	14.5
Tidbinbilla	2962	100	2675	90.3	0	0	26	0.9	261	8.8
Robledo	4413	100	2835	64.2	1291	29.3	84	1.9	203	4.6
Total	9238	100	7095	76.8	1291	14	118	1.3	734	7.9

some are not modeled at all. Thus, there is always the danger of introducing systematic errors into a tracking data fit by constraining to the previous determined terrestrial tracking station positions in accordance with the associated variance/covariance matrix. It was with this perspective that the entire parameter list is assigned *a priori* standard deviations which in effect unconstrain the parameters. The parameter *a priori* standard deviations are:

- (1) Surveyor VI selenocentric distance: 10 km
- (2) Surveyor VI selenocentric latitude: 5.0 deg (150 km)
- (3) Surveyor VI selenocentric longitude: 5.0 deg (150 km)
- (4) Pioneer DSS geocentric distance: 300 m
- (5) Pioneer DSS geocentric longitude: 0.005 deg (0.5 km)
- (6) Tidbinbilla DSS geocentric distance: 300 m
- (7) Tidbinbilla DSS geocentric longitude: 0.005 deg (0.5 km)
- (8) Robledo DSS geocentric distance: 300 m
- (9) Robledo DSS geocentric longitude: 0.005 deg (0.5 km)

The initial estimate of Surveyor VI's location was derived from the cruise tracking data reduction corrected for thruster braking which occurred during Surveyor VI's lunar descent (Table 16 and Ref. 2).

Station locations were those ascertained from Mariner IV data reduction (Table 17 and SPS 37-48, Vol. II, pp. 12-22).

**e. Lunar ephemerides.** Two lunar ephemerides are used: (1) Lunar Ephemeris 4 (LE 4), which was coupled with the JPL planetary ephemeris to produce Develop-

mental Ephemeris 19 (DE 19) and is currently being distributed by JPL to all NASA project ephemeris users (Refs. 3 and 4); and (2) Lunar Ephemeris 5 (LE 5), which was coupled with the JPL planetary ephemeris to create Developmental Ephemeris (DE 29) and is an extensive refinement of LE 4 (SPS 37-48, Vol. III, pp. 33-38).

LE 4 can be regarded as the modern-evolved Brown lunar theory. LE 4 has recently been discovered to have radial components of position and velocity which deviate from observations (SPS 37-48, Vol. II, pp. 4-12).

LE 5 is a numerical integration of the equations of motion which uses LE 4 positions as input observables (SPS 37-48, Vol. III, pp. 33-38). Essentially, this amounts to a smoothed LE 4, which is gravitationally consistent.

**f. Parameter solution vectors.** Three Surveyor VI postlanded data reductions are presented. Two of the solutions employ compressed 5-min data points and a third fit uses scrubbed noncompressed (1 point/min) data. DE 19/LE 4 is used in one of the compressed data fits; DE 29/LE 5 is used in the other two solutions.

Surveyor VI position parameters and DSS locations as determined by the three solutions are presented in Table 16 with formal standard deviations specified.

The Surveyor VI position error ellipsoids derived from the LE 5 and LE 4 employments, coupled with identical normalized data samples, have the same respective dimensions. There is a large relative displacement of the error ellipsoid centers, which is attributed to the different ephemerides used. The selenocentric components of the relative displacement are:

- 8000 m, radially
- 550 m, lunar latitude
- 1800 m, lunar longitude

Table 16. Parameter solutions

Parameters <sup>a</sup>	A priori		Compressed data			Noncompressed data	
	Parameter estimates	$\sigma$	DE 19/LE 4 parameter solution	$\sigma$	DE 29/LE 5 parameter solution	DE 29/LE 5 parameter solution	$\sigma$
RADS, km	1736.0	10.0	1744.027	0.894	1736.439	1736.528	0.840
LATS, deg	0.437	5.0	0.474	0.007	0.459	0.460	0.006
LONS, deg	358.630	5.0	358.65102	0.019	358.63229	358.62941	0.018
Pioneer DSS <sup>b</sup>							
$r_s$ , km	5206.333	0.24	5206.332	0.002	5206.332	5206.332	0.002
LO, deg	243.15070	0.005	243.15079	0.001	243.15081	243.105082	0.001
Tidbinbilla DSS <sup>b</sup>							
$r_s$ , km	5205.348	0.24	5205.342	0.002	5205.342	5205.342	0.002
LO, deg	148.98140	0.005	148.98153	0.001	148.98156	148.98157	0.001
Robledo DSS <sup>b</sup>							
$r_s$ , km	4862.601	0.23	4862.606	0.002	4862.606	4862.606	0.001
LO, deg	355.75114	0.005	355.75126	0.001	355.75126	355.75128	0.001

<sup>a</sup>RADS = selenocentric distance of Surveyor VI.  
LATS = selenocentric latitude of Surveyor VI.  
LONS = selenocentric longitude of Surveyor VI.  
 $r_s$  = spin axis distance of DSS.  
LO = geocentric longitude of DSS.

<sup>b</sup>Terrestrial tracking station location reference to 1903.0 pole.

Table 17. Summary of deep space station locations

DSS	Source	Spin axis distance $r_s$ , m	Longitude $\lambda$ , deg	DSS	Source	Spin axis distance $r_s$ , m	Longitude $\lambda$ , deg
Pioneer	Surveyor I	5206.3276	243.15085	Tidbinbilla (contd)	Surveyor VI (DE 29/LE 5)	.3395	.98157
	Surveyor III	—	—		Combined Ranger position of Echo DSS corrected to Tidbinbilla DSS by Mariner IV delta values	.3403	.98157
	Surveyor V	.2670	.15114		Goddard survey	.2940	.98006
	Surveyor VI (DE 19/LE 4)	.3317	.15081	Robledo	Surveyor I	—	—
	Surveyor VI (DE 29/LE 5)	.3315	.15083		Surveyor III	4862.5993	355.75101
	Combined Ranger position of Echo DSS corrected to Pioneer DSS by land survey	.3266	.15089		Surveyor V	.5992	.75149
	Combined Ranger position of Echo DSS corrected to Pioneer DSS by Mariner IV delta values	.3725	.15090		Surveyor VI (DE 19/LE 4)	.6031	.75120
	Goddard survey	.3718	.15094		Surveyor VI (DE 29/LE 5)	.6045	.75120
					Combined Ranger position of Echo DSS corrected to Robledo DSS by Mariner IV delta values	.6077	.75122
Tidbinbilla	Surveyor I	5205.3474	148.98130		JPL land survey	.6482	.75182
	Surveyor III	.3581	.98127				
	Surveyor V	.3553	.98175				
	Surveyor VI (DE 19/LE 4)	.3423	.98147				



LE 4 and LE 5, coupled with identical data samples, were used to reduce *Surveyor I* postlanded tracking data. A similar relative displacement of the two *Surveyor I* positions resulted (SPS 37-48, Vol. II, pp. 4-7).

The two LE 5 fits, one using noncompressed data (1 point/min) and the other solutions using compressed data (5 min/point), also produced different probe loca-

tions. However, this small relative displacement reflects data and computer noise and is quite acceptable since it is well within the confidence levels specified. The separation of the two *Surveyor VI* position determinations is:

- 1 m, radially
- 30 m, lunar latitude
- 90 m, lunar longitude

**Table 18. Summary of Surveyor VI location determinations**

Source	Seleno-centric latitude $\Phi$ , deg N	$\sigma_{\Phi}$	Seleno-centric longitude $\lambda$ , deg	$\sigma_{\lambda}$	Lunar radius $R$ , m	$\sigma_R$
1 <sup>a</sup>	0.49	—	358.60	—	—	—
2 <sup>b</sup>	0.437	0.065	358.630	0.006	—	—
3 <sup>c</sup>	0.474	0.007	358.651	0.019	1744.04	0.89
4 <sup>d</sup>	0.459	0.007	358.632	0.019	1736.44	0.89
5 <sup>e</sup>	0.460	0.006	358.629	0.018	1741.468	0.84

<sup>a</sup> Derived from comparison of Lunar Orbiter IV photograph with Surveyor VI lunar sight and the Orthographic Atlas (E. A. Whitaker, Lunar and Planetary Laboratory, University of Arizona).

<sup>b</sup> Terminal cruise SPODP position (cruise data; Ref. 2).

<sup>c</sup> SPODP data reduction, using DE 19/LE 4 (compressed postlanded Surveyor data).

<sup>d</sup> SPODP data reduction, using DE 29/LE 5 (compressed postlanded Surveyor data).

<sup>e</sup> SPODP data reduction, using DE 29/LE 5 (noncompressed postlanded Surveyor data).

The relative displacements of the *Surveyor VI* selenocentric position error ellipses are graphically pictured in Fig. 65.

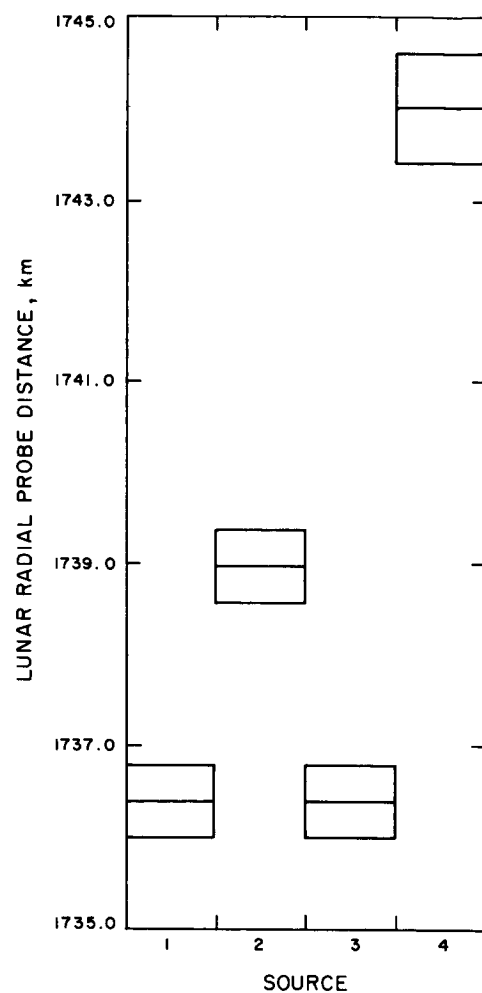
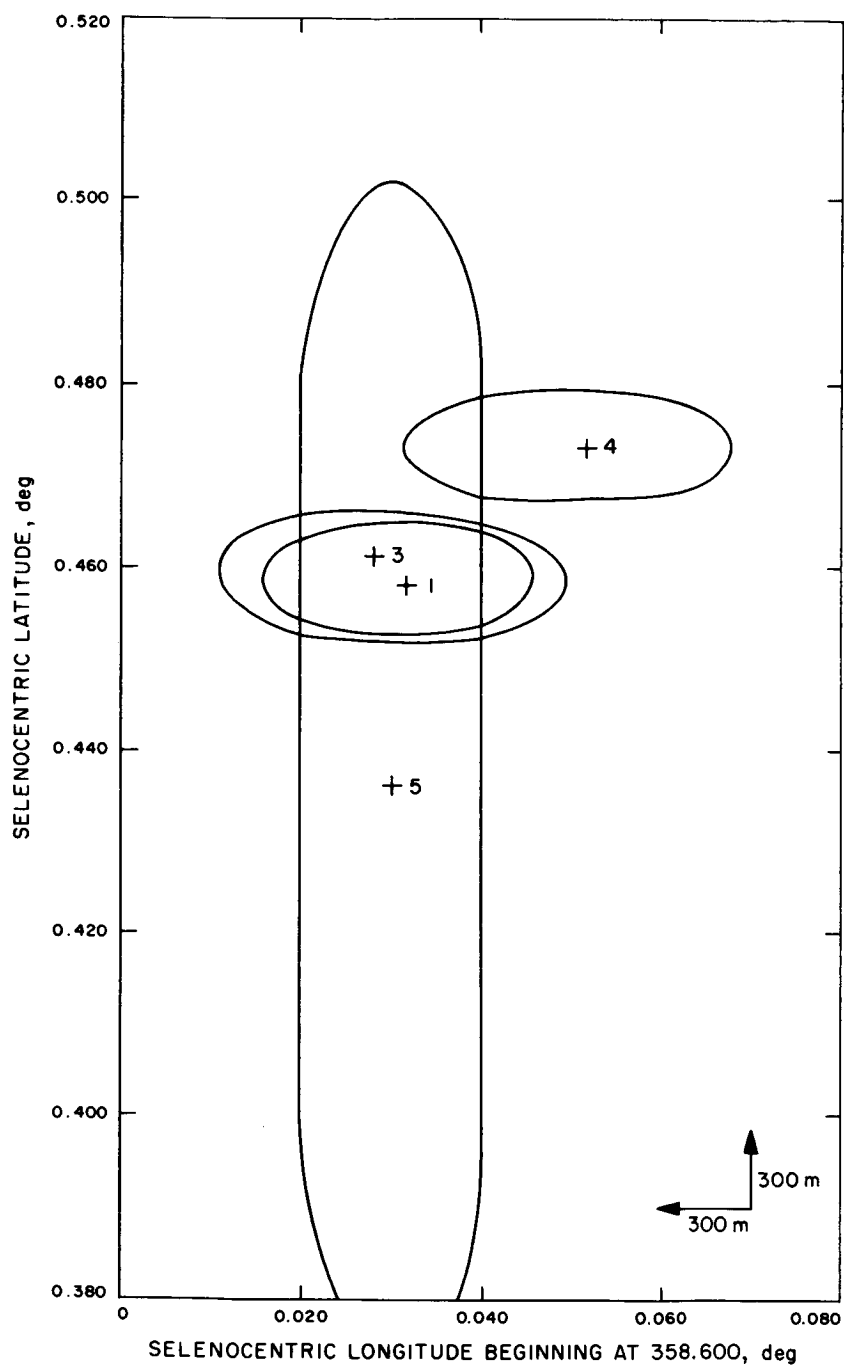
The *Surveyor VI* position solutions, which were obtained from *Lunar Orbiter IV* photographs and from *Surveyor VI* cruise data fit, are tabulated in Table 18.

The statistical dependence of one parameter in relation to other parameters within a recursive least-squares fit can be inferred from the correlations of the parameter in question and the remaining parameter list. The small magnitudes of the parameter correlations in the correlation matrices (Table 19) indicate the relative statistical independence of the parameters. A model weakness to be noted is the high correlation exhibited between all selenocentric and geocentric longitude determinations. The resolution of all parameters was essentially comparable in each of the solutions.

**Table 19. Correlation matrix (DE 29/LE 5, compressed data fit)**

Parameter <sup>a</sup>	$\sigma$	Surveyor VI			Pioneer DSS		Tidbinbilla DSS		Robledo DSS	
		RADS	LATS	LONS	RI	LO	RI	LO	RI	LO
RADS	0.894	1.0	0.795	-0.698	0.322	0.698	0.392	0.691	0.047	0.705
LATS	0.007		1.0	-0.817	0.270	0.793	0.347	0.796	0.101	0.793
LONS	0.019			1.0	-0.358	-0.981	-0.396	-0.991	0.131	-0.988
Pioneer DSS										
RI	0.002				1.0	0.308	0.164	0.357	-0.061	0.360
LO	0.001					1.0	0.393	0.973	-0.135	0.971
Tidbinbilla DSS										
RI	0.002						1.0	0.352	-0.038	0.397
LO	0.001							1.0		
Robledo DSS										
RI	0.002								1.0	-0.092
LO	0.001									1.0

<sup>a</sup> RADS = selenocentric distance from Surveyor VI.  
LATS = selenocentric latitude of Surveyor VI.  
LONS = selenocentric longitude of Surveyor VI.  
RI = geocentric distance of DSS.  
LO = geocentric longitude of DSS.



#### SOURCE

- 1 SPODP DATA REDUCTION (DE 29/LE 5, NORMALIZED 5-min DATA POINTS)
- 2 AERONAUTICAL CHARTS AND INSTRUMENTS CENTER (ACIC) LUNAR CHARTS
- 3 SPODP DATA REDUCTION (DE 29/LE 5, NO DATA COMPRESSION)
- 4 SPODP DATA REDUCTION (DE 19/LE 4, NORMALIZED 5-min DATA POINTS)

Fig. 65. Error ellipse displacements

**g. O - C residuals.** The thoroughness of the data validity testing techniques in conjunction with the sophistication of the SPODP model failed to produce a good data fit. The O - C residuals exhibited traits which demonstrate that the data are not being modeled accurately. In terms of past experience, these solutions are relatively good, but in an absolute sense the model's evolution has not proceeded far enough. Diurnal periodicities and longer-termed patterns coupled with high-frequency data and computer noise are the obvious deficiencies of the data fits.

The standard deviation of the high-frequency noise associated with the 1-point/min data sample (with resolver data) is 0.002 Hz (0.73 mm/s).

The longer-term periodicities demonstrated by DE 19/LE 4 O - C residual sets (Figs. 66-68) are as anticipated. The residual sinusoidal pattern is descriptive of the range-rate differences between LE 5 and LE 4 (SPS 37-48, Vol. II, pp. 7-12) after least-squares minimization has been attempted (Figs. 66-69). LE 5 is a better model of lunar motion than LE 4.

The absence of any detectable long-term pattern in the DE 29/LE 5 O - C residual sets indicates the ability of LE 5 to model the lunar motion (Figs. 69-71).

The diurnal nature of the *Surveyor VI* O - C residuals is of the same nature as the daily variations identified with the *Surveyor I*, *III*, and *V* O - C residuals. J. D. Mulholland is currently investigating this phenomenon (SPS 37-49, Vol. II, pp. 4-6). Estimates have been made of the combined effects of the  $J_{20}$  defect (incorrect coefficient of the second harmonic term of the harmonic series used to describe the lunar gravitational potential) and the suspected faulty fitting of observations to Brown's lunar theory. Although present findings are inconclusive, a high correlation between the combined functions and the diurnal trait of the *Surveyor I* O - C residuals (Fig. 72) has been demonstrated.

A comparison of residual sets and the suspected error functions fails to provide the assurance that there is a relationship between the *Surveyor VI* residuals and these suspected error functions (Figs. 73 and 74; there is no comparison for the Pioneer DSS).

**h. Other error sources.** Although the current evolved lunar ephemeris is an acknowledged but unevaluated error source which warrants the evaluation efforts under-

way, the ephemeris is not the sole error source. Other model limitations include tropospheric refraction model errors and the omission of ionospheric charged particle effects.

The tropospheric refraction indices  $N$  employed in the SPODP solutions for the DSSs are set at 340. Recent research by A. Liu<sup>8</sup> has provided indications that the following refraction indices  $N$  are more precise:

Pioneer DSS:  $N_{11} = 240$

Tidbinbilla DSS:  $N_{42} = 300$

Robledo DSS:  $N_{61} = 310$

The influence of atmospheric refraction is primarily a phase retardation coupled with a bending of the ray path and a consequential lengthening of the ray path. If a ranging data type is acquired, improper modeling of refraction is viewed as a station-probe apparent range change during the course of a pass. If a range-rate data type is acquired, refraction model errors will indicate a station-probe relative acceleration as the elevation of the observation changes. Utilizing Liu's formulation, an error of 100 units in  $N$  generates O - C residuals of 0.5 Hz for horizon range-rate observations.

The Pioneer DSS most frequently, in comparison to the other stations, acquired low-elevation tracking data. An examination of Fig. 64 shows significant elevation-dependent O - C residual biases which correlate remarkably well with the computed refraction error functions. Examination of Figs. 64b and c pertaining to the Tidbinbilla DSS and the Robledo DSS reveals evidence of like influences. Future analysis will incorporate the more precise refraction indices and it is hoped that the O - C residual elevation-dependent characteristics will be diminished appreciably.

Up to the present time, ionospheric charged particle effects have been omitted from model consideration. The reasoned residual signature resulting from this omission is similar to the tropospheric refraction error function signature; however, the ionospheric influence on the tracking data is of a lesser magnitude. A history of ionosphere activity for the first lunar day of *Surveyor VI* is being compiled by M. Davies (Stanford University Electronics Laboratories). Once this information is available, the correlation of the O - C residuals with refraction and ionosphere will be investigated more fully.

<sup>8</sup>Refer to Article 3 in this Subsection (C).

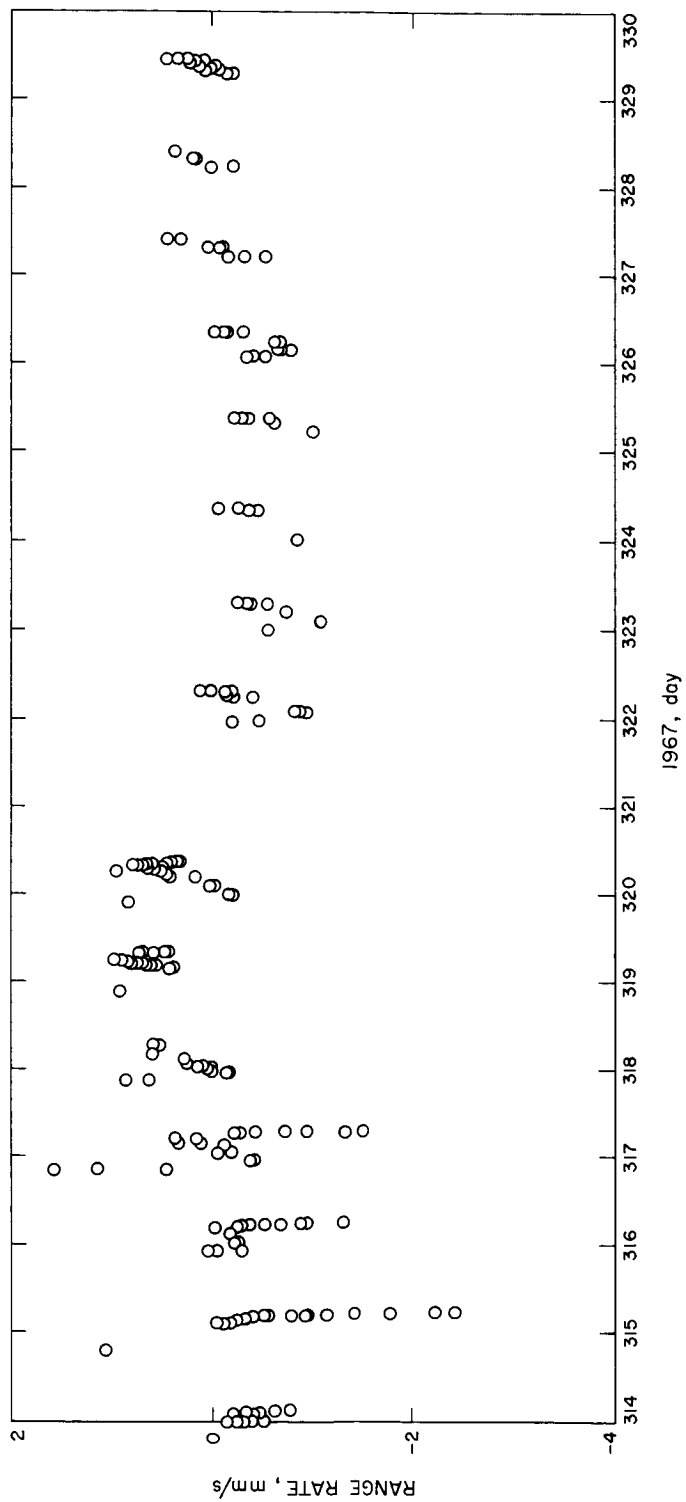


Fig. 66. Pioneer DSS O - C residual set (Surveyor VI, first lunar day, DE 19/LE 4, compressed 5-min data points)

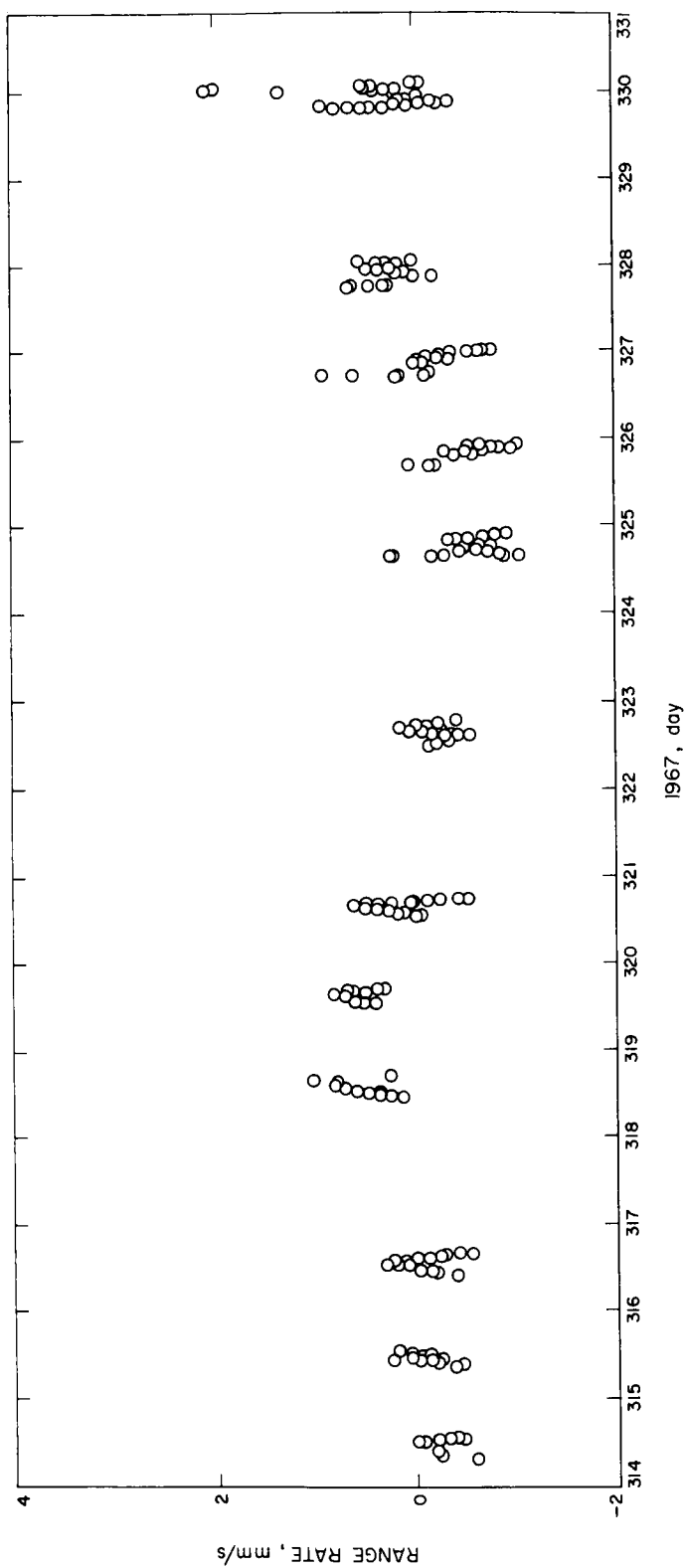


Fig. 67. Tidbinbilla DSS O — C residual set (Surveyor VI, first lunar day, DE 19/LE 4, compressed 5-min data points)

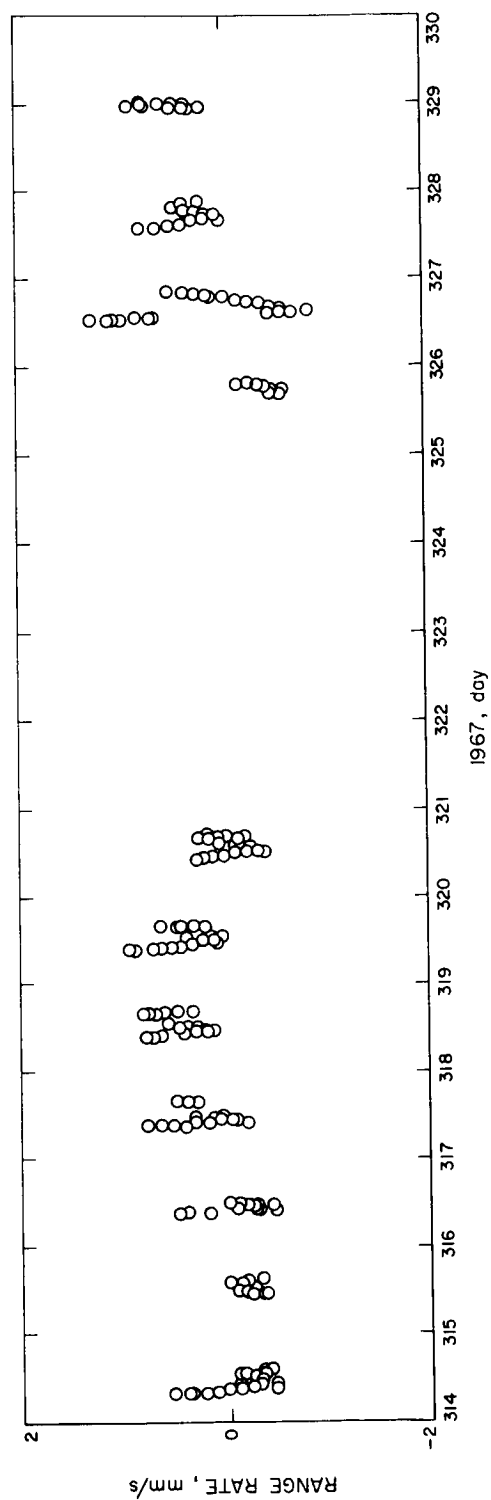


Fig. 68. Robledo DSS O — C residual set (Surveyor VI, first lunar day, DE 19/LE 4, compressed 5-min data points)

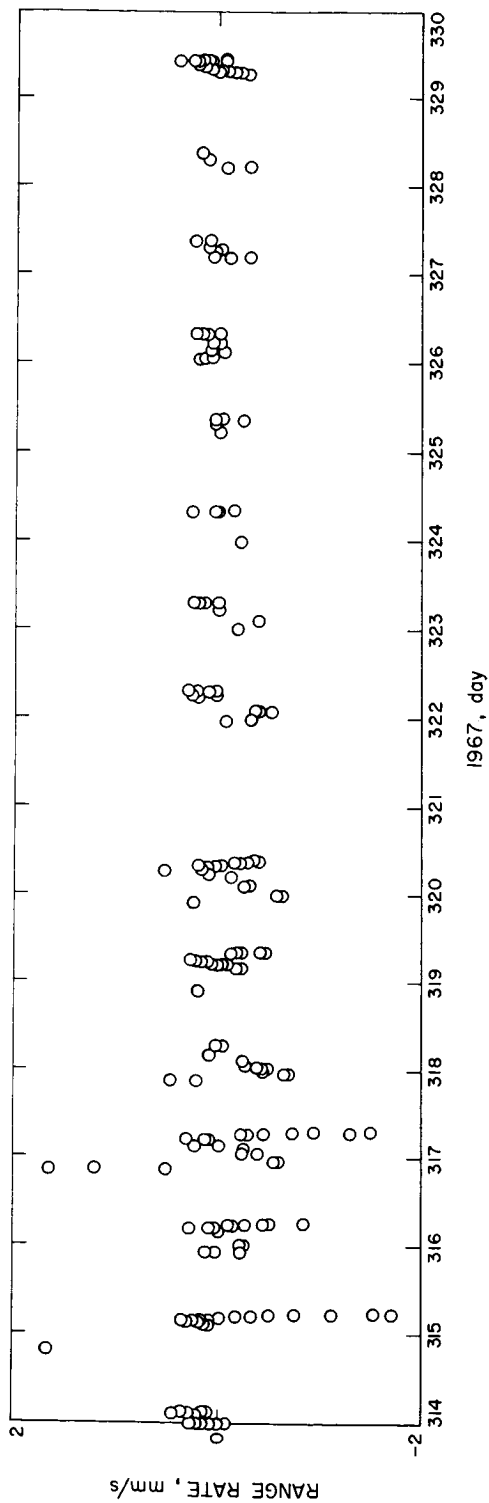


Fig. 69. Pioneer DSS O — C residual set (Surveyor VI, first lunar day,  
DE 29/LE 5, compressed 5-min data points)

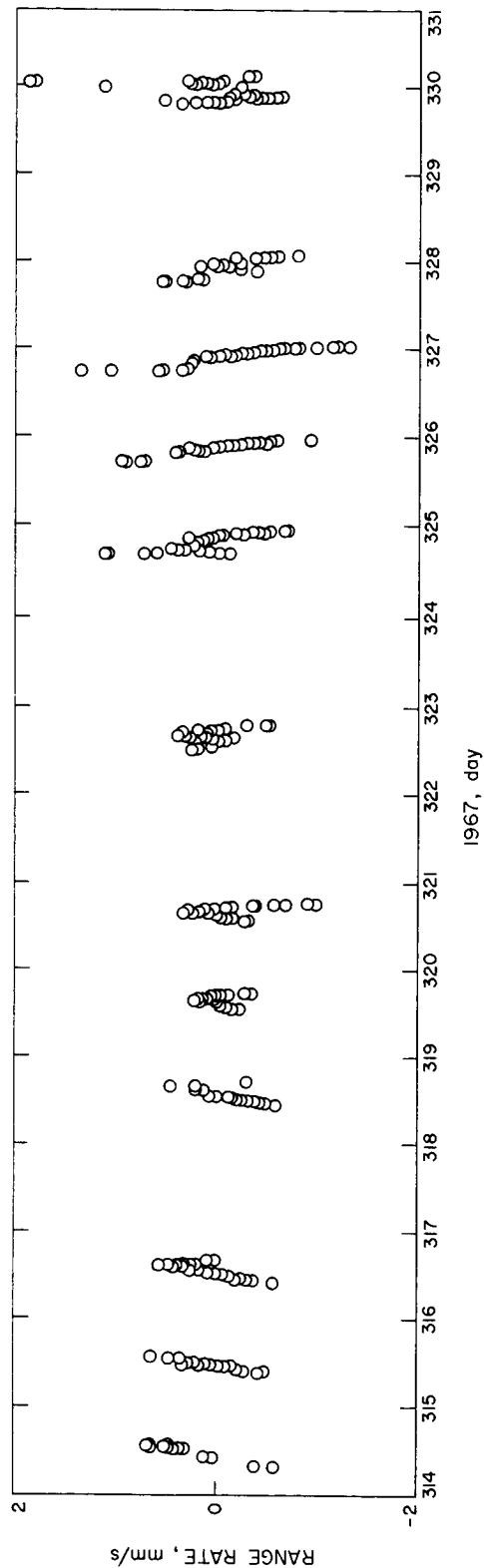


Fig. 70. Tidbinbilla DSS O — C residual set (Surveyor VI, first lunar day,  
DE 29/LE 5, compressed 5-min data points)

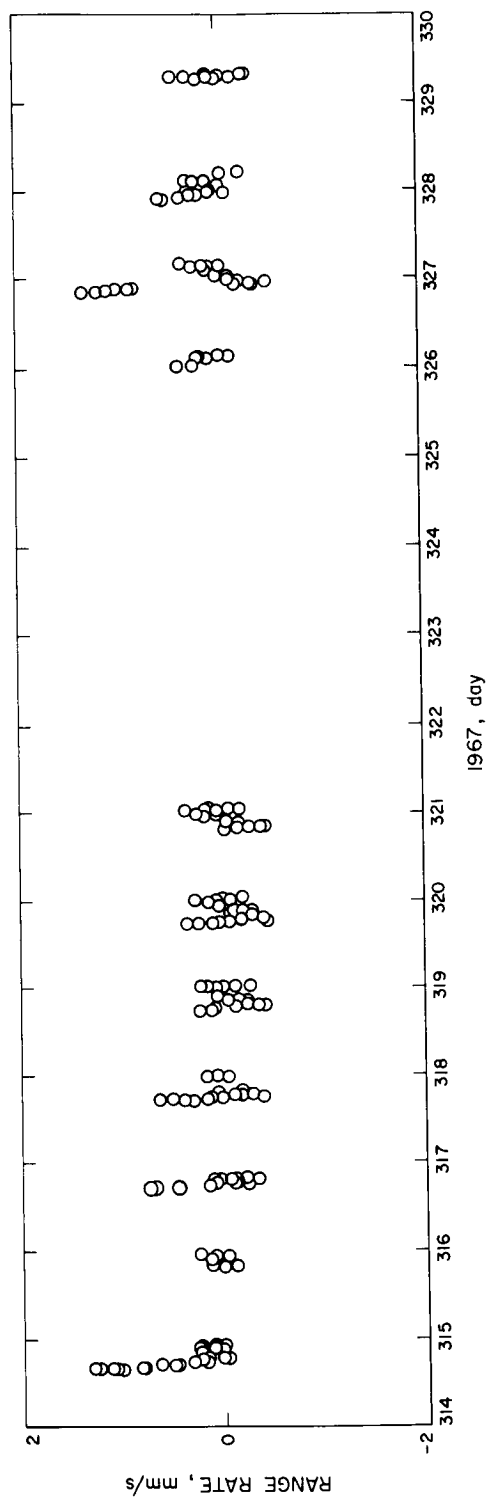
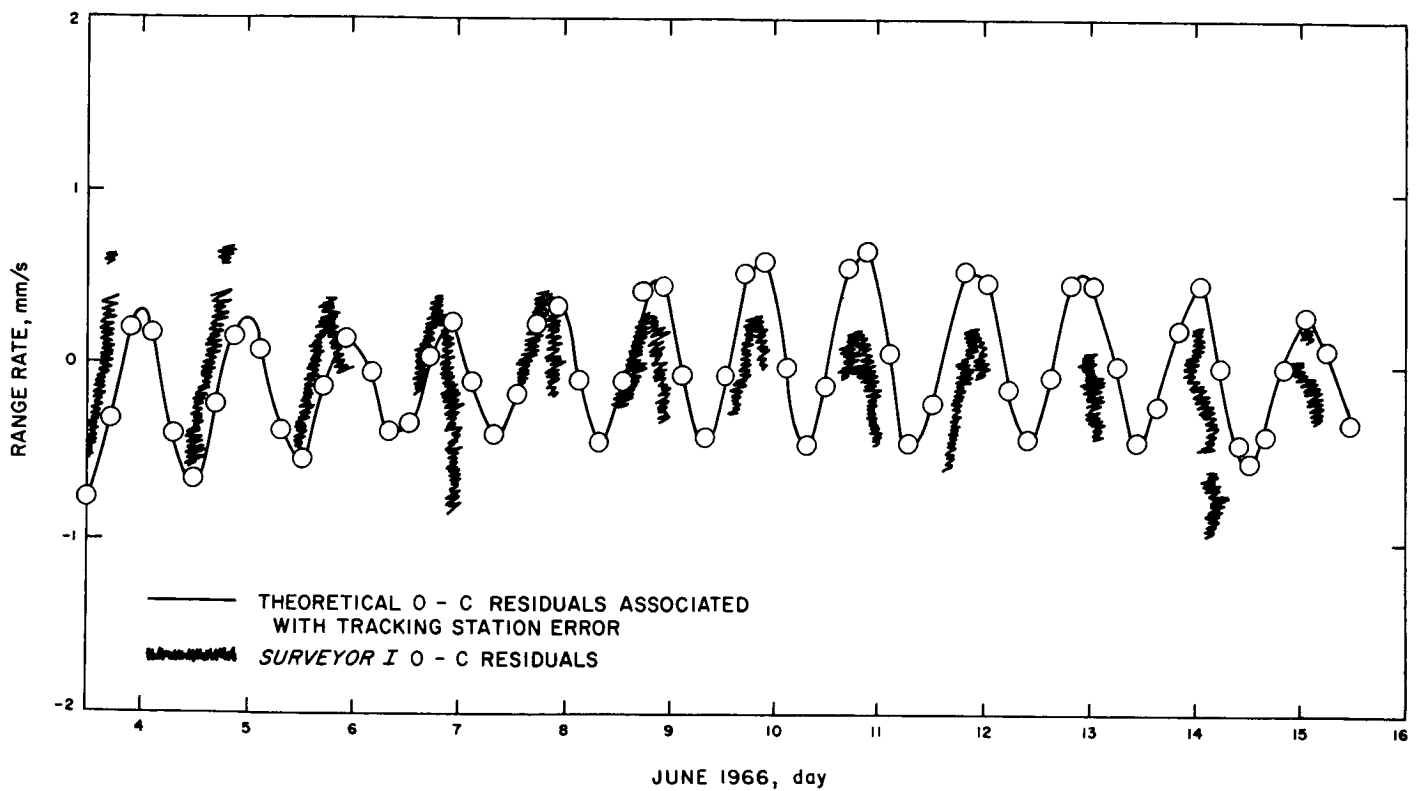


Fig. 71. Robledo DSS O - C residual set (Surveyor VI, first lunar day, DE 29/LE 5, compressed 5-min data points)



**Fig. 72. Surveyor I Tidbinbilla DSS O - C residuals vs suspected ephemeris-dependent tracking station longitude error**



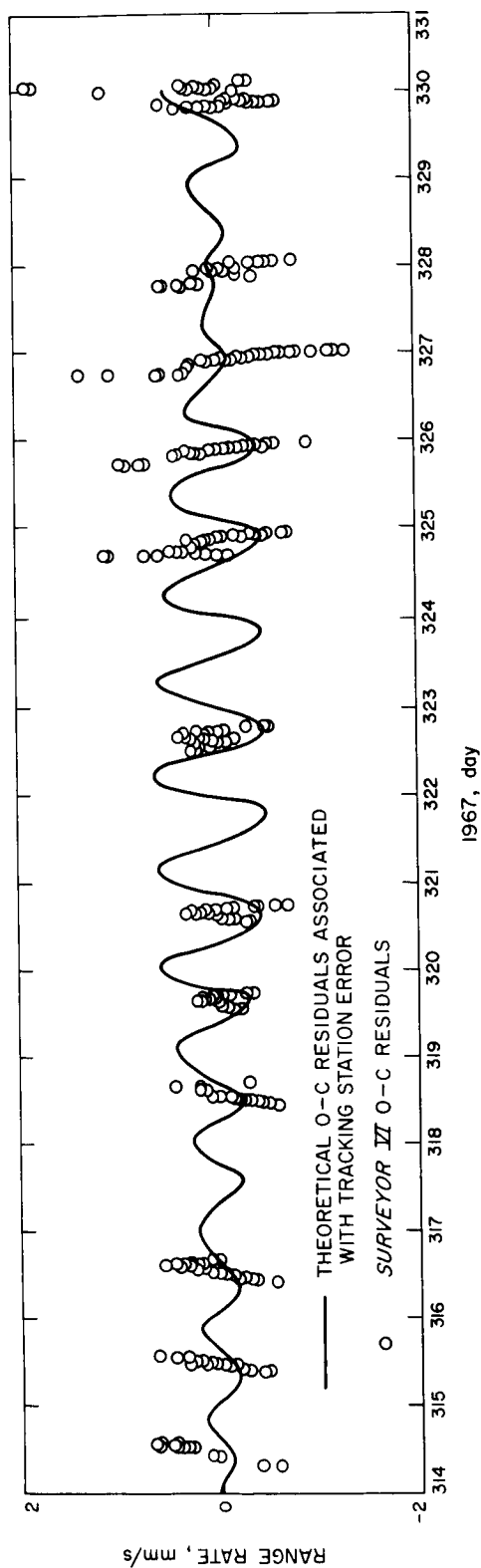


Fig. 73. Surveyor VI Tidbinbilla DSS O - C residuals vs suspected ephemeris-dependent tracking station longitude error

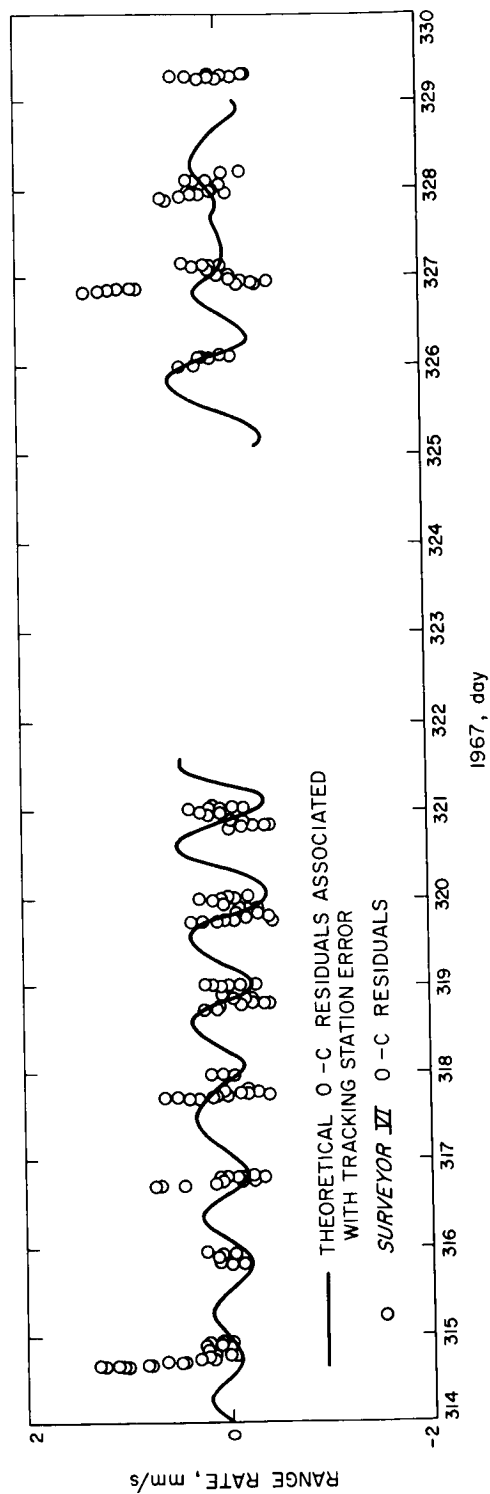


Fig. 74. Surveyor VI Robledo DSS O - C residuals vs suspected ephemeris-dependent tracking station longitude error

## References

1. Warner, M. R., and Nead, M. W., *SPODP—Single Precision Orbit Determination Program*, Technical Memorandum 33-204. Jet Propulsion Laboratory, Pasadena, Calif., Feb. 15, 1965.
2. *Surveyor VI Mission Report. Part I: Mission Description and Performance*, Technical Report 32-1262. Jet Propulsion Laboratory, Pasadena, Calif. (to be published).
3. Lawson, C. L., *Announcement of JPL Developmental Ephemeris No. 19*, Technical Memorandum 33-162. Jet Propulsion Laboratory, Pasadena, Calif., Apr. 13, 1967.
4. Mulholland, J. D., and Block, N., *JPL Lunar Ephemeris Number 4*, Technical Memorandum 33-346. Jet Propulsion Laboratory, Pasadena, Calif., Aug. 1, 1967.

## 7. Mariner V Real-Time Cruise and Encounter Orbit Determination Results,<sup>9</sup> G. E. Pease

**a. Introduction.** This article describes the orbit determination accuracies achieved during the real-time *Mariner V* cruise and Venus encounter flight operations, and the real-time solutions for relevant physical constants. The cruise period began June 19, 1967, 23:09 UT, following a midcourse maneuver at L + 5 days. For a description of the pre-midcourse orbit determination results, refer to SPS 37-49, Vol. II, pp. 6-10.

During the 4-mo cruise period, least-squares estimates were made of solar radiation pressure on the spacecraft tracking station coordinates and the earth-moon mass ratio. These estimates are based on analysis of doppler (range rate) and ranging tracking data obtained through the DSN. Frequent orbit determination resulted in the predicted target area that is described in this article and compared with the actual arrival point.

<sup>9</sup>The author acknowledges the contributions made by S. J. Reinbold, J. Ball, S. K. Wong, and J. D. Anderson of JPL to the results presented in this article.

**Table 20. Mark IA ranging data obtained during *Mariner V* mission**

DSS	Date, 1967		Number of points <sup>a</sup>
	Start	Stop	
Pioneer	6/20	6/29	2390
Echo	6/30	7/02	1503
Woomera	6/21	6/22	714
Tidbinbilla	6/24	7/06	3031
Robledo	6/20	6/29	2720
Cebreros	7/06	7/06	48

<sup>a</sup> Sampling interval was 60 s.

The probe reached the closest approach point of its Venus flyby trajectory on October 19, 1967, 17:35:55 UT. During the period of time when it is relatively close to Venus, the predominant gravitational attraction of the planet allows a very precise determination of the planet's mass from tracking data. In addition, the planet serves as a fixed reference point to which station locations and the astronomical unit may be tied. The real-time orbit determination accuracies achieved in this phase of the mission also serve as an indication of capabilities for future planetary flyby missions, e.g., *Mariner Mars* 1969.

## b. Tracking data coverage

**Two-way doppler data.** The primary tracking data type for the *Mariner V* mission is S-band two-way phase-coherent counted doppler data (CC3). The S-band conversion factor for units is approximately 1 m/s = 15.3 Hz. Approximately 6,600 compressed doppler points, counted at 600 intervals, are available from seven DSSs during the 4-mo cruise portion of the flight.

**Ranging data.** In addition to doppler data, two types of ranging measurement were performed during cruise with the Mark IA system at the DSSs shown in Table 20 and with the Mark II ranging system at Mars DSS. Mark IA range units (RU) are defined as follows:

$$\rho_{DSIF} = \left[ \frac{15(\Delta t + \epsilon)}{221} 96f_q \right] \bmod 785762208$$

where

$\rho_{DSIF}$  = measured round-trip interval in RU

$\Delta t$  = round-trip light time in UTC (Universal Time Coordinated) seconds

$f_q$  = transmitter reference frequency  $\simeq 22$  MHz

$\epsilon$  = time delay in seconds from station equipment, spacecraft transponder, and intervening space plasma-ionospheric medium

785762208 = code length of system in RU

The Mark IA ranging system is limited to an effective one-way range of about  $5.8 \times 10^6$  km, attained July 6, 1967 (see Table 20).

The Mark II (planetary) ranging system at Mars DSS measures the round-trip delay directly in nanoseconds. The

code length of the equipment is 1.00947/1.0002 s, hence

$$\rho_{\text{planetary}} = [10^9 (\Delta t + \epsilon)] \bmod \frac{1.00947 \times 10^9}{1.0002}$$

With the use of the Mark II equipment and the 210-ft antenna at Mars DSS, Mark II ranging measurements can be made to planetary distances, as the name of the data type implies. During the *Mariner V* mission, approximately 7000 points of 60-s sampled planetary ranging were obtained between July 21 and November 20, 1967.

**Tracking data statistics.** Table 21 shows the manner in which ranging data noise increases as a function of range when processed by the single-precision orbit determination program (SPODP). Statistics are given for individual passes of tracking data on the days shown, where  $\rho$  is the one-way spacecraft range in meters, and standard deviations on the PRU (planetary range unit) and RU have been converted to  $\sigma_\rho$ . The last column shows that eight-

**Table 21. Mars DSS PRU and Pioneer, Echo, Tidbinbilla, and Cebresos DSS RU residuals**

Date, 1967	$\sigma_{\text{PRU}}$	$\sigma_\rho$ , m	$\rho$ , m	$\sigma_\rho/\rho$
<b>Mars DSS planetary range unit (PRU) residuals (standard deviation)</b>				
6/21	103	15	0.18E10	0.83E-8
7/10	492	74	0.68E10	1.09E-8
7/22	628	94	1.00E10	0.94E-8
7/23	654	98	1.03E10	0.95E-8
7/28	730	110	1.19E10	0.92E-8
10/6	3580	537	6.25E10	0.86E-8
10/10	5600	840	6.78E10	1.23E-8
<b>Pioneer DSS RU residuals (standard deviation)</b>				
6/21	—	20	0.18E10	1.11E-8
6/22	—	26	0.21E10	1.24E-8
6/23	—	30	0.24E10	1.25E-8
6/24	—	36	0.27E10	1.33E-8
6/26	—	37	0.30E10	1.23E-8
6/27	—	40	0.33E10	1.21E-8
6/28	—	41	0.36E10	1.14E-8
6/29	—	62	0.39E10	1.59E-8
<b>Echo DSS RU residuals (standard deviation)</b>				
7/1	—	43	0.42E10	1.02E-8
7/2	—	45	0.45E10	1.00E-8
<b>Tidbinbilla DSS last RU residuals</b>				
7/6	—	53	0.58E10	0.91E-8
<b>Cebresos DSS last RU residuals</b>				
7/6	—	61	0.58E10	1.05E-8

place accuracy is being retained in the computations, which is all that may be expected of a single-precision program with a floating-point word length of 27 binary bits.

Doppler residuals do not display large numerical truncation and roundoff as a function of range, but are nevertheless limited by the single-precision program and by the stability of the reference frequency standard over the light-time interval. Table 22 shows a sample of cruise doppler residual statistics reduced by the SPODP. Although the doppler is continuously counted and sampled once every minute, this data has been averaged over 10-min intervals<sup>10</sup> to reduce the total number of points to a manageable level. These statistics reflect the precision of the least-squares fit over a long arc (3 mo). Table 22 also gives combined ranging statistics through July 28, 1967. The degradation from fitting a long arc is more apparent here than in the individual pass statistics of Table 21. This, of course, means that individual passes are biased differently, partly from single-precision truncation and partly from the nature of the least-squares fitting process.

### c. Cruise solutions for physical constants

**Solar radiation pressure.** During cruise, continuous least-squares estimates were made of  $\gamma_B$ , the solar radiation pressure coefficient defined as

$$1 + \gamma_B = \frac{mR^2\ddot{R}_{SP}}{kA}$$

where

$m$  = spacecraft mass, nominally 245.71 kg

$k = 1.031 \times 10^8$ , a solar radiation coefficient

$R$  = sun-probe distance in km

$\ddot{R}_{SP}$  = perturbative acceleration from solar radiation pressure in km/s<sup>2</sup>

$A$  = spacecraft effective area normal to  $R$ , nominally 6.60519 m<sup>2</sup>

The time history of these solutions is shown in Fig. 75. There appears to be a distinct trend towards lower pressure with increasing time. The physical interpretation of this phenomenon could be that an actual degradation of the total reflectance of the spacecraft took place during

<sup>10</sup>The data represents the range change over 10 min divided by the  $T_c = 600$ -s count time, i.e., only every tenth doppler counter reading is used.

Table 22. CC3, PRU, and RU residuals by station

DSS	Number of points	rms, Hz	First moment $\mu$ , Hz	$\sigma$ , Hz	rms, mm/s	$\mu$ , mm/s	$\sigma$ , mm/s
CC3 residuals (cruise data, $T_c = 600$ s)							
Pioneer	422	0.00348	-0.000395	0.00346	0.227	-0.0258	0.226
Echo	255	0.00400	-0.000356	0.00398	0.261	-0.0233	0.260
Mars	165	0.00433	-0.000976	0.00421	0.283	-0.0638	0.275
Woomera	311	0.00368	-0.000452	0.00365	0.241	-0.0295	0.239
Tidbinbilla	770	0.00312	-0.000762	0.00302	0.204	-0.0498	0.197
Robledo	831	0.00411	-0.000682	0.00405	0.269	-0.0446	0.265
Cebreros	172	0.00473	-0.000158	0.00473	0.309	-0.0103	0.309
Total	2926	0.00378	-0.000595	0.00373	0.247	-0.0389	0.244
PRU residuals through July 29, 1967							
Mars	847	868.9	-433.4	753.1	130	-65	113
RU residuals							
Pioneer	240	45.4	0.251	45.4	47	0.3	47
Echo	65	52.6	-30.1	43.1	55	-31	45
Woomera	74	59.4	54.1	24.4	62	57	26
Tidbinbilla	298	55.3	-17.5	52.4	58	-18	55
Robledo	285	49.9	0.255	49.9	52	0.3	52
Cebreros	6	59.5	-10.5	58.6	62	-11	61
Total	968	51.6	-3.2	51.5	54	-3	54

cruise. For instance, temperature monitoring of the bus indicates that the absorptance of the bus radiation shield may have increased by approximately 30% through UV darkening, according to L. Dumas of JPL. This would cause a corresponding decrease in reflectivity of the shield, which could account for a decrease in  $\gamma_B$  of up to 0.007. There is, in addition, the possibility of a decrease in specularity of the shield which Dumas estimated could cause a  $\gamma_B$  decrease of as much as 0.028. As seen in Fig. 75, the observed change in  $\gamma_B$  is on the order of 0.06, or nearly twice as much as the maximum combined effect of the above explanations. Since the standard deviations on the orbit solutions for  $\gamma_B$  are typically less than 0.01, it seems likely that the effect is real. The use of ranging data, in particular, adds great strength to the cruise solutions. The possibility remains, however, that the observed effect is at least partially due to a small force other than solar radiation pressure. This could result from a systematic decoupling of the attitude control gas jets torques which could, in turn, result from problems such as temperature differential between the sunlit jets and the shaded jets. Disturbance torques of 9 dyn-cm are commonly observed on *Mariner V* attitude control limit cycle telemetry, amounting to about  $1.5 \times 10^{-7}$  cm/s<sup>2</sup>

translational acceleration. This could account for a  $\gamma_B$  change of 0.05, or nearly the entire observed effect if the resultant forces are entirely in the correct direction. The net forces are in the process of being analyzed.

*Station locations.* Least-squares estimates of station locations based on post-midcourse maneuver tracking data are shown in Tables 23 and 24. The *a priori* standard deviations for spin-axis distance  $r_s$  and longitude  $\lambda$  are  $\tilde{\sigma}_{r_s} = 24$  m and  $\tilde{\sigma}_{\lambda} = 50$  m, respectively. Table 23 shows the solutions for perpendicular distance off the earth's spin axis, reduced to the mean pole of 1900-1905, and the associated standard deviations. These are labeled by post-midcourse orbit number, as in Fig. 75, and a time indicating when the orbit computation was performed. In general, the solutions are consistent to  $\pm 5$  m; e.g., Fig. 76 shows the Echo DSS portion of Table 23 in plotted form with the vertical bar representing the formal standard deviation.

Table 24 lists the *Mariner* cruise longitude solutions reduced to the mean pole of 1900-1905. The salient feature of these solutions is the 25- to 30-m difference between early and late cruise solutions. The high values obtained

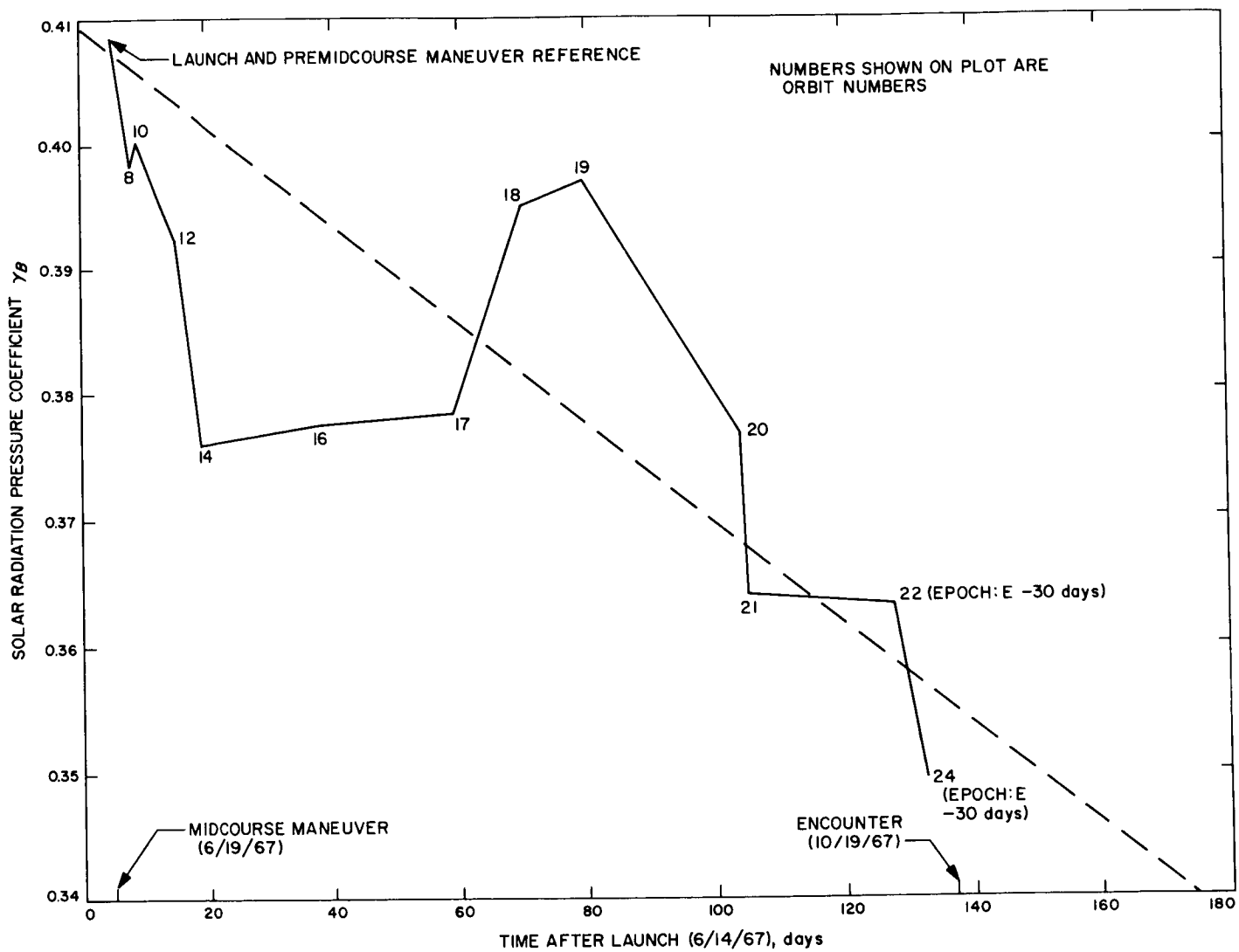


Fig. 75. Mariner V cruise solutions for solar pressure coefficient

Table 23. Mariner V cruise and encounter solutions for distance off spin axis

Orbit identification		Pioneer DSS		Echo DSS		Mars DSS		Woomera DSS		Tidbinbilla DSS		Robledo DSS		Cabreros DSS	
Time, <sup>a</sup> event $\pm$ days, h	Post/ ODP <sup>b</sup>	Distance off spin axis, km	$\sigma$ , m	Distance off spin axis, km	$\sigma$ , m	Distance off spin axis, km	$\sigma$ , m	Distance off spin axis, km	$\sigma$ , m	Distance off spin axis, km	$\sigma$ , m	Distance off spin axis, km	$\sigma$ , m	Distance off spin axis, km	$\sigma$ , m
Mariner V cruise solutions															
MC + 2 days	6	5206.3316	12	—	—	—	—	5450.2048	12	—	—	4862.6034	11	—	—
MC + 2 days	7	5206.3320	14	—	—	—	—	5450.2048	14	—	—	4862.6030	13	—	—
MC + 3 days	8	5206.3301	11	—	—	—	—	5450.2042	10	—	—	4862.6012	10	—	—
MC + 6 days	10	5206.3275	7	5212.0384	12	—	—	5450.2022	8	5205.3513	8	4862.5994	7	—	—
MC + 9 days	12	5206.3280	9	5212.0380	13	—	—	5450.2012	11	5205.3483	9	4862.5964	8	—	—
MC + 12 days	14	5206.3280	4	5212.0396	6	—	—	5450.2004	5	5205.3479	3	4862.5978	4	—	—
MC + 20 days	15	5206.3282	3	5212.0418	4	—	—	5450.2000	38	5205.3476	3	4862.5975	4	4860.8099	7
MC + 28 days	16	5206.3292	3	5212.0436	3	—	—	5450.2011	3	5205.3492	2	4862.5983	4	4860.8095	5
MC + 44 days	17	5206.3337	2	—	—	5203.9897	3	5450.2047	3	5205.3499	1	4862.6018	2	4860.8106	5
MC + 62 days	18	5206.3317	2	—	—	5203.9874	3	—	—	5205.3487	4	4862.6019	1	4860.8093	5
MC + 70 days	19	5206.3314	2	5212.0408	2	5203.9871	2	—	—	5205.3480	1	4862.6004	1	—	—
MC + 90 days	20	5206.3314	2	5212.0457	2	5203.9900	3	—	—	5205.3486	1	4862.6022	1	—	—
MC + 113 days	22	5206.3327	1	—	—	5203.9938	2	5450.1971	1	5205.3481	1	4862.6019	1	4860.8128	1
MC to E - 4 days	25	—	—	5212.0481	2	5203.9967	2	5450.1981	1	5205.3483	1	4862.6044	1	4860.8165	1
Mean value		5206.3304	—	5212.0420	—	5203.9907	—	5450.2014	—	5205.3487	—	4862.6006	—	4860.8114	—
Mariner V encounter solutions															
E - 20 days to E - 1 day	1026	—	—	5212.0672	3	5204.0135	5	—	—	5205.3444	3	—	—	4860.8477	2
E - 5 days to E - 12 h	1027	—	—	5212.0481	5	5203.9940	6	5450.1952	5	5205.3470	1	—	—	4860.8163	4
E - 5 days to E - 12 h	2027	—	—	5212.0422	5	5203.9885	6	5450.1995	5	5205.3477	1	—	—	4860.8121	4
E - 5 days 17 h to E - 10 h	1028	—	—	5212.0479	5	5203.9900	6	5450.1906	5	5205.3425	1	—	—	4860.8199	4
E - 5 days 17 h to E - 8 h	1029	—	—	5212.0464	5	5203.9940	6	5450.1944	5	5205.3421	1	—	—	4860.8141	4
E - 5 days 17 h to E - 8 h	2029	—	—	5212.0504	5	5203.9985	6	5450.1983	6	5205.3481	1	—	—	—	—
E - 5 days 17 h to E - 5 h	1030	—	—	5212.0484	5	5203.9989	5	5450.1976	5	5205.3479	1	—	—	4860.8069	4
E - 5 days 17 h to E - 4 h	2030	—	—	5212.0510	5	5203.9971	5	5450.1994	5	5205.3470	1	—	—	4860.8121	4
E - 5 days 17 h to E + 1 h	1031	—	—	5212.0484	5	5203.9954	4	5450.1934	5	5205.3451	1	—	—	4860.8132	3
E - 5 days 17 h to E + 1 h	1032	—	—	5212.0464	4	5203.9901	3	5450.1974	4	5205.3388	1	—	—	4860.8108	3
E + 1 day		—	—	—	—	—	—	—	—	—	—	—	—	—	—
E - 5 days 17 h to E + 1 day	2032	—	—	5212.0422	3	5203.9885	3	5450.1995	3	5205.3477	1	—	—	4860.8121	1
E - 5 days to E + 5 days <sup>c</sup>	—	—	—	5212.0497	3	5203.9863	3	5450.2021	3	5205.3422	1	—	—	4860.8112	2
Mean value		—	—	5212.05348	—	5203.9945	—	5450.1970	—	5205.3450	—	—	—	4860.8160	—

<sup>a</sup> MC = midcourse maneuver; E = encounter.  
<sup>b</sup> Post for cruise solutions; ODP for encounter solutions.  
<sup>c</sup> Best encounter solution to date.

Table 24. Mariner V cruise and encounter solutions for DSS geocentric longitudes

Orbit Identification		Pioneer DSS		Echo DSS		Mars DSS		Woomera DSS		Tidbinbilla DSS		Robledo DSS		Cabreros DSS	
		DSS geocentric longitude, deg	$\sigma$ , deg $\times 10^{-5}$	DSS geocentric longitude, deg	$\sigma$ , deg $\times 10^{-5}$	DSS geocentric longitude, deg	$\sigma$ , deg $\times 10^{-5}$	DSS geocentric longitude, deg	$\sigma$ , deg $\times 10^{-5}$	DSS geocentric longitude, deg	$\sigma$ , deg $\times 10^{-5}$	DSS geocentric longitude, deg	$\sigma$ , deg $\times 10^{-5}$	DSS geocentric longitude, deg	$\sigma$ , deg $\times 10^{-5}$
Mariner V cruise solutions															
MC + 2 days	6	243.15100	30	—	—	—	—	136.88789	31	—	—	355.75140	30	—	—
MC + 2 days	7	243.15100	30	—	—	—	—	136.88789	32	—	—	355.75140	30	—	—
MC + 3 days	8	243.15100	29	—	—	—	—	136.88788	29	—	—	355.75139	29	—	—
MC + 6 days	10	243.15095	22	243.19478	23	—	—	136.88784	22	148.98160	22	355.75134	22	—	—
MC + 9 days	12	243.15091	22	243.19480	23	—	—	136.88779	22	148.98161	22	355.75130	22	—	—
MC + 12 days	14	243.15085	20	243.19479	21	—	—	136.88774	21	148.98152	20	355.75123	20	—	—
MC + 20 days	15	243.15078	18	243.19472	18	—	—	136.88766	18	148.98144	18	355.75115	18	355.63238	18
MC + 28 days	16	243.15072	18	243.19466	18	—	—	136.88763	18	148.98139	17	355.75110	18	355.63234	18
MC + 44 days	17	243.15075	2	—	—	243.11068	3	136.88767	2	148.98144	2	355.75117	2	355.63239	4
MC + 62 days	18	243.15072	2	—	—	243.11063	2	—	—	148.98137	1	355.75110	1	355.63231	5
MC + 70 days	19	243.15070	2	243.19467	2	243.11064	2	—	—	148.98137	2	355.75110	2	—	—
MC + 90 days	20	243.15074	2	243.19465	2	243.11066	2	—	—	148.98140	1	355.75113	1	—	—
MC + 113 days	22	243.15071	2	—	—	243.11058	2	136.88754	1	148.98135	1	355.75108	1	355.63218	1
MC to E - 4 days	25	—	—	243.19461	1	243.11059	2	136.88756	1	148.98140	1	355.75114	1	355.63222	1
Mean value		243.150833	—	243.194710	—	243.110630	—	136.887735	—	148.981444	—	355.751216	—	355.632303	—
Mariner V encounter solutions															
E - 20 days to E - 1 day	1026	—	—	243.19455	3	243.11065	4	—	—	148.98139	3	—	—	355.63224	3
E - 5 days to E - 12 h	1027	—	—	243.19474	19	243.11067	19	136.88767	19	148.98143	20	—	—	355.63236	19
E - 5 days to E - 12 h	2027	—	—	243.19460	19	243.11058	20	136.88751	20	148.98132	20	—	—	355.63222	19
E - 5 days 17 h to E - 10 h	1028	—	—	243.19470	19	243.11068	19	136.88765	19	148.98143	20	—	—	355.63236	19
E - 5 days 17 h to E - 8 h	1029	—	—	243.19476	19	243.11071	19	136.88769	19	148.98150	20	—	—	355.63240	19
E - 5 days 17 h to E - 8 h	2029	—	—	243.19459	5	243.11054	5	136.88751	5	148.98134	9	—	—	—	—
E - 5 days 17 h to E - 5 h	1030	—	—	243.19465	19	243.11058	19	136.88756	19	148.98136	20	—	—	355.63228	19
E - 5 days 17 h to E - 4 h	2030	—	—	243.19476	16	243.11071	16	136.88769	16	148.98152	17	—	—	355.63240	16
E - 5 days 17 h to E + 1 h	1031	—	—	243.19470	6	243.11064	5	136.88763	5	148.98142	8	—	—	355.63234	4
E - 5 days 17 h to E + 1 h	1032	—	—	243.19474	5	243.11065	5	136.88774	4	148.98149	8	—	—	355.63239	4
E + 1 day		—	—	—	—	—	—	—	—	—	—	—	—	—	—
E - 5 days 17 h to E + 1 day	2032	—	—	243.19487	7	243.11081	7	136.88779	7	148.98159	9	—	—	355.63249	6
E - 5 days to E + 5 days <sup>c</sup>	—	—	—	243.19495	3	243.11091	3	136.88786	3	148.98168	7	—	—	355.63259	3
Mean value		—	—	243.194717	—	243.110677	—	136.887663	—	148.981455	—	—	—	355.632370	—

<sup>a</sup> MC = midcourse maneuver; E = encounter.  
<sup>b</sup> Post for cruise solutions; ODP for encounter solutions.  
<sup>c</sup> Best encounter solution to date.

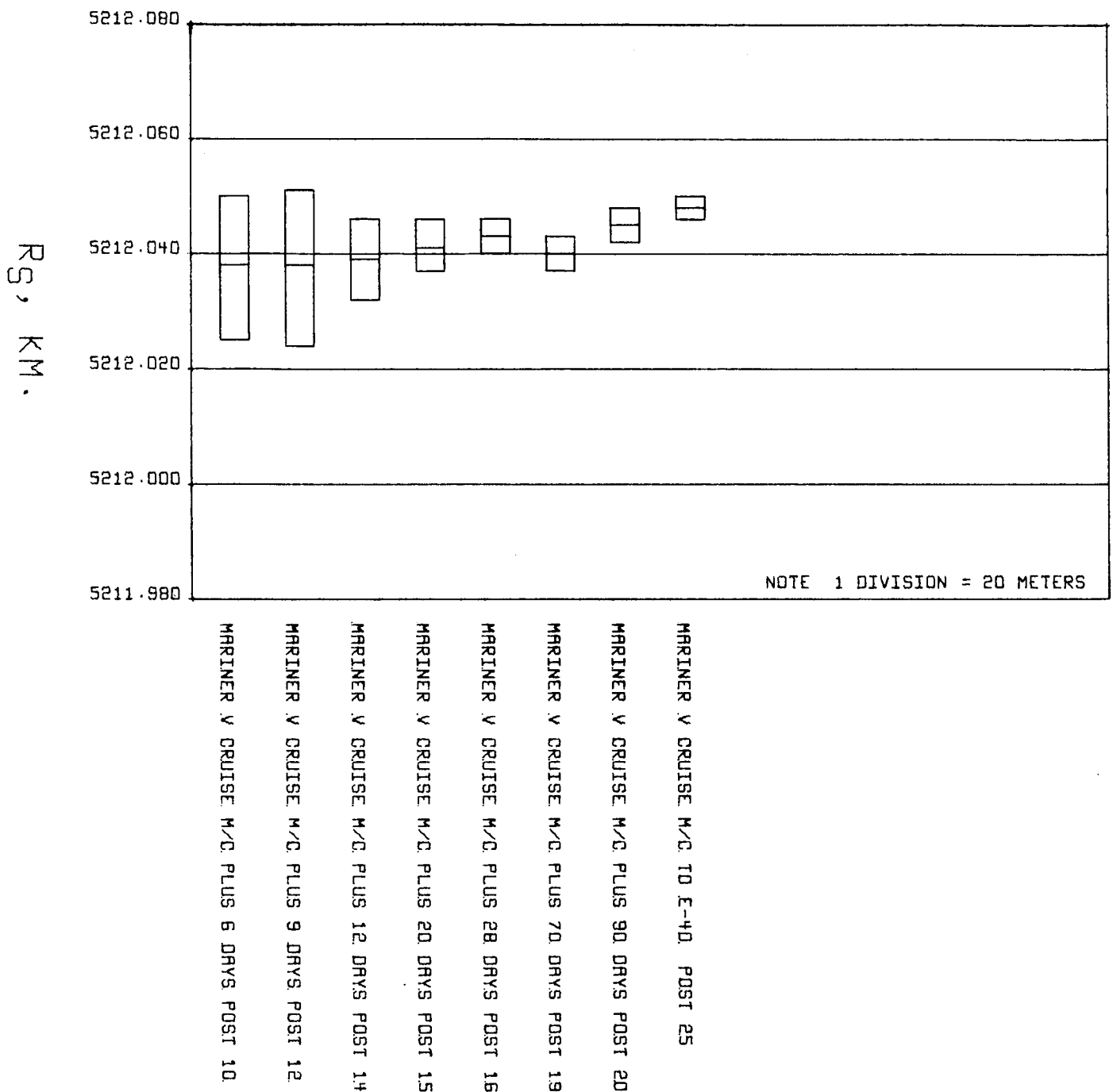


Fig. 76. Echo DSS distance off spin axis: cruise data, earth-fixed system (referenced to 1903.0 pole)

shortly after midcourse maneuver tend to be in good agreement with the longitudes obtained before the maneuver, whereas the late cruise solutions tend to be close to those obtained during encounter. Runs up to Post 14 did not represent WWV - UT timing differences, whereas later runs used a polynomial representation of

these differences. The timing error caused by making WWV - UT = 0 is about 10 ms on June 19, or 4 m in longitude. The remaining differences are probably due to earth-sun ephemeris errors. The longitude solutions for Echo DSS are plotted in Fig. 77 as a representative sample.



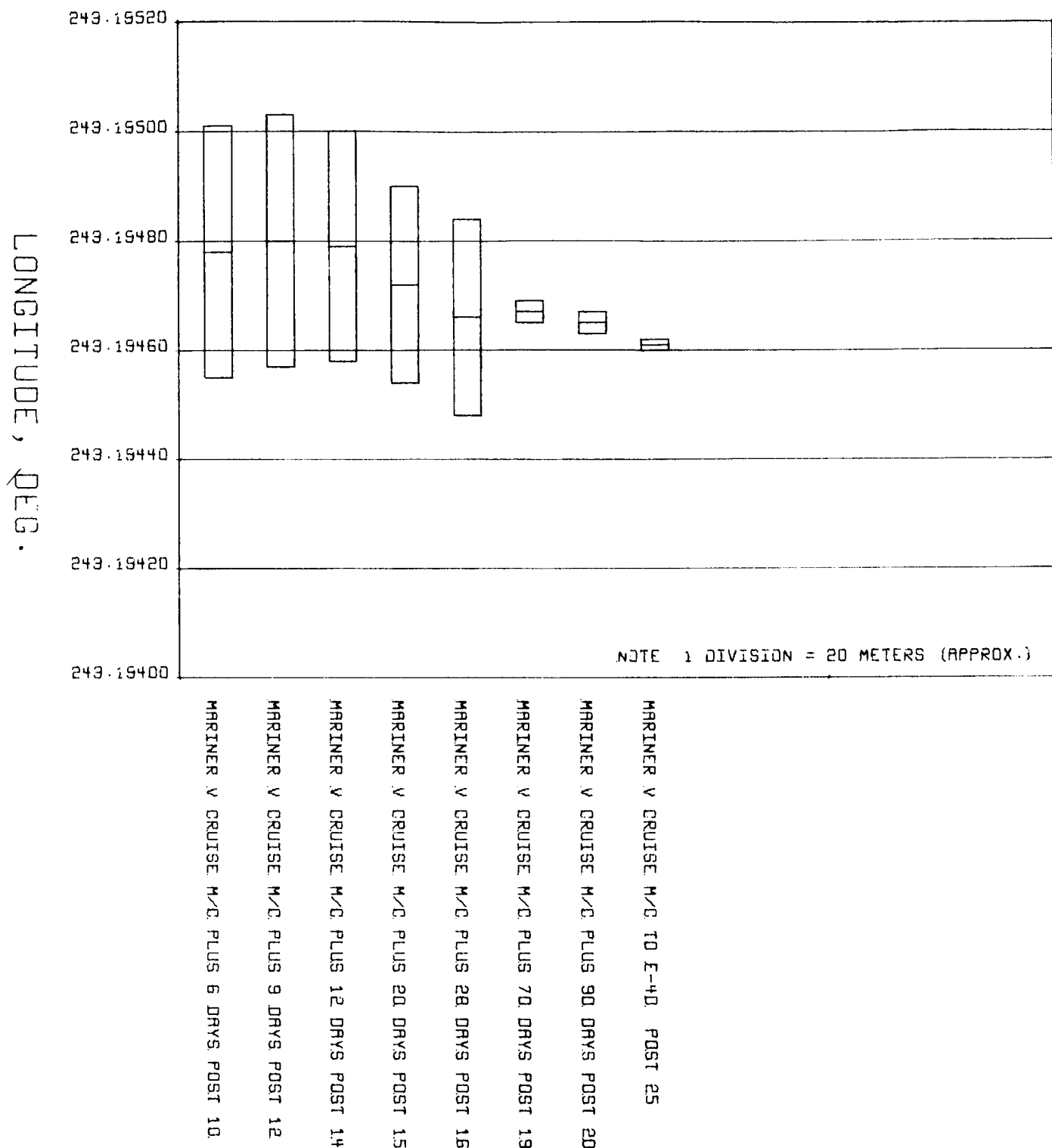


Fig. 77. Echo DSS geocentric longitude: cruise data, earth-fixed system (referenced to 1903.0 pole)

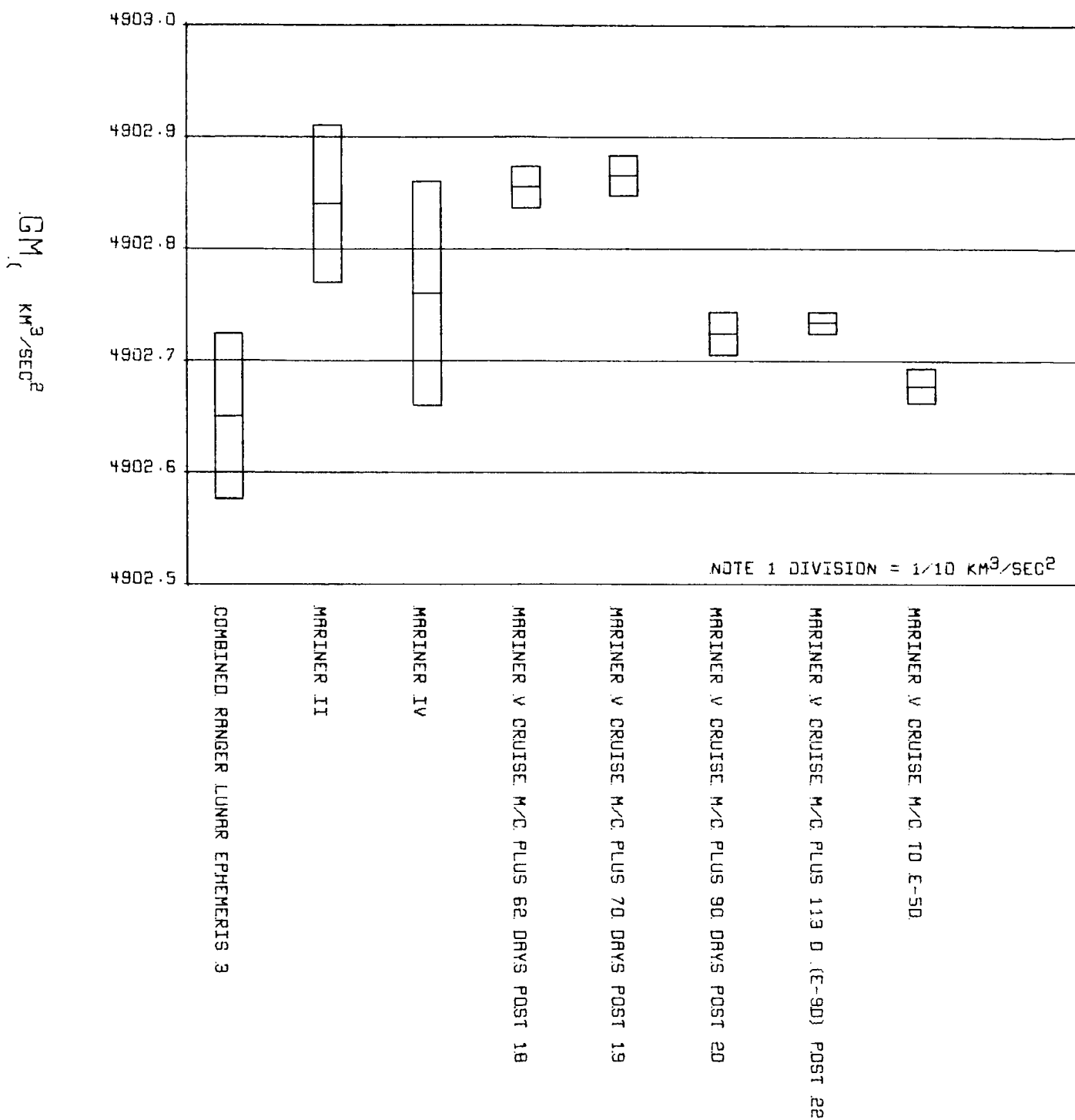


Fig. 78. GM Moon from combined Ranges, Mariners II, IV and V

*Cruise solutions for mass of moon.* Fig. 78 shows the lunar gravitational constant solutions based upon the combined *Ranger* Block III missions (see SPS 37-44, Vol. III, pp. 11-28), *Mariner II* (Ref. 1) and *Mariner IV* (Ref. 2), and *Mariner V* in real time. The low *Ranger* result,  $GM_{\epsilon} = 4902.6493 \text{ km}^3/\text{s}^2$ , was obtained by measuring the effect of the lunar gravity field on the probe acceleration. The *Mariner* results, on the other hand, measure the barycentric motion of the tracking station over the long cruise interval, and are, therefore, in reality a determination of the earth-moon mass ratio, assuming a known value for the earth-moon distance from optical and radar observations. The *Mariner II* result,  $GM_{\epsilon} = 4902.8442 \text{ km}^3/\text{s}^2$ , is based upon the *Ranger* earth gravitational constant,  $GM_{\oplus} = 398,601.27 \text{ km}^3/\text{s}^2$ , yielding a mass ratio of  $\mu^{-1} = 81.3000 \pm 0.0011$ . The *Mariner IV* value also uses the *Ranger*  $GM_{\oplus}$  to obtain  $\mu^{-1} = 81.30147 \pm 0.0016$  from  $GM_{\epsilon} = 4902.756 \pm 0.1 \text{ km}^3/\text{s}^2$ . The real-time *Mariner V* solutions, shown in Fig. 78, display a sharp break between data spans incorporating 2 and 3 mo of data, respectively. The explanation of this phenomenon is not known at this time, but is probably

related to ephemeris errors of the earth-moon barycenter. The formal program statistics do not include the effect of such error sources. If a representative value were to be given for the real-time cruise solutions for  $GM_{\epsilon}$ , it would have to be between the two extremes of 4902.86 and 4902.68  $\text{km}^3/\text{s}^2$ . A realistic evaluation of the real-time results yields  $GM_{\epsilon} = 4902.77 \pm 0.1 \text{ km}^3/\text{s}^2$ . Since all *Mariner V* solutions assume a value  $GM_{\oplus} = 398,601.33$ , the corresponding real-time estimate of  $\mu^{-1}$  is  $81.30125 \pm 0.00166$ .

The gravitational constant values given in Fig. 79 reflect the result of an effort to estimate physical constants, including  $GM_{\epsilon}$ , by careful postprocessing of the cruise data for the *Mariner* celestial mechanics experiment. These results seem to indicate a value of  $GM_{\epsilon} = 4902.81 \pm 0.5 \text{ km}^3/\text{s}^2$ , yielding  $\mu^{-1} = 81.30059 \pm 0.00083$ . This value is remarkably close to the *Mariner II* mass ratio, and is in good agreement with the *Mariner IV* value. The discrepancy between the real-time and the post-processed values is due to a difference in the relative weighting between doppler data and ranging and the amount of

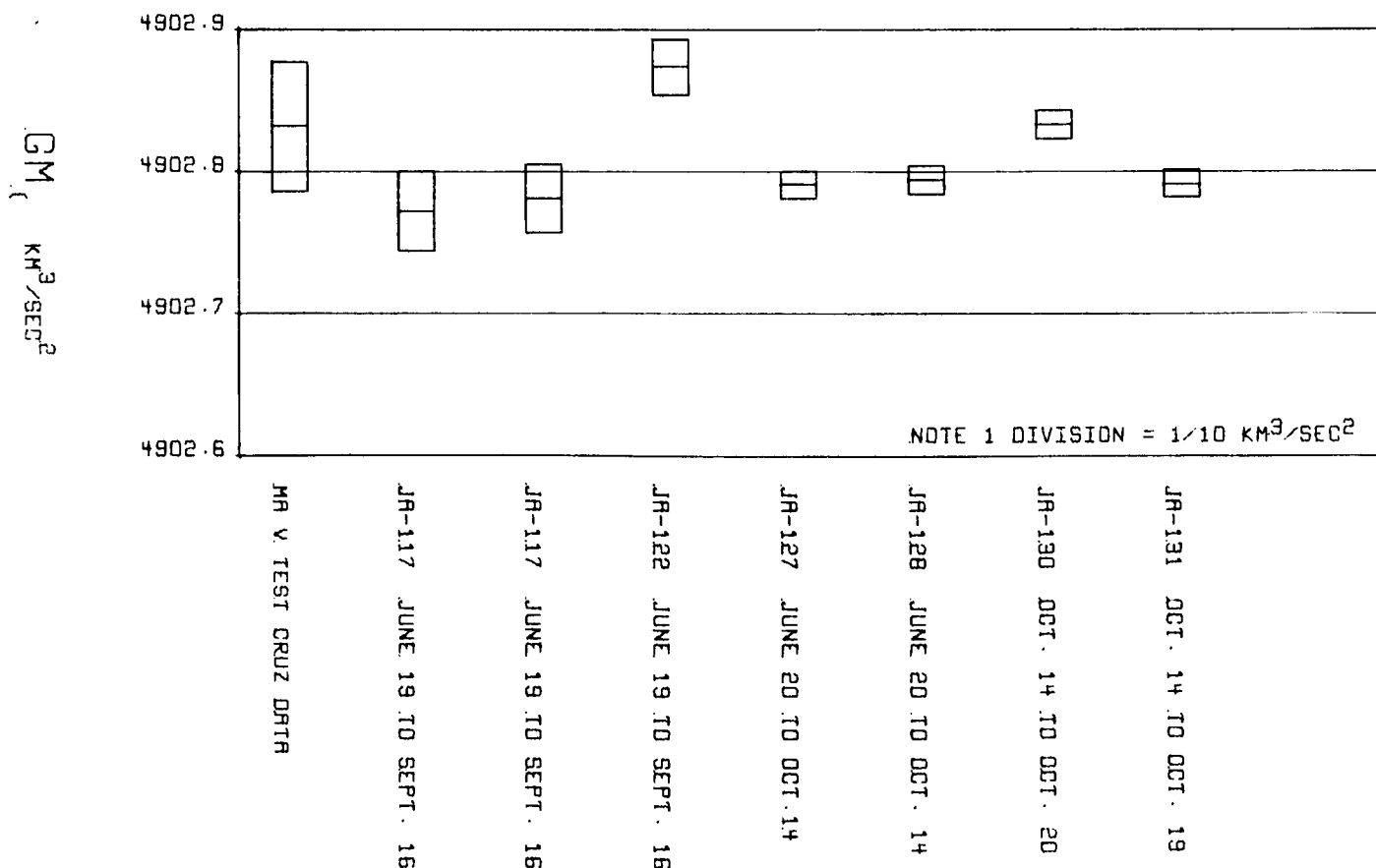


Fig. 79. GM Moon from *Mariner V* post-cruise analysis

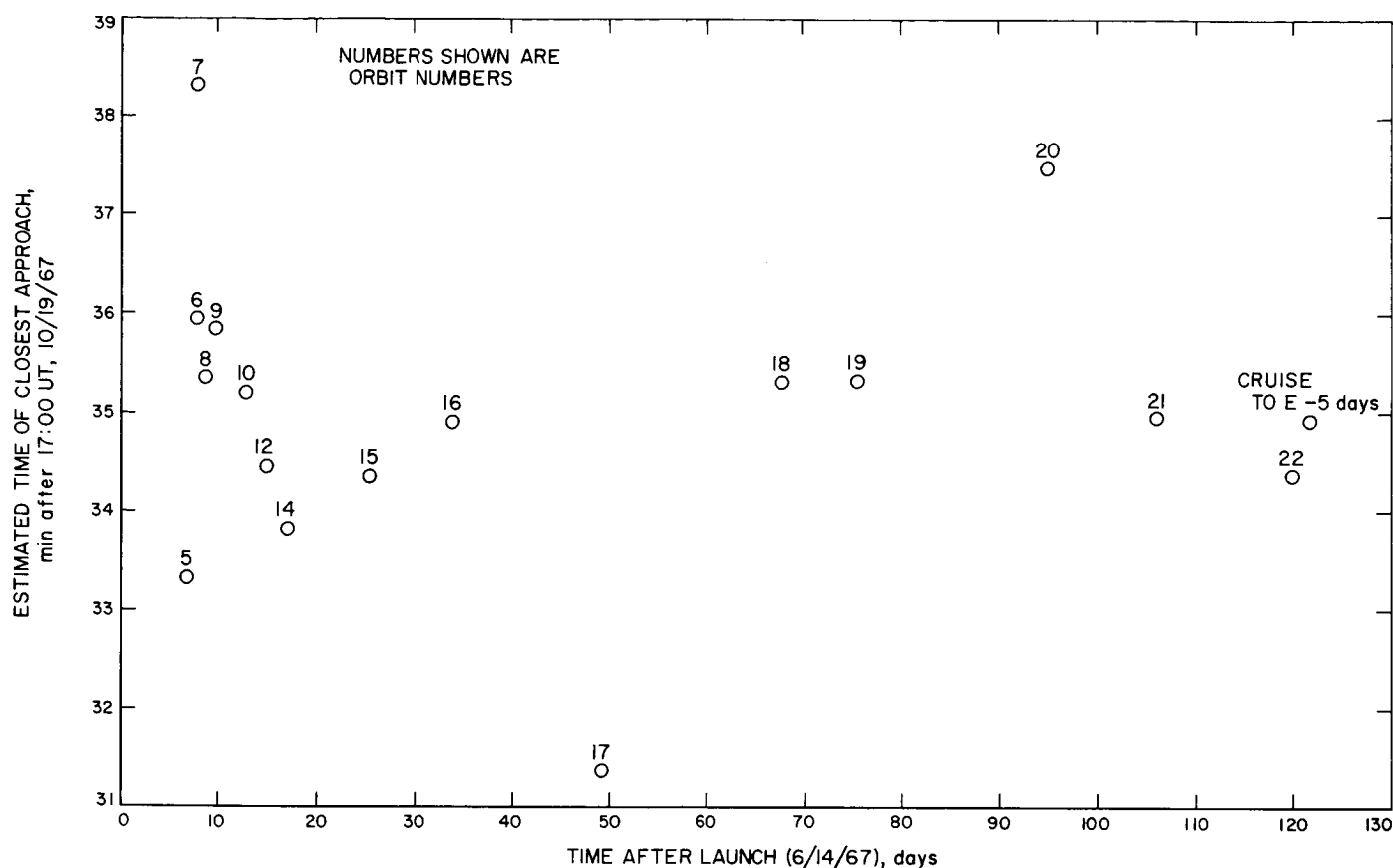


Fig. 80. Closest approach time in minutes past October 19, 1967, 17:00 UT

data fit. The post-processed reductions weight doppler more heavily with respect to ranging, and, in general, do not include as much late data in the fit.

#### d. Target parameters from cruise solutions

**Time of closest approach.** The cruise orbit estimates of time of closest approach to Venus are shown in Fig. 80. It is seen that the solutions cluster around 17:35 UT on October 19, 1967. The actual UT encounter time was 17:34:55, demonstrating that the cruise solutions were not afflicted with detectable systematic errors in the flight-time parameter. Such errors, amounting to several minutes, were observed with *Mariner II* and *Mariner IV*. They may be attributed to ephemeris and astronomical unit errors as well as small non-gravitational forces such as solar radiation pressure and attitude control gas leaks.

**B-plane target point.** A standard measurement of trajectory aiming point is the position of the incoming asymptote in the B-plane, i.e., in the plane normal to the asymptote and passing through the center of the target planet. Figure 81 shows the predicted aiming points

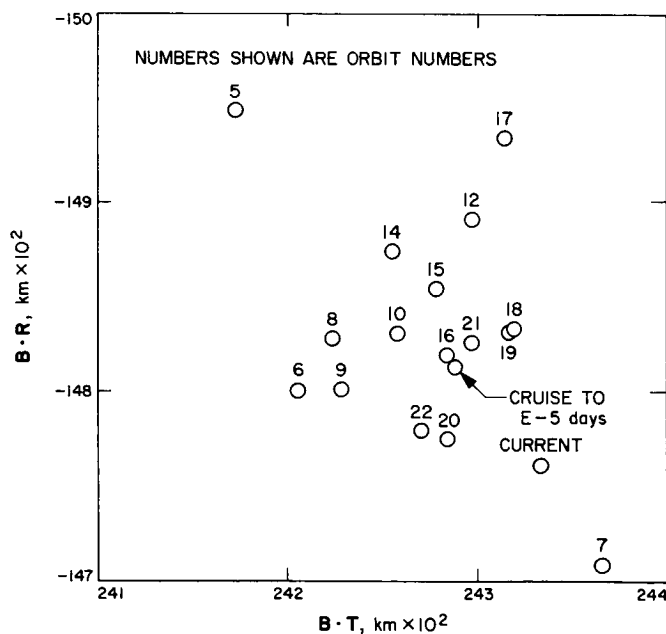


Fig. 81. Ecliptic B-plane aiming point from cruise orbit determination

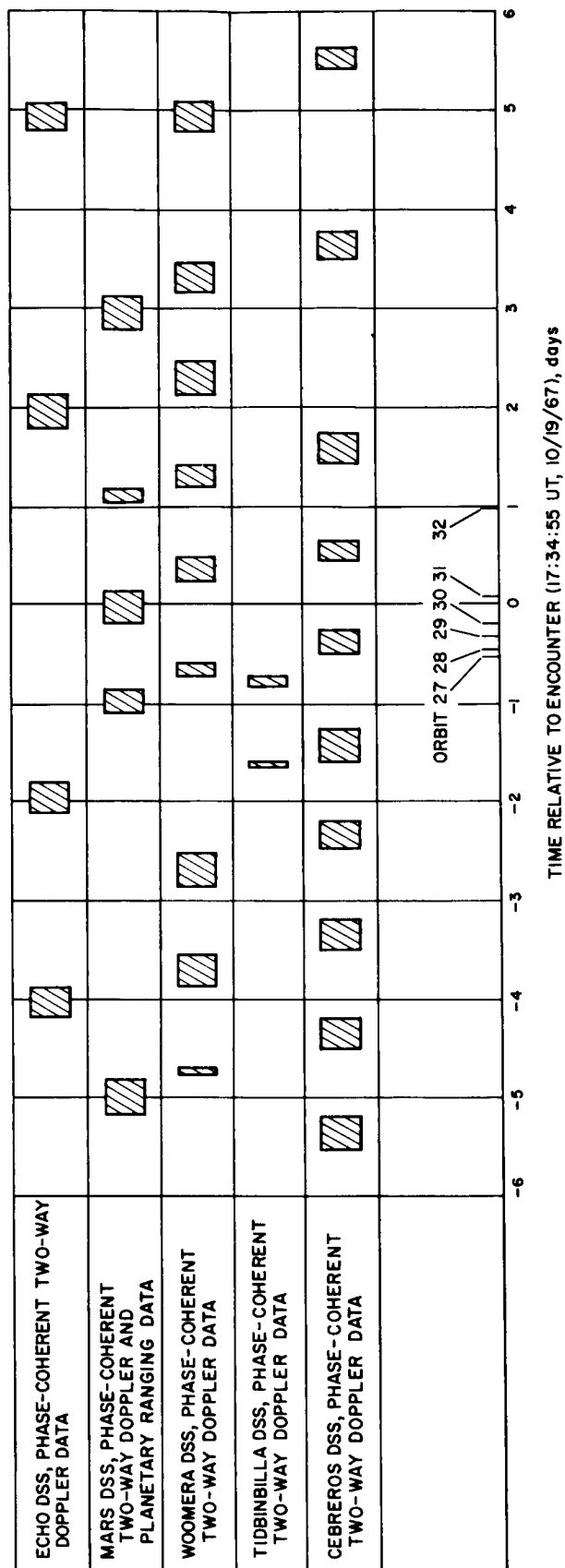


Fig. 82. Station view periods, Mariner V Project

from cruise orbit determination in planet-centered **B**-plane components  $\mathbf{B} \cdot \mathbf{R}$  and  $\mathbf{B} \cdot \mathbf{T}$ , where **T** is in the ecliptic plane and **R** is normal to **T**. The solutions appear to randomly cluster about  $\mathbf{B} \cdot \mathbf{R} = -14,830$  km and  $\mathbf{B} \cdot \mathbf{T} = 24,270$  km. They are noticeably offset on the plot from the current post-encounter solution of  $\mathbf{B} \cdot \mathbf{R} = -14,761.9 \pm 1$  km,  $\mathbf{B} \cdot \mathbf{T} = 24,334.3 \pm 1$  km. This offset of about 100 km is probably mainly attributable to earth-Venus ephemeris errors, station location errors, and timing errors. It compares very favorably with comparable errors of 1000 km for *Mariner II* and *Mariner IV*. In the case of *Mariner II*, the spacecraft had relatively high leakage rates from attitude control gas jets, while *Mariner IV* was troubled by an inaccurate astronomical unit and planetary ephemeris.

#### e. Real-time encounter orbit estimation procedures

**Tracking data acquisition.** During the period  $E - 12$  h to  $E + 3$  h, 11 orbits were run on two IBM 7044-7094 computer strings as tracking data were acquired in real time by the DSN. The tracking data distribution from  $E - 6$  days to  $E + 6$  days is shown in Fig. 82. The real-time encounter orbits utilized data from  $E - 5$  days to  $E + 1$  h, while the post-encounter analyses made use of the full 10 days.

**Orbit estimation procedure.** Orbits run on the prime computer string were labeled with a "10" prefix, while those run as backup support were given a "20" prefix. The prime runs estimated spacecraft trajectory, astronomical unit, and station locations; the backup runs estimated various combinations of parameters, including Venus ephemeris elements.

**Real-time encounter aiming point estimates.** The primary excursions noted in the real-time encounter orbits were in the direction normal to the **B**-vector. Thus, the solutions line up very nearly along a line normal to **B** in the **R-T** plane (see Fig. 83). The total variation amounts to 900 km, or 1.8 deg measured from planet center. This is in good agreement with the predicted uncertainties.<sup>11</sup> The major error source seems to be numerical instability in station location and Venus ephemeris solutions. The current best estimate, based upon 10 days of encounter tracking data, is shown in Fig. 83. The systematic offset of the solutions from the current value is about 100 km, which is somewhat smaller than the total scatter. Interestingly, this offset is in the opposite direction from the cruise solutions. The current

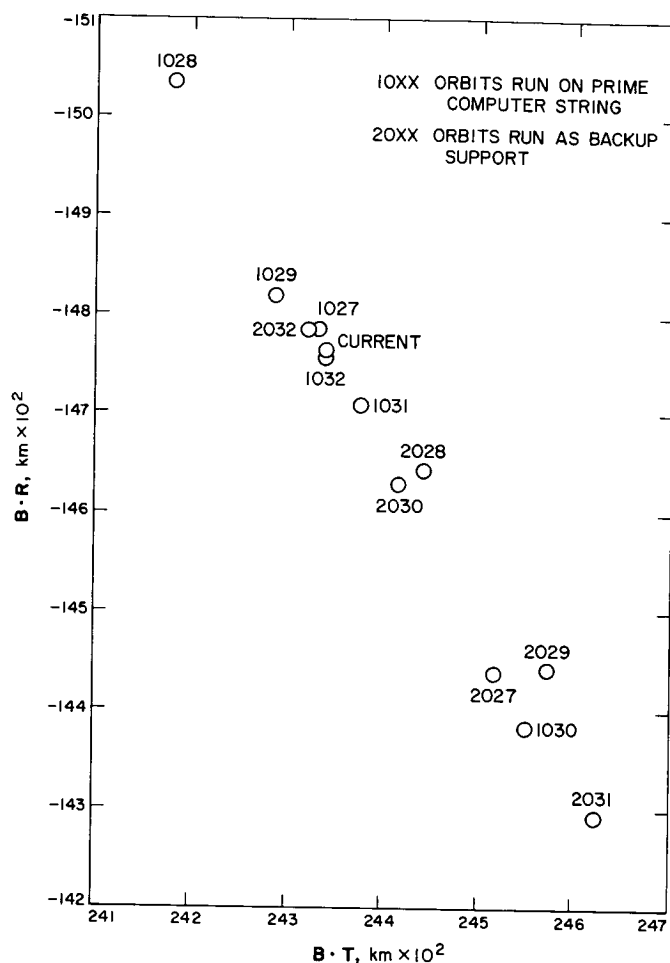


Fig. 83. Real-time Mariner V encounter B-plane estimates

values of  $\mathbf{B} \cdot \mathbf{R} = -14,761.9$  km,  $\mathbf{B} \cdot \mathbf{T} = 24,334.3$  km are known to  $\pm 1$  km.

**Solution for astronomical unit.** The radar value of  $149,597,900 \pm 100$  km was adopted as an *a priori* starting value in the encounter runs. The solutions showed no tendency to deviate significantly from this value within the limitations of single precision, indicating the following three possibilities: (1) the radar value is correct within  $\pm 100$  km, (2) ephemeris errors in the range direction are within  $\pm 100$  km, and (3) the strength of the single-precision solution is not great enough to detect errors of the order of 100 km. The latter possibility may be ruled out, as the ranging data is sufficiently powerful to establish the earth-Venus distance to better than  $\pm 10$  km even in single precision, although the program cannot separate Venus ephemeris error in the range direction from error in the astronomical unit. The current best

<sup>11</sup>Pease, G. E., *Mariner Venus 67 Orbit Determination Characteristics and Accuracy*, June 9, 1967 (JPL internal document).

*Mariner V* astronomical unit solution yields 149,597,904  $\pm$  44 km, assuming ephemeris corrections discussed below.

**Ephemeris error.** Pre-encounter estimates of ephemeris errors were hampered by low numerical stability and unfavorable partial derivatives. Thus, these solutions were not accurate to the approximately 100 km required to define ephemeris errors. The planetary ephemeris used successfully for the mission was the highly accurate JPL development ephemeris 24 (DE 24), utilizing radar corrections to the older optical ephemeris. The current *Mariner V* solution for corrections to the DE 24 position of Venus at 17:35:33.138 UT, October 19, is in the earth equatorial coordinates  $x = -0.76 \pm 23$  km,  $y = -29.23 \pm 12$  km, and  $z = 11.95 \pm 34$  km. The ability to measure such relatively small corrections to the astronomical unit and planetary ephemeris must be credited, in large part, to the planetary ranging system used with *Mariner V*.

**Encounter station location solutions.** Table 24 shows the *Mariner V* encounter solutions for station locations reduced to the mean pole of 1900-1905. Solutions, and their standard deviations, for distance off the earth's spin axis  $r_s$  are tabulated by station number and station longitudes  $\lambda$ . Assumed *a priori* standard deviations were the same as for cruise ( $\sigma r_s = 24$  m,  $\sigma \lambda = 50$  m). Except for orbit 1026,  $r_s$  solutions exhibit very few systematic trends. Orbit 1026 was run with an earlier data span, did not estimate the astronomical unit, and did not include ranging data in the fit. Comparing the other solutions with Table 23, it is seen that the cruise and encounter spin-axis distance solutions are in good agreement. The encounter solutions for Echo DSS spin axis are plotted in Fig. 84 as an example.

Although considerably noisier than the spin-axis estimates, the encounter solutions for station longitude are in good agreement with the cruise longitude solutions (see Table 24). The high random noise is due to numerical instability in the single-precision orbit program. Note the trend toward increasing longitude with increasing data in contrast to the opposite trend in the cruise solutions. This trend is clearly seen in Fig. 85 which is a representative plot for Echo DSS. The longitudes deduced from the tracking data taken from  $E - 5$  days to  $E + 5$  days are, in general, even higher than the early cruise longitudes. The longitude determinations in deep space, under the gravitational influence of the sun, are systematically lower by about 25 m than those in the gravitational presence of earth and Venus. This indicates the existence of significant earth-sun ephemeris errors of the order of 300 km.

The total spread in mean station locations during encounter operations on the prime computer string amounts to  $\Delta r_s = 4$  m,  $\Delta \lambda = 12$  m. These are important quantities, as theory predicts the uncertainty in station locations to be a predominant error source. For *Mariner Mars 1969*, such station location errors correspond to **B**-plane errors of 156 and 192 km, or 180 km normal to the **B**-vector. This represents the scatter, but not systematic error sources such as ephemeris error. If the *Mariner Mars 1969 B*-vector has a magnitude of 7000 km, this scatter from station location error will amount to about 1.5 deg in angular measure from the center of the planet as opposed to a total from all error sources of 1.8 deg for *Mariner V*. It should be noted that this is the critical pointing direction for the *Mariner Mars 1969 UV* photometer experiment.

**Mass of Venus.** The mass of Venus is the astrodynamical quantity most precisely determined by *Mariner V* encounter tracking data. This is because (1) the Venus-centered hyperbolic encounter trajectory is curved nearly 90 deg by the gravitational influence of the planet, and (2) this trajectory bending is very accurately measured by doppler tracking data. The 1962 *Mariner II* spacecraft, utilizing L-band doppler data and a planetary ephemeris based solely on optical observations, yielded a sun-Venus mass ratio of  $408,505 \pm 6$  (SPS 37-44, Vol. III, pp. 11-28). This value was used as *a priori* information in the *Mariner V* encounter solutions, but the *a priori* standard deviation was enlarged to 150 to avoid possible biasing of the solution towards the *Mariner II* result. The current *Mariner V* estimate of the sun-Venus mass ratio is  $408,522.66 \pm 3$ . This is based upon doppler and ranging tracking data taken from  $E - 5$  days to  $E + 5$  days, assuming  $GM_\odot = 1,327,125 \times 10^4$  km<sup>3</sup>/s<sup>2</sup> and an astronomical unit of 149,597,904 km, so  $GM_v = 324,859.6 \pm 3$  km<sup>3</sup>/s<sup>2</sup>.

**f. Conclusions.** Orbit determination on *Mariner V* has led to the most precise target prediction of any planetary mission to date. This is due primarily to the recent improvement of planetary ephemerides at JPL and to the use of a spacecraft ranging system for the first time on a planetary mission. Also, a great deal of extremely valuable operational experience was gained during the previous missions, especially as regards the use of *a priori* constraints to orbital parameters.

To make comparable improvements in the future, more work must be done in improving planetary ephemerides through optical, radar, and spacecraft tracking data. Station-location coordinates must be further improved by more refined analysis of present spacecraft data. At present, such analysis is limited by the numerical precision of the computer programs. Present work on the JPL

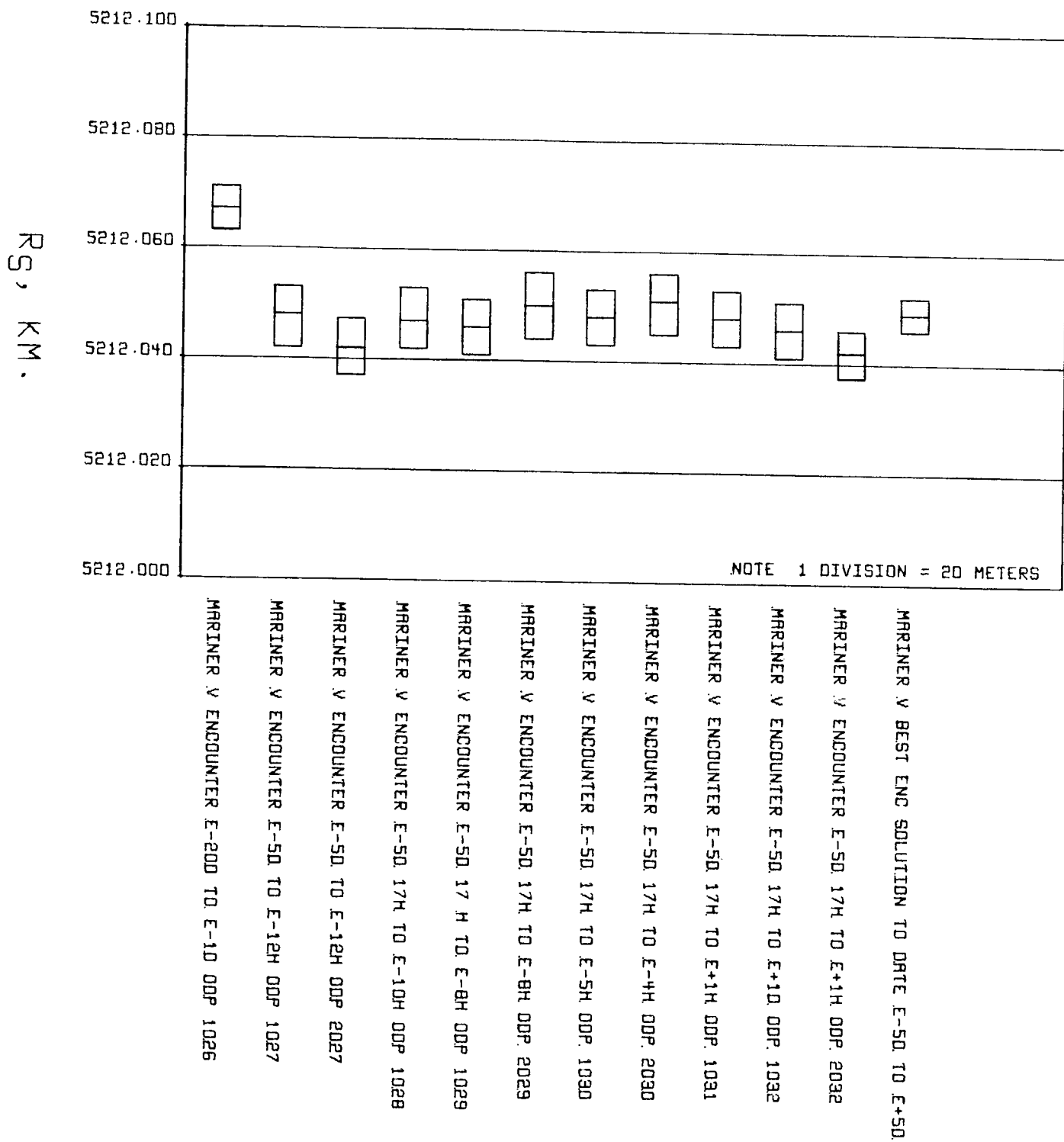


Fig. 84. Echo DSS distance off spin axis: encounter data, earth-fixed system (referenced to 1903.0 pole)



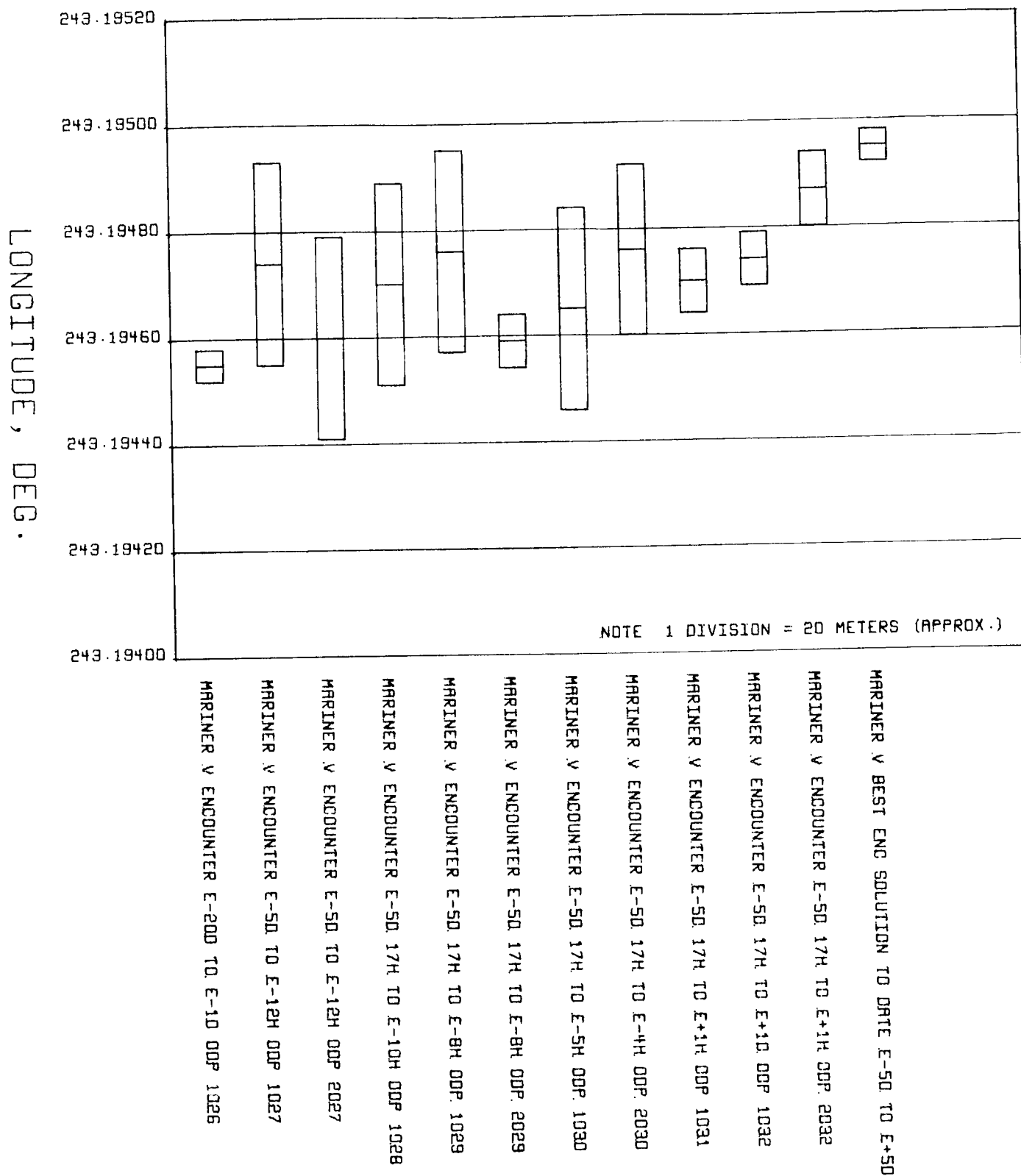


Fig. 85. Echo DSS geocentric longitude: encounter data, earth-fixed system (referenced to 1903.0 pole)

double-precision orbit determination program (DPODP) should remove numerical limitations. Lastly, planetary spacecraft must be developed with even "cleaner" attitude control systems than *Mariner V*, as minute accelerations of the order of  $10^{-5}$  mm/s<sup>2</sup> may cause hundreds of kilometers of target error prediction.

#### References

1. Anderson, J. D., *Determination of the Masses of the Moon and Venus and The Astronomical Unit from Radio Tracking Data of the Mariner II Spacecraft*, Technical Report 32-816, Jet Propulsion Laboratory, Pasadena, Calif., July 1, 1967.
2. Null, G. W., *The Mariner IV Flight Path and Its Determination From Radio Tracking Data*, Technical Report 32-1108, Jet Propulsion Laboratory, Pasadena, Calif., Aug. 1, 1967.

#### 8. Pioneer VIII — A Comparison of the Preflight Nominal and Actual Trajectories, J. F. Gallagher

**a. Introduction.** On December 13, 1967, only 0.265 s after the opening of the launch window at 14:08 GMT, *Pioneer VIII* was launched on a very successful trajectory. This article discusses a comparison of the preflight nominal trajectory with the actual trajectory. The preflight nominal trajectory was targeted by engineers of the McDonnell-Douglas Corp.; the actual trajectory is considered to be the one described by the most recent orbit determination solution for this reporting period. That solution was based on data taken from a few days after launch to January 10, 1968, a total of about 25 days of tracking data.

**b. Comparison at Woomera DSS rise.** After the spacecraft is injected into its escape trajectory, the first really important trajectory event is initial acquisition by the DSN. *Pioneer VIII* initial acquisition was accomplished by Woomera DSS. A comparison of the preflight nominal and actual trajectories at initial acquisition is given in Table 25. For initial acquisition of *Pioneer VIII*, pre-launch tracking data analysis indicated that rise time and rise azimuth were the controlling factors for anomalies caused by trajectory dispersions. The acquisition-aid antenna, mounted on the 85-ft antenna, has a beam width of about 16 deg meaning that the actual rise azimuth should not differ from the nominal by more than 8 deg. If it does, search procedures must be initiated. Table 25 shows that the actual trajectory was very satisfactory in this respect. The 27 s early rise seen in Table 25 was handled by simply pointing the antenna at the nominal rise azimuth location well in advance of the nominal rise time. This advance time was determined by prelaunch studies. In both the nominal and the actual trajectories, the rise at the station was governed by the hour-angle

**Table 25. A comparison of the preflight nominal and actual trajectories at Woomera DSS rise**

Trajectory	Woomera DSS rise time, Dec. 13, 1967	Azimuth, deg	Elevation, deg	Hour angle, deg	Declination, deg
Preflight nominal	14:57:18	258.063	7.143	90.0	-13.885
Actual	14:56:51	258.662	6.793	90.0	-13.194

stop on the antenna. Hence, the rise elevation is about 7 deg rather than the usual 2 or 3 deg.

**c. Comparison at injection plus 23 h.** The next important trajectory item is the earth-probe-sun angle at 23 h past injection. This angle should be close to 30 deg at that time in order to properly perform the Step II orientation maneuver. The success of the entire mission depends upon this maneuver, which orients the spacecraft spin axis normal to the sun-earth-probe plane (and therefore nearly normal to the ecliptic plane) causing the high-gain antenna to illuminate the earth throughout the mission. The nature of the Step II orientation maneuver precludes an actual earth-probe-sun angle of more than 2 or 3 deg below the 30-deg design value, although the angle can be considerably larger than this value. Above 30 deg, the earth-probe-sun angle is controlled by considerations other than those of the Step II orientation maneuver. The nominal trajectory showed an earth-probe-sun angle of 29.72 deg; the actual trajectory showed an earth-probe-sun angle of 31.04 deg. The actual trajectory, therefore, erred on the high side which is more favorable for the maneuver than an error on the low side. In this respect, then, the actual trajectory was a success.

**d. Comparison at syzygy.** The next important trajectory event is the passage through syzygy with the sun and earth. (Syzygy is the nearly straight-line configuration of three celestial bodies.) The syzygy passage was of direct interest to the scientific objectives of the mission rather than indirect, as was the case with the Woomera DSS rise and the earth-probe-sun angle at injection plus 23 h. For scientific purposes, the earth-probe distance at syzygy should have been no more than 500 earth radii, and the distance out of the ecliptic between  $\pm 10$  earth radii. The nominal trajectory met this objective quite well. The earth-probe distance and distance out of the ecliptic at syzygy on the nominal trajectory were 506 and -6.14 earth radii, respectively; for the actual trajectory, the figures were 463 and 9.30, respectively. The syzygy comparison is summarized in Table 26.

**Table 26. A comparison of the preflight nominal and actual trajectories at syzygy with the sun and earth**

Trajectory	Syzygy passage time, 1968	Earth-probe distance, earth radii	Distance out of ecliptic, earth radii
Preflight nominal	Jan. 16, 20:24	506	-6.14
Actual	Jan. 18, 14:24	463	9.30

The actual trajectory was an improvement over the nominal in the matter of the earth-probe distance at syzygy. The project scientists wanted a closer syzygy than the nominal 500 earth radii, but a design value as far below 500 earth radii as desired ran the risk of not escaping the earth at all in the event of a substandard third-stage burn. Therefore, the error on the low side of 500 earth radii must be considered favorable. The difference between the nominal figure of -6.14 and the actual 9.30 earth radii for the distance out of the ecliptic was fortunate. Had the difference of about 15 earth radii been in the other direction, the resulting 21 earth radii below the ecliptic would have put the spacecraft well outside the desired limits. It is therefore concluded that the trajectory also was a success in the matter of syzygy geometry.

*e. Comparison of the heliocentric trajectories.* There were very clear requirements on the aphelion distance and the inclination of the heliocentric orbit plane to the

**Table 27. A comparison of some of the characteristics of the heliocentric orbits of the preflight nominal and actual trajectories**

Trajectory	Aphelion passage time, 1968	Aphelion distance, AU	Inclination, deg	Longitude at aphelion, deg
Preflight nominal	June 12, 05:01	1.099	0.025	247.5
Actual	June 15, 14:58	1.088	0.058	252.4

ecliptic. The aphelion distance was to be not more than about 1.13 AU for reasons of power generated by solar cells, and not less than about 1.03 AU in order that the measurements of fields and particles would be in the proper regions of space near earth's orbit. The inclination of the heliocentric orbit plane to the ecliptic was to be less than 0.2 deg to enable the high-gain antenna to continue to illuminate the earth for long periods, and also to reduce, or eliminate, the number of necessary repetitions of the Step II orientation maneuver. A summary of the comparison of the preflight nominal and actual trajectories with respect to several heliocentric quantities is shown in Table 27. From this table it can be seen that, in this respect also, the actual trajectory was a success. The aphelion distance was quite close to the nominal and missed on the safe side, i.e., in the direction of more power from the solar batteries.

## IV. Development and Implementation

### A. SFOF Development

#### 1. Advanced Data Systems Project: Higher Level Programming Language, W. N. Walker

*a. Introduction.* The purpose of the advanced data systems (ADS) project is to provide a series of recommendations and standards for the SFOF computing system of the 1970s. One of the areas in which recommendations are to be made and standards established is that of higher-level programming languages. It is anticipated that application programming will be restricted to the use of higher-level languages in the operational system.

The advantages of using a standard higher-level language are:

- (1) A more easily defined, implemented, and controlled interface between the projects (application programs) and the DSN (operating system and equipment) is provided.
- (2) Development, verification, and certification of application programs is simplified.
- (3) More easily transferable documentation is provided.

- (4) The possibility of the use of application programs from other facilities is increased.
- (5) The SFOF installation becomes more site-independent.

Within the ADS project, seven tasks have been identified as being related to the use of a standard programming language. Two of the task areas are directly concerned with specifying the standard programming language. The remaining tasks investigate activities associated with the use of a standard programming language. A description of the important elements involved in each of the tasks follows.

#### *b. Programming language task descriptions*

*Programming language standards — 1969.* To aid in establishing and demonstrating some of the conceptual designs of the final recommended operational system, a pilot system is planned which is to be operational in 1969. In order to gain insight into the problems associated with establishing programming language standards for the operational system, standards for the pilot system will be established. In addition, a model of the language requirements of the DSN functional subsystems suitable for use

in examining and evaluating higher-level languages will be developed.

*Programming language standards — 1972.* The functional capabilities of the higher-level languages will be evaluated against the model of the language requirements of the DSN functional subsystems. The compiling, operating, and storage efficiency of the compilers of various manufacturers for the higher-level languages will be investigated. Also, a study shall be conducted into the use of higher-level languages by outside sources in comparable data systems. From these efforts, a recommendation regarding the selection of the standard programming language for the operational system shall be prepared.

*Special purpose languages — 1972.* The functional capabilities of selected existent special-purpose languages will be evaluated against the model of the language requirements of the DSN functional subsystems. A study will be conducted into the use of special-purpose languages and techniques by outside sources in comparable data systems. A study will also be conducted into the possibility of the development of a JPL special-purpose language. The results of the studies will be used to prepare a recommendation regarding the use of special-purpose languages for the operational system.

*Conversion of existing programs.* A standard will be developed for evaluating the cost, complexity, and trade-off considerations for the conversion programs for the current SFOF computing system to the recommended operational system. The evaluation standard will be used to analyze the current JPL application programs to determine which programs should be converted, on what time scale, and to what design criteria.

*Compiler characteristics.* A study analyzing the relative merits of the different compiler techniques and the usage of different compiler types in comparable installations will be conducted. A recommendation regarding the types of compilers and their functional usage in the operational system will be prepared.

*Software documentation standards.* Software documentation standards will be developed for the technical documentation required in the development of computer programs for the operational system. Standards will be developed for the statement of programming requirements, program design, program development, and program validation, for both the operating system and the application programming areas.

*Computer-aided software documentation.* A study will be conducted into the feasibility and desirability of developing and/or utilizing computer-aided documentation capabilities. Computer-aided documentation capabilities will be investigated both from the viewpoint of developing new documents and from maintaining already produced documents. A recommendation shall be prepared as to the development and utilization of machine-aided documentation within the operational system.

## **2. Advanced Data Systems Project: Operating System Recommendations, R. E. Loesh**

*a. Introduction.* In the last 12 years significant technical computer hardware advances have been made by all of the leading computer manufacturers. Coupled with this computer hardware advancement has come an entirely new concept of internal software automation (operating systems) designed to maximize utilization of the computers. The trend has been to allow the computer to perform more of the job scheduling, file control, space allocation, program and data residence decisions, input/output queuing, configuration control, error detection and correction, and system and data validation.

*b. Trend toward operating system development.* This trend has occurred largely because of the following:

- (1) Faster computer speeds.
- (2) Availability of a variety of main memory and auxiliary storage devices.
- (3) Coupling of many processing units so as to share memories and input/output interfaces and equipments.
- (4) Recent emphasis of on-line processing.
- (5) Real-time processing.
- (6) Remote batch processing.
- (7) Time-sharing systems.

To gain any reasonable efficiency through the use of these advantages, the decisions and actions previously made by man (computer programmer, operator, and users) had to be automated to meet the decision time requirements as well as the optimization and standardization required. In many cases, man exercises only an override or veto capability. However, it should be noted that while man has less control of details, he has greater policy control.

Contributions to the operating system have resulted from the development of:

- (1) Increased computer speeds.
- (2) Cheaper, larger, and faster main memory and storage devices.
- (3) Paging concepts.
- (4) Segmentation techniques.
- (5) Special addressing electronics.
- (6) Increased number of base registers.
- (7) Associative memory.
- (8) Trap and interrupt electronics.
- (9) Improved core-swapping electronics.
- (10) Scheduling algorithm.
- (11) Core allocation algorithm.
- (12) Reentrant coding technique.
- (13) Read-only memory concept.
- (14) Memory-use and -protect electronics.
- (15) Coupling and controlling of processing unit concepts.
- (16) Memory-sharing electronics.
- (17) Emergence of time-sharing concepts.
- (18) Improved error detection and correction techniques.
- (19) Multiprogramming technique.

Many of the above concepts and techniques are either in the early stages of development and their value is not yet clear, are in conflict with one another, or are applicable to particular job mixes or types of problems. Some add to system complexity and reduce reliability or are costly and time-consuming. The present development stage of each must be considered in developing an operating system to support the DSN responsibilities in the 1970s. A recommendation can be made only after thorough supporting investigation, analysis, comparison, and evaluation have taken place.

**c. ADS project operating system recommendation approach.** There are seven ADS project studies directly supporting the operating system recommendation:

- (1) SFOF operating system requirements, Task 4B1.
- (2) Operating system analysis, Task 4B2.
- (3) Operating system overhead, Task 4B5.

(4) System modeling, Task 497.

(5) Operating system management, Task 4B3.

(6) Second-generation yardstick, Task 4B6.

(7) 1972 operating system recommendation, Task 4B4.

In addition to these, several other ADS project studies will indirectly support the operating system recommendation.

Task 4B1 is to gather the SFOF operating system requirements. This study will be done in two phases: the first phase will be a 3- to 4-month activity to take a cursory look at what other ADS task cognizant engineers expect to require and to develop the technology for gathering the requirements; the second phase will be a 7- to 9-month activity beginning in the fall of 1968, which will develop the requirements in detail.

Task 4B2 will use the work of the SFOF operating system requirements study to emphasize capabilities to be stressed in the test packages. This task will provide: information on which operating system capabilities are presently available in the industry, detailed knowledge of the techniques they utilize, and an evaluation of their value.

Task 4B5 will work in concert with Task 4B2 to measure the time and core costs of the different operating systems as a whole, as well as their individual capabilities and techniques. This study will also utilize some of the services of Task 497 to optimize the particular set of operating system capabilities and techniques best suited for the SFOF.

Task 497 is a service to all of the studies. One of its main purposes will be to assist in the modeling of operating systems.

Task 4B3 will lag the above studies by about nine months to take advantage of the knowledge and experience gained. It will be a study of accounting techniques, control parameters, equipment allocation considerations, operator and job submission procedures, and organization and authority structures of the operation system management. It will also provide guiding information to management on operating system analysis and evaluation.

Task 4B6 will be done in parallel with other studies. This study will define the job mix, gather data relating to operating system functions, express system operations by ratios, and allow for demonstration of third-generation concepts. These results and demonstrations will support

the system modeling study by providing input parameters. It will also strongly support the operating system recommendation study by providing second-generation measures to compare with the results of increased capability studies.

Task 4B4 will be the culmination of the other studies. It will not begin until each of the other studies are approximately 90% complete. The preceding studies will produce an aggregate of recommendations concerning all aspects of operating systems and JPL requirements. This study will assimilate these findings and those of the other relevant ADS project studies to produce a coordinated recommendation. The recommendation will be so written that if a set of capabilities is developed for the SFOF different from the one indicated by our analysis, the results of the studies could be reanalyzed and new recommendations could be made without revising any of the tasks except Task 4B4.

### 3. SFOF Mission Display System, C. A. Yamarone and C. J. DeForrest

**a. Objective.** The principal objective of the SFOF mission display system (MDS) was to fulfill the following functional requirements:

- (1) Large-area display.

- (2) Flexibility.

- (3) Four-mission display capability.

The system design was to be based on functional requirements, SFOF space allocations, resources available, and current technology. The contract for the system was issued to Northrop Nortronics.

**b. Capabilities.** The MDS is basically an alphanumeric and graphic projection display of four  $7 \times 8$  ft mission screens (Fig. 1). The MDS can supply the SFOF/DSN operational and gallery area personnel with mission-independent and mission-dependent summary information in color and also provide a good-quality monochrome image for SFOF closed-circuit TV distribution. Live video projections of launch activities are supplied by two Eidaphor video projectors and graphic information is displayed on the two major mission screens (Fig. 1).

**c. General description.** Each of four projection displays are made up of: one  $7 \times 8$  ft back projection screen, one four-projector cabinet, one plotting projector, one spotting projector, one reference projector, one electronic equipment cabinet, TTY console, support chief console, one tracing table control console and automatic send and receive (ASR 35) TTY keyboard (Fig. 2). The

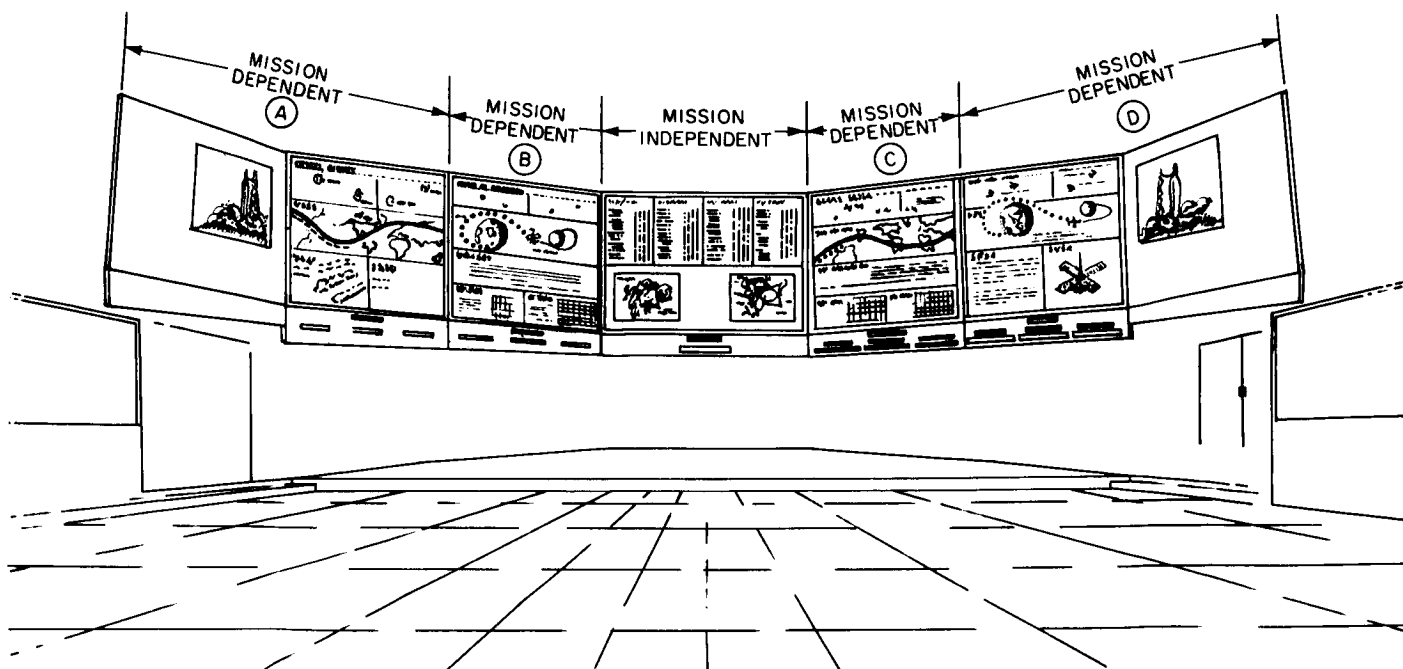


Fig. 1. New MDS configuration

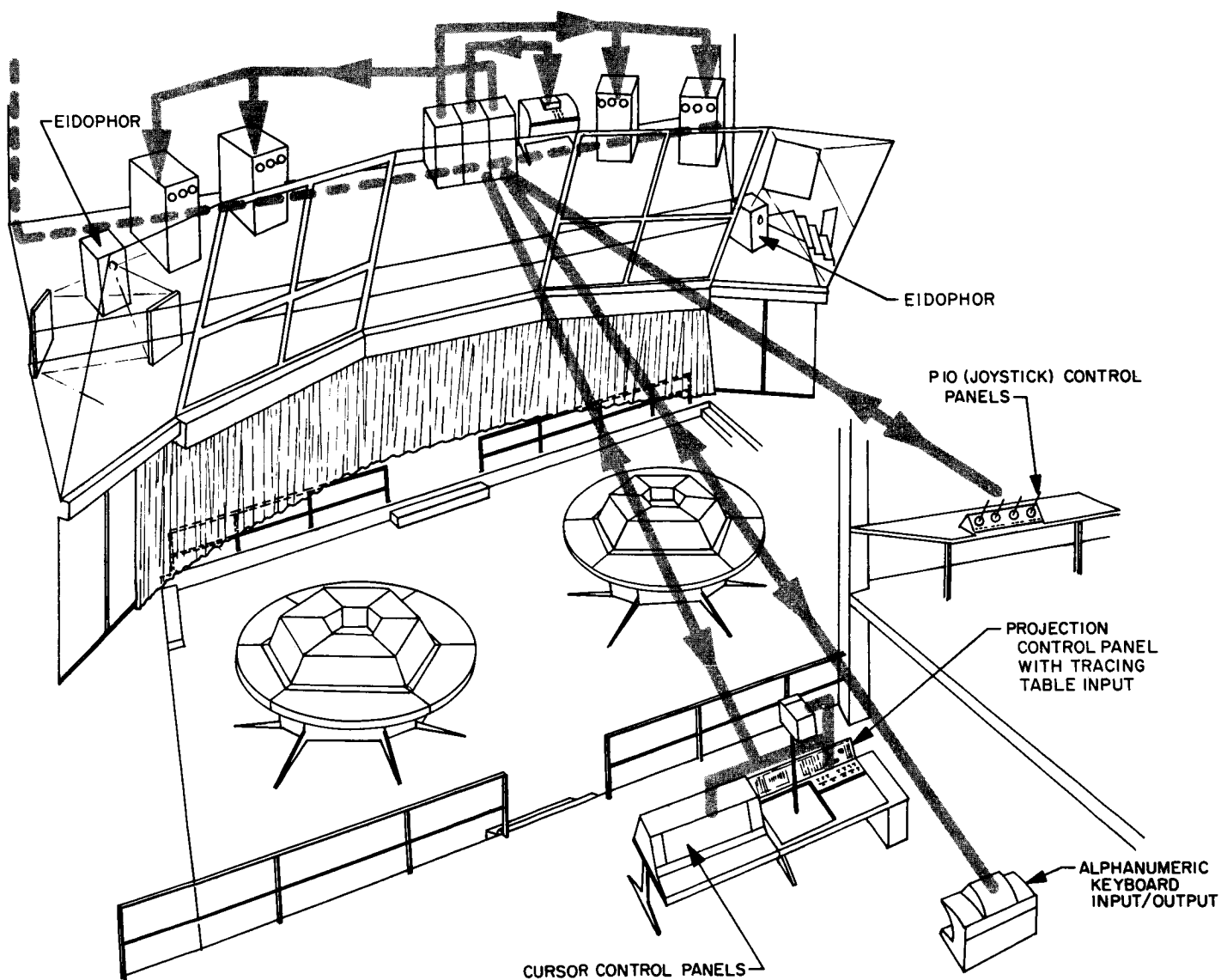


Fig. 2. MDS projection display



MDS equipment is so arranged that, except for maintenance and up/down power operations in the rear of the display screen, this system is fully operated from the support chief/tracing table console area.

*d. Projection system.* Each of the three projectors which make up a mission projector array are precision optical projectors which can nearly perfectly overlay (orthogonally) their individual images on one screen (Fig. 3), i.e., three identical slides projected simultaneously from the three projectors would produce only one image on the same screen.

*e. Plotting projection.* The plotting projector has the following features:

- (1) A remotely controlled servo plotting system.
- (2) Precision overlay optics.
- (3) A symbol plotting speed of six symbols per second from an ASR 35-keyboard control.

(4) Control from the tracing table console of six selectable plotting colors, 40 randomly selectable slides per magazine, and a remote illuminator on-off control.

(5) A keyboard control of the following plotting projector functions:

- (a) Sequential slide change.
- (b) In-and-out of plot control.
- (c) Cartesian coordinate positioning of plotting stylus.
- (d) Semiautomatic selection of three symbol sizes: 1.2%, 2.4%, 3.6% of screen width plus appropriate offsets per symbol.

*f. Reference projection.* This projector has the same function as a plotting projector, except that the reference projector does not have plotting or sequential slide selection inputs or capability.

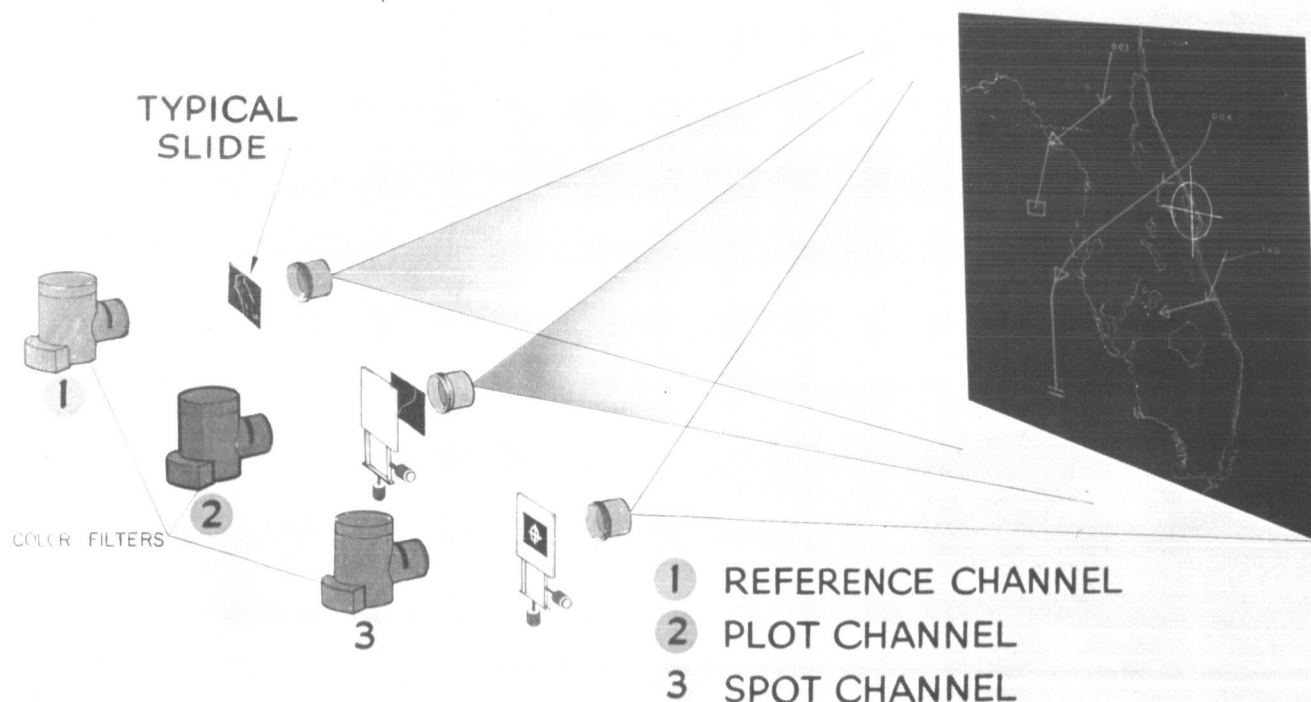


Fig. 3. Vigicon overlay technique

**g. Spotting projection.** The spotting projector has these features:

- (a) A remotely controlled servo spot-positioning system with analog inputs from the joystick, tracing table, and cursor's digital-to-analog converter.
- (b) Precision overlay optics.
- (c) A manual single slide change of a plotting slide for spotting and cursor functions.
- (d) Control from the tracing table console of six colors and remote illuminator on-off switch.

**h. Cursor (mission event) capability.** The cursor feature is provided by the use of a spotting projector. This spotting projector is driven by a Minneapolis Honeywell DDP 416 computer input and provides via cursor control panel selection four inputs of preprogrammed counters per mission screen. These programmable counters may be programmed for a cursor full screen travel of from 3 min to 90 days. The initial programming provides full-screen deflection of the cursor line in 45 min, 90 min, 15 h, and 24 h. The DDP 416 computer receives a synchronizing input from the SFOF time system's normal and simulation generators, one sync input per mission set of four counters. The MDS also receives eight hold in-

puts, two for each mission set of four counters for semi-automatic SFOF time control of the cursor's sync inputs.

**i. Mission support.** The MDS equipment supported a complete mission of *Surveyor VII* in January 1968. This coverage included such various phases as: launch, earth orbit, space tracking, midcourse, and lunar touchdown (Fig. 4). The following multi-colored displays were used:

**Mark events.** Two slides of 26 events were updated during initial phase of mission from monitoring of Air Force Eastern Test Range net. See Fig. 4, far left screen.

**Earth tracking.** One slide provided updated position of spacecraft on earth-predicted tracks and the acquisition and loss of signal chart of tracking sites and picket ships. (Fig. 4, second from left.)

**Mission events.** Several slides and cursor time scales were used to show continuous events during the mission with respect to time (Fig. 4).

**DSIF view periods.** Two slides covered the 24-h day with a continuous 12-h look-ahead. This display plotted rise and set times of each deep space station, and the transmission configuration (send only, send and receive,

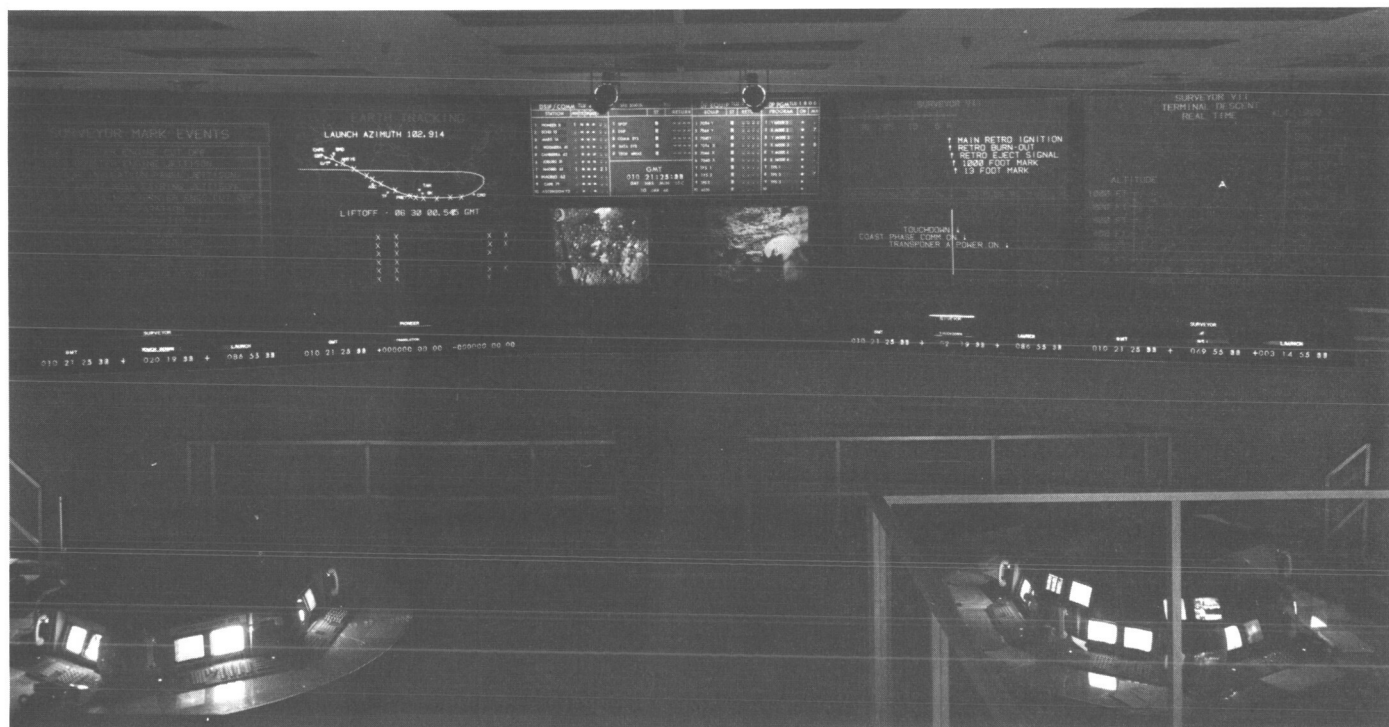


Fig. 4. SFOF mission display system

or receive only) by use of arrows, from a deep space station antenna symbol to a *Surveyor* spacecraft symbol.

**Terminal descent.** This display was used to show in real-time the descent of the spacecraft onto the lunar surface. The actual input for this display was originated from spacecraft transmission. The capabilities of the display were implemented by using a symbol of *Surveyor* spacecraft, during actual descent, to show position on velocity versus altitude plot and had a plotter projector recording the actual output of the telemetry processing system digital-to-analog converter. The terminal descent display was viewed in real-time on network television from SFOF closed-circuit TV monitors in the Von Karman auditorium (Fig 4, far right screen).

**Deep space station received signal (-dBm).** One slide was updated each hour to show signal strength during mission.

**Velocity and distance versus time.** One slide was shown of a canned plot to depict relative expectant velocity versus time and distance versus time.

#### **4. Communications Processor/7044 Computer Redesign System Test Series, R. G. Polansky**

**a. Introduction.** During the period from January 1, 1968 through May 15, 1968, a series of tests will be run on the SFOF's communications processor (CP) and 7044 computer redesign hardware and software to establish the behavior of this system under various loading conditions; the results of the tests will be used to develop better operating procedures and to recommend design changes.

The tests will be run using a Mode 2 SFOF hardware system (7044-Disk-7094 combination) and the Mod 2 version of the communications processor program. This will make the results most applicable to projects which will be using the SFOF data processing capabilities for the next several years, e.g., *Mariner Mars 1969*.

The test plans and sequence of events (SOE) used in these tests will become part of a library of entries in the DSN documentation tree. These test plans and SOEs can later be put to use in the running of SFOF, and GCF capability verification tests.

At this time, two test plans and two SOEs have been generated, and the first test in the series has been run. This test is described, along with its preliminary results, in this article.

**b. Test description.** The first test used *Mariner Venus 67* data, input to the system at both 8½ and 33½ bits/s. Data sources used were the telemetry processing station's phone line formatter for high-speed data and the communications processor system for teletype data. The objectives of the test were to determine:

- (1) The effects of increasing the number of TTY output devices being used by the CP/7044 system.
- (2) The effects of 7094 computer program activities on the CP and 7044 computer delay characteristics.
- (3) The effects of Mode 2 and Mode 3 predict transmission on the CP and 7044 computer delay characteristics.
- (4) The effects of Goddard high-speed (MUX) data on the above characteristics.
- (5) The cause of the delays in routing TTY telemetry data through the CP, to the 7044 computer and to a TTY machine. (This is a typical *Mariner* configuration.)

**c. Results.** The results obtained from the first test are necessarily preliminary. They consist primarily of delays in the overall system and a group of statistics gathered from the CP during the test. It is noted that the characteristics determined agree almost completely with the functional design of the system as originally specified. The delay times were:

- (1) No measurable delays in 100-words/min teleprinter responses were caused by running 7094 computer programs.
- (2) The delay between the time the CP took the data from the 7044 computer to the time it displayed it on a 100-words/min teleprinter averaged 7.93 s. High values of 16 and low values of 4 s were noted. There appeared to be no correlation in these delays to incoming bit rate, to incoming data source (TTY or high speed), or to the number of teleprinters being used.
- (3) The delay between the time the data is available to the CP and the time it is accepted by the CP averaged ten ms; however, several notable exceptions occurred. First, transmission of a NASCOM header to the CP caused up to a 2.2-s wait. Second, transmission of predicts to one TTY machine caused a delay of up to 3.3 s. Last, transmission of predicts to two TTY machines caused delays up to 7.9 s. It seems reasonable that the delays noted are a

function of the length of the predict transmission. This will be tested in more detail later. The delays caused by predict transmission seems to be independent of computer Mode 2 or Mode 3 operation.

- (4) Inbound data in the TTY burst mode was played through the CP and output on a TTY machine. The average delay in the CP was 21.1 s, with highs of 28 s and lows of 14 s. It is felt that these delays would be uniformly less if the incoming data was continuous. This will be verified in a future test.

#### **d. CP statistics**

- (1) The busy rate during CP idle condition was about 8%.
- (2) The average busy rate of the CP during the test was 13%.
- (3) The maximum busy rate observed was 84%. This figure existed for a little more than 1 s and occurred when all 17 TTY data printers, both predict display machines, and the Goddard MUX interface were in use.
- (4) An average of 4 to 6 s elapsed between the time the CP received the data and the time it was written onto the drum.
- (5) A maximum of 23 simultaneous drum input/output (I/O) requests were made during the test. This corresponded with one I/O request made for each input and output to the CP. (It happened that each I/O element used in the test requested service at this one time.)
- (6) It appeared that TTY machine activity tied up pack areas for 4 to 6 s at a peak value equal to twice the number of machines in use. The rest value was a half of this peak value and persisted until the next data burst was received from the 7044 computer. The 4- to 6-s figure may be a function of the data line length from the 7044 computer. This will be determined in a future test.
- (7) The maximum number of pack areas used was 42. This occurred at maximum system loading for this test (see item 3).
- (8) The maximum number of validation table entries observed was six. In theory, there should be one for each message received by the CP.

## **B. GCF Development**

### **1. Configuration Changes, F. E. Bond, Jr.**

The design of the capabilities of the DSN/GCF is based on the known requirements imposed by DSN commitments to support the communications needs of user agencies. Since these requirements are subject to continual revision, the configuration of the DSN/GCF is constantly undergoing change. As a result of the completion of the *Surveyor* Project activities, three changes resulted: (1) the teletype and voice circuits from the SFOF to the Hughes Aircraft Company were removed; (2) the 6-MHz link between the SFOF and the Goldstone area used for video transmission was also removed; and (3) two voice circuits normally used during launch operations between the SFOF and Cape Kennedy were removed.

Configuration changes made to the DSN/GCF not directly related to flight projects include upgrading of several SFOF-to-Goldstone teletype circuits from 45.45 baud (60 words/min) to 74.2 baud (100 words/min). In addition, a major milestone was reached in February 1968 with the implementation of the Modification 2 program relative to the JPL communications processor. Other changes to the DSN/GCF were made with the deletion of several voice and teletype circuits used as common-user trunks between the SFOF and NASCOM.

## **C. DSIF Development**

### **1. 210-ft Antenna Tower Positional Stability, H. D. McGinness**

**a. Introduction.** The positional reference of the 210-ft antenna at Mars DSS is provided by the master equatorial, which is mounted on top of the instrument tower, as shown in Fig. 5. In order to utilize the accuracy of the master equatorial, it is necessary to limit the angular movement of the instrument tower top to a value approximately equal to the error of the master equatorial. As described in SPS 37-46, Vol. III, pp. 115-119, the master equatorial error could be taken as 2 or 3 arc sec.

Among the factors that could contribute to angular displacements of the tower top are: material dimensional instability, movement of the soil beneath the tower, and temperature gradients within the tower structure. It is believed that temperature-gradient effects are the most significant, and to these effects has been directed the most attention.

**b. Instrument tower measurements.** Both temperature and angular change measurements have been made on

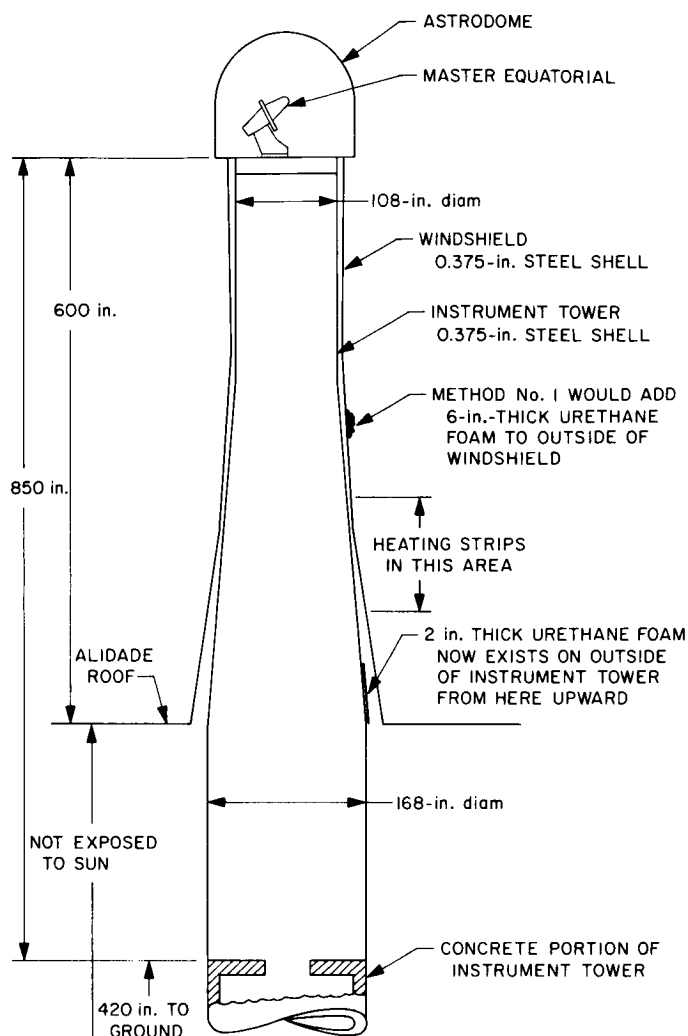


Fig. 5. Instrument tower configuration

various parts of the tower structure. Temperature measurements have been made on various portions of the windshield which surrounds a portion of the tower. Most of the angular change measurements were made with a pair of Ideal Aerosmith Model DCTM-11 precision recording levels. During one test the level readings were compared to those obtained by directing the master equatorial's autocollimator toward a gravity mirror. As the two sets of readings were very nearly the same, considerable confidence in the accuracy of the levels was established.

Temperature differences across the windshield were measured by surface thermometers. Temperature differences across the tower were measured by both mercury thermometers and thermocouples.

Figure 6 shows the results of the level readings made over a 36-h period in December 1966 during a time

when the antenna was stationary at 180 deg azimuth and 5 deg elevation. The levels were placed on the tower top just beside the master equatorial and aligned so that one measured rotation about a north-south axis and the other measured rotation about an east-west axis. During this entire period, the wind did not exceed 10 mph, and the days were bright and clear. Temperature measurements were made hourly. It was found that the maximum temperature difference across the windshield, measured approximately 60 in. above the alidade roof, was 29°F. This represents the difference between the sunny side and the shady side of the windshield. The maximum measured difference across the tower was approximately 1°F. Under these conditions it would be expected that some evidence of a daily cycle would be manifest in the level records. An examination of Fig. 6 does show such a cycle. Moreover, the general movement of the tower was that which was expected, considering that the sun was on the south side. (The convention used in all of the level records is that of the right-hand screw; that is, the angular displacement sense of an arrowline is that of a right-hand screw turning so as to advance in the direction of the arrowline. The angular change magnitude is proportional to the length of the arrowline.)

It may be seen in Fig. 6 that between 08:00 and 14:00, the bright sun hours, the tower rotation is generally about an east-west axis, which corresponds to the south side of the tower being heated. The maximum total excursion during this 36-h period was 6.7 arc sec.

In July 1967 similar level measurements were made over a 168-h period. During these tests the levels were located inside the master equatorial base rather than on the floor beside it. These tests were made during the normal operation of the antenna, and no daily cyclic pattern was expected or discovered. The total angular excursion of the master equatorial base was 12.7 arc sec.

In May 1967 the two levels were moved to the top of the concrete portion of the instrument tower and aligned with the north and east axes. As Fig. 5 shows, the concrete portion of the tower is always shaded; however, it is exposed to drafts when certain doors are open. The angular displacement of the concrete tower top over a 48-h period is shown in Fig. 7 from which it may be seen that the total excursion was 3.2 arc sec.

Since it is known that a finite amount of static coupling exists between the instrument tower and the antenna pedestal (the two masses are connected by soil), it was wondered whether any significant portion of the 3.2 arc sec



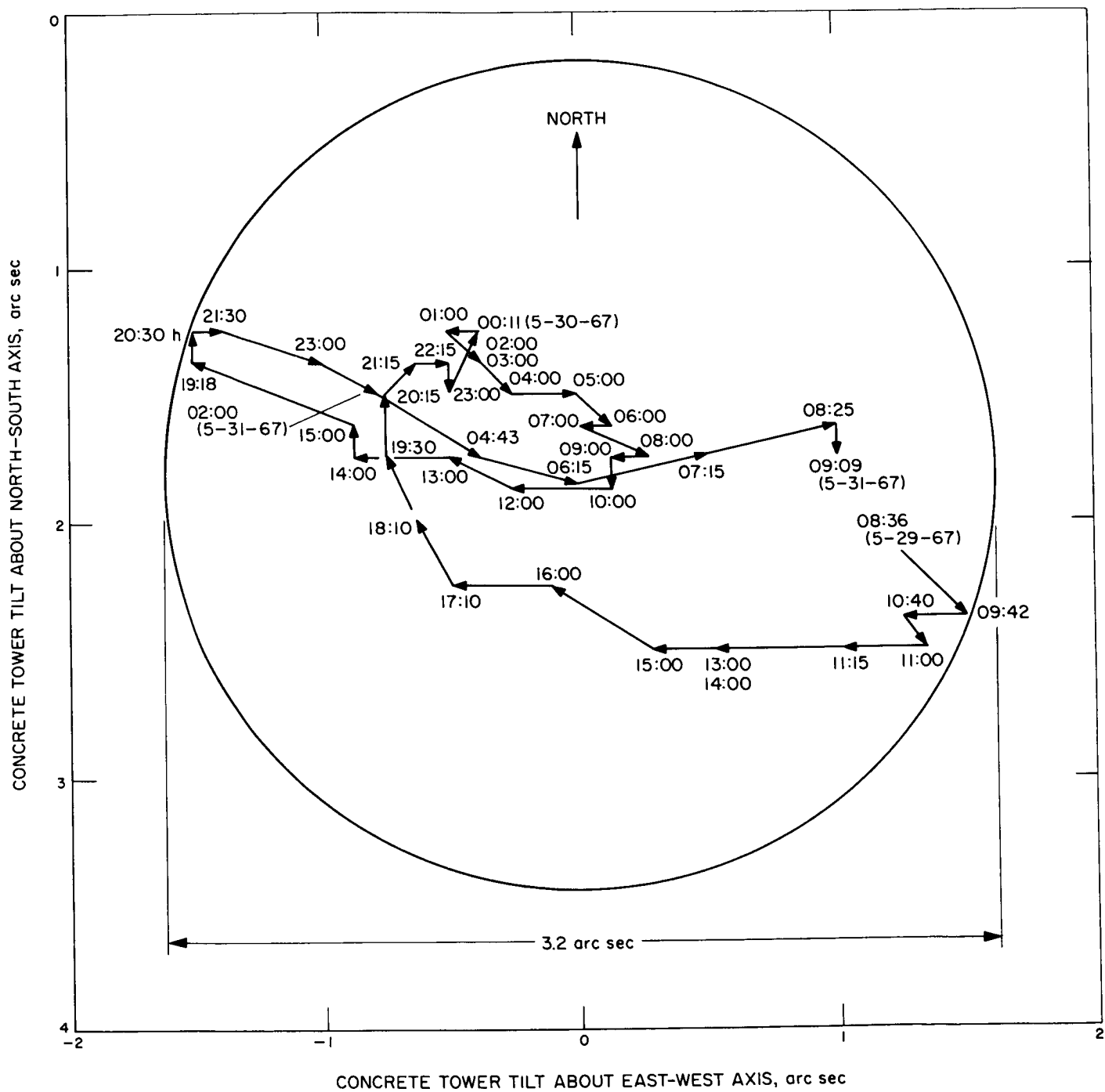


Fig. 7. Tilt at top of concrete portion of instrument tower over 48-h period during antenna operation

was caused by this coupling. During a windy night the levels were recorded while the antenna was slewed quickly over its complete ranges in both azimuth and elevation. The total angular excursion of the levels was approximately 0.10 arc sec, therefore, it must be inferred that the 3.2 arc sec excursion was caused by thermal gradients in the concrete portion of the instrument tower.

The foregoing measurements have established that the angular excursion of the instrument tower top is large compared to the master equatorial error and that temperature gradients within the tower structure are primarily responsible for its movement.

#### c. Methods for reducing instrument tower movement.

The following methods for reducing the tower movement have been investigated:

- (1) Addition of insulation to outside of windshield.
- (2) Establishment of convection air currents inside the tower for the purpose of increasing heat transfer across the tower and thereby decreasing the temperature difference across the tower.
- (3) Augmentation of heat transfer from hot to cold side through water coils attached to the inside of tower wall.
- (4) Installation of servo controlled heating system.

**Method 1.** A simplified model for method I was arrived at by first considering the tower and windshield as being infinitely long so that the heat-transfer problem became a two dimensional one. Next, it was assumed that the concentric windshield, insulation, and tower, each of circular cross section, were transformed into "concentric squares." It was assumed that one edge of the outermost square was at constant temperature  $T_0$  and that the opposite outermost edge was at constant temperature  $T_n$ . For the proportions involved here, it turned out that the conductive heat transfer through the connecting walls, that is, the walls perpendicular to walls  $T_0$  and  $T_n$ , was negligible. Thus, the simplified model became a series of parallel plates separated by insulators, as shown in Fig. 8. A much more refined model was considered and a computer solution was developed. Its numerical results were very nearly the same as those of the simplified model. Since the simplified model is amenable to an algebraic solution, it will be presented. Given the configuration of infinite parallel plates, shown in Fig. 8, having a constant temperature difference  $(T_0 - T_n)$  across the assembly of plates, the problem is to determine  $(T_3 - T_4)$ , the tem-

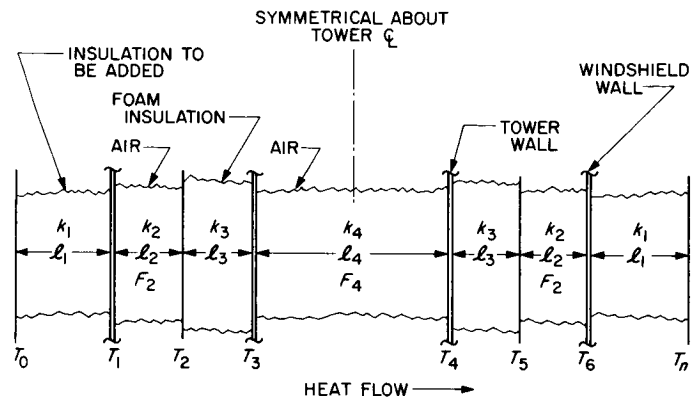


Fig. 8. Simplified heat-transfer model of instrument tower

perature difference across the instrument tower. The simplified solution is given by the following equation:

$$\frac{T_3 - T_4}{T_0 - T_n} = \frac{1}{1.18 F_4 \left[ 2 \left( \frac{l_1}{k_1} + \frac{l_3}{k_3} + \frac{1}{1.18 F_2 + \frac{k_2}{l_2}} \right) + \frac{1}{1.18 F_4} \right]} \quad (1)$$

where

$l_1$  and  $l_2$  are in ft

$k_1, k_2, k_3$  are in Btu/(h-ft-°F)

$$F = \text{emissivity factor} = \frac{1}{\frac{1}{E_1} + \frac{1}{E_2} - 1}$$

with  $E_1$  and  $E_2$  representing the emissivities of the two radiating surfaces.

Equation (1) was derived by linearizing the  $(T_i^4 - T_{i+1}^4)$  term in the radiation equation. Such an approximation is justified because any temperature difference involved in the problem at hand is small compared to the absolute temperature.

From Eq. (1) it may be seen that in order to obtain a small  $T_3 - T_4$ , it is desirable to have all  $l/k$  ratios large,  $F_4$  large, and  $F_2$  small. It is thought that  $F_4$  for the tower cannot be increased appreciably over its present value, since the existing surfaces are dull and rough, thus producing high emissivities. Also, it is not feasible to change  $F_2$  from its present value. If the following realistic values,  $k_1 = 0.025$ ,  $k_2 = 0.015$ ,  $k_3 = 0.05$ ,  $l_2 = 0.125$ ,  $l_3 = 0.166$ ,



$F_2 = F_4 = 0.818$  are substituted into Eq. (1), there is obtained:

$$\frac{T_3 - T_4}{T_0 - T_n} = \frac{1.033}{80l_1 + 9.51} \quad (2)$$

where  $l_1$  is in feet.

The existing windshield does not have insulation on its outer surface, thus the present  $T_3 - T_4$  value is obtained by setting  $l_1 = 0$  in Eq. (2). The ratio of  $T_3 - T_4$  with added insulation to  $T_3 - T_4$  of present design is:

$$\frac{(T_3 - T_4)_{\text{new}}}{(T_3 - T_4)_{\text{present}}} = \frac{1}{8.42 l_1 + 1} \quad (3)$$

where  $l_1$  is in feet.

**Method II.** One of the heat-transfer analyses showed that convection air currents inside the instrument tower might be effective in reducing the temperature gradient

across the tower. Because of the uncertainty of the value of the surface coefficient, a conclusion could not be reached from this analysis; therefore, it was tested experimentally by installing two 1-hp, 10,000-ft<sup>3</sup>/min electric fans on the top of the concrete portion of the instrument tower (Fig. 5). They were spaced 180 deg apart near the tower wall and aligned to blow the air helically upward. Smoke traces at various places within the tower showed that the air flow was as expected; that is, it spiraled upward around the inner wall and returned downward through the center. Level records made over a 24-h period with both fans on were compared with records made over the next 24 h with both fans off. As there was no significant difference in the total excursion (7.25 and 7.85 arc sec) of the two tests, it must be concluded that a practical amount of air circulation within the instrument tower cannot reduce the tower movement to an acceptable value.

**Method III.** If water is circulated within helical coils attached to the inside of the tower wall, the temperature gradient across the tower can be reduced. A heat-transfer

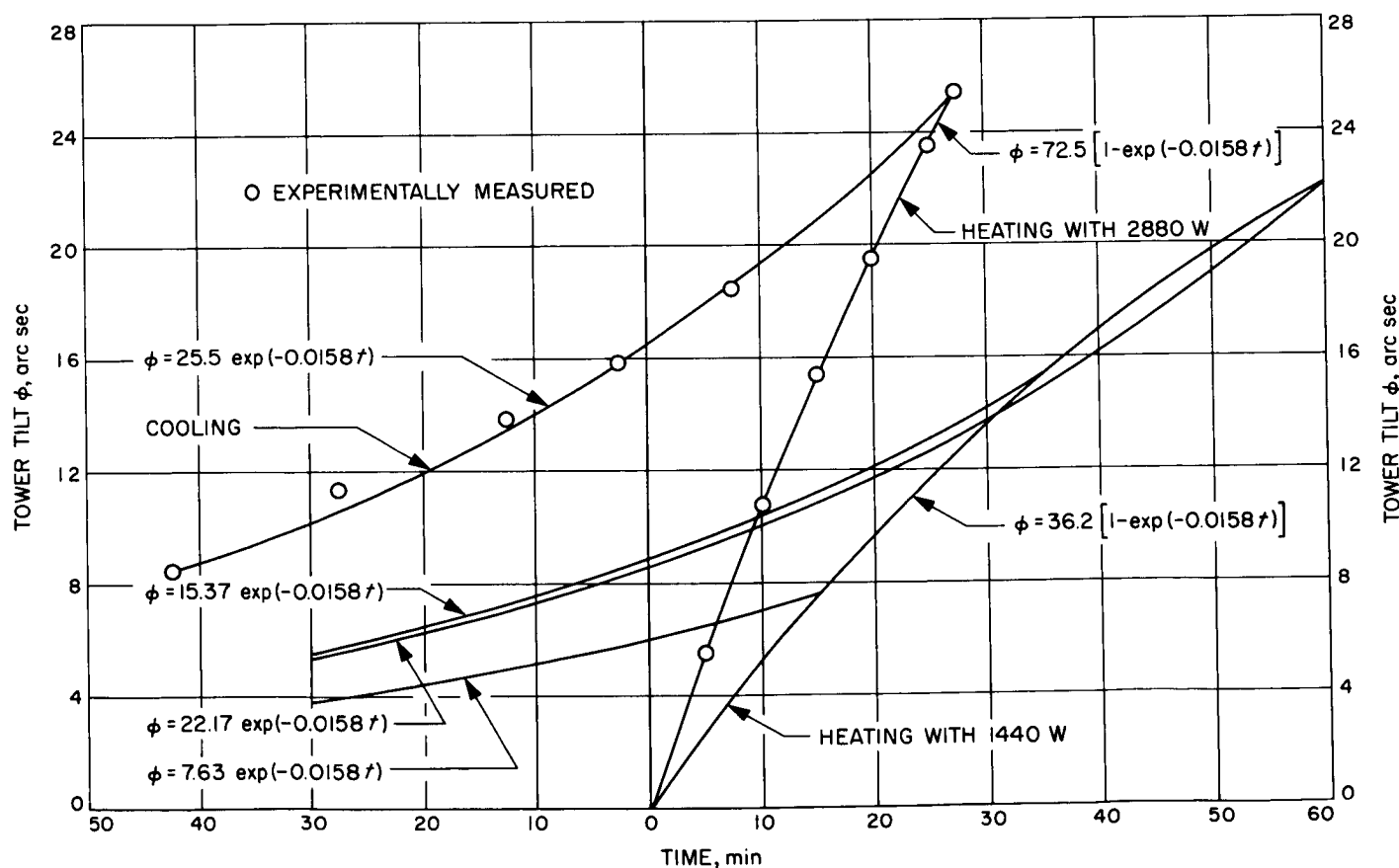


Fig. 9. Tower tilt versus time during heating and cooling of tower

analysis of this method was made from which the following conclusions were reached:

- (1) In order to reduce the existing temperature gradient by a factor of 5, the water cooling coils must be spaced 8 in., or less, apart.
- (2) In order to obtain sufficient heat transfer between the coiled tubing and the tower walls, the tubing must be fastened continuously to the wall and fastened in a manner, such as by brazing, that would produce good conductivity characteristics.
- (3) Approximately one mile of tubing would be required; hence the installation of such a system would be costly and would require an exorbitant amount of time.

**Method IV.** A servo-system, which control heats the tower so as to negate the larger portion of its motion caused by extraneous heating, was investigated. Preliminary calculations showed that ample tower motion could be obtained from a heating strip pattern of 2880 W. Four sets of heating strips were installed on the inside of the tower wall in the region shown in Fig. 5. The four sets were spaced 90 deg apart, and each set formed a rectangular pattern approximately  $72 \times 72$  in. When all strips in a pattern were energized, the dissipation was 2880 W. By energizing only alternate strips, the dissipation was 1440 W per pattern. By energizing the north or south strips, a plus or minus rotation about the east-west axis is obtained. By energizing the east or west strips, a plus or minus rotation about the north-south axis is obtained. Hence, by the proper distribution of current to the strips, a rotation about any horizontal axis may be obtained. If two level sensors, oriented properly, are employed to control the current to the strips, the tower level error may be kept within prescribed limits.

In Fig. 9 is shown the experimentally measured tower tilt plotted against time for the case of 2880 W at the north-side heater. The solid curves are theoretical, with parameters set to match the experimental curves. Since the rate of tower tilt is much faster than would be required, another set of calculated curves for 1440 W is also shown in the figure. It would appear that this rate of heating would always be adequate.

In Fig. 10 is shown the servo-system response for the case of heating each strip pattern with 1440 W. Two initial error curves are shown; namely, one for 5 and one for 10 arc sec initial error. If the servo-system is turned on when the initial errors are as indicated, the curves show the times required to reach lesser error values.

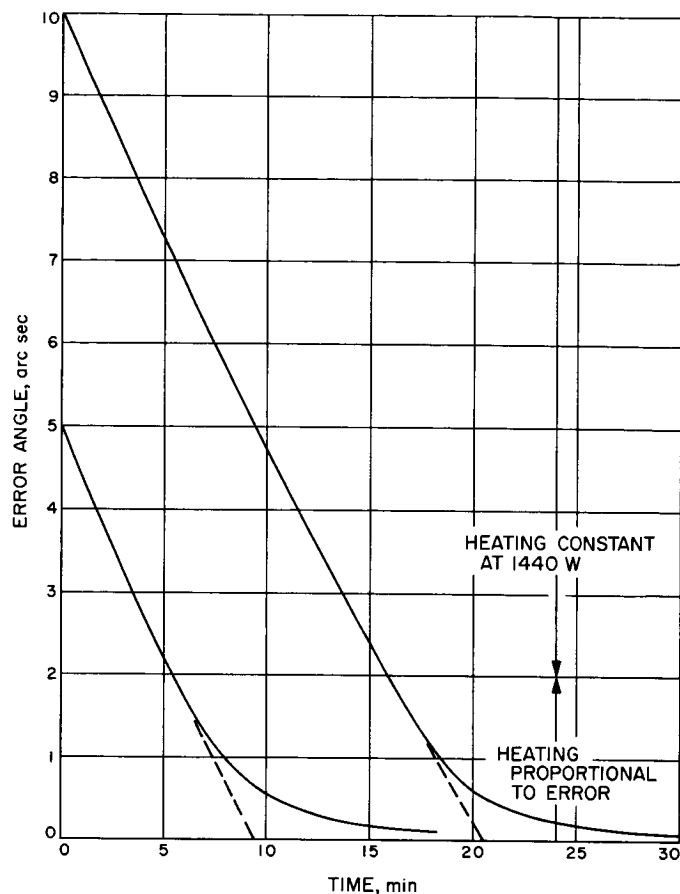


Fig. 10. Servo-system response

**d. Evaluation and conclusion.** The largest total angular excursion of the instrument tower top measured so far is 12.7 arc sec. This occurred continuously over a period of 168 h in July 1967 while the antenna was operating. It is unfortunate indeed that sensitive levels which can be recorded continually during dynamic conditions have not been available. It is not known what the maximum excursion is over a period of a year.

The largest total angular excursion of the top of the concrete tower measured so far is 3.2 arc sec. This occurred over a period of 48 h in May 1967, while the antenna was operating. The concrete portion of the antenna is surrounded by the cable wrap-up system in such a way that it is not practicable to add insulation to its outer surface.

If method I (the addition of insulation to the windshield) is used to reduce the tower movement, how much reduction can be expected? Additional insulation will not affect the 3.2 arc sec motion of the concrete tower. Assume that the steel tower moves  $12.7 - 3.2 = 9.5$  arc sec

with respect to the concrete tower. It is only this portion of the total movement that can be reduced by insulation. The maximum practical amount of urethane foam insulation which can be added is approximately 5 or 6 in. or 0.50 ft. With this value of  $l_1$  substituted into Eq. (3), there results:

$$\frac{(T_3 - T_4)_{\text{new}}}{(T_3 - T_4)_{\text{present}}} = \frac{1}{5.21}$$

which means that the temperature gradient across the steel tower has been reduced by a factor of 5.2. Thus, the 9.5 arc sec would reduce to 1.8 arc sec. The total excursion of the tower top on this basis would be  $1.8 + 3.2 = 5$  arc sec. The coefficient of conductivity of the added insulation was taken as 0.025 Btu/h-ft-°F in the derivation of Eq. (3). As this value is the lowest value of the material under consideration, a more realistic value would be higher, approximately twice as much, or 0.05. (Imperfect joints, cracks in the insulation, water absorption, etc., will tend to increase the effective value of the conductivity coefficient.) Therefore, a better estimate for the total excursion of the instrument tower top after the addition of insulation is 6.3 arc sec or approximately half as much as it is now. A disadvantage to the addition of urethane foam is that it is slightly flammable.

The success of a servo-control system depends largely upon obtaining or developing a suitable level sensor. Given such a sensor, there is no reason to doubt that the heating strips would hold the total excursion to within 2 arc sec or less, even though the uncontrolled excursion might be several times as great as that measured so far.

At the present time, experiments are being conducted on level sensors. The results of these experiments will appear in a later report.

## 2. 210-ft Antenna Quadripod Structural Analysis,

M. S. Katow and S. R. Paine

**a. Introduction.** The RF efficiency of the standard symmetric type of paraboloidal antenna is degraded markedly by the aperture blockage due to the subreflector or primary feed device and its supporting structure. The subreflector and the quadripod of the 210-ft antenna block, on the RF basis, approximately 6% of the aperture area and cause a gain loss of 0.62 dB or about 12% drop in aperture efficiency (SPS 37-42, Vol. III, p. 37).

The feasibility design study requirement was that the optical aperture blockage of the quadripod legs be lim-

ited to less than 8% of the aperture area. Accordingly, the final structural design by the antenna contractor considered the following additional design requirements:

- (1) The strength to lift a 62-klb feed cone load by the cone-hoisting system.
- (2) The natural frequencies of vibration about the three axes for use in the antenna-pointing servo-system studies.
- (3) The gravity deflections of the subreflector to minimize the overall uncompensated RF beam shifts with respect to the intermediate reference mirror.
- (4) The strength of the quadripod assembly to withstand a 120-mph wind with the antenna in stowed position.

This report describes the analytical and field analysis efforts made by JPL to check the compliance of the design calculations to requirements (1) and (2) only. The next report will discuss the design requirement (3).

**b. Discussion of design requirement (1).** The quadripod is shown in place on the 210-ft antenna in Fig. 11. The two top cone-hoisting pulleys are hinge-connected on the bottom side of each of the two upper legs of the quadripod. Figure 11 also shows the bottom pulleys of the hoist temporarily stowed against eyebolts on the center hub of the reflector structure.

The original design analysis of the quadripod was based on the STIFF-EIG (1) computer program with its limited 130 degrees of freedom. This required idealization of the structure to reduce the number of joints for the analysis of the one-quarter section of structural data. Thus some secondary bar members were lumped together in the analysis. The computation resulted in outputs of bar stresses, joint deflections, and the natural frequencies and deflected shapes for the first six modes of vibration.

The analytical checking analysis was set up for computation using the STAIR (2) program which was modified at JPL (SPS 37-46, Vol. III, p. 113). A complete one-half of the truss assembly of the quadripod which included every bar member was input to the program. By the use of symmetric and antisymmetric restraints at the joints, on the cutting plane, all static loading conditions could be analyzed. However, for the discussion of the design requirement (1) as listed above, only the symmetric hoisting load of 26 klb at 6-deg elevation angle will be considered at this time.

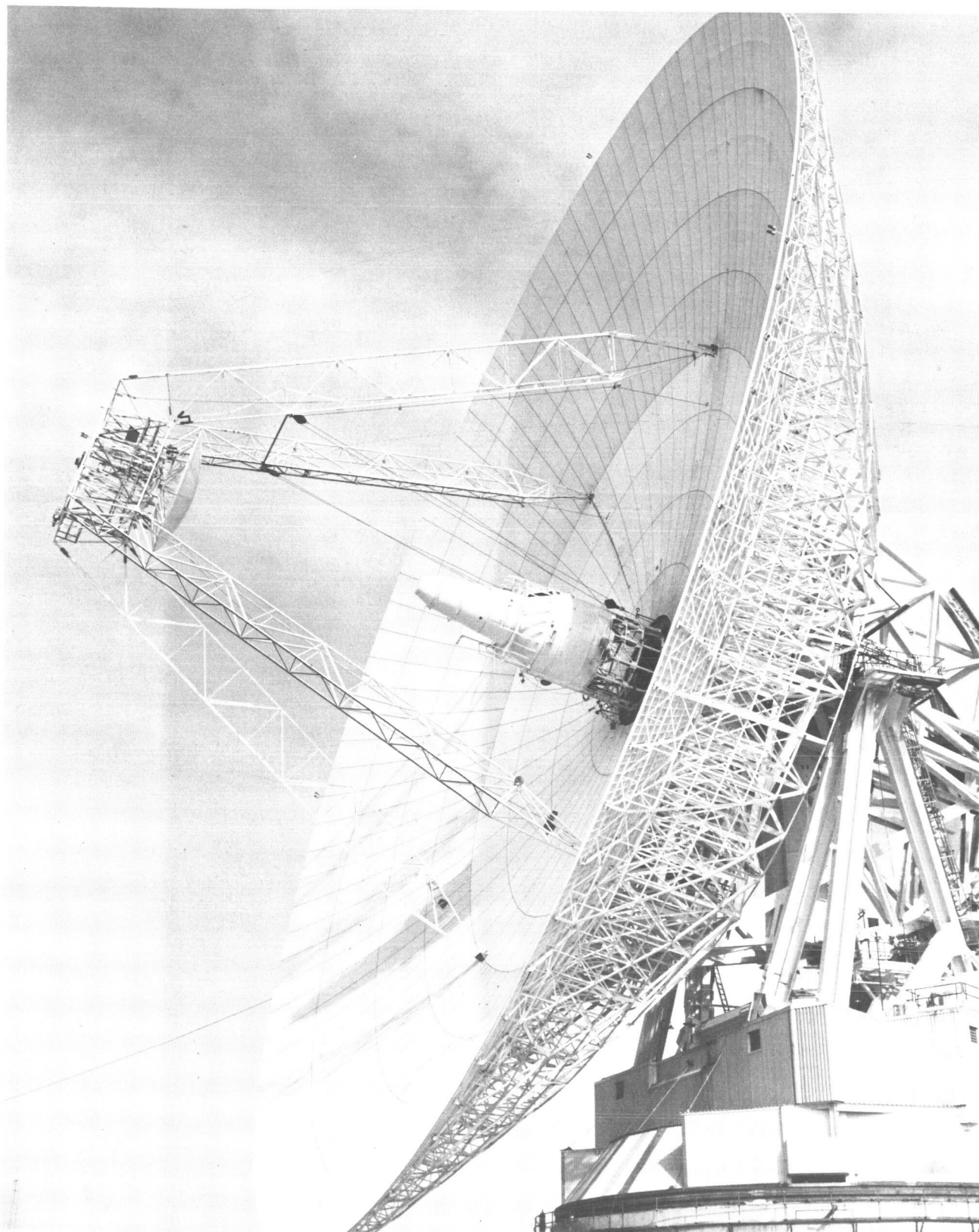
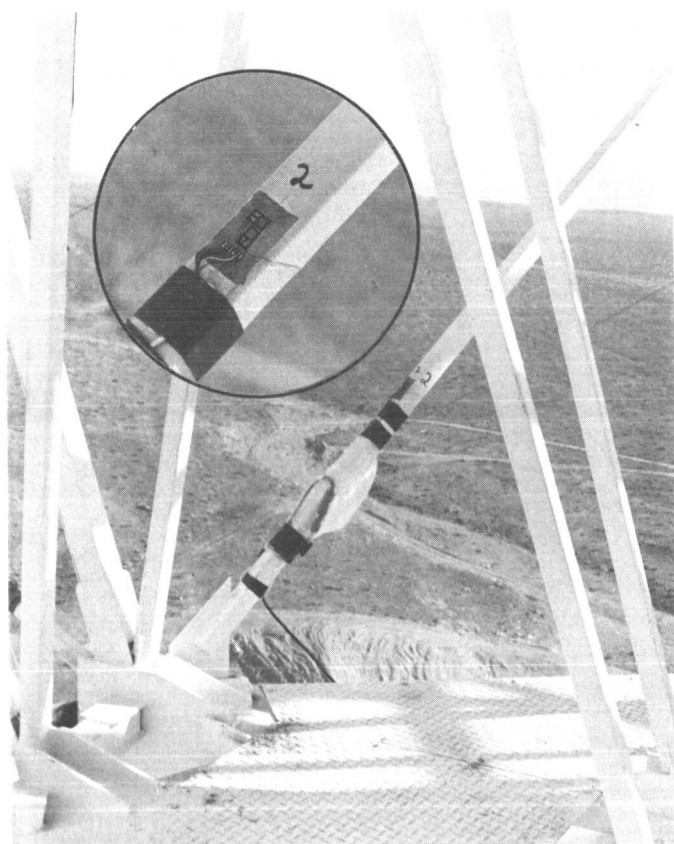


Fig. 11. 210-ft Antenna quadripod

The six bar members of high stresses as determined by the STAIR computations were checked in the field by the application of foil-type strain gages. Figure 12 shows a typical installation on a bar member in the apex structure of the quadripod. The enlarged view shows an active gage member mounted parallel to the stress direction with the temperature-compensating gage attached at right angles to the active gage. A duplicate installation on the opposite side of the square tube member was wired so that only the axial stress was measured.

Table 1 compares the bar member forces measured by the strain-gage field test and the forces computed by the STAIR computer analysis as well as by the rigid joint six-degrees-of-freedom SAMIS (3) computation, which will be discussed in Section C. The bar forces showed reasonable comparison checks between the field and analytical computer analysis when the cross-sectional areas of the bar members were obtained from the catalog tables, and the temperature-compensating gages were mounted directly on the member with an assumed Poisson's ratio of 0.3 used in the calculations.



**Fig. 12. 210-ft Antenna quadripod apex strain gage installation**

**Table 1. 210-ft Antenna quadripod static analysis<sup>a</sup> — field measurement versus analytical computations**

Bar member				Bar forces, klb		
No.	STAIR No.	SAMIS No.	Area, in. <sup>2</sup>	Field strain gage	STAIR (pin-jointed)	SAMIS (rigid-jointed)
1	201-205	79-55	3.089	-30.4	-36.12	-31.28
2	313-411	75-111	1.00	- 4.6	- 4.82	- 5.88
3	303-304	71-73	1.00	- 7.72	- 7.16	- 6.58
4	211-220	63-60	0.807	- 5.97	- 8.38	- 7.13
5	307-310	78-81	1.00	- 4.96	- 6.30	- 4.94
6	311-316	85-98	1.00	- 7.14	- 6.00	- 6.68

<sup>a</sup> 26-klb Cone hoist with quadripod at 6-deg elevation angle.

As a result of the check analysis, a total of ten bars were reinforced and a retractable tension strut between the two upper legs was added, as shown in Fig. 11, between the attaching points of the hoisting pulleys.

*c. Discussion of design requirement (2).* With the development of the JPL-organized SAMIS (3) structural computing program at a more recent date, a field versus analytical check was made on the natural frequency of the quadripod about the axis of symmetry. This mode of vibration was selected because it was the lowest and could be easily excited for stopwatch measurement. A man about halfway up one of the legs could excite the vibration by shifting his weight in synchronization with the mode and develop sufficient amplitude to measure at least 10 complete cycles.

The results are delineated in Table 2 and show that the answer from the rigid joint analysis compares closely with the field-measured data. This provides a sound simulated structure on which the design changes can be added to test the effects on the natural frequency.

**Table 2. 210-ft Antenna quadripod dynamic analysis — field measurement versus analytical computations**

Analysis method	Natural frequency/mode, Hz			
	1st <sup>1</sup>	2nd	3rd	4th
Field measurement	1.33	—	—	—
SAMIS-computed (pin-jointed)	0.99	1.94	2.45	3.34
SAMIS-computed (rigid-jointed)	1.29	2.15	3.81	3.98

<sup>a</sup> Vibration about the symmetric axis.



The SAMIS analysis used the maximum available programmed 43 discrete masses with the stiffness matrix built up from the one-half structure, using every bar member and with six degrees of freedom per joint. To simplify the input, the square tubes of the actual structure were assumed to be round.

Since the fundamental vibrational mode is about an axis which does not result in a RF beam shift in a symmetric cassegrain-type of antenna, only the higher modes are usually of interest to the antenna-pointing servo analysis.

### References

1. Wada, B. K., *Stiffness Matrix Structural Analysis*, Technical Report 32-774, Jet Propulsion Laboratory, Pasadena, Calif. Oct. 1965.
2. STAIR (*Structural Analysis Interpretive Routine*) *Instruction Manual*, Lincoln Manual 48. Lincoln Laboratory, Massachusetts Institute of Technology, Cambridge, Mass., Mar. 1962.
3. Lang, T. E., *Summary of the Functions and Capabilities of the Structural Analysis and Matrix Interpretive System (SAMIS) Computer Program*, Technical Report 32-1075, Jet Propulsion Laboratory, Pasadena, Calif., Apr. 1, 1967.

### 3. 450-kW Transmitter Mechanical Design, C. P. Wiggins and V. B. Lobb

**a. Introduction.** The 450-kW klystron is one of the largest and heaviest electronic devices to be mounted on a steerable antenna for operational use. Transmission losses in waveguide and rotary joints would be prohibitive if the klystron were placed on the ground. Larger and heavier klystrons are in use for long-range pulse radar; however, these are normally installed on the ground, since the low-frequency and low average power permit long high-loss transmission paths.

The transmitter cabinet containing the klystron will be located in the electronics room which has been installed on the 85-ft Az-El antenna at the Venus Deep Space Station. With the antenna at zenith, the klystron will be in a vertical position; at the horizon, the klystron will be tipped 90 deg. The cabinet design was required to protect the klystron from mechanical forces transmitted through the rigid waveguide due to relative motion between the electronics room and the cassegrain cone and to reduce deflections between klystron and cabinet to an acceptable level.

**b. Klystron stiffness.** The klystron, focus magnet, and cathode oil tank together weigh 1200 lb and stand 7 ft

tall. The cathode oil tank is flanged for attachment to the cabinet floor; the focus magnet is bolted on top of the cathode oil tank, and the klystron to the top of the magnet. Before the cabinet structural design could be completed, it was necessary to measure the deflection of the klystron window relative to the mounting flange of the cathode oil tank, since the window is attached to the klystron by a soft copper waveguide and is not capable of withstanding any appreciable force. The manufacturer had not measured these deflections, due to lack of suitable facilities.

In order to make these measurements, the klystron assembly was mounted on a large inspection fixture (Rotab) capable of tilting and rotating. The Rotab was attached to a horizontal rotary table set flush with the shop floor, and deflections were observed with optical inspection equipment.

The klystron is shown just prior to insertion in the focus magnet in Fig. 13. The cathode tank and magnet

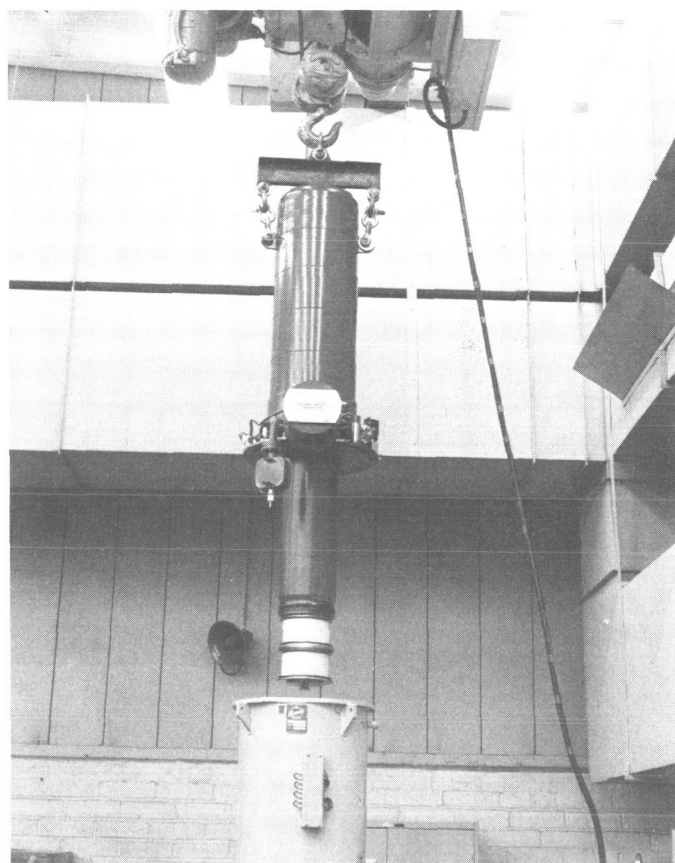
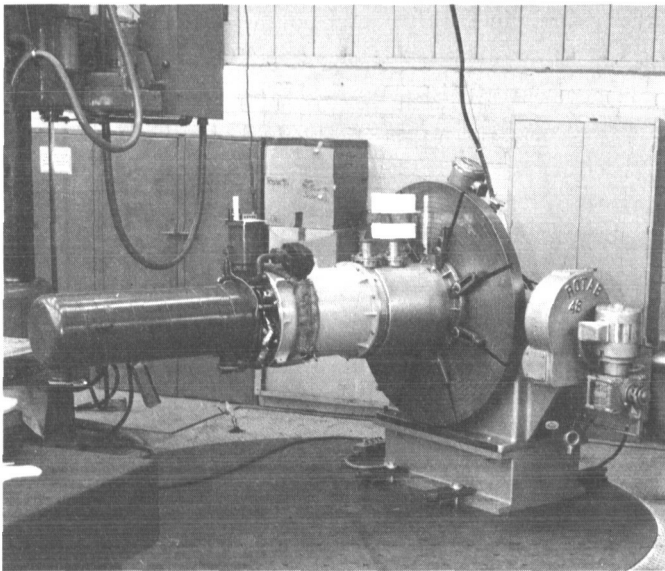
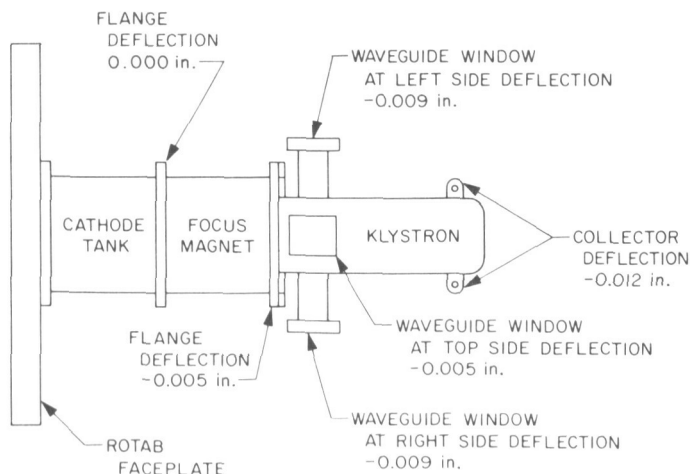


Fig. 13. 450-kW Klystron prior to insertion in assembled magnet and cathode tank

have already been assembled on the inspection fixture. The klystron assembly has been tipped over to horizontal in Fig. 14. In this position, three sets of observations were made with window up as shown in Fig. 14, window horizontal right, and window horizontal left. These were readily accomplished by rotating the circular table. The results (Fig. 15) show no deflection of the top of the cathode tank with respect to the base. The top flange of the magnet deflected 0.005 in., but the window sagged an additional 0.004 in. in the horizontal positions. When the window was vertical, the deflection was identical to that of the top of the magnet.



**Fig. 14. Deflection measurements, with klystron assembly horizontal**



**Fig. 15. Klystron deflection measurement**

The magnet deflection has been restricted by the addition of four  $\frac{3}{4}$ -in. stainless steel turnbuckles joining the cabinet to the four lugs on the top of the magnet. The residual 0.004-in. window sagging is probably due to the unsupported mass of the window assembly. This has been corrected in the transmitter by bolting the window to a waveguide assembly which is rigidly attached to the cabinet.

*c. Transmitter cabinet design.* The design problems associated with the development of the transmitter cabinet were varied. The following are the main problems that were considered:

*Allowable transmitter cabinet deflections for proper support of klystron tube.* Data on the stiffness of the transmitter cabinet was required to determine the amount of deflection that would occur due to the following:

- (1) Weight of the klystron tube.
- (2) Weight of the cabinet and equipment.
- (3) Weight of the waveguide.
- (4) Applied waveguide loads due to differential deflections.

The transmitter cabinet was modeled for the computer analysis as a three-dimensional space frame which consisted of tubular members. The computer analysis of the cabinet was developed during the design period of the cabinet, during which JPL furnished the vendor with inputs as to its structural configuration. The computer model had 25 joints and 56 members. It was analyzed for six different load conditions: the four previously mentioned conditions plus two transverse load cases caused by inertial loading due to antenna braking.

The computer analysis was run on the STRESS computer program and also on the JPL STIFF-EIG program as a check. The analysis provided member stresses and the structural distortions of the cabinet.

The analysis of the structure indicated the need for additional stiffness at the klystron tube to bring the deflections to within allowable limits (0.002 at the window in the tube).

The differential deflections between the feed cone and transmitter caused loads to be placed on the transmitter cabinet introduced by the interconnecting waveguide run. These applied loads proved to be too great for the klystron window to withstand. Therefore, the cabinet was redesigned to carry these loads.

*Allowable heat losses to the room from the transmitter.* The 450-kW transmitter has the potential to dissipate a megawatt of heat to its enclosure. Most of this heat is removed by cooling water flowing at 300 gpm. On a hot day this water can be as hot as 150°F, while the room temperature is on the order of 70°F. It soon was realized that it was not feasible to try to dissipate this quantity of heat by air conditioning. A search for an insulation that would shield the room from this heat produced a suitable material that could be placed on the transmitter cabinet and reduce the heat input to the room. The room itself was insulated, and an air-conditioning system was selected which would keep the electronic hardware temperature within safe limits.

*Individual handling of the klystron tube.* The handling of the klystron tube was a difficult problem, as the tube is a costly and delicate piece of equipment. The need to be able to place, remove, and handle this klystron tube (7 ft long and weighing more than half a ton) required a bridge-type electric hoist that could be driven in both directions. The original concept was to remove the tube through the top of the cabinet and the dish backup structure, but the backup structure (above the room) will not allow this. Instead, a traveling crane was provided to lift the klystron a few inches off the cabinet floor (after the top and front member of the cabinet has been removed) and remove the klystron horizontally from the cabinet. The klystron is then moved through a cargo door in the room and lowered to the ground. A type of hoist was selected which would not subject the klystron to sudden starts, stops, or jerks and yet be capable of moving in three directions. The tube itself had to be carefully placed and aligned in the cabinet. A special custom-machined alignment plate was installed in the transmitter cabinet for this purpose, along with special adjusting fasteners for the tube at its midheight.

*d. Future plans.* Upon completion of the structural work on the antenna, the transmitter will be installed in the antenna (March 1968) and the deflection measurements repeated.

#### 4. High-Power Tests of 2388-MHz Feed, R. L. Leu and M. A. Gregg

*a. Introduction.* Tests were conducted to establish the RF power limit of the Venus DSS 2388-MHz feed using the 450-kW transmitter. It was demonstrated that the feed will radiate 450 kW, provided the turnstile junction probe is water-cooled. In addition, the results showed that the turnstile junction and rotary joint required cooling.

*b. Preliminary feed tests.* Initially the feed was tested to determine the RF power limit of the existing feed without modification. The 450-kW transmitter is presently located in the cone storage area at the Venus DSS. The 2388-MHz feed was removed from the cassegrain cone assembly and mounted on top of the 450-kW transmitter klystron cabinet (Fig. 16). By raising the cone hoist, the feed could then radiate through the access hole in the roof. A waveguide switch was installed to allow the transmitter to be switched between the feed and the water load. The installation of the switch served two purposes: (1) to permit RF calibration using the water load as a calorimeter, and (2) to permit testing of the waveguide switch as part of the 450-kW transmitter subsystem.

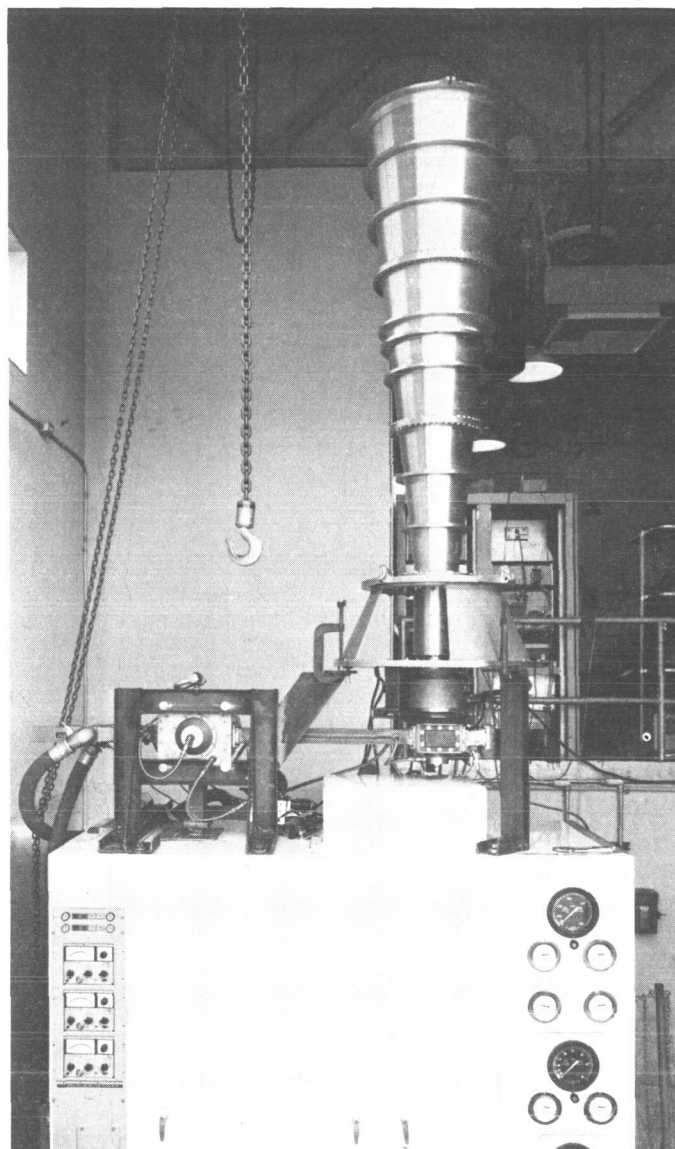


Fig. 16. 2388-MHz feed and transmitter assembly



Thermocouples were attached to the bottom of the turnstile junction probe and to the rotary joint, which is the first circuit element after the turnstile junction. The temperature of the two feed elements is recorded in Table 3 at each transmitter RF power level. Extremely high temperatures were measured on the turnstile junction probe and rotary joint. The RF power limit of the feed was approximately 250 kW, due to excessive reflected RF power and high temperature of the turnstile junction probe at 300 kW. Repeated attempts to radiate 300 kW failed.

**c. Feed modification.** As a result of the above tests, it was decided to water-cool the probe and retest the feed. The center portion of the probe was drilled, and a length of tubing was inserted to provide water circulation for the entire length of the probe. The modification is shown in Fig. 17. With the feed reassembled using the water-cooled probe, it was retested, and the power level of 450 kW was attained. In addition to the two previous feed elements measured, a third thermocouple was attached to the base of the turnstile junction to measure the temperature gradient between the junction and the probe. The feed

**Table 3. Temperatures of turnstile junction probe and rotary joint**

Elapsed time, min	Power level, kW	Temperature, °F	
		Probe	Rotary joint
30	200	177.5	130
30	250	230.0	180
10	300	250.0	210 (Transmitter off due to excessive reflected power)

**Table 4. Results of cooling**

Elapsed time, h:min	Power level, kW	Temperature, °F			Flow rate of probe, gal/min
		Junction	Probe	Rotary joint	
00:00	450	76.0	116.0	120.5	3
02:00	450	82.0	120.0	124.5	3
03:00	450	148.0	134.5	162.5	3
03:30	450	180.0	140.5	199.5	3
04:10*	450	190.0	143.5	227.0	3

\*Temperatures stabilized at this point.

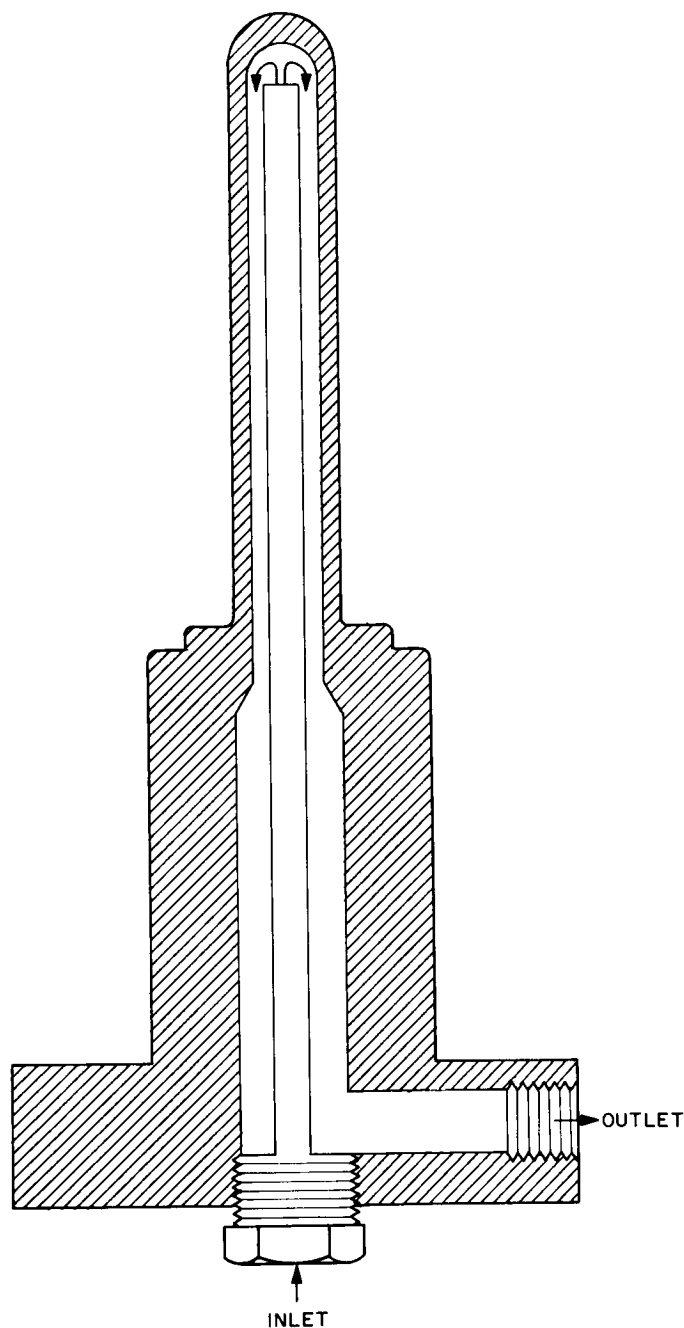


**Fig. 17. Probe and turnstile junction**

was operated at 450 kW for a period of 4 h, and the recorded temperatures indicate that the water-cooled probe is satisfactory, but water cooling should be added to the turnstile junction and the rotary joint.

Table 4 shows the results of cooling the probe. With cooling, the probe was operating better than 100°F below its previous temperature at 300 kW with no cooling.

By increasing the flow rate through the probe, it is possible to decrease the probe temperature even more.

*d. Future modifications.* The feed was removed from atop the transmitter and disassembled to add water cooling to the turnstile junction and the rotary joint. After the changes are completed, the feed will be reinstalled and tested.

#### **5. Lunar Bounce Clock Synchronization Project, J. R. Smith**

A precision clock-synchronization network is being established to meet the requirements of the DSN. The system being used was described in SPS 37-43, Vol. III, pp. 92-106 and SPS 37-45, Vol. III, pp. 72-75. Some preliminary results of the field experiments were discussed in SPS 37-47, Vol. II, pp. 90-92.

Several additional accuracy checks have been made by comparing clock difference measurements made with the moon-bounce system between the transmitter at the Venus DSS and the receiver at the National Bureau of Standards (NBS) in Boulder, Colorado, and similar difference measurements obtained by transporting a cesium clock between the same two stations. These checks have shown that clock difference measurements can easily be made with the moon-bounce system to an accuracy of 5  $\mu$ s or better.

One significant problem has been discovered during the early field work with the system. Failure of the tunnel diode amplifier due to RF overload of the tunnel diode has occurred once at Pioneer DSS, and twice at Tidbinbilla DSS. All three failures have occurred within a few weeks of installation. The first failure at Tidbinbilla DSS was the amplifier used for all the initial testing at Echo DSS, where the equipment was located relatively far away from the 85-ft antenna, and for the tests at JPL, where the equipment operated satisfactorily for 6 wk. No failure has occurred at NBS, where the equipment has been in operation for 6 mo. It would appear then, that the failures are related to the presence of the high-power S-band transmitters located nearby at Pioneer and Tidbinbilla DSSs. The power delivered to the amplifiers by the antenna has been measured for various positions of the moon-bounce antenna and the 85-ft antenna with the S-band transmitter on. The highest power level was observed at Tidbinbilla DSS when the moon-bounce antenna was pointed toward the intersite microwave antennas, but this was at least 30 dB below that necessary to damage the tunnel diode. Long-term recordings were made at Pioneer DSS to determine if aircraft radar signals

could be responsible, with completely negative results. No satisfactory test for RF pickup on the power cable to the amplifier has been devised, but this seems to be a possible source.

One amplifier has been fitted with a higher power dissipation tunnel diode by the manufacturer, a pin-diode power limiter has been installed between the antenna and the amplifier, and additional filtering has been installed on the power leads. This modified amplifier has survived at Pioneer DSS for 2 mo. All amplifiers will be fitted with these modifications.

#### **6. Venus DSS Operations, E. B. Jackson, J. D. Campbell, M. A. Gregg, and A. L. Price**

*a. Experimental activities.* During the period of December 16, 1967 through February 15, 1968, the 30-ft antenna at the Venus DSS continued to be used in a time-synchronization experiment at 8.45 GHz and for passive radiometric observations of the planet Venus at 23 GHz. The 85-ft antenna, undergoing extensive strengthening modifications, was not in operational service during this period.

The monostatic planetary radar experiment (SPS 37-49, Vol. II, p. 132), operating on the Mars DSS 210-ft antenna with the planet Venus as a target, continues to work well, although the one-way range on February 15 had increased to  $202 \times 10^6$  km. On January 15th, the received signal strength in the total spectrum, matched polarization mode, was  $-175$  dBmW, compared to a predicted signal strength of  $-173$  dBmW. (One-way range on January 15 was  $174.3 \times 10^6$  km.)

Extensive testing was conducted on the X-band cassegrain cone (XCE) while it was removed from the antenna. This testing was to obtain data from which not only over-all system temperature could be computed, but also the value of the individual contributors to this over-all system temperature; e.g., contributions from cosmic noise, maser noise, and waveguide and coaxial insertion losses, etc. Specifically, measurements were made with the maser input terminated in: (a) the feedhorn, (b) liquid helium-cooled termination, (c) liquid nitrogen-cooled termination, and (d) ambient temperature termination. Calculations made from the resulting data indicated an over-all system temperature of 32°K for the XCE cone setting on the ground looking toward zenith.

Major activities of the station were not operational due to extensive modifications being made to transmitting systems, antenna structure, and data processing equipment.

### **b. Subsystem performance**

*Receiving systems.* Due to the station shutdown, all of the receivers were out of operation during this reporting period. The only exception to this was the intermittent use of the 8448- to 30-MHz converter as an X-band transmitter output and modulation monitor. The 455-kHz portion of the Mod IV receiver was also used in conjunction with the monostatic planetary radar operation at the Mars DSS at 2388 MHz. This was accomplished by feeding the 455-kHz signal from the Mars DSS receiver, via the microwave link, into the Venus DSS Mod IV receiver.

*Transmitting systems.* The R&D transmitter system has been used for testing, evaluation, and modification for this reporting period. The X-band transmitter has operated for 16 time synchronization experiments for a total beam time of 34.5 h with no failures.

*Servo systems.* The 30-ft az-el antenna was used for tracking operations for time synchronization through this period.

There were no operations of the 85-ft az-el antenna scheduled during this period due to structural modifications.

### **c. System improvements**

*Antenna systems.* The installation of the electronics room and the accompanying structural modifications have been completed at the 85-ft az-el antenna. The dish surface panels are presently being installed. The scheduled shutdown period has been extended for approximately 1 mo, and it is now expected that the antenna will be operational again on or about April 1, 1968.

*Receiving systems.* The proposed receiver module testing program has been implemented, and testing is proceeding as time allows.

The water-cooling system for the receiver cold plates has been modified in an effort to correct the temperature regulation problem. This modification required the installation of a new liquid-to-air heat exchanger under the subfloor in the control room. The heat exchanger is placed in the direct path of the refrigerated, temperature-regulated air entering the subfloor area. The water temperature is thus being controlled by the building air-

conditioning equipment instead of a separate refrigeration and heating system. This also reduces the load on the building heating system by approximately 80,000 Btu, the amount of auxiliary heating supplied to the previously installed cooling equipment to compensate for insufficient heating load.

*Transmitting systems.* The flow meters for the heat exchanger were installed in the transmitter room for direct reading of flow rate and to prevent freezing of meters during cold weather. Also, a compact, variable power supply was fabricated for use in calibration of 450-kW klystron circuits, and the crowbar cabinet was rebuilt to accommodate the complete crowbar system including the 1-H choke and the 1- $\mu$ F capacitor. Other high-voltage components were relocated, and various components for the assembly of the new high-voltage crowbar cabinet were fabricated.

*d. Test and support.* Mounting brackets for the waveguide switch and the 100-kW 2388-MHz feedhorn and turnstile junction were fabricated to enable testing with the 450-kW transmitter. In the initial test, the probe in the turnstile junction exceeded temperatures of 200°F after operating at 300 kW for only a short period of time. A new water-cooled probe was fabricated (Fig. 17 of Sect. IV-c-4) and new tests were run with 3 gal/min of water through the switch and the probe.

## **7. DSIF Station Control and Data Equipment, E. Bann, R. N. Flanders, A. Burke, J. K. Woo, D. Hersey, P. C. Harrison, and E. A. Garcia**

*a. Introduction.* This article gives the status of the DSIF station control and data equipment as of February 1968. This equipment consists of the antenna pointing subsystem (APS), digital instrumentation subsystem (DIS), the telemetry and command processor (TCP), station monitor console (SMC), the frequency and timing subsystem (FTS), and the multiple-mission support equipment (MMSE). The MMSE implementation is essentially complete and this is the concluding article.

*b. Antenna pointing subsystem phase I.* The APS has been implemented in the DSIF stations to provide the capability of positioning the station antenna by computer control. Implementation has been on an interim basis, at the Pioneer, Echo, Woomera, Tidbinbilla, Robledo, Cebreros, and Ascension Island DSSs. Mars DSS is operational with APS Phase I (APS-I). The interim APS and APS-I have been described in previous articles.)

APS-I installations at the other deep space stations are scheduled as follows:

DSS	Date, 1968
Echo	3-15 to 3-29
Robledo	4-15 to 5-3
Tidbinbilla	5-6 to 5-24
Woomera	6-3 to 6-21
Johannesburg	6-3 to 6-19
Cebreros	6-24 to 7-12

SDS 910 computers will be retrofit and installed at Echo, Woomera, Johannesburg, and Cebreros DSSs, concurrent with DIS-II and TCP-II installations at these stations.

*c. Digital instrumentation subsystem Phase II.* The digital instrumentation subsystem Phase II (DIS-II), together with the DSIF Phase I monitor program, directs the function of monitoring the various subsystems within the stations of the DSIF. The DIS-II operates in conjunction with the station monitor and control console Phase II (SMC-II) to provide for the display and recording of system configuration, status and performance data, and for the transmission of alarm and status messages to the SFOF.

The present activities entail the continued implementation of the DIS-II within the DSIF.

The definition of DIS-II hardware interfaces is substantially complete. Software interfaces consisting of message contents and formats have been established. The DIS-II equipment procurement is in process, with deliveries scheduled to begin late in the first quarter of 1968. Deliveries are scheduled to continue into the third quarter of 1968.

System and subsystem cables for stations receiving the DIS-II are presently being defined, and fabrication and installation are expected to be completed prior to the currently projected operational date of September 1, 1968. Definition of the DSIF monitor system Phase I program is essentially complete, and the software detailed design document is under review.

*d. Telemetry and command processor Phase II.* The telemetry and command processor Phase II (TCP-II) provides the DSIF with a mission-independent telemetry and

command processing capability for real-time operation. The TCP-II is in the process of expansion (TCP-II-C) to increase the telemetry data processing capability to support the DSIF multiple-mission telemetry system.

The DSN ground communication system is in the process of changing the teletype send-and-receive capability from 60 to 100 words/min. The TCP-II communications buffer interfaces with the ground communication system teletype circuits so that it is necessary to change the communications buffer send-and-receive channels from 60 to 100 words/min. The modules required for this change in the communications buffer are scheduled for delivery in March 1968 and will be installed into the DSSs during the months of March and April of 1968.

The high-speed data line (HSDL) register of the TCP-II transmits telemetry data via NASCOM. The HSDL register will be modified to interface with the high-speed block multiplexer/error detection encoder decoder (BMXR/EDED/HSDL) modem in the DSIF Ground Communications Facility.

Telemetry data is transferred from the TCP-II computer (SDS 920) to the HSDL register under interrupt control by way of parallel output channel. The data is then transmitted to the BMXR/EDED/HSDL modem as a serial bit stream in synchronism with clock pulses supplied to the HSDL register by the BMXR/EDED/HSDL modem. Control signals are provided as interlocks for regulating the flow of data between the HSDL register and the BMXR/EDED/HSDL modem.

The HSDL modification kits are scheduled for delivery in July 1968 and will be implemented in DSSs to support early *Mariner* Mars 1969 testing.

*e. Station monitor console Phase II.* The Phase II monitor console differs from the Phase I console by having an X-Y recorder, a countdown clock, and the program alarm control panel. These additions in conjunction with the Phase II digital instrumentation system greatly enhance the monitoring capability of the station monitor console.

A breadboard model of the program alarm and control panel was constructed, and several modifications to the design and panel markings were found to be necessary. The program alarm logic and control panel, as modified, will provide an intermittent audible alarm and flashing red light upon receipt of an alarm signal from the DIS-II subsystem. In conjunction with this alarm signal the DIS

also supplies ten condition signals to indicators on the control panel. Under the control of the DIS, should a subsystem or configuration condition become faulty, an alarm signal is provided to the program alarm logic, causing the horn and flashing light to actuate.

The console operator acknowledges the alarm by depressing a switch on the control panel causing the audible alarm and flashing light to turn off. The subsystem and configuration lights are not affected by resetting the alarm and will continuously indicate the current conditions. A signal corresponding to the state of the flip-flop which controls the audible alarm and flashing light is supplied to the digital instrumentation system for recording.

The program alarm and control panel also provides a switch for each of the ten subsystem or configuration indicators to enable the console operator to request a printout on the line printer of the DIS-monitored parameters pertaining to a particular subsystem.

The operator may indicate his nonconcurrence with an indicated alarm by another switch on the control panel. The switch causes either a one-time nonconcur signal or a sustained nonconcur signal to be provided to the digital instrumentation system, where it is included in the alarm message sent to the SFOF.

These modifications are presently being built into the prototype panel.

**f. Frequency and timing subsystem.** The functional design of FTS-II is complete, and a contract was awarded to assist in detail design, fabrication, and evaluation of a prototype unit. The logic design is 80% complete, and the mechanical design is approximately 60% complete. Evaluation of the prototype should begin during the final week of February and proceed to completion approximately March 15, 1968. Production of the five subsystems required for *Mariner Mars 1969* stations will begin after evaluation of the prototype.

#### **g. Multiple-mission support equipment**

**Mission Support Recording (MSR).** Upon completion of the *Surveyor* Project the MSR's analog recording equipment will be removed from the Pioneer, Tidbinbilla, and Robledo DSSs. The Echo DSS will be the only station having an MSR assembly; however, the MSR equipment and operation will be assigned to the *Pioneer* Project as mission-dependent equipment.

Future multiple-mission support area recording requirements will be fulfilled in digital format by the TCP-II-C assembly.

**Communications interface assembly.** Procurement of items required to expand the communications interface assembly, to meet *Mariner Mars 1969* requirements, is on schedule and implementation at the stations is expected by June 1968.

**System simulation assembly (SIM).** Delivery of SIM Phase I interface panels and their subsequent implementation conclude the development and implementation plans for this assembly.

### **8. DSIF/Ground Communications Interface Assembly, E. A. Garcia**

**a. Introduction.** Increased demand for real-time data processing at the deep space stations and at the SFOF has continued to place emphasis on the need to use the high-speed data line (HSDL) instead of teletype for transmission of data between the deep space stations and the SFOF. Looking at the total data stream requirements, it became apparent that there are a number of data streams that potentially will have to be time-multiplexed and demultiplexed, to and from the HSDL, if the DSN is to use the communications system efficiently. With the advent of the *Mariner Mars 1969* Project, and future projects that will require real-time data processing, the deep space stations are being implemented with a high-speed data block multiplexer and the DSIF/ground communications interface assembly (DGI).

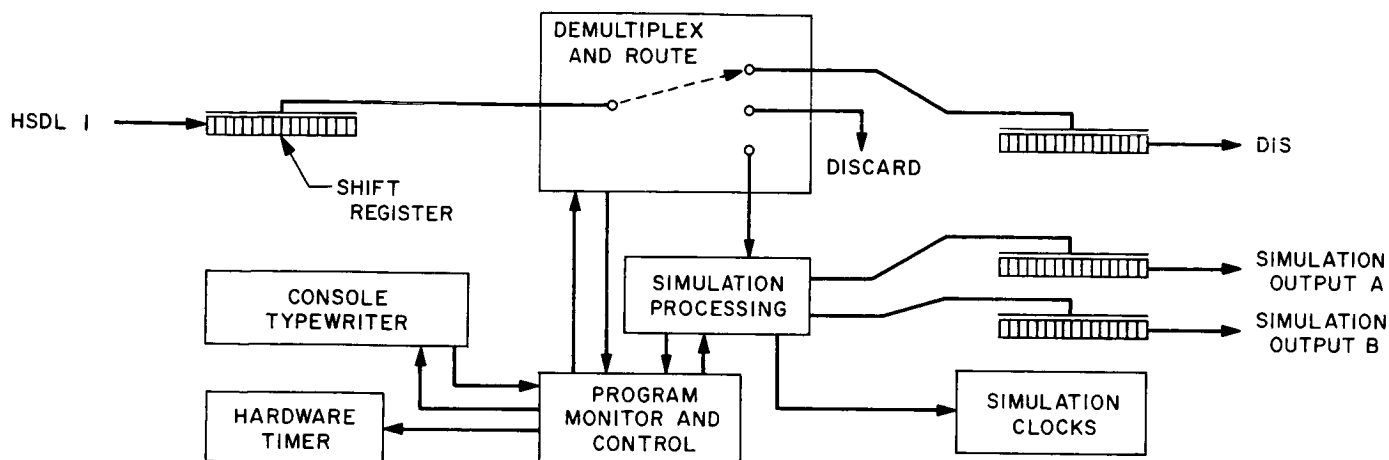
**b. Description.** The DGI assembly consists of one SDS 910 computer and a communications buffer cabinet. The SDS 910 computer, its program, and the peripheral hardware, which comprise the DGI assembly, will:

- (1) Demultiplex high-speed automatic data switching system (ADSS) formatted data blocks and route these blocks to designated DSS subsystems.
- (2) Receive simulated spacecraft data contained in ADSS blocks, and retransmit this data, on two separate channels, at spacecraft rates to system simulation equipment.
- (3) Receive data blocks, in ADSS format from four DSS subsystems, and multiplex these blocks into two HSDL circuits.
- (4) Receive teletype (TTY) data from DSS subsystems, format it into ADSS data blocks and time-multiplex it into the high-speed data circuits.

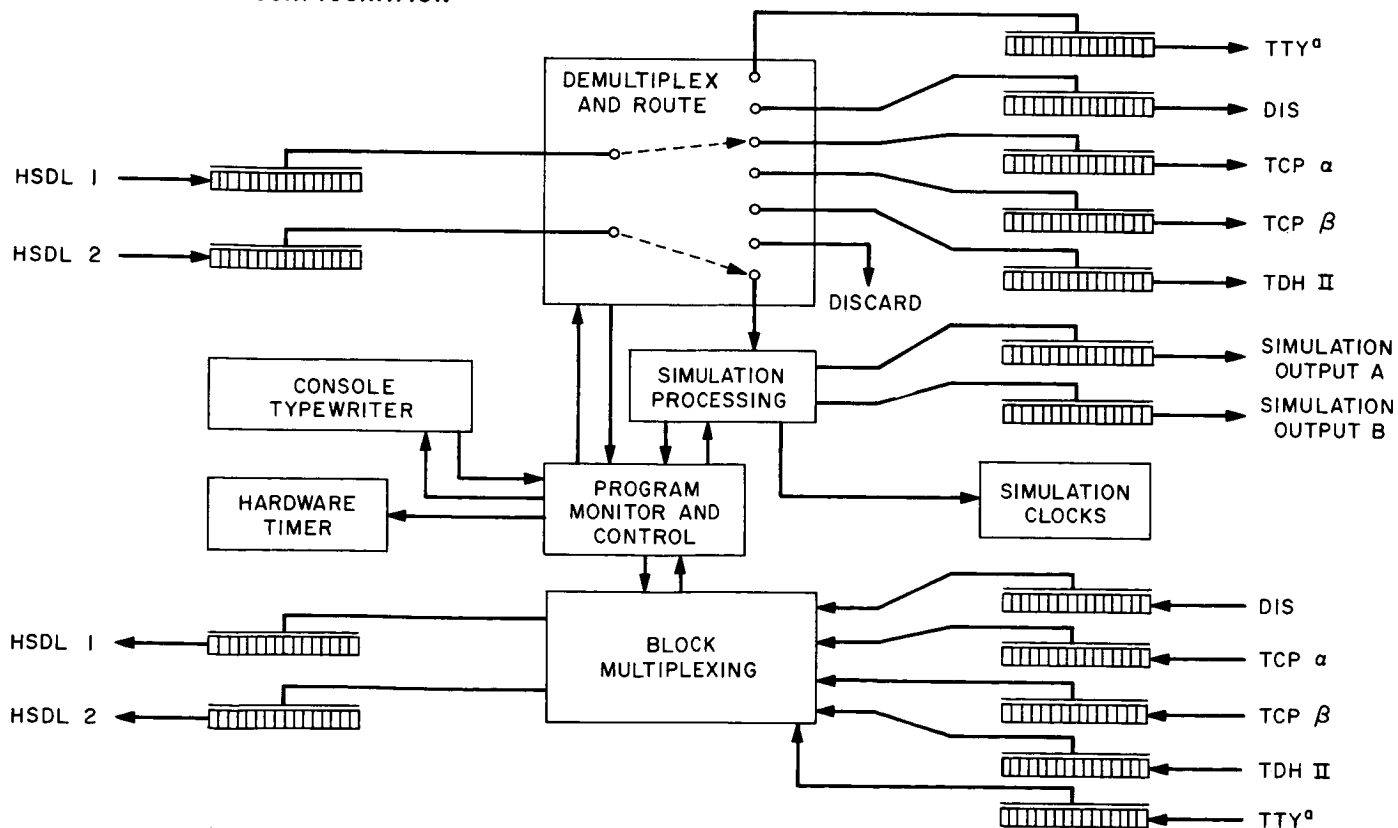
(5) Receive TTY data contained in ADSS blocks, format into TTY compatible words and transmit to designated TTY assemblies.

(6) Monitor the internal performance of the assembly, as well as the performance of the high-speed data circuits.

### PHASE I CONFIGURATION



### PHASE II CONFIGURATION



<sup>a</sup>PHASE III ADDITION

Fig. 18. DGI assembly functional configurations

### *c. DGI implementation plan (general)*

The DGI (Fig. 18) will be implemented in three phases.

*Phase I.* The Phase I DGI will:

- (1) Provide high-speed data demultiplexing from one high-speed data circuit.
- (2) Route ADSS data blocks to the digital instrumentation subsystem (DIS).
- (3) Process ADSS data blocks containing spacecraft simulated data and output, under computer control, two data streams at spacecraft bit rates.
- (4) Provide all decoding and control functions required for Phase I and II implementation plans.
- (5) Provide software and hardware monitor program and circuits required to determine proper operation of the DGI and HSDL circuits.

*Phase II.* In addition to the capabilities provided by Phase I, the Phase II DGI will:

- (1) Provide high-speed data demultiplexing from two high-speed data circuits.
- (2) Route ADSS data blocks to three additional DSS subsystems; telemetry and command processors (TCP), Alpha and Beta and to the tracking data-handling subsystem II (TDH-II).
- (3) Accept ADSS formatted data blocks from the DIS, TCP-Alpha, TCP-Beta and TDH-II and time-multiplex them into one or two HSDL circuits.

*Phase III.* In addition to the Phase I and II capabilities the Phase III DGI will:

- (1) Receive TTY data from DSS subsystems, format it into ADSS data blocks and time-multiplex into the high-speed data circuits.
- (2) Receive TTY data contained in ADSS blocks, format into TTY-compatible words, and transmit to designated TTY assemblies.

*d. Theory of operation.* The execution of data input/output operations will be under interrupt control, and the computer will use parallel output (POT) and parallel input (PIN) operations for transferring data to and from the DGI's communications buffer. The computer typewriter will serve as the operator interface.

*Data Format—ADSS.* All data processed by the DGI will be received in the form of ADSS formatted blocks at

a rate of 2400 bits/s. The block format consists of 600 or 1200 bits. The 120-bit header (five 24-bit lines) contains the following information:

- (1) 24-bit sync pattern. Line 1:

111001000110111001000110

(octal 71067106 as seen by the computer).

- (2) Source code. Indicates station or origin of the data. This data is not used by the DGI software.
- (3) Destination code. Indicates destination of the data block. This data is not used by the DGI.
- (4) Data format code. Type designations will be: 600-bit block, 1200-bit block, 600-bit filler block, and 1200-bit filler block. Actual numerical codes for each type will be supplied as data at program load.
- (5) Simulation indicator.
- (6) Mission-independent data type (MIDT). The DGI will use the MIDT to determine proper block routing. Acceptable data type designations in Phase I will be: DSN monitoring, predictions, text, simulation, and filler. Actual numerical codes for each type will be supplied as data at program load. Up to ten data types may be acceptable in the future.
- (7) Mission-dependent data type (MDDT). The MDDT will be used in the simulation portion of the program to determine block content. Acceptable designations will be: simulated engineering data, simulated science data, and simulation control data. Specific numerical codes for each type will be supplied as data at program load.
- (8) Spacecraft number. Each spacecraft will be assigned a unique number. This data is not used in processing, but the latest received spacecraft number will be available at operator request.
- (9) The time of day. Expressed as a binary count of one-hundredths of seconds. The latest time tag will be available at operator request.
- (10) Annotation. This data is ignored for all blocks inbound to the DGI.
- (11) Day of year. The numerical day of year is contained in binary-coded decimal form.
- (12) Data block serial number. Separate sequences of serial numbers will be generated for each MIDT at the data source. Filler blocks will contain a fixed serial number of octal 4210.

The data portion of a block extends from line 6 through the first 12 bits of line 24 (or 49). Blocks inbound to the DGI on HSD lines will contain an error status.

*Input register.* For each data channel supplying an input to the DGI, a 24-bit register is provided as part of the DGI buffer. The data will be serially shifted into a register, and then transferred in 24-bit segments to computer core locations, using parallel input techniques. Each input register will be gated onto the SDS 910 parallel input connector. Logic associated with each register provides block sync correlation.

*Control and status inputs.* Signals or inputs required for control and/or status are: (1) interrupts, (2) buffer status word, and (3) typewriter.

- (1) Interrupts. Each input and output register is capable of generating an interrupt. The interrupt will usually indicate that the register is awaiting data input or data extraction. A timing interrupt is presented to the computer at 100-ms intervals, and is used for all functions requiring time reference.
- (2) Buffer Status Word. One word of buffer status bits is available to the computer. It contains information such as register availability and hardware logic states. This word is accessed by the computer when needed by instructions.
- (3) Typewriter Input. A means is provided for the following types of typewriter input: (a) Data input in response to a program request for parameters needed for execution; (b) Operator request for real-time information, such as counts, values, time, operational modes, etc; and (c) Control of program and hardware operations. Specifically, any command entry contained in simulation data shall be executable from the typewriter. Any variable mode of program operation is selectable from the typewriter. The capability to reset all alarm flags in the software monitor is also included.

*Data outputs.* Data outputs consist of: (1) data routed to the DSS subsystems, (2) data fed to the two simulation outputs, and (3) data multiplexed for transmission over HSD lines.

Output format for ADSS data blocks will be identical to input format, with the exception of the annotation field, which indicates the means by which the block was routed.

The bit streams outputted by the simulation program have no block format, but in commutator mode the channel sequence is a function of the commutating scheme.

- (1) Output Register. All output data is transferred to a selected 24-bit register in the DGI buffer, using single-word parallel output operations from the computer. The data word is then transmitted to its destination by a serial shifting operation, which is clocked either by the hardware or an external timing source.
- (2) Output to DSS Subsystems. DSS subsystems to which DGI will send data include the DIS, TDH-II, TCP-Alpha, and TCP-Beta. Transmission to the DIS only is planned for Phase I. Transmission of a block to a DSS subsystem will not begin until the entire block has been received from one of the HSD lines.
- (3) Output to Simulation Circuits. Simulation data is transmitted in bit stream form, so that there is no first word or last word. The engineering or science register is ready for reloading when an interrupt is received, by the computer, from the respective circuitry.
- (4) Output to HSD Circuits (Phase II Only). When the multiplexing portion of the computer program is ready to transmit a block, the sequence of events involved is the same as for sending to a DSS subsystem. After the availability of the desired register is verified by checking the appropriate status bit, all words except the last are loaded and transmitted. The loading of the last data word will here also require use of a special EOM.

*Control outputs.* Control outputs consist of all activation pulses sent by the computer to the DGI's buffer for the purpose of setting or resetting logic.

- (1) Input register control: HSD inputs. If for any reason a block of data inputted from an HSD circuit is rejected by the program prior to receiving the entire block, the appropriate input register must be returned to search mode.
- (2) Input register control: DSS inputs (Phase II only). If the buffers in the multiplexing portion of the program become full, further DSS inputs can be delayed. When a normal condition is reestablished, inputs can be enabled.
- (3) Simulation Start Control. In certain instances the computer must send an activation pulse to either the science or engineering register in order to



enable or re-enable the serial output of data. This is necessary at the initial start of a simulation data stream, and in cases where the data stream has been momentarily interrupted. The register clock will automatically become disabled if the computer is unable to react to an interrupt generated by the output register (e.g., the buffer is empty or output inhibited).

*Simulated data rate control.* When a rate change is indicated for simulated data by input control information, an appropriate activation pulse is generated. Under program control, verification of the execution of each function is obtained by testing the buffer's status word.

*Notification outputs.* Notification outputs consist of all messages typed on the computer's typewriter for operator information or action.

*DGI internal monitoring: HSD.* Certain statistics on the HSD circuits performance are derived from routine tests and the block error status bits. Internal computer counters are included in the program to maintain the following counts:

- (1) Total number of headers received.
- (2) Number of routed blocks with errors indicated.
- (3) Number of blocks routed on basis of perfect MIDT fit, but with errors indicated.
- (4) Number of blocks routed on basis of serial number match.
- (5) Number of blocks routed on basis of MIDT fit with 1-bit error.
- (6) Number of blocks routed on basis of simulation bits equal 11.
- (7) Number of unrecognizable blocks discarded.

*DGI internal monitoring: DGI.* The DGI's buffer requires an activation pulse from the computer every 100 ms. This pulse resets the hardware timer, and keeps it from expiring. The expired condition indicates that the DGI is nonoperational.

The presence of this pulse is based upon software determination that the program functions are being executed normally. The inability of the program to verify the execution of a hardware control function shall prevent the pulse, until the operator performs an alarm reset.

The source of timing to the computer is provided by the frequency and timing subsystem (FTS), in the form of an interrupt every 100 ms.

## 9. DSIF Control Room Reconfiguration, R. L. Weber

*a. Introduction.* The DSIF is about to undergo a re-configuration and upgrading program of unprecedented magnitude. Many existing equipments will be modified, and several new equipments and subsystems will be installed and tested for the first time as part of the DSIF system. Preparation for the *Mariner* Mars 1969 mission is in progress and includes: antenna and servo drive improvements; control room reconfiguration and new equipment; and communications room reconfiguration and new equipment implementation. Only the control room configuration is discussed in this article.

*b. New configuration.* There are now approximately 70 racks of equipment in a normal DSIF control room. New subsystems will cause a net increase of 13 racks to the control room and one additional junction rack to the control room plenum. This increase in rack complement constitutes an addition or expansion of the following subsystems:

- (1) Receiver for the receiver-exciter III-C assembly upgrade and the addition of subcarrier demodulator assemblies.
- (2) Telemetry and command processor Phase II-C additions.
- (3) DSIF/GCF interface.
- (4) Antenna-pointing subsystem Phase I.
- (5) Digital instrumentation subsystem Phase II modification.
- (6) Frequency and timing subsystem Phase II and II-B modification, including X-band clock synchronization.
- (7) System junction module modification.

The communications room equipment will be grouped together in a centralized communications area, and provision will be made for the addition of future equipment. The following is a typical complement of equipment in the communications room:

- (1) Nine automatic send/receive teletypes.
- (2) Two high-speed data racks.
- (3) Three communications control groups.

- In addition, space is provided for a planned communication processor, a communication junction module, and a test equipment rack.

other operational concern was the visibility of all the operator positions from the station monitor console. The telemetry and command data subsystem and several other minor subsystems were not visible to the station monitor console. In the plans for expansion, the factors receiving first consideration were first those affecting operator convenience and efficiency, and, secondly, those contributing to station uniformity.

After reviewing the existing arrangements in the various deep space stations, it was considered most advantageous to place all racks along the outside walls. This allows a 360-deg visual sweep by the station shift



supervisor to all operator positions. The station monitor console will be placed in front of the antenna-pointing servo and receiver racks. By locating the Station Operations Director close to these time-dependent subsystems, the best control and supervision of the cognizant operators will be assured.

To conform to this plan, the control room configuration at Woomera and Johannesburg DSSs will be rotated 90 deg. This will occlude the antenna from the vision of the servo operator, but will be compensated for by a closed-circuit television system. Future expansion, with the exception of Echo DSS, will be in the direction along the long dimension of the control room and away from the antenna-pointing subsystem and station monitor console equipments. This will be possible with the displacement of a minimum of existing racks. Echo DSS will require a physical addition to the control room behind the antenna-pointing subsystem, and this will require movement of all subsystems, including the antenna pointing, antenna servo, and receiver.

A typical station control room layout is illustrated in Fig. 19.

Control room layouts have been devised and approved for all DSIF MMT stations (i.e., Echo, Compatibility Test Area, Woomera, Johannesburg, Cebreros, and Cape Kennedy).

A special layout for the control room of the 210-ft antenna at Mars DSS has been devised.

The antenna upgrade (where applicable) and implementation of the subsystem equipments at the various stations are as follows:

DSS	Reconfiguration period
Pioneer	July 1 to November 30, 1968
Echo	February 12 to June 30, 1968
Mars	August 15 to December 31, 1968
Woomera	March 4 to August 31, 1968
Tidbinbilla	October 1 to December 31, 1968
Johannesburg	March 5 to July 15, 1968
Robledo	January 1 to February 28, 1969
Cebreros	May 1 to July 20, 1968
Cape Kennedy	March 21 to July 15, 1968

## 10. Compatibility Test Area Antenna Mechanical Installation, C. Lundy

During development, the various spacecraft are assembled in one building (Building 179), tested in a ten-foot space simulator (Building 248), and finally checked out in an environmental laboratory (Building 144). In order to check out the spacecraft relative to the simulated ground control station, these three locations must be linked with the S-band control and test equipment (Building 125). To implement this tie between these three buildings and the simulated S-band ground control radio net, six 6-ft solid parabolic antennas are used. The layout of the four buildings is shown in Fig. 20.

A parabolic reflector acts like a sail when a strong wind exerts a force on it; consequently, the mounting structure must be designed to withstand the worst probable conditions. The mounting structures for the six paraboloids are designed to survive 120-mph gusts. This requires that the supports for a 6-ft-diam dish be stable when loaded with a 2000-lb force.

Standard 4-in. water pipe is a convenient material for a small antenna mast. If one end is solidly fixed to a building and a 2000-lb load is applied to the free end, the pipe will not bend or fail structurally unless the lever arm exceeds 6 ft. Thus, with strong commercially fabricated brackets to mount the antennas to 4-in. pipe, the only requirement for mounting is a configuration which satisfies the wind load and RF intervisibility requirements.

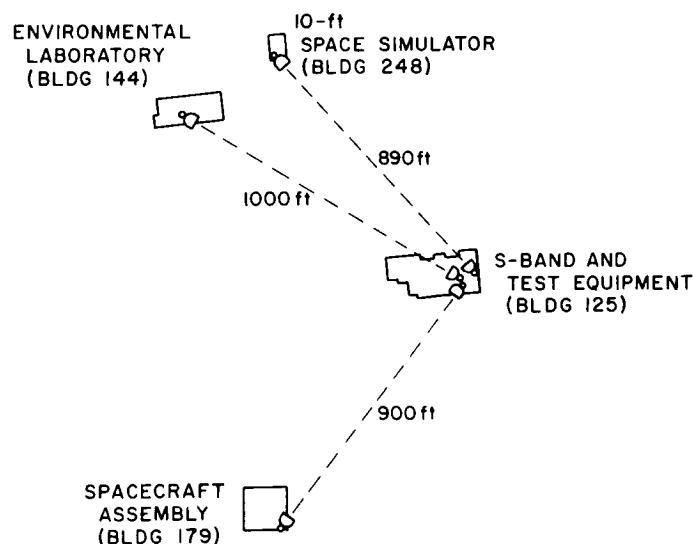


Fig. 20. Layout for Compatibility Test Area antenna installation

Building 125 requires three antennas. The problem of mounting them was complicated by the high parapet surrounding the only suitable roof area. Building 125 is framed with wood, so there are no strong points on which to anchor a mast. The solution was to make a three-legged tower of pipes, strongly cross-braced (Fig. 21). The three pipes extend through the roof downward into a shallow attic. The base of each leg terminates in a forged steel flange, which in turn is bolted to a gridwork of angle iron bars. The bars make up a broad base and are bolted to the wooden joists which are part of the building. In this way the strong force exerted by the wind is distributed safely into many joists, and no wooden connection is overloaded.

Buildings 179 and 248 are framed with steel, and the masts could be cantilevered from strong beams and braced to other strong elements of the building structure. In Building 179 the braces are inside the building; on Building 248 the braces are above the roof, but hidden by the parapet.

On Building 144 the location chosen is on the wall of a set-back wing which has wooden studs. A steel H-shaped support structure was fabricated in which the parallel bars are channel iron and the cross-bar is 4-in. pipe. The



Fig. 21. Three-legged pipe support for antennas

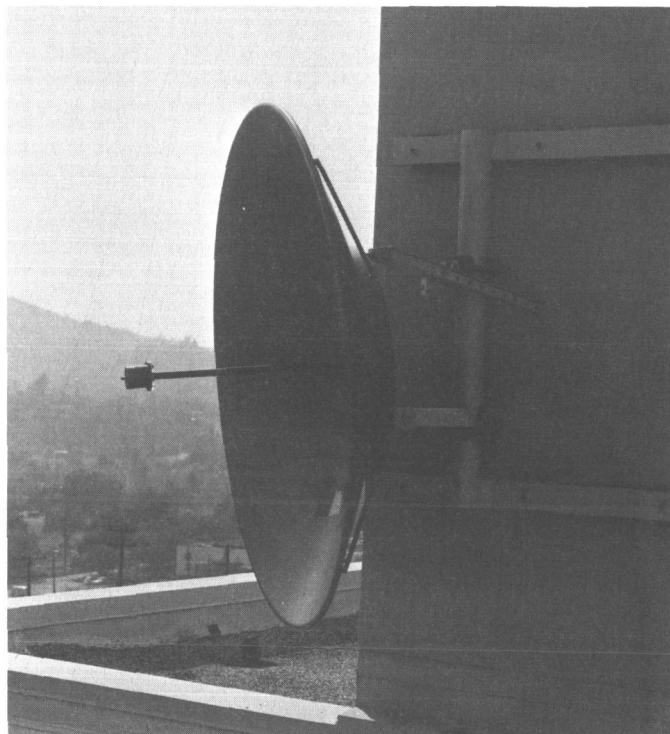


Fig. 22. Wall support for antenna

support is attached to the side of the wall by a vertical 4-in. pipe and bolted through the wall to matching channels on the inside. In this manner the load is distributed over several studs. The antenna is supported at the middle of the pipe (Fig. 22).

## 11. Compatibility Test Area Implementation, R. C. Rydgig

*a. Introduction.* The previous article (SPS 37-49, Vol. II, pp. 133-137), discussed the need for the Compatibility Test Area (CTA) and described the proposed facility. This article will describe the implementation.

*b. CTA location.* The CTA was installed at JPL in Building 125. This site was selected because it was centrally located, and antennas on the roof were in view of antennas located at the Environmental Test Lab, the 10-ft space simulator, and the Spacecraft Assembly Facility.

*c. Facilities modifications.* On October 18, 1967, the modification work began. Existing lights were removed and replaced with adequate RFI-shielded fluorescent lights. Acoustical ceiling tiles were removed and replaced. Isolated 75-kV-A power sources and related wiring and ac outlets were installed. An adequate grounding system was provided. A 2-ft-high flooring (suitable for computers)

was installed over two thirds of the room, and tile was installed over the remaining one third of the room. A series of water and gas lines were raised, repaired, and concealed within the ceiling to accommodate the installation of a 10-ft-high screen room. One wall was rebuilt to eliminate shelves, counter top, and small sliding doors. An 8-ft-square opening was made in a second wall to allow access to the screen room. A separate air-conditioning system was installed to provide sufficient forced-air cooling for the electronic equipment.

With minor exceptions the facilities modifications were completed on schedule, and by December 4 installation of electronic equipment was begun.

*d. Equipment installation.* During the month of December the following equipment was installed and checked out: receiver-exciter and ranging; frequency and timing

subsystem; one half of the telemetry and command processor; MDE cabinet (telemetry and command data handling, Block I); system junction module and system cables; temporary microwave switching and patching equipment; an S-band transistorized low-noise amplifier; spacecraft screen room; spacecraft equipment in the MDE area; and overhead cable trays and cables for the spacecraft equipment.

On January 4, 1968, the CTA began conducting software tests for the *Mariner* Mars 1969 Project. The station, however, could not be considered fully operational until the remaining equipment was installed. During the months of January and February the following equipment was installed: teletypes; high-speed data lines (interim); high-rate correlator and high-rate subcarrier demodulator assembly (experimental); station communications control group; simulation recorder and FR-1400 recorder; second



Fig. 23. Compatibility Test Area partial installation

half of the telemetry and command processor; multiple-mission telemetry equipment; antennas and RF links to other buildings; and tactical intercommunications.

With minor exceptions this completed the installation of equipment planned for the CTA in its present configuration. No additional equipment can be installed until additional space is made available. Figure 23 shows partial installation.

**e. Testing.** In the majority of cases as the equipment was installed, it was tested at the subsystem level. As the equipment was put into operation to support *Mariner Mars 1969* tests, the system interfaces were tested and problems resolved. Overall system tests will be performed: (1) as new test descriptions matching the CTA configuration are generated, and (2) as station time is available.

**f. Operational status.** To allow the implementation of the CTA and the *Mariner Mars 1969* support to proceed concurrently, the CTA was declared operational as of January 4, 1968. The CTA is scheduled to become fully operational in March 1968.

## 12. Bolt Characteristics Test Program—Phase 2,

V. B. Lobb and D. L. Lambdin

As discussed in SPS 37-49, Vol. II, pp. 151-152, the bolt characteristics test program is divided into five phases. Phase 1 has been completed and was reported in SPS 37-47, Vol. II, pp. 135-138; this article reports the completion of Phase 2.

**a. Preliminary test.** The preliminary test of the instrumentation revealed several problems:

- (1) A calibration error, by a factor of two, in the computer program handling the test hardware bolt rotation transducer outputs. This error has been corrected.
- (2) Several of the components of the test fixture (the bolt-head holding fixture and nut-turning fixture) were of insufficient material hardness and strength for the volume of testing and for the stresses involved, and showed excessive brinelling and wear in areas of critical tolerance. These items were replaced with components of sufficient hardness and greater strength.
- (3) The end-wrench type of gripping of the bolt head in the test fixture produces erroneous data in that its two-point grip of the bolt head produces highly localized stresses in the area of the junction of the

bolt head and the bolt shaft, causing premature bolt failures. This indicates that in the field, only box or socket-type wrenches should be used.

- (4) Erroneous and negative readings are obtained if the cam on the twist readout shaft is not mechanically balanced.

**b. Fastener-characteristic measurement problems and their solutions.** The following problems were encountered in the measurement of fastener characteristics:

- (1) Apparent insufficient *nut rotation* for finger-tight to snug-tight, and snug-tight to final tight positions.

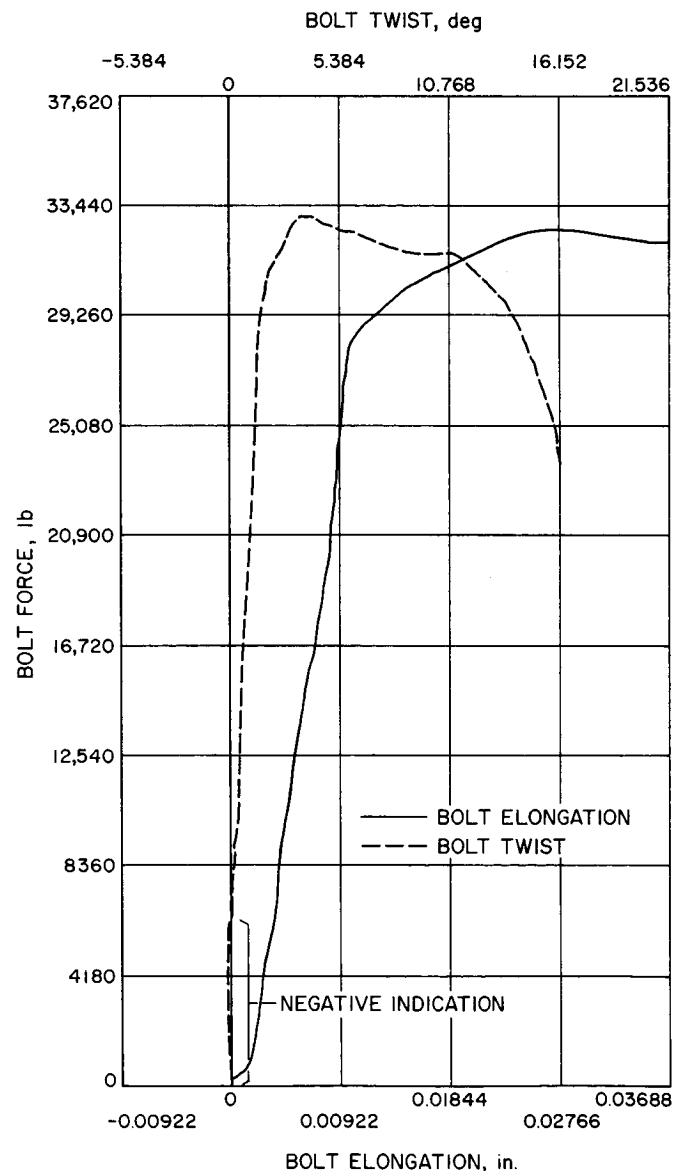


Fig. 24. Bolt-shank-twist transducer data

- (2) At times *bolt-shank-twist* transducer output (Fig. 24) would go negative (indicating an opposite direction to the nut rotation) during the initial nut rotations from finger-tight to snug-tight position.
- (3) *Bolt elongation* was larger (at proof load) than identical bolts tested by other research organizations.

The solutions to the above problems arrived at during the preliminary tests are:

**Nut rotation.** The nut rotation, in fractions of a turn [from finger-tight to snug to final tight (Table 5)] was less than that measured in a commercial hydraulic bolt calibrator. The difference in the elastic modulus of the solid-force washer versus the bulk modulus of the con-

finer fluid accounts for a total of an eighth to a quarter of a turn less for the solid-force washer configurations.

The other variance in nut rotation resulted from the difficulty caused by bolt specimen setup. It was found during the preliminary test that it was necessary to tighten the nut of the bolt sufficiently to eliminate looseness of the attached readout mechanisms; otherwise variance in the finger-tight position resulted. An initial small clamping force (500 lb) was tried so that a repeatable position for finger-tight could be maintained. This worked well and will be used in the Phase 3 and 4 bolt testing periods (the nut rotation for 500 lb was measured and will be included in the final report).

**Bolt shank twist.** The apparent reversing of direction by the bolt shank twist in relation to the applied nut rotation was the most difficult problem to solve. Three separate problems had to be solved in order to find the solution. Initially, the influence of each of the three problems was to be evaluated, but due to the magnitude of the deviation (a few hundredths of a degree) no specific individual quantitative evaluation could be made. The following lists two of the separate problems and their solutions, and a generalized explanation of the possible source of the third effect, with no solution.

The first problem was the binding of the twist readout fixture due to its misalignment to the bolt and nut during installation in the holding and turning fixture. It was solved by machining the connecting shaft down from a  $\frac{3}{8}$ - to a  $\frac{1}{4}$ -in. diam (for 2 in. length) to form a flexible coupling. The flexible coupling reacts to a marked change in the connecting shaft's stiffness (reduced by a factor of 40), and hence reduces the shaft's ability to transmit a binding force or moment; yet, it still has the ability to transmit the bolt shank twist and elongation.

The second problem was the looseness in the bolt test setup at the finger-tight position which caused negative movement of the rotation readout (a small negative moment is applied to the readout shaft by the offset weight of the cam). It was solved by starting the finger-tight position with a slight bolt force of 500 lb (as described previously), thus eliminating the looseness. Secondly, the weight of the cam was counterbalanced to eliminate the negative moment or to give a slight positive moment.

The first and second solutions were applied (not including the counterbalance of the cam) during the preliminary test period, and the magnitude and length of the negative rotation was markedly reduced. It changed to read zero

**Table 5. Summary output for five-bolt series test<sup>a</sup>**

Parameter	Value
Mean time, s $\times 10^{-1}$	
To snug tight	109
To proof load	180
Mean load at snug, lb	7,539
Mean load at proof, lb	28,063
Standard deviation at proof, lb	26
Mean load at rupture, lb	40,702
Mean elongation, in. $\times 10^{-4}$	
At snug	48
At proof	100
At rupture	456
Average turns, 1/16 turns	
To snug from finger tight	2.5
To proof from snug tight	2.4
To rupture from snug tight	11.8
Average ratio of bolt shank torque/input torque	
At elastic load	137/100
Mean axial stress, psi	
At snug	22,542
At elastic	41,985
At proof	83,910
At ultimate	121,698
Mean torsion stress	
At snug	40,392
At elastic	59,243
Mean combined stress	
At snug	39,030
At elastic	67,192
<sup>a</sup> Bolt description, Series 005: ASTM A325 Plating B Lubrication 003 Nut type: plain	



twist for a one eighth of a turn nut rotation, or on occasion a slight negative twist. This error residual is not significant, and no further effort was expended on its solution.

**Bolt elongation.** The problem of bolt elongation measurements giving values larger than previous research data for identical fasteners was investigated. Initial efforts were to find if the bolt-holding fixture was flexing because of the axial friction forces between the nut-turning fixture and the nut during rotation. A dial indicator was used to check for flexure, and a movement of 0.002 in. was found. Even though this is small, it was corrected by increasing the size of the bolt-holding fixture.

The above-detected slight error did not account for the 0.003- to 0.005-in. difference. The difference in the technique of measuring the bolt was investigated next. The bolt length measurements which were done previously were made with center-drilled bolts. This was done to allow precision measurement of the bolt length with a ball bearing and micrometer capable of reading to 0.0001 in. Initial bolt lengths were measured, the nut was tightened to give the proof load, the bolt length was again measured, and from this the elongation of the bolt was obtained. In the JPL instrumentation the bolt head was held in a fixture and the elongation was measured as the bolt was tightened from the free end of the bolt. Thus, if there were any flexure or movement of the bolt due to its head geometry, this would also be read. Upon investigation it was found that the bolt heads are concave, for manufacturing reasons.

JPL then ran a series of tests in which the deflection of the bolt head at proof load was measured (also intermediate points), with the following results:

Bolt	Elongation, in.
Bolt 1	0.0035
Bolt 2	0.0035
Bolt 3	0.0040
Bolt 4	0.0038
Bolt 5	0.0048

This gave an average elongation of 0.0039 in. and accounted for the difference; that is, the deflection in the concave head to flatten it out before elongation in the bolt.

**c. Preliminary results.** The following information (other than that related to preliminary tests of the instrumentation and its modifications) resulted from Phase 2:

- (1) The difference in the quantitative values for turn-of-the-nut angular rotation between bulk modulus or hydraulic type calibrators (such as the Skidmore-Wilhelm calibrator) and force washer types, necessitates a modification to the turn-of-the-nut method. The difference in total nut angular rotation is one sixth to one fourth of a turn greater for the hydraulic-type calibrator than the force washer type. This greater angular rotation is necessary in order to be within a plastic range of the bolt's stress/strain curve.

This new procedure is being incorporated in the revised heavy duty bolt tensioning and installation procedure.

- (2) In the field, the bolt-nut assembly should not be tightened or held by an end wrench. Either a box or socket-type grip should be used.

### 13. Antenna Mechanical Field Instrumentation Modules, C. Lundy and D. I. Lambdin

**a. Introduction.** The field instrumentation assemblies for the DSIF antenna mechanical subsystem, prior to the module concept discussed here, were designed for two usages:

- (1) The Goldstone DSCC stations used large van-type trailers (40 to 50 ft in length). These trailers required a tractor to transport them.
- (2) For overseas and JPL use throughout the operational net, a half-size military trailer (20 to 30 ft in length) was used.

The half-size trailers provided all the instrumentation, shop, and housing supplied by the larger trailers in a more compact arrangement. The purpose of the conversion from the full-size to the half-size trailer was to avoid excessive shipping costs.

**b. First half-size trailer design.** Experience with the use of the first half-size trailer revealed further problems:

- (1) In any given year the trailer spent 6 to 8 mo in transit; that is, 3 to 4 mo each way as a result of custom clearances at both ends, packing, ship availability, ship in-transit time, loading, and unloading. Therefore, its logistics were a significant problem.
- (2) Rough handling at the docks and long exposure to salt atmosphere necessitated extensive refurbishing after every third overseas trip.



- (3) Long in-transit periods during which the equipment was unavailable dictated the need for redundant equipment.

*c. New configuration.* Because of the aforementioned problems, other approaches were investigated, based on the following considerations:

- (1) The more up-to-date stations eliminate the need for the previous extensive housekeeping and office equipment.
- (2) Prediction of needed equipment can now be made; therefore, the shipping of the whole spectrum of available equipment is no longer necessary.

- (3) The instrumentation (especially in the case of the larger antennas) was usually needed in the antenna structures and not at the trailer.

- (4) Excessively sophisticated instrumentation is generally not required in the field.

It was resolved that two instrumentation modules, configured within standard-size DSIF racks, could supply all the expected needs. They are currently being fabricated.

Figure 25 shows a conceptual sketch of the final module configurations. The modular field instrumentation assembly is composed of two units. Each unit is a standard DSIF-size electronics equipment rack, shock-mounted, inside a weatherproof shipping case which also serves as

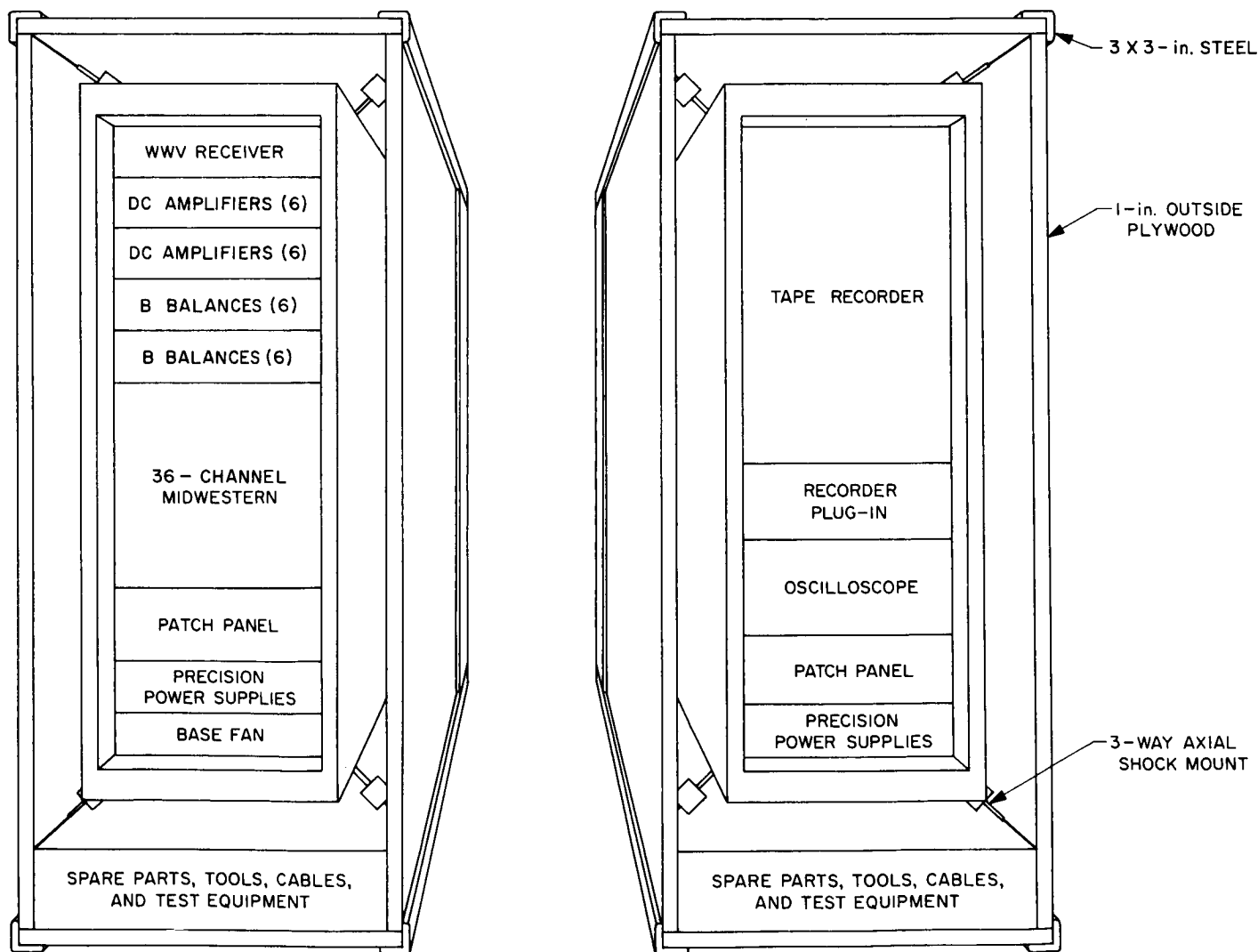


Fig. 25. Final module configurations

its storage and mounting base when used in the field. Thus, these modules can be used indoors or out-of-doors.

As can be seen in Fig. 25, the units can be operated individually or tied together via their patch panels for parallel recording when both in-field data review and home-base digital handling are required. In addition, storage drawers are included in the base of each unit for patch cables, small tools, and test or calibration instruments.

A rough breadboard version of Unit 1 was used at Robledo and Cebreros DSSs to test the design and the facility of shipping. The experiment was very satisfactory, and the present shipping-storage case was designed as a result. When completed, the new modular field instrumentation assembly concept should make significant contributions in cost savings relative to shipping and elimination of redundant equipment as well as in increased versatility and hardware availability.

#### 14. DSN S-Band Receiver-Exciter Upgrade,

*J. H. Wilcher and C. Chatburn*

The history and performance of the various S-band receiver-exciter designs, starting with the GSDS 1964 model, are described in previous SPS articles. The Block III C design is covered in SPS 37-42, Vol. III, pp. 77-83.

Receiver-exciter subsystems for the DSN have been supplied over a period of 4 yr. Consequently, the Pioneer, Echo, Woomera, Tidbinbilla, Robledo, and Cape Kennedy DSSs are equipped with Block I subsystems; the Mars, Johannesburg, and Cebreros DSSs with Block II subsystems; and the Compatibility Test Area is equipped with a Block III C subsystem.

All deep space station receiver-exciter will be upgraded to Block III C to improve their performance as well as to provide uniform equipment for the DSN. In addition, other features are being added to the receiver-exciter to provide the capability of operating with the subcarrier demodulator assembly for *Mariner* Mars 1969 support and to provide a reduction in receiver loop noise bandwidth for support of the *Pioneer* missions.

The upgrade cycle at each station will be approximately 5-12 wk. The implementation schedule as presently planned is shown in Fig. 26.

#### 15. DSIF Monitor System Phase I Program, *R. M. Thomas*

*a. Introduction.* The DSIF monitor system Phase I (MS-I) is a first step in a planned program to develop full automation for the DSN and DSIF deep space stations.

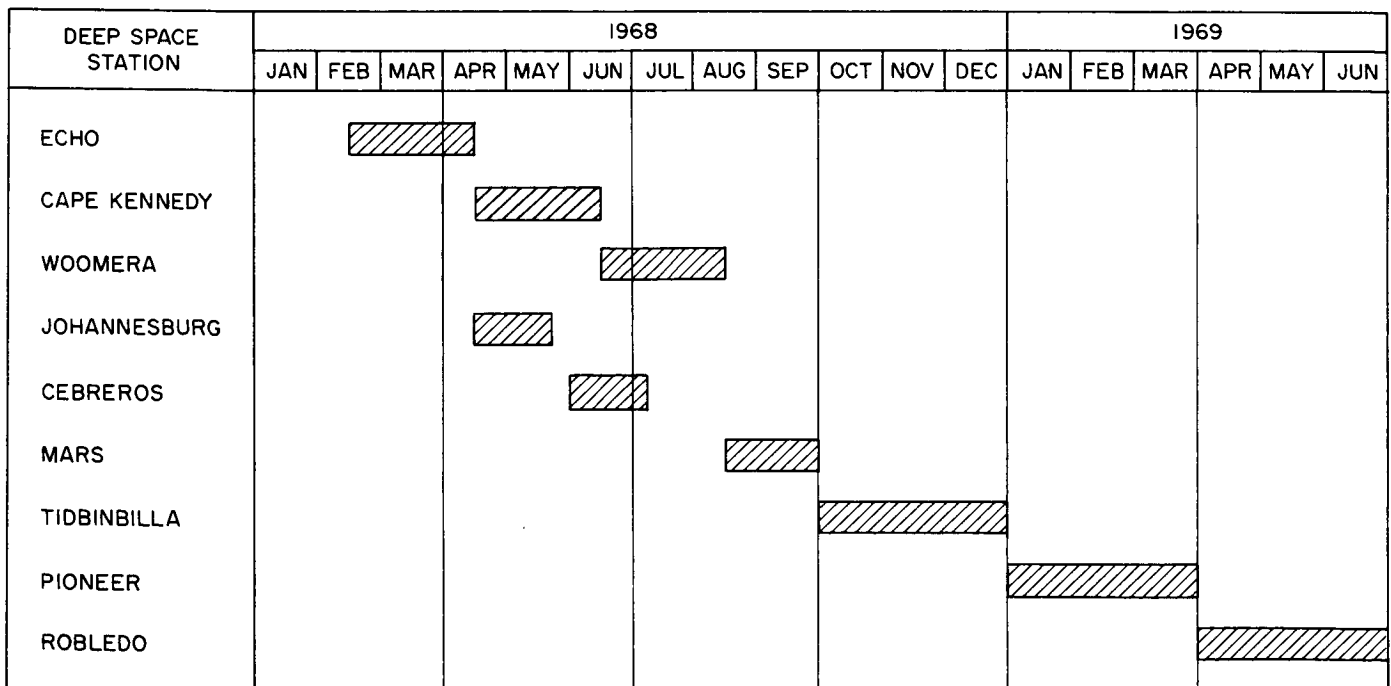


Fig. 26. Implementation schedule for Block III C receiver

The computer program for the MS-I is presently being prepared and will operate in the digital instrumentation subsystem Block II (DIS II) hardware for *Mariner Mars 1969*. This article is intended to give a general description of the various functions of the program.

Basically the MS-I program provides the following monitoring functions:

- (1) Real-time monitoring of deep-space-station configuration and performance.
- (2) Interrange vector (IRV) computation capability.
- (3) Mean and standard deviation computations for static phase error, signal-to-noise ratio, signal strength, doppler, automatic gain control, hour angle, declination, and ranging.
- (4) Transmitter forward power conversion.
- (5) Provision for interfacing with the high-speed data lines (between the DSIF and the SFOF).
- (6) Generation of alarms for the DSIF and the SFOF when parameters exceed specified tolerances.
- (7) Line printer and page printer outputs.
- (8) X-Y plotter display of five parameters.

The DSIF MS-I program will be contained in an SDS 920 computer with a 16-kiloword core memory capacity. The DIS consists of an SDS 920 computer (16-kiloword core memory), W and Y-buffers (interlaced), photoreader, paper punch, typewriter, plotter, page printer, line printer, dual channel magpak, and two magnetic tape units.

**b. Program operation.** The DIS will monitor switch positions (station configuration) by utilizing operating mode (OPM) table words, DSIF switch words, and mask words. It will also monitor station performance, make numerous computations (previously noted) utilizing algorithms contained in this article, output alarm conditions, and system performance reports, and provide data to the high-speed data line to be transmitted to the SFOF. Each word associated with station configuration will contain approximately 168 bits (7 computer words). Configuration monitoring is implemented by examination of each bit of the mask that contains a *one* and comparing the corresponding bits of the OPM table word and DSIF switch word. Any changes observed will be printed out. No comparison is made if the bit position in the mask word contains a *zero*.

Key parameters (ten) from the DIS are routed to the station monitor and control console (SMC) for visual

display. There are DSIF and DSN alarms for each of these parameters based upon predetermined upper and lower limits. A DSN alarm indicates that a parameter is outside the committed mission limits. A DSIF alarm indicates that a parameter has exceeded a narrower set of limits and is in danger of exceeding the committed limits. A DSIF alarm is not transmitted outside the deep space station.

A red light will be illuminated on the SMC, and a horn will sound when a DSIF or DSN alarm occurs. DSIF and DSN alarms will be printed on a line printer per a specified format. DSN alarms are transmitted to the SFOF as they occur. In addition to an alarm condition, there is a 5-min periodic line printer output of numerous other parameters. Each station manager has a *concur/non-concur* option for each alarm that is generated.

**c. Output.** The monitor program output functions include: alarm messages (on occurrence), periodic reports [at 10-s intervals when using high-speed data line (HSDL) or 5-min intervals when using teletype (TTY)], summary reports (once per pass or upon request), and permanent station performance and failure data in magnetic tape and tabular form. The alarm messages are concise descriptions of the failed function and are displayed locally at the deep space station via a page printer and line printer.

The alarm message is also transmitted to the SFOF by way of a HSDL or TTY communication channel. Alarm messages will be generated for the following functions: (1) microwave configuration, (2) subsystem configuration, (3) subsystem status, (4) signal strength/static phase error, (5) doppler, (6) angle, (7) range, (8) transmitter and receiver/exciter, (9) telemetry and command processor (TCP) and, (10) subcarrier demodulator assembly (SDA). Actuation of the appropriate sense switch on the SMC will provide a high-resolution printout of the failed function at the full sample rate with suitably annotated messages.

The periodic report may be output on the station line printer and by HSDL or TTY to the SFOF. The periodic report contains a more detailed description of the station performance and the status of selected critical parameters. The summary report will contain a brief summary of significant events occurring during the pass, together with a tally of the alarm conditions encountered. The permanent record of station performance and failure data will be maintained in magnetic tape and tabular form. The magnetic tape will contain raw unprocessed data exclusively, with suitable referencing for postmission analysis.

The program contains an on-site magnetic tape listing capability to permit the station magnetic tape log to be output on the station line printer. This mode may be selected under sense switch control to provide a near real-time review of a tracking anomaly or subsystem failure.

Outputs are also presented in a visual display on the SMC. An audible alarm may be activated under program control. An X-Y recorder with a programmable paper change is also located in the SMC to display selected parameters in graphical form as continuous curves or discrete points. These parameters are: doppler mean, doppler noise, received signal strength, hour angle residuals, and declination residuals. The MS-I is to be implemented concurrently with the hardware development and installation of the DIS II within the DSIF. The completion of both activities is presently scheduled for September 1968.

**d. Generation of data for transmission.** Considerable data are monitored directly, and are transmitted if there is a requirement. Other data are generated by making use of algorithms. A discussion of each algorithm follows:

**Signal strength.** The predicted values for received signal strength are generated in the SFOF and transmitted to the DSIF via TTY. Automatic gain control (AGC) dc voltages  $V_i$  are converted to dBm using

$$\text{dBm}_i = A0 + A1V_i = A2V_i^2 + A3V_i^3$$

where  $A0$ ,  $A1$ ,  $A2$  and  $A3$  are AGC curve-fit coefficients computed during the pretrack countdown. There will be a set of coefficients for each receiver and each expected configuration. It follows that

$$\mu_{\text{dBm}} = \frac{\sum_{i=1}^N \text{dBm}_i}{N} = \text{signal strength mean}$$

and

$$\sigma_{\text{dBm}} = \left[ \frac{\sum_{i=1}^N (\text{dBm}_i)^2 - \frac{\left[ \sum_{i=1}^N \text{dBm}_i \right]^2}{N}}{n-1} \right]^{1/2}$$

= standard deviation about the mean signal strength

**Ranging.** A ranging algorithm was developed for the purpose of evaluating the quality of the ranging data at each deep space station.

Discussion of this algorithm in a detailed manner will be discussed in a later SPS edition.

**Telemetry signal-to-noise ratio.** This signal-to-noise ratio (SNR) algorithm measures the quality of the telemetry signal at the subcarrier demodulator output. This SNR (SPS 37-27, Vol. IV, pp. 169-184) is also used to determine the modulation index, which is a function of the difference between the SNR for the spacecraft carrier and the spacecraft subcarrier. This index provides a means by which spacecraft/DSIF malfunctions can be isolated.

The SNR is computed using the following algorithm:

$$\text{SNR} = 10 \log (\mu/\sigma)^2$$

where

$$x = \sum_{i=1}^N |X_i|$$

$$X_s = \sum_{i=1}^N X_i^2$$

$N = 1000$  is the number of samples per interval chosen by empirical means

$\text{SNR}_i$  = the SNR over the interval containing 1000 integrated values (e.g., if  $i = 1$  then  $\text{SNR}_1$  = SNR for the first 1000 integrated values)

and

$|X_i|$  is obtained as a subcarrier demodulator assembly (SDA) integrator output in the TCP periodic message.

The  $\mu_1$  and  $\sigma_1$  used to compute  $\text{SNR}_1$  would be computed as follows:

$$\mu_1 = \frac{\left[ \sum_{i=1}^{1000} |X_i| \right]}{1000}$$

$$\sigma_1 = \left[ \frac{\sum_{i=1}^{1000} X_i^2 - \frac{\left[ \sum_{i=1}^{1000} |X_i| \right]^2}{1000}}{999} \right]^{1/2}$$

and

$$\mu_{SNR} = \frac{\left( \sum_{i=0}^k SNR_i \right)}{k}$$

= mean of the SNRs

where  $k$  is the mean of the SNRs (varies between 1 and 30 and is normally stored as an input constant as 15), and

$$\sigma_{SNR} = \left[ \frac{\sum_{i=1}^k (SNR_i)^2 - \frac{\left( \sum_{i=1}^k (SNR_i) \right)^2}{k}}{k-1} \right]^{1/2}$$

= standard deviation about the mean of the SNR

The predicted SNR will be available from the SFOF via TTY. The mean of the SNRs is compared to predictions, and an alarm generated if the absolute value of the observed minus predicted exceeds an input tolerance. An alarm will also be generated if the standard deviation exceeds an input tolerance.

**Doppler data.** A synopsis of this algorithm can be stated in the following manner: doppler data (one-, two-, and three-way) are detrended, blunder points are detected, a least-squares approximation is generated (using orthogonal polynomials), and then mean and standard deviations are computed. Detrending is the subtracting of an estimated mean value doppler sequence value from a doppler sequence. Blunder points are detected invalid doppler samples.

**Static phase error.** Static phase error (SPE) is an indication of the stress on the station's receiver carrier loop. If this error exceed  $\pm 30$  deg, the receiver lock is marginal.

SPE is computed as follows:

$$SPE = \frac{V_{SPE}}{\alpha K_{\phi} K_{F(S)}} = \frac{(12.736)V_{SPE}}{\alpha}$$

where

$V_{SPE}$  = sampled SPE voltage

$K_{\phi}$  = phase detector gain constant = 0.3488

$K_{F(S)}$  = RF loop filter gain constant = 0.90

and

$$\alpha = \left[ \frac{0.785 \rho_H + 0.4768 \rho_H^2}{1 + 1.024 \rho_H + 0.4768 \rho_H^2} \right]$$

The band-pass limiter signal suppression factor  $\rho_H$  is computed as follows:

$$10 \log_{10} \rho_H = P_s \text{ (dBm)} - [-165.2 + 10 \log_{10} T_s]$$

$$\rho_H = 10^{[P_s \text{ (dBm)} - (-165.2 + 10 \log_{10} T_s)] (0.1)}$$

where

$T_s$  = measured total systems noise temperature in °K

$P_s \text{ (dBm)}$  = AGC dc voltage converted to dBm

**Transmitter forward power conversion.** A 0- to 5-Vdc signal is supplied to the DIS and, based upon the mission involved, one of seven sets of characteristics (voltage versus forward power output) will be selected to provide for transmitter forward power determination. The computer is initialized to one set of these characteristics.

**Interrange vector capability.** An IRV capability exists for near-earth orbits (up to 250,000 km) with an acceptable error of  $\pm 0.03$  deg for angles and a rate of  $\pm 0.5$  m/s after 24 h of integration. This program will provide HA-dec or az-el and one-, two-, and three-way doppler with specified tolerances.

**DSIF to SFOF transmission of data.** The DSIF MS-I program contained in the SDS 920 computer presents to the HSDL a selected subset of parameters for transmission to the SFOF. This selected subset is derived from the sets of parameters supplied to the DIS from the various subsystems within the DSIF. TTY is used for this transmission if the HSDL becomes inoperative. HSD can be transmitted at a rate of 2400 bits/s (100 computer words/s). For present plans, the transmission of the 600 bit discrete/exception HSD block every 10 s is acceptable. Occurrence of an exception will result in immediate transmission of a data block. It follows that transmissions can occur any time and that a *maximum* of 10 s will

elapse between transmissions. The selected subset of parameters uses 444 of the 600 bits per HSD block. The remaining bits are used to make up the NASA header.

*SFOF to DSIF transmission of data.* The primary means for all output to the DSIF is by TTY, and voice communication is used as a backup. The monitor criteria data (initialization, configuration, and performance) is punched on cards, processed, and transmitted to the station via TTY. This data is then stored on a magpak at the station and can be selected and changed in real-time by TTY input from the SFOF. Text traffic and commands can also be transmitted by TTY from the SFOF. The following approach and format were developed for DSIF and/or SFOF access to all data on magpak:

- (1) A dual magpak will be used to store all monitor criteria data from the SFOF. This data can be

changed in real-time (during the time a spacecraft is being tracked).

- (2) TTY or keyboard can be used for initialization.

All monitor criteria data on the dual magpak are in accordance with the following format:

Set No.	Subset No.	Parameter No.	Value of parameter (fixed point)
XX	XX	XXX	XXXXXXXXXXXXX

To access any parameter requires only that the desired set no., subset no., and parameter no. be input by TTY or keyboard.

## V. Operations and Facilities

### A. SFOF Operations

#### 1. SFOF Training Program, L. H. White and G. S. Voden

*a. Introduction.* A recognized need of the SFOF has been to establish a means whereby a substantial guarantee could be given that operations support personnel were fully prepared to perform their tasks and that the SFOF state-of-readiness included sufficient in-depth skill distribution to meet any crisis condition. The period September 1967 through January 1968 was allowed for establishing job definitions and skill levels and formulating the training program.

*b. Objectives.* The objectives of the program are: to provide a documented reference source for personnel qualification and training requirements; to establish standards for preparation of training plans; to ensure a continuing review of changing technology translated into new job and skill requirements; and to optimize the effective utilization of personnel.

*c. Scope.* The program as now established comprises the entire SFOF mission-independent function. Included

in these requirements are interfaces with both the GCF and the DSIF, as well as flight projects during periods when these are operating in the SFOF.

There are four basic job areas covered by the program: (1) Communications, which contains 17 job titles and 50 specific sub-tasks, (2) Operations and support, which covers 26 job titles and 113 sub-tasks, (3) Data systems and processing, which contains 24 job titles and 48 sub-tasks, and (4) Project support, which contains 22 job titles and 49 sub-tasks.

Each of the sub-task qualification requirements has been defined qualitatively and quantitatively within four skill levels: orientation, familiarization, and knowledge and experience. *Orientation* consists of identification of the major units of a system and of the subsystem function. *Familiarization* involves functional analysis and equipment operation with emphasis on significant data flow, interfaces and operation actions. The *knowledge* level involves a detailed analysis of the subject; adequate, normal, and emergency operating information and procedures are provided to permit equipment malfunctions to be specified and remedial action recommended.

By November 7, 1968, all personnel will be fully qualified by the program.

## **B. GCF Operations**

### **1. Flight Project Support, F. E. Bond, Jr.**

*a. Pioneer Project.* During January and February, 1968, the GCF continued to provide the communications support for *Pioneers VI, VII, and VIII*. Project and spacecraft personnel located at Ames Research Center and Redondo Beach, California, respectively, received real-time science and engineering telemetry data from the tracking stations relayed through the communications processor at the SFOF to these locations by means of discrete teletype circuits installed for this purpose. For the *Pioneer* Project, the GCF switching equipment in the SFOF functions as a data relay station rather than a terminal station, as in the case of other SFOF-centered flight projects.

*b. Surveyor Project.* Early in January 1968, the GCF successfully supported the *Surveyor VII* launch, midcourse maneuver, touchdown, and first lunar day operations. The GCF actively supported the laser experiment conducted during *Surveyor VII* operations, wherein laser beams sent from astronomical laboratories on the earth were received and recorded by *Surveyor VII*. The resulting pictures were then relayed from the spacecraft to the SFOF for analysis and interpretation. The GCF support of the *Surveyor* Project was discontinued in the latter part of February 1968 upon completion of the *Surveyor VII* mission.

*c. Lunar Orbiter Project.* In late January 1968, the *Lunar Orbiter* Project tracking operations were concluded.

## **C. Facility Engineering**

### **1. Feeder Selectivity Switching Between Generated and Commercial Power Services at Deep Space Tracking Stations, L. H. Kushner**

*a. Introduction.* The electrical power requirements of a deep space tracking station are similar to many commercial installations utilizing electronically activated types of computers or data-processing equipments that are very sensitive to fluctuations of voltage or frequency.

Scientific and engineering facilities normally purchase power from local municipal power companies for all their system loads, which are divided into two major types: (1) electronic, including sensitive computers and data-

processing equipment, and (2) all others, including air-conditioning and other bulk-type incremental cycling loads. Unless special steps are taken, there is a reflection of transient voltages and frequency instability resulting from large in-rush currents that are common to type 2 loads. Since both types of loads are served from a single commercial power source, this reflection has an adverse effect on normal operation of the sensitive electronic equipment. In order for the electronic equipment to operate properly, these disturbances must be filtered out or isolated. Extensive studies are under way to provide such a filtering network system, but to date no practical and economical system has been perfected.

The present method utilized at some deep space stations for separating the electronic-type loads from the motor-type loads is by providing a two-bus system. The two buses in these systems are designated the electronic (E) bus and the utility (U) bus. Each of these bus systems is completely isolated from the other as to generation and distribution. During mission periods, separate diesel engine generators are used to serve the critical loads of each of these two bus systems. During nonmission periods commercial power is used, and the supply to the E-bus is filtered through a substation built-in regulator. Stations that are not equipped with a commercial power service must remain on local generated power supply to all systems continually. The feeder selectivity system is applicable only to stations having both locally generated power and commercial power services.

*b. Tracking station growth.* The original configuration of a tracking station was single-mission oriented. During the mission mode, the entire station would operate on power derived from the local diesel engine generator plant. During periods of nonmission, the entire station would operate from commercial power. The single-mission configuration has in recent years given way to a multiple-mission configuration as necessitated by economics and the necessity to track several spacecraft concurrently.

*c. Multiple-mission activity.* A typical example of a multiple-mission tracking station is a DSN/MSFN station consisting of the following functional areas:

#### *Mission-independent equipment (MIE) area*

- (1) Transmitter power supply.
- (2) Antenna drive.
- (3) Basic operations electronics.
- (4) Station powerplant.



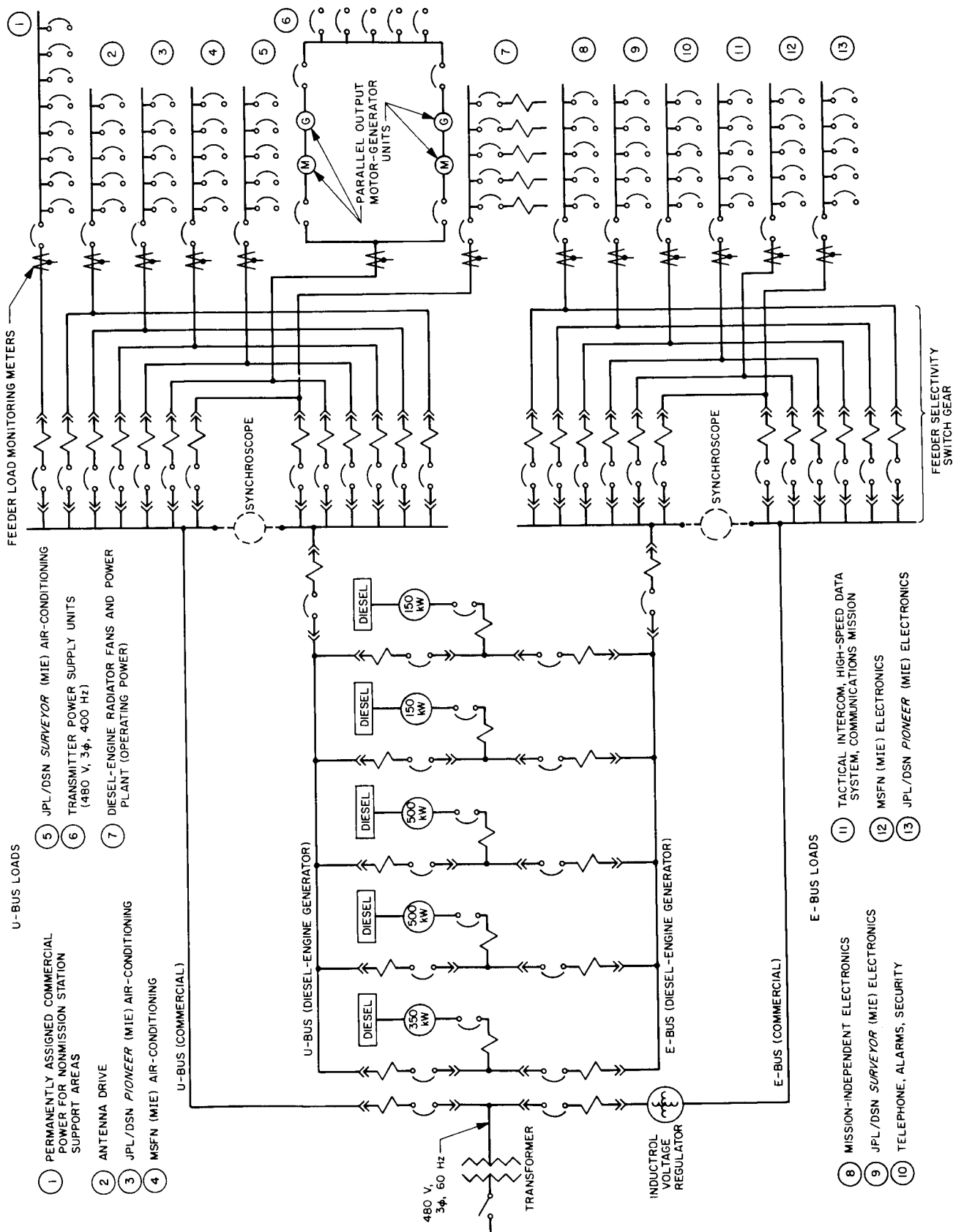


Fig. 1. Feeder selectivity switching system

### *Mission-dependent equipment (MDE) area*

- (1) MSFN electronics.
- (2) DSN *Surveyor* electronics.
- (3) DSN *Pioneer* electronics.

The functional areas required for a mission include *all* mission-independent equipment areas and any *one* of the mission-dependent equipment areas. When the station is in a nonmission mode, all of the above listed areas are served from the commercial power service. When the station is in an MSFN mission mode, all MIE areas (1 to 4) and MDE-MSFN electronics (1) are served via either E-bus or U-bus derived from the local power generating plant. Separate E-bus supply feeders are provided for mission electronic loads, and separate U-bus supply feeders are provided for mission motor loads. All other areas are served from the commercial power service.

During period of a *Surveyor* mission mode, all MIE areas and MDE-*Surveyor* electronics were served from the generated power E-bus and U-bus. All other areas were served from the commercial power service. A similar power distribution configuration was made up for *Pioneer* mission-mode.

A station may be called on to participate in tracking exercises that require a combination of modes. For example, one mission could be in a critical tracking phase, and at the same time the MSFN area could be participating in a simulation or net integration test, and simultaneously the equipment for another mission could be undergoing a system check-out test. For such a multiple-function activity the power requirements for all MIE and MDE areas would be served from the local diesel-engine generator plant. However, the capacity of the power generating plant is limited, and thus is not sufficient to serve all loads simultaneously and still maintain the required back-up for power reliability. It is evident, therefore, that a predetermined schedule of power priority must be established. This priority would select the station areas to be supplied generated power during scheduled periods, while the remaining portions of the station would necessarily be served from commercial power. Areas of the station could be transferred from commercial power to generated power or vice versa by means of push-button control using a feeder selectivity switching system.

**d. Feeder selectivity switching system.** The basic function of a feeder selectivity switching system as exists now in the prototype configuration at the Pioneer DSS

(Fig. 1) is to permit uninterrupted transfer of E-bus and U-bus power feeder circuits between generated and commercial power supplies as dictated by mission-mode requirements. The advantages of this feeder selectivity switching are as follows:

- (1) An existing diesel-engine generator plant capacity can serve a larger mission and operational area.
- (2) A commercial power service can be used to back up generated power supply for mission U-bus service.
- (3) Maximum use of commercial power service, and minimum use of diesel-engine generated power. (The cost of generated power is ten times that of commercial power.)
- (4) Push-button control of feeder transfer when necessitated by limited diesel power generation capability.

## **2. SFOF Uninterruptible Power System,**

*W. C. Tiedge and J. G. Grosch*

**a. Introduction.** The necessity for reliable power to support the SFOF data-processing and operations activities has been long apparent. The utility company power, while reasonably continuous, occasionally exceeds tolerances acceptable to data-processing equipment. When this happens, the equipment shuts down automatically. The restart has taken from 1 to 8 h, an untenable delay. To assure reliability during mission-critical periods, standby generators were used to supply power. Operating such equipment is relatively expensive, and the possibility of a failure is always present.

**b. Studies.** Studies made of available equipment and the experiences of other similar critical installations indicated that a buffer is needed between the utility power supply and the data-processing equipment. The buffer that has the most promise is the solid-state uninterruptible power system (UPS) which is also termed "no-break power." The use of rotating equipment to perform this function was considered but rejected because it is inherently less reliable, and because it is not available in the size to handle the requirement of 750 kV-A.

The state of the art of solid-state UPS has not advanced to the point where standard units in the usual ratings for power equipment are available. Only custom equipment, based on the customer's specific requirements, has been built. A number of agencies that operate real-time computers have a UPS in operation or are in the process of procuring it. Unfortunately, there is no unanimity of requirements, so virtually every unit built is a prototype to

some degree, and the unit costs vary widely with the stringency of the specifications.

*c. Design.* The operating principle of UPS is shown in Fig. 2. Incoming ac is converted to dc, which charges

batteries and also powers inverters. The inverters convert the dc back to ac which is capable of being precisely controlled for frequency, voltage, and wave form. If the ac power fails, the batteries will continue to supply dc power until standby generation equipment can be started

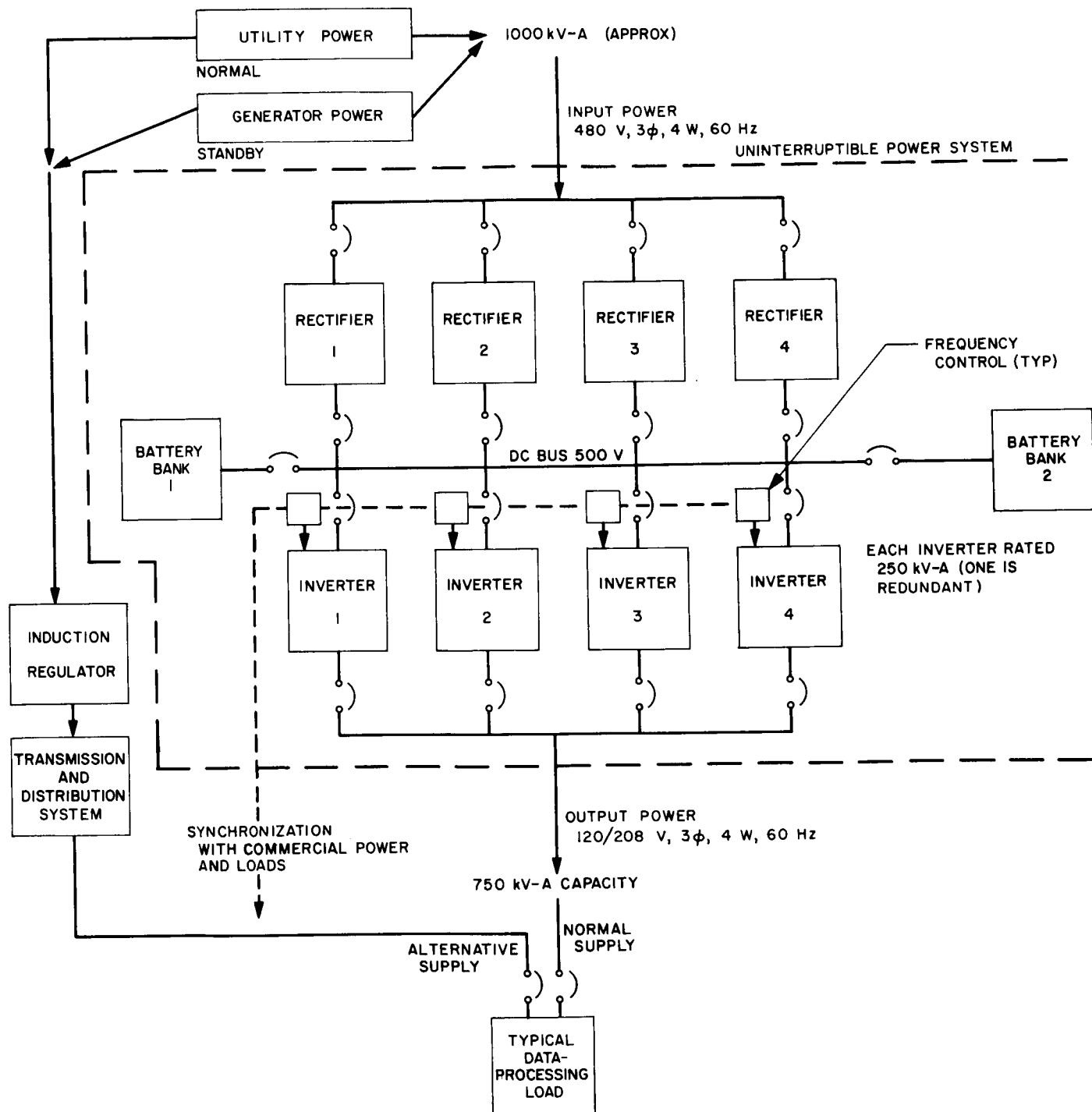


Fig. 2. SFOP uninterruptible power system

to supply ac. The output power is thus independent of any abnormalities that affect the ac from the utility company system. A number of safeguards are built into the equipment: current carrying devices are derated and paralleled; redundant major modules are provided and fed through quick-acting disconnect devices so that a defective module will be isolated automatically and safely; and repairs are simplified by use of plug-in assemblies. A mean time between failures of 80,000 h is anticipated.

To achieve the ultimate in reliability for the power supply, the UPS must be supported with a standby power plant of sufficient capacity to carry it and the rest of the SFOF power requirements in event of a total prolonged failure of the utility company power, a double distribution system, and a utility monitoring system.

The standby power plant is designed as an underground structure, adjacent to the SFOF, that will house up to four 1350-kW dual-fuel engine generators, a new utility system control room, and auxiliary equipment.

The double distribution system is achieved by building a new system in parallel with the existing one to all of the key loads in the building. Thus, it becomes a redundant means to supply these loads in event the normal system fails or is to be shut down for maintenance.

The utility monitoring system will sense all of the important characteristics of the building utilities and fire alarms, report alarms and out-of-tolerance conditions, and also provide the remote control of some elements. Operators will supervise 24 h a day to observe, receive reports, and take any corrective action necessary.

The design of the systems described is complete, with the exception of the monitoring system. Procurement action for the UPS is scheduled for March 1968. Eventual completion is anticipated by March 1970.

### **3. Robledo de Chavela Foundation Study, A. A. Riewe**

**a. Introduction.** A foundation study was conducted at the Robledo Deep Space Station in Robledo de Chavela, Spain to determine if adequate foundation support could be obtained for a 210-ft-diam antenna within the existing station property, and to develop the necessary configuration for the foundation components, provided satisfactory support existed. A contract for the study was awarded to the Donald R. Warren Company of Los Angeles on

July 20, 1967. Field work was accomplished during the period of August 2, 1967 through August 16, 1967. Laboratory testing, engineering analysis, and report preparation were completed December 30, 1967. An additional contract was awarded to Dames and Moore, Iberia, S. A., through the Naval Facilities Engineering Command (Contracts), Spain. This contract was for a geological and geophysical study of the site and the general area.

**b. Scope of study.** Briefly, the foundation study included: observation of the drilling of borings made at the locations shown on Fig. 3; sampling operations; laboratory testing of selected samples, and engineering analysis in order to formulate recommendations. The areas of study include the following:

- (1) Minimum dimensions and depths of embedment of the pedestal and instrument tower foundation components.
- (2) Expected dead load settlements of the foundation components.
- (3) Rotational stability of both components of the foundation structure under given lateral (wind) load conditions.
- (4) Excavation, backfilling, and dewatering recommendations.

Rotational stability and dead load settlements were determined. The configuration was developed to give the minimum foundation system size compatible with the maximum allowable rotations and settlements, assuming a static lateral load condition.

**c. Regional surface characteristics, geology and seismicity.** The site is located within the property limits of the existing Robledo DSS, approximately 35 mi west of Madrid in the Robledo de Chavela region.

The Robledo de Chavela region is near the eastern edge of the Sierra de Guadarrama, within a zone of crystalline rocks which form the mountain range. This crystalline complex is a granitic batholith which was emplaced into highly metamorphosed rocks. After formation of the batholith, the region was subjected to forces which resulted in the development of a normal faulting pattern of "graben" and "horst" blocks. The weakened fault planes acted as avenues for upward-migrating magmatic fluids which caused the formation of dikes and veins within the older rock.

The activity during Tertiary times resulted in uplift and subsequent rapid erosion of the Guadarrama complex. The eroded material was deposited as relatively thick sedimentary layers on the Madrid plain east of the site.

The regional geologic pattern is repeated in the site area on a smaller scale. Bedrock is predominantly granitic with included metamorphic rocks. An exposure of metamorphic rock (gneiss and mica schist) outcrops on the site west of Boring 1. Anomalies noted in the seismic profiles indicate that metamorphic rocks may be present east of Boring B-3. The metamorphic rocks trend almost east-west through the site. This enclave of metamorphic rocks included in the granitic matrix affects to some degree the movement of ground water and the engineering properties of the derived soils.

The granitic rocks are the predominant type in the proposed site area and are found below the proposed antenna location. As noted in the outcrops and borings, small quartz, aplite, and pegmatite dikes cross the granitic country rock.

The small valley in which the site is located is most likely controlled by a fault, trending north northeast-south southwest.

*Rock types:* As stated above, two general rock types were found at the site: granitic and metamorphic.

The granitic rocks vary gradually from a quartz monzonite to an orthosic granite porphyry. The porphyry is somewhat more easily weathered than the monzonite and may be slightly weaker in compression. Decomposition has occurred to a depth of about 10 ft at the boring sites, and the amount of weathering decreases rapidly below this depth. Weathering along some joints has resulted in thin sand-silt seams, as observed at 19 ft in Boring 1 and at 16 ft in Borings 2 and 3. No clay seams were noted in the borings, pits, or outcrops studied.

Metamorphic rocks include granite gneiss, biotite schist, metaquartzite, and calc-silicate hornfels, found in limited zones within the granitic matrix. The rocks outcrop west of the proposed antenna location and may be located beneath the surface to the east and southeast. These metamorphic zones appear to be of limited extent.

A degree of serpentinization was noted within the gneissic rock in the outcrop. It has occurred along some

joints less than an inch thick, or diffused in the rock mass in the proximity of the joints. This serpentinization is a result of hydrothermal alteration of ferromagnesium minerals in the gneiss, and the rock in the serpentinized areas is probably somewhat weaker than the unaltered gneiss.

A newly constructed water well, southeast of the proposed antenna location, is believed to penetrate calc-silicate hornfels. The reported ease of excavating the well indicates deep weathering or low strength of the rock.

Surface material was examined to a depth of 5 ft in test pits at the center of the proposed antenna location and in shallower pits excavated along the seismic profiles. Auger cuttings to depths of 5 to 7 ft were also examined. Only a very shallow top soil exists—usually no more than 1 ft thick, underlain by decomposed quartz monzonite. The decomposition varies, and, in the area of the proposed antenna, competent rock appears at a depth of about 10 ft. In other areas, away from the proposed site, decomposition may extend to 30 ft. Decomposition is more or less complete to depths of 3 to 5 ft; the rock has broken down into sand and gravel-size particles. Below this depth, decomposition grades into the weathered rock.

*Structure and faulting:* The area has been modified by faulting and weathering. The basin in which the site is located is bounded on both sides by rock ridges. The basin may be delineated by normal faulting occurring along its flanks, but no direct geologic evidence of basin formation was noted.

Joints have developed in the rock from pressures induced by tectonic activity. An almost random pattern is shown with no predominant direction; however, patterns noted nearest to the proposed antenna show fewer joint directions than the others. Jointing has been intensified by the weathering action so that test pits, outcrops, and cores taken from shallow depths in the borings show joints at spacings of from 2 in. to a foot. Below this depth, the joints are usually closed, though occasionally they have a mineralized filling of from ¼- to ¾-in. thick.

The site is located on the north flank of a north-northeast-south-southwest trending valley. A fault is believed to exist in the valley near the northwest property line of the site. The fault is suggested by topographic expression, by more intensive jointing in the rock, by chloritization or serpentinization of the rock in the area, and by the existence of deeper weathering as observed

from the seismic profiles. There is no indication of any recent activity along the fault.

**Ground water:** Moisture was noted in the pits excavated in the decomposed granitic rocks at a depth of about 4 ft. The water levels observed during the field observation on August 22, 1967 were 7.5 ft in Boring 1 and 6.9 ft in Boring 3. Although these measurements do not present enough data to be conclusive, the hydraulic gradient, as observed in the borings, appears to be low and indicates low permeability in the rock and overlying material.

The rock as seen in the borings is not closely jointed, and many of the joints present are closed or filled. Little water movement can be expected through the sound rock.

The newly constructed water well has reportedly produced adequate water supplies. The well is located in the valley, along the trace of the suspected fault and in at least some calc-silicate hornfels rock that may be more permeable than the surrounding country rock. Permeabilities would be higher in fractured rock of the fault zone, and it is suspected that subsurface water moves more rapidly along the fault to the well. Springs have been reported in the valley below the well location. It has also been reported that the springs have dried up since production was begun in the well.

**Natural hazards:** Hazards of flood, landslides, or earthquake should not reach serious proportions at the site. The site is well above the existing drainage, and no steep or unstable natural slopes are present within the site area. The maximum level of seismicity reported in the area has been on the order of Modified Mercalli IV. This low degree of shaking should not damage even moderately well-built structures, and would disturb operations only very infrequently.

**d. Subsurface profile.** Interpretation of seismic data indicates a two-layered profile in the area of the proposed site with the upper layer (designated V-1) consisting of decomposed and weathered bedrock and the lower layer (designated V-2) consisting of the lightly to relatively unweathered bedrock.

The average seismic velocities for the two layers was interpreted to be 2600 and 14,200 ft/s for layers V-1 and V-2, respectively. The average depth of the V-1, V-2 interface is on the order of 14 ft below existing grade. Use of Poissons' ratio of 0.25 with the above average seismic velocities indicates computed average seismic

moduli ( $E_{\text{seis}}$ ) of 0.20 and  $6.0 \times 10^6$  psi for V-1 and V-2, respectively. The average value for the elastic modulus ( $E_{\text{st}}$ ) for the V-2 layer determined by laboratory tests was  $6.2 \times 10^6$  which indicates a very good correlation.

Three borings were made at the locations shown in Fig. 3, to depths ranging from 36 to 51 ft below existing grades. A shallow zone of topsoil ranging in depth from 1 to 3 ft was underlain by a 3- to 5-ft-thick zone of weathered, partially decomposed and fractured granitic bedrock, which in turn transitioned to a relatively unweathered but fractured and/or jointed granitic bedrock to the depths explored. The bedrock was observed to be in a relatively fresh condition below depths of 24, 20 and 17 ft in Borings 1, 2, and 3, respectively.

Table 1 was formulated in order to provide a relative degree of competence guideline which was used as an aid in establishing minimum recommended depths of embedment for the foundation system components.

**e. Modulus of elasticity determination.** The critical factor in the foundation system evaluation is the action of the foundation materials in the elastic range; that is, behavior under repeated loading and unloading which is the basis of the rotational stability analysis for the unit under maximum load conditions. This factor is analyzed on the basis of first determining the governing modulus of elasticity in compression of the materials representing the foundation structure. The modulus of elasticity determinations were made by use of conventional heavy-duty laboratory compression loading apparatus with the samples being instrumented with the SR-4 type of strain measuring devices. A sample height-to-diameter ratio of 2.0 was maintained so as to reduce introduction of non-axial stress conditions within the sample.

**Table 1. Recommended depths of embedment**

Bedrock condition	Depth range, ft		
	B-1	B-2	B-3
Weathered and decomposed matrix	1 ½-8	1 ½-5	4 ½-7
Unweathered matrix <sup>a</sup>			
Moderate weathering and some decomposition along joints	8-11	5-13	7(+)-10
Unweathered matrix <sup>b</sup>			
Slight weathering along joints	11-24	13-20	10-17
Fresh matrix only			
Very slight staining along joints	24***	20***	17

<sup>a</sup>Material recommended for support of pedestal ring footing.

<sup>b</sup>Material recommended for support of instrument tower footing.

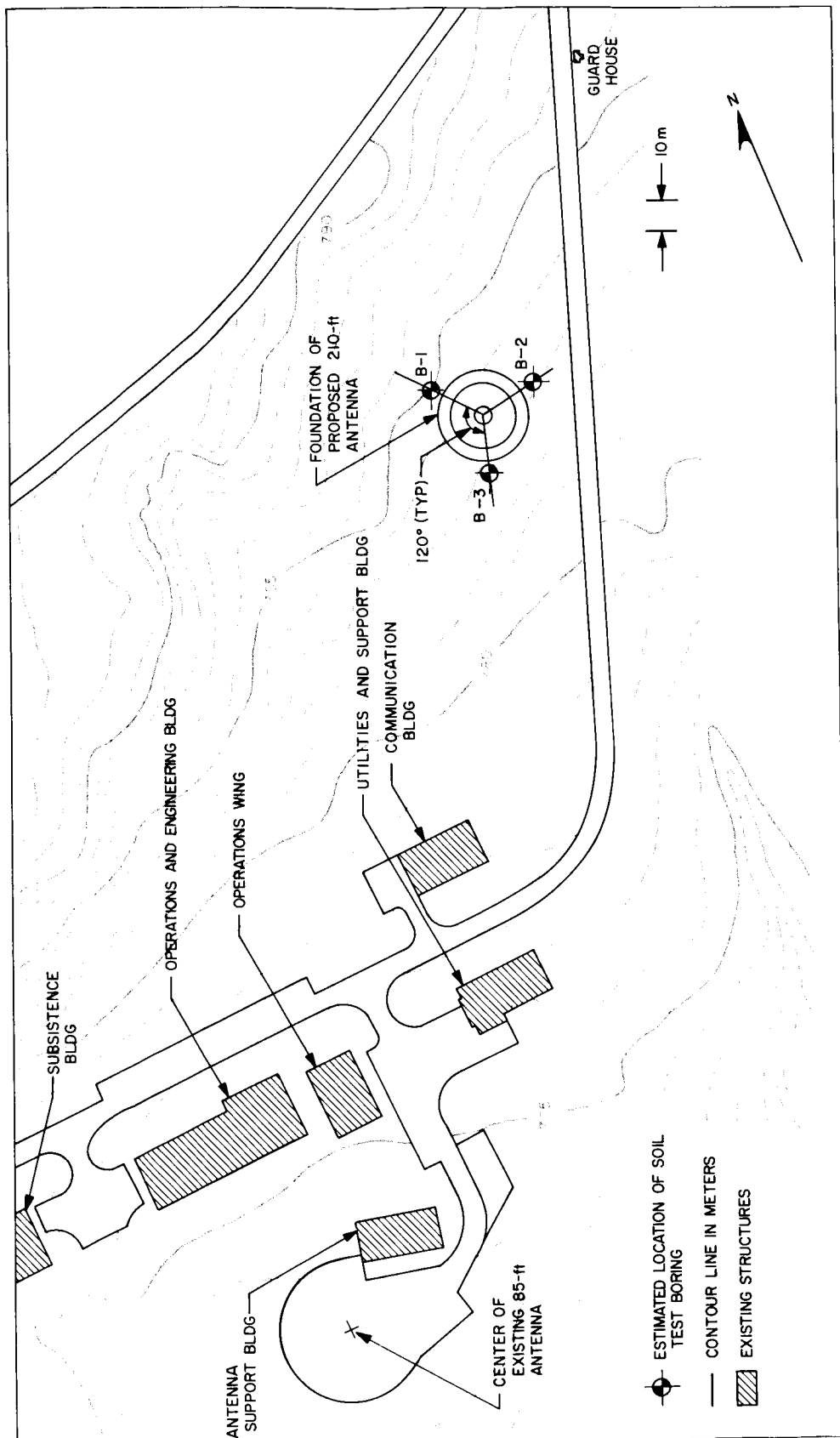
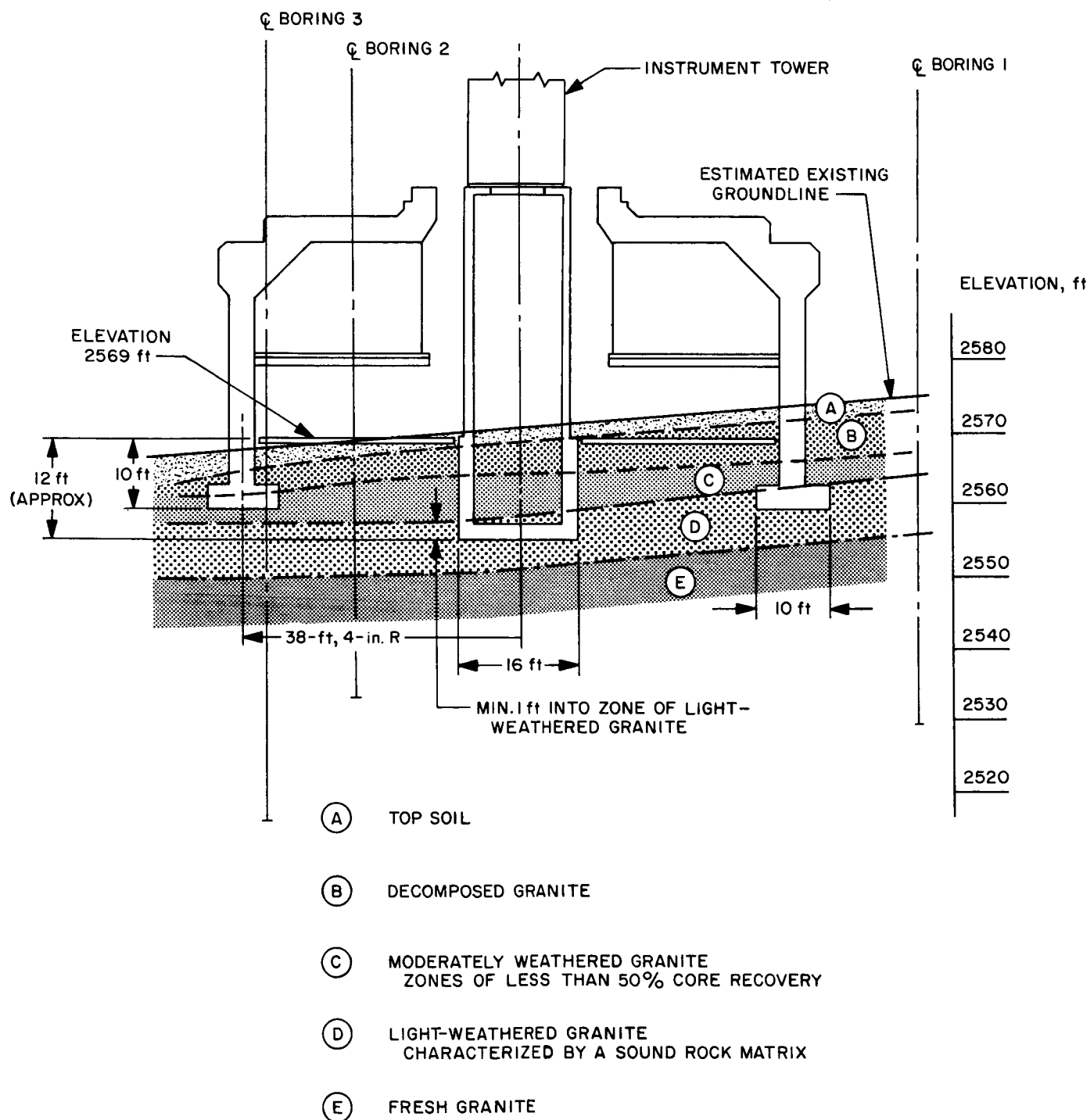


Fig. 3. Plan of borings



**Fig. 4. Recommended basic foundation system configuration**



**Design compression modulus:** Laboratory tests including specific gravity, density, unconfined compression, and modulus of elasticity ( $E_{st}$ ) were performed on selected rock core samples. Direct use of the average or lowest laboratory test modulus of elasticity value in the foundation stability analysis would yield extremely erroneous answers due primarily to the discontinuity effects of joint and fractured compression. A rock analyst was consulted to develop a rational procedure for obtaining a proper design compression modulus which would take into account the effect of the discontinuity factors. This evaluation was done by means of the rock quality designation (RQD) system developed by Professor D. U. Deere, University of Illinois.

Based on the RQD evaluation and utilizing a safety factor of five, a design compression modulus of  $0.38 \times 10^6$  psi was selected.

**f. Causes of foundation movement.** The causes of foundation movement and the method of analysis were discussed in SPS 37-38, Vol. II, p. 175 and will not be repeated here. Results of the stability analysis are summarized in Table 2.

**Table 2. Stability analysis**

Stability condition	Allowable values	Values for recommended configuration of foundation
Dead load settlement of instrument tower silo footing	0.25 in.	0.02 in.
Dead load settlement of antenna pedestal ring footing	0.50 in.	0.02 in.
Wind load rotation of instrument tower silo about a horizontal axis	2.0 seconds of arc	0.2 seconds of arc
Wind load rotation of antenna pedestal ring footing about a horizontal axis	5.0 seconds of arc	1.0 seconds of arc

The recommended basic foundation system configuration for which the Table 2 applies is shown in Fig. 4. This figure also indicates the approximate subsurface profile in relation to the recommended configuration.

**g. Dewatering.** It does not appear that there will be any major problem related to ground water on the subject site. Almost complete interception of the seepage can be expected if the pits or trenches are excavated at least to the contact between the decomposed granite bedrock and Zone A material, as shown on Fig. 4.

#### **4. DSIF Communications Facilities, E. L. Yinger**

New standardized communications room layouts for all deep space stations have been prepared. These layouts locate the communications rooms, wherever feasible, adjacent to operations control rooms. See Section IV-c-9 of this SPS.

Preliminary engineering is complete, and formal documentation is being prepared for updating the tactical intercom at all deep space stations.

Installation of a new dial telephone central office at the Goldstone DSCC has been completed, and additional trunking facilities to Barstow and JPL have been provided.

Contracts to relocate the Western Union terminal and microwave link terminals at Goldstone DSCC are presently being negotiated. This relocation will take place in March and April 1968.

#### **5. Goldstone DSCC Minor Construction Progress,**

*W. W. Lord and B. M. Sweetser*

**a. General.** Construction of the water supply and sewage disposal systems for the entire Goldstone DSCC is scheduled for completion in March 1968.

**b. Pioneer DSS.** Construction has been completed on an addition to the laboratory building G-18. This extension provides 3200 ft<sup>2</sup> of additional floor space.

Upgrading of the air-conditioning systems in the control building G-1, the generator building G-3, and the hydromechanical building G-19 has been completed.

**c. Echo DSS.** Construction has been completed on the 3500-ft<sup>2</sup> addition to the communication building G-33 and the 5000-ft<sup>2</sup> addition to the logistical stores building G-38. Construction has also been completed on the new security building G-43.

Upgrading of evaporating cooling systems has been completed on the generator building G-27 and the warehouse building G-41.

Construction for the Echo cafeteria modification is scheduled to start in late May.

**d. Mars DSS.** Design studies have been initiated on the high-powered transmitter facilities. This project consists of a 600 ft<sup>2</sup> building located due north of the antenna

to house the transmitter/rectifier equipment. Also included are equipment pads for the large motor generator set, pure water equipment, pumps, and cooling towers. Design is scheduled for completion in May with construction scheduled for about January 1, 1969.

A single design and construction contract has been awarded for a new operations support building. This building is a two-story structure  $60 \times 90$  ft, of concrete block construction. The second floor contains a 3600-ft<sup>2</sup> control room plus offices. The first floor of the building contains a 3600-ft<sup>2</sup> air plenum to provide air cooling to electronic equipment above. The first floor also contains a 960 ft<sup>2</sup> communications room. An RF protection

tunnel has been provided leading from the operations support building to the antenna base. This tunnel is  $6 \times 8$  ft in cross section and will carry the power and signal cables connecting the antenna to the support building. Construction of this facility was started on February 28, 1968 with scheduled completion in late August of this year.

Construction has started on a smoke and fire detection system for the antenna control room and the R&D room in the alidade building of the 210-ft antenna.

Construction has been completed on increased evaporative cooling capacity in the generator building G-81.